Design, Syntheses, and Magnetic Properties of Dy(III)-based Single-Molecule Magnets and Isotopologues

Zur Erlangung des akademischen Grades eines

DOKTORS DER NATURWISSENSCHAFTEN

(Dr. rer. nat.)

von der KIT-Fakultät für Chemie und Biowissenschaften

des Karlsruher Instituts für Technologie (KIT)

genehmigte

DISSERTATION

von

M.Sc. Ting-Ting Ruan

aus

Shandong, China

Referent: Prof. Dr. Mario Ruben

Korreferentin: Prof. Dr. Annie Powell

Tag der mündlichen Prüfung: 24.04.2023

Declaration

I hereby declare that:

1. This work was done wholly while in candidature for a research degree at the KIT.

2. The whole thesis was written by me, and no other sources other than the specified were used.

3. The rules for ensuring the good scientific practice of the Karlsruhe Institute of Technology (KIT) have been used, and the submission and archiving of the primary data, in accordance with section A(6) of the rules for ensuring the good scientific practice of KIT, has been ensured.

4. The electronic version of the work is consistent with the written version.

5. Where I have consulted the published work of others, this is always clearly attributed.

6. I have acknowledged all main sources of help.

7. Where the thesis is based on work done by myself jointly with others, I have made clear exactly what was done by others and what I have contributed myself.

8. Furthermore, I declare that I did not undertake any previous doctoral studies, and I am currently not enrolled in any other ongoing doctoral procedure.

Ting-Ting Ruan

Deklaration

Ich erkläre:

1. Diese Arbeit wurde vollständig während der Kandidatur für ein Forschungsstudium am KIT durchgeführt.
2. Die gesamte Arbeit wurde von mir verfasst und es wurden keine anderen Quellen als die angegebenen verwendet.
3. Es wurden Maßnahmen zur Sicherstellung einer guten wissenschaftlichen Praxis des Karlsruher Instituts für Technologie (KIT) angewendet und die Übermittlung und Archivierung der Primärdaten gemäß Abschnitt A(6) der Regeln zur Sicherstellung einer guten wissenschaftlichen Praxis des KIT sichergestellt.
4. Die elektronische Fassung des Werkes entspricht der schriftlichen Fassung.
5. Im Fall, dass ich die veröffentlichten Arbeiten anderer konsultiert habe, wird dies immer eindeutig zugeordnet.
6. Ich habe alle wichtigen Hilfsquellen zur kenntlich gemacht.
7. Wenn die Arbeit auf Arbeiten basiert, die ich gemeinsam mit anderen geleistet habe, habe ich kenntlich gemacht, was von anderen geleistet wurde und was ich selbst beigesteuert habe.
8. Des Weiteren erkläre ich, dass ich kein vorheriges Promotionsstudium absolviert habe und mich derzeit nicht in einem anderen laufenden Promotionsverfahren befinde.

Ting-Ting Ruan

Table of contents

Abstract

Single-molecule magnets (SMMs) have a wide range of potential applications in molecular spintronics, high-density information storage materials, and quantum computing. Due to the inherent strong spin-orbital coupling effect and, consequently, the very high magnetic anisotropy of the $^6H_{15/2}$ ground state, Dy(III) ions are currently among the best candidates for SMMs. This thesis focuses on constructing Dy(III) single molecular magnets based on different β-diketonate and additional auxiliary ligands. The main work is be divided into the following three parts:

1. In Chapter 2, six mononuclear Dy(III) complexes are described based on four different β-diketonate ligands, tmhd, BTFA, NTFA, and hfac, as well as two auxiliary ligands, $POPh_3$ and 2,5-tpy. The synthesized complexes are $[Dy(thmd)_3(POPh_3)]$ (2-**1**), $[Dy(thmd)_3(2,5\text{-tpy})]$ (2-**2**), $[Dy(BTFA)_3(2,5\text{-tpy})]$ (2-**3**), $[Dy(NTFA)_3(2,5\text{-tpy})]$ (2-**4**), $[Dy(NTFA)_3(2,5\text{-tpy})\cdot C_2H_5OH]$ (2-**5**), and $[Dy(hfac)_3(2,5\text{-tpy})(H_2O)\cdot(2,5\text{-tpy})]$ (2-**6**). The Dy(III) ion in complex 2-**1** is placed in a N_2O_5 coordination environment. The overall geometry is best described as a capped octahedron with C_{3v} ligand field symmetry around the Dy(III). In complexes 2-**2**, 2-**3**, 2-**4**, and 2-**5**, the Dy(III) ions are placed in a N_2O_6 coordination environment. The geometry of the complexes is best described as square antiprism with D_{4d} symmetry. The coordination geometry of complex 2-**6** is the spherical capped square antiprism with C_{4v} symmetry; the Dy(III) ion is placed in the N_2O_7 coordination environment. Magnetic investigations evidence that all the complexes are SMMs with energy barriers (U_{eff}) of 35.5 K (2-**1**, H_{dc} = 1200 Oe), 36.7 K (2-**2**, H_{dc} = 800 Oe), 16.6 K (2-**3**, H_{dc} = 0 Oe), 75.5 K (2-**4**, H_{dc} = 0 Oe), 63.9 K (2-**5**, H_{dc} = 0 Oe), 5.3 K (2-**6**, H_{dc} = 800 Oe). The unique relaxation properties exhibited by the complexes are a result of the varying coordination environment surrounding the Dy(III) ions. This work demonstrates that the SMM properties can be modulated by subtle changes in the coordination environment resulting from changes in the substituents of β-diketonate ligands.

2. In Chapter 3, seven dinuclear Dy(III) complexes are successfully synthesized using isotopically enriched ^{163}Dy(III), ^{164}Dy(III) and commercial Dy(III) with three distinct sets of bridging ligands, 2,2':5',5'':2'',2'''-Quaterpyridine (bisbpy), 1,6,7,12-Tetraazaperylene (TAPE), 3,6-bis(2-pyridyl)-1,2,4,5-tetrazine (bptz) as well as three *β*-diketonates as co-ligands, tmhd, BTFA, and NTFA. In case of the bptz ligand we observed an unexpected ring opening reaction forming N'-[(E)-pyrazin-2-yl)methylidene]pyrazine-2-carbohydrazonate (PHZP). The following are the structural formula of the complexes: $[(Dy(tmhd)_3)_2(bisbpy)\ CH_2Cl_2]$ (3-**1**), $[^{163}Dy_2(tmhd)_6(TAPE)]$ (3-**2**), $[^{164}Dy_2(tmhd)_6(TAPE)]$ (3-**3**), $[Dy_2(BTFA)_6(TAPE)]$ (3-**4**) $[Dy_2(NTFA)_6(TAPE)]$ (3-**5**), $[(^{163}Dy(BTFA)_2)_2(PHZP)_2]$ (3-**6**) and $[(^{164}Dy(BTFA)_2)_2(PHZP)_2]$ (3-**7**). For complexes 3-**1** – 3-**5**, all the Dy(III) ions are placed in the N_2O_6 coordination environment, the Dy(III) ions of complex 3-**1** are both with D_{4d} symmetry, while the geometries of all the Dy(III) ions are best described as with D_{2d} symmetry for complexes 3-**2**, 3-**3**, and 3-**5**, and D_{4d} symmetry for complex 3-**4**. In complexes 3-**6** and 3-**7**, the Dy1 ions are in a spherical tricapped trigonal prism D_{3h} symmetry. For Dy2 in 3-**6** and 3-**7**, the geometry is better described as a Muffin architecture with *C*s symmetry. All complexes are zero field SMMs— U_{eff} values of 30.8 (3-**1**), 80.6 (3-**2**), 73.3 (3-**3**), 47.0 (3-**4**), 24.5 K (3-**5**), 50.7 (3-**6**), and 57.1 K (3-**7**) are obtained. Comparing complexes 3-**2**-3-**5**, the lowest energy barrier is observed in complex 3-**5** due to the presence of electron-donating groups in the *β*-diketonate co-ligands. This indicates that it is possible to tune the magnetic properties of dinuclear Dy(III) complexes by changing the substituents on the *β*-diketonate ligands. The results of the μ-SQUID experiments, at low temperatures, between 3-**2**$^{(I = 5/2)}$, 3-**3**$^{(I = 0)}$ and 3-**6**$^{(I = 5/2)}$, 3-**7**$^{(I = 0)}$ showed that the nuclear spin plays a crucial part in the relaxation process, and the Dy-Dy distances impact the strength of the intramolecular exchange coupling.

3. Chapter 4, two trinuclear Dy(III) complexes—$[Dy_3(tmhd)_9(TBB)]$ (4-**1**) and $[Dy_3(tmhd)_9(TBPB)\cdot CH_2Cl_2]$ (4-**2**)—are successfully synthesized using two different bridging ligands, 1,3,5-tri(2,2′-bipyridin-5-yl)benzene (TBB) and 1,3,5-tris{[2,2'-bipyridin-5-ylethynyl]phenyl}benzene (TBPB) and the same *β*-diketonate ligand,

tmhd, namely. In both complexes, the Dy(III) ions are in square-antiprismatic N_2O_6 coordination environment with D_{4d} axial symmetry. The complexes are zero field SMMs with U_{eff} = 75.6 K (4-**1**) and 92.5 K (4-**2**), as inferred from the AC susceptibility measurements. The determined U_{eff} values for the complexes are nominal despite the axially symmetric ligand field around the Dy(III) ions. The different natures of the N-donor ligands induce changes in the coordination microenvironment, giving rise to distinct dynamic magnetic behaviors.

Zusammenfasung

Einzelmolekülmagnete (SMMs, single molecule magnets) haben ein großes Spektrum an potenziellen Einsatzgebieten in z.B. molekularer Spintronik, Datenspeichern mit hoher Aufzeichnungsdichte oder in Quantencomputern. Aufgrund der starken Spin-Bahn Kopplung und dem daraus resultierenden stark anisotropen $^6H_{15/2}$ Grundzustand, sind Dy(III) Ionen die derzeit vielversprechendste Basis für SMMs. Diese Thesis behandelt Dy(III)-Einzelmolekülmagnete auf Basis von unterschiedlichen *β*-Diketonat- sowie zusätzlichen Hilfsliganden. Die Arbeit ist in folgende drei Abschnitte unterteilt:

1. Kapitel 2: Es wurden sechs mononukleare Dy(III) Komplexe, basierend auf vier verschiedenen *β*-Diketonatliganden (tmdh, BTFA, NTFA, hfac) und zwei Hilfsliganden ($POPh_3$, 2,5-tpy), synthetisiert. Die gefundenen Komplexe sind $[Dy(tmhd)_3(POPh_3)]$ (2-**1**), $[Dy(tmhd)_3(2,5\text{-tpy})]$ (2-**2**), $[Dy(BTFA)_3(2,5\text{-tpy})]$ (2-**3**), $[Dy(NTFA)_3(2,5\text{-tpy})]$ (2-**4**), $[Dy(NTFA)_3(2,5\text{-tpy})\cdot C_2H_5OH]$ (2-**5**) und $[Dy(hfac)_3(2,5\text{-tpy})(H_2O)\cdot(2,5\text{-tpy})]$ (2-**6**). Das Dy(III) Ion in Komplex 2-**1** befindet sich in einer N_2O_6 Koordinationsumgebung, die am besten als überkapptes Oktaeder mit C_{3v} Symmetrie beschrieben wird. In den Komplexen 2-**2**, 2-**3**, 2-**4** und 2-**5** befindet sich das Dy(III) Ion ebenfalls in einer N_2O_6 Umgebung, allerdings besser beschrieben als quadratisches Antiprisma mit D_{4d} Symmetrie. Die Koordinationsgeometrie in Komplex 2-**6** ist ein kugelförmiges quadratisches Antiprisma mit C_{2v} Symmetrie, bei der sich das Dy(III) in einer N_2O_7 Umgebung befindet. Magnetische Untersuchungen haben gezeigt, dass alle dieser Komplexe SMMs sind. Die Energiebarrieren (U_{eff}) wurden bestimmt mit 35,5 K (2-**1**, H_{dc} = 1200 Oe), 36,7 K (2-**2**, H_{dc} = 800 Oe), 16,6 K (2-**3**, H_{dc} = 0 Oe), 75,5 K (2-**4**, H_{dc} = 0 Oe), 63,9 K (2-**5**, H_{dc} = 0 Oe) und 5,3 K (2-**6**, H_{dc} = 800 Oe). Die jeweiligen Relaxationseigenschaften ergeben sich durch die veränderte Koordinationsumgebung der Dy(III) Ionen. Diese Arbeit zeigt, wie die SMM Eigenschaften, durch Änderungen der Substituenten der *β*-Diketonatliganden und der sich dadurch ändernden Koordinationsumgebung, beeinflusst werden können.

2. Kapitel 3: Unter Verwendung von isotopisch angereichertem ^{163}Dy und ^{164}Dy, sowie

mit kommerziell erhältlichem Dy wurden sieben dinukleare Dy(III) Komplexe erfolgreich synthetisiert. Basierend auf drei unterschiedlichen Brückenliganden, 2,2‘:5‘,5‘‘:2‘‘,2‘‘‘-Quarterpyridin (bisbpy), 1,6,7,12-Tetraazaperylen (TAPE) und 3,6-bis(2-pyridyl)-1,2,4,5-tetrazin (bptz), sowie drei verschiedenen *β*-Diketonatliganden, tmhd, BTFA und NFTA, wurden verschiedene Komplexe erhalten. Bei der Verwendung des bptz Liganden beobachtet wir eine unerwartete Ringöffnungsreaktion zu dem neuen Liganden N'-[(E)-pyrazin-2-yl)methylidene]pyrazine-2-carbohydrazonate (PHZP). Die erhaltenen Komplexe sind: $[(Dy(tmhd)_3)_2(bisbpy)\cdot CH_2Cl_2]$ (3-**1**), $[^{163}Dy_2(tmhd)_6(tape)]$ (3-**2**), $[^{164}Dy_2(tmhd)_6(tape)]$ (3-**3**), $[Dy_2(BTFA)_6(tape)]$ (3-**4**), $[Dy_2(NTFA)_6(tape)]$ (3-**5**), $[(^{163}Dy(BTFA)_2)_2(PHZP)_2]$ (3-**6**) und $[(^{164}Dy(BTFA)_2)_2(PHZP)_2]$ (3-**7**). In den Komplexen 3-**1**, 3-**2**, 3-**3**, 3-**4** und 3-**5** befinden sich die Dy(III) jeweils in einer N_2O_6 Umgebung mit D_{4d} Symmetrie, für die Verbindungen 3-**1** und 3-**4**, und mit D_{2d} Symmetrie in 3-**2**, 3-**3** und 3-**5**. In den Komplexen 3-**6** und 3-**7** befinden sich die Dy1-Positionen in einer kugelförmig dreifach überkappten trigonalen Prisma D_{3h}-Symmetrie. Die Dy2-Positionen werden besser beschrieben durch eine Muffin Struktur mit C_s-Symmetrie. Alle diese Komplexe sind SMMs ohne angelegtes externes Magnetfeld mit U_{eff} Werten von 30,8 K (3-**1**), 80,6 K (3-**2**), 73,3 K (3-**3**), 47,0 K (3-**4**), 24,5 K (3-**5**), 50,7 K (3-**6**) und 57,1 K (3-**7**). Vergleicht man die Komplexe 3-**2** bis 3-**5**, zeigt 3-**5** die niedrigste Energiebarriere, aufgrund der elektronenschiebenden Gruppen am *β*-Diketonat. Das beweist, dass der Austausch der Substituenten am *β*-Diketonat eine Möglichkeit darstellt, die magnetischen Eigenschaften dinuklearer Dy(III) Komplexe abzustimmen. Die Ergebnisse von μ-SQUID Messungen an 3-$\mathbf{2}^{(I = 5/2)}$, 3-$\mathbf{3}^{(I = 0)}$, 3-$\mathbf{6}^{(I = 5/2)}$ und 3-$\mathbf{7}^{(I = 0)}$, bei tiefen Temperaturen, zeigen das der Kernspin eine entscheidende Rolle für den Relaxationsprozess spielt und die Dy-Dy Entfernungen die Intensität der intramolekularen Austauschwechselwirkungen beeinflussen.

3. Kaptiel 4: Zwei trinukleare Dy(III) Komplexe – $[Dy_3(tmhd)_9(TBB)]$ (4-**1**) und $[Dy_3(tmhd)_9(TBPB)\cdot CH_2Cl_2]$ (4-**2**) – basierend auf den beiden Brückenliganden 1,3,5-tri(2,2‘-bipyridin-5-yl)benzol (TBB) und 1,3,5-tris{[2,2‘-bipyridin-5-ylenthynyl]phenyl}benzol (TBPB) sowie dem *β*-Diketonat tmhd, wurden erfolgreich synthetisiert. In beiden Komplexen befinden sich die Dy(III) Ionen in einer quadratisch

antiprismatischen N_2O_6 Koordinationsumgebung mit D_{4d} Symmetrie. Die Komplexe zeigen SMM Verhalten im Nullfeld mit U_{eff} = 75,6 K (4-**1**) und 92,5 K (4-**2**), bestimmt durch AC Suszeptibilitätsmessungen. Die Unterschiede der beiden N-Donorliganden bewirken geringe Veränderungen in der Mikroumgebung und führen dadurch zu unterschiedlichem magnetischem Verhalten.

Chapter 1. Introduction

1.1 Introduction to molecular magnetism

The amount of information is growing exponentially in the context of the present big data era, and how to store and process enormous amounts of information in a limited space has come to the forefront of discussion. Thus, the focus has been shifted towards the development of new storage and processing technologies, and the topic is of contemporary interest. Magnetic materials play an important role in the field of information technology[1,2]. However, the superparamagnetic effect of traditional magnetic materials restricts storage densities[3]. On the other hand, information processing technologies harnessing quantum effects, termed as quantum information processing (QIP), have been actively pursued to increase the processing speed[4]. It has been proposed that magnetic materials possessing exotic quantum magnetic phenomena such as quantum tunneling of magnetization (QTM) are useful for developing QIP architectures. Therefore, the development of magnetic materials featuring beneficial magnetic properties is necessary to increase storage density and create quantum information processing devices, such as quantum computers. A recent demonstration of the implementation of the Grover algorithm utilizing electronic and nuclear spin degrees of freedom is an important development in the context of the above discussion[5].
In recent times, molecule-based magnets have gained global attention due to their significance in both fundamental scientific research and technological advancements[6,7]. Compared with traditional magnetic materials, molecular magnetic materials have the advantages of low density, easy processing, and chemical controllability. With the application of new experimental techniques and the development of theoretical research, many novel magnetic phenomena have been discovered in molecular magnetic materials[8-11], especially the study of single-molecule magnets (SMMs) that can exhibit hysteresis behavior similar to traditional magnets at the molecular limit.
SMMs are a novel class of materials characterized by their slow relaxation of magnetization and related magnetic properties, which are determined by the properties of individual molecules rather than a bulk region. This unique property offers the potential to store information in each molecule, making SMMs promising for future data storage technologies[12,13]. Additionally, the quantum mechanical phenomena that

occur within the molecules, such as quantum tunneling, make SMMs a potential candidate for use in quantum computers[14-16]. The first single-molecule magnet (SMM), $[Mn_{12}O_{12}(O_2CMe)_{16}(H_2O)_4]$[17], which displayed magnetic hysteresis below a specific blocking temperature (T_B) was discovered in the early 1990s. The properties of these magnets have been studied in-depth during the past three decades and their application propensity have been demonstrated. However, realistic technological application based on SMMs is yet to be achieved. Therefore, development and studies on novel SMMs are necessary to understand the factors controlling SMM characteristic. Such a knowledge would be handy to harness SMMs with technologically relevant magnetic properties.

1.2 Single-molecule magnets (SMMs)

The first reported SMMs have been metal cluster molecules composed exclusively of transition metal ions and organic molecules. These multi-metal complexes display characteristics similar to superparamagnetism and demonstrate magnet-like behavior below their blocking temperature. In order for a complex to exhibit SMM behavior, it must fulfill two specific requirements: a large spin ground state (S) and a negative uniaxial anisotropy (D). The energy barrier for spin reversal is given by $S^2|D|$ and (S^2-1/4)|D| for integer and half-integer spins, respectively.

Although the synthesis of $[Mn_{12}O_{12}(O_2CMe)_{16}(H_2O)_4]$ (Mn_{12}) was carried out by Lis[18] in 1980, it was not until the early 1990s that the SMM property was discovered by R. Sessoli et al[8]. As shown in Figure. 1.1, the Mn_{12} complex is comprised of four Mn^{IV}

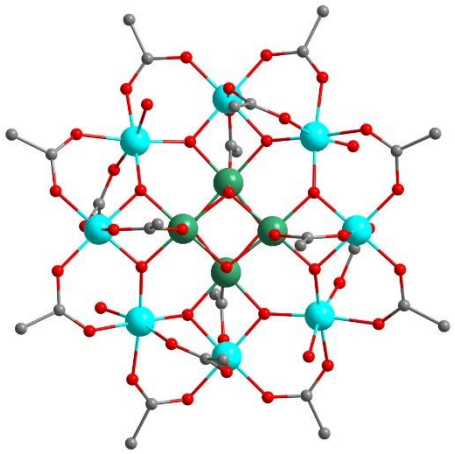

Figure 1.1 The molecular structure of $\{Mn_{12}\}$. Hydrogen atoms have been omitted for clarity. Color code: bright blue (Mn^{III}), dark green (Mn^{IV}), red (O) and grey(C).

ions (S = 3/2) located in the center of the cluster and eight Mn^{III} ions (S = 2) located in the periphery of the cluster. All Mn^{III} ions in the outside shell are ferromagnetically coupled, while Mn^{IV} ions are also ferromagnetically coupled with each other inside the cubic center. These two sets of Mn ions interact to produce an anti-ferromagnetic coupling, leading to a ground state of S = 10.

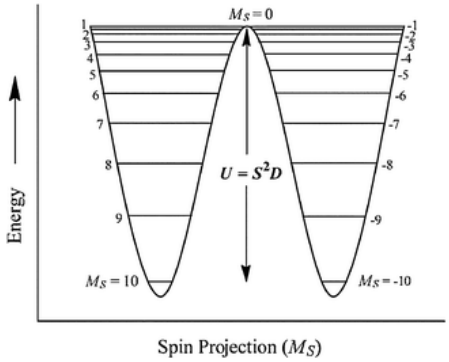

Figure 1.2 The energy barrier U_{eff} for the reversal of the spins between the spin 'up' (M_s = 10) and 'down' (M_s = -10) state for Mn_{12} complex. Copyright © 2009, Royal Chemical Society.

The energy barrier which is approximately $S^2|D|$ will separate the two sub levels, these sub-levels correspond to the spin-up and spin-down states, with m_s = 10 and -10, respectively (Figure 1.2). The variations in spin orientations give rise to the possible uses of SMMs in information storage. When the temperature is raised, the thermal energy will exceed the energy barrier between the two states as a result of thermal agitation. Above the blocking temperature, the molecule will turn paramagnetic and stop functioning as a magnet. The application of SMMs in information storage is restricted due to the randomization of spins, which causes the loss of information. Hence, the primary focus of this field is to synthesize SMMs with high energy barriers, achieved through techniques that either enhance the total spin ground state of a molecule or increase its magnetic anisotropy.

Since the discovery of the first transition metal single-molecule magnet Mn_{12}, a large number of transition metal Mn cluster single-molecule magnets have been reported[19-22]. In addition, single-molecule magnets based on transition metal clusters of Fe[23-26], Co[27-31], Ni[32,33], V[34-36], have also been reported. In order to obtain a single-molecule magnet with superior performance, it is necessary to obtain a molecule with a high spin ground state and a large uniaxial magnetic anisotropy. Early researchers have been focusing on the synthesis of multinuclear transition metal SMMs to improve the ground state spin. In 2016, the Powell research team reported that the ground state spin value

S of $Mn^{III}_{12}Mn^{II}_{7}$ compounds reached 83/2. Nonetheless, the anisotropy parameter D is nearly zero[37]. A subsequently reported multinuclear Mn_{84} complex showed a ground-state spin value of only 6, and does not exhibit the expected behavior of high-energy-barrier SMM[38]. The magnetic anisotropy and magnetic interaction of two Mn_6 clusters with comparable structures were examined by Ruiz and colleagues in 2008, and the findings revealed that the anisotropy energy barrier is primarily dependent on the strength of the spin-orbit coupling, and cannot be achieved only by raising S and D values[39]. Many findings demonstrate that it is frequently challenging to achieve both a large uniaxial magnetic anisotropy and a high spin ground state in the same system. Consequently, it is not possible to create single-molecule magnets with large energy barriers solely by increasing the ground state spin value.

Based on the above research results, the researchers found that the introduction of paramagnetic rare earth metal ions (Ln^{III}) into SMMs may better tackle the above problems. The reason is that the presence of a large number of unpaired electrons and strong spin-orbit coupling in paramagnetic rare earth ions. Paramagnetic rare earth ions possess unquenched orbital angular momentum, which leads to the generation of stronger magnetic anisotropy. As a result, Ln^{III}-based SMMs can exhibit more pronounced spin reversal barriers than their transition metal counterparts, thereby presenting a novel approach for creating single-molecule magnets with high-energy barriers[40].

1.3 Ln^{III} SMMs

1.3.1 Mononuclear Ln-SMMs

The mononuclear SMMs (single-ion magnets, SIMs) exhibit a relatively simple molecular structure, which renders them a good theoretical model for understanding SMMs. The magnetodynamic behavior of SIMs is related to the following factors: 1. The spin ground state of metal ions; 2. Magnetic anisotropy caused by spin-orbit coupling; 3. The symmetry of the crystal field. Among them, the high symmetry crystal field can effectively suppress the QTM process. Therefore, in order to enhance the performance of Dy(III)-SMMs, it is important to create high ligand field symmetry around Ln^{III} ions; square prism (D_{4d}), pentagonal bipyramidal (D_{5h}), hexagonal bipyramidal (D_{6h}) and linear dicoordinated ($C_{\infty v}$) ligand field configurations are

desirable.

In 2003, Ishikawa et al. discovered the first examples of rare earth single ion $[Pc_2Ln]^-$ (Ln = Tb, Dy; Pc = dianion of phthalocyanine) SMMs[41]. As shown in Figure 1.3a, the central Ln^{III} ion is sandwiched by the two Pc ligands. Both complexes exhibit the slow magnetization relaxation behavior. The spin reversal energy barrier of the diluted complexes are 230 cm^{-1} and 28 cm^{-1} for $[Pc_2Tb]^-$ and $[Pc_2Dy]^-$, respectively. In the same year, Ishikawa et al. also tested the magnetic susceptibility and calculated the energy separation between m_J states of ground state multiplets in a series of isomorphic complexes[42], and the results showed that only the ground states of Tb^{III} and Dy^{III} ions have large angular momentum quantum numbers, which is the key to the behavior of SMMs. In 2004, a neutral $[Pc_2Ln]^0$ having an open shell π electronic system was synthesized by one-electron oxidation of $[Pc_2Ln]^-$ occurs on the ligand side[43]. The magnetic results indicated that the oxidation of ligands in the anionic $[Pc_2Ln]^-$ complex caused a significant increase in the temperature range where the magnetization response displayed a phase lag in response to the time-varying external magnetic field. In the π-radical $[Pc_2Ln]^0$ complex, the peaks of the out-of-phase component of AC susceptibility were observed at 50, 43, and 36 K, respectively, with AC magnetic fields of 10^3, 10^2, and 10 Hz. These values were more than 10 K higher compared to the corresponding values of the anionic complex that had a closed-shell π-system (Fig 1.4). In 2008, the anionic $[Pc_2Ln]^-$ complexes are oxidized to form two cationic complexes $[Pc_2Tb]^+$ and $[Pc_2Dy]^+$ by the same group. The oxidation of the complexes causes the coordination polyhedron to contract longitudinally, as shown in Figure 1.5. This contraction leads to a notable rise in the effective barrier for spin reversal[44].

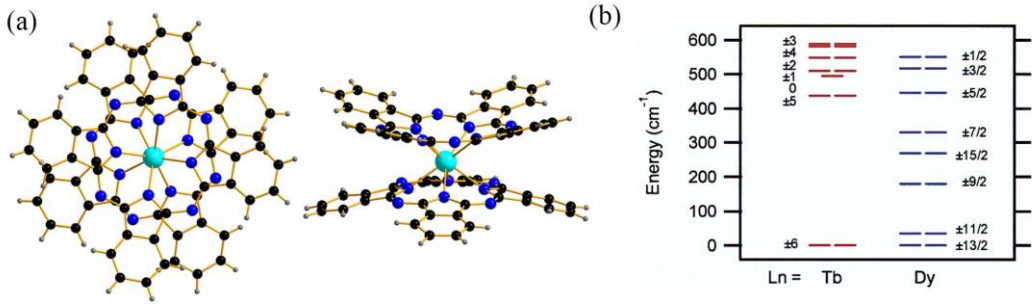

Figure 1.3 (a) The molecular structure of $[Pc_2Ln]^-$. Bright blue (Ln = Tb, Dy), dark blue (N), black (C) and grey (H). (b) Energy diagram for the ground-state multiplets of $[Pc_2Ln]^-$ (Ln = Tb, Dy, Ho, Er, Tm, or Yb). Copyright© 2011, Royal Chemical Society.

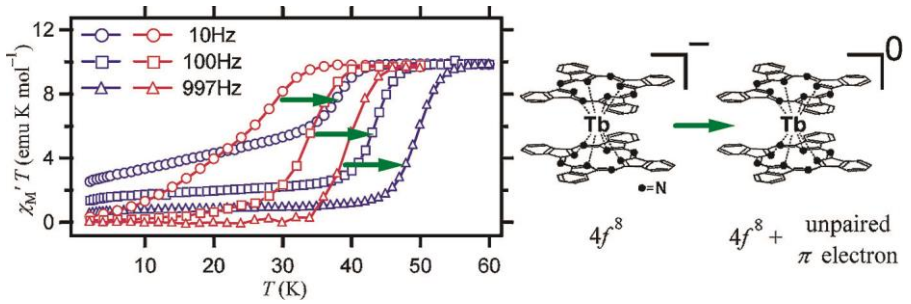

Figure 1.6 Plots of $\chi_M'T$ against temperature T for sample of $[Pc_2Tb]^0$ (purple line) and $[Pc_2Tb]^-$ (red line) under an zero-dc field (right). Structures of $[Pc_2Tb]^0$ (purple line) and $[Pc_2Tb]^-$ (right). Copyright © 2004, American Chemical Society.

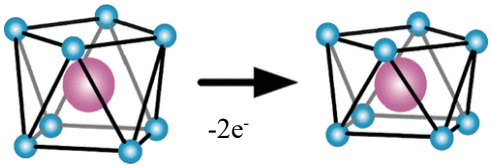

Figure 1.5 Longitudinal Contraction of a Square-Antiprism Coordination Polyhedron. Adapted with permission from ref 42.

Subsequent studies have shown that the effective energy barrier of the complex can be improved by modifying the phthalocyanine ligand (Figure 1.6). The sandwich-type tetrapyrrole lanthanide SIM (Pc)Tb{Pc[N(C_4H_9)$_2$]$_8$} which Jiang et al. published in 2017 has the highest magnetic performance of PC-derived material to date, with a high blocking temperature (T_B) of 30 K and a significant effective spin-reversal energy barrier of U_{eff} = 939 K[45].

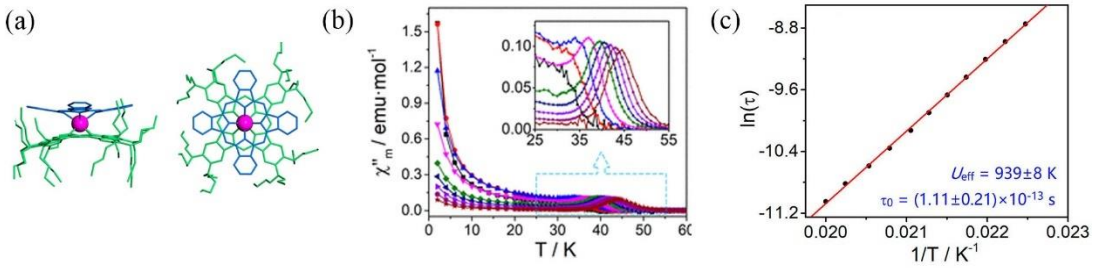

Figure 1.4 Single crystal molecular structures of {(Pc)Tb{Pc[N(C_4H_9)$_2$]$_8$} (a) in side (left) and top (right) view with all H and disorder C atoms omitted for clarity. Tb (purple), unsubstituted Pc (blue), Pc[N(C_4H_9)$_2$]$_8$ (green). (b) Temperature dependence of out-of-phase (χ'') ac magnetic susceptibility of (Pc)Tb{Pc[N(C_4H_9)$_2$]$_8$}. (c) The plots of ln(τ) vs. 1/T for {(Pc)Tb{Pc[N(C_4H_9)$_2$]$_8$}. Copyright © 2017, American Chemical Society.

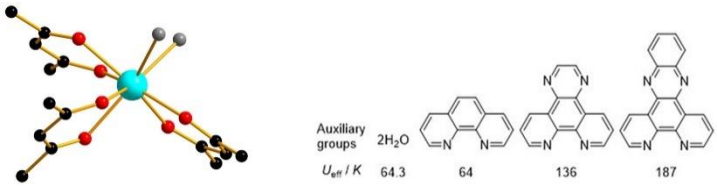

Figure 1.7 Structures of the *β*-diketone-based dysprosium (III) complexes. Bright blue (Dy), red (O), black (C) and grey (auxiliary groups). Reproduced from Ref. 44, 50.

A number of Ln-SMMs compounds based on *β*-diketones [Ln(acac)$_3$(H$_2$O)$_2$] (Ln = Dy, Ho, or Er, and acac = acetylacetonate) with a local symmetry close to D_{4d} were published in 2010 by Gao Song's research team[46] (Fig 1.7). The effective energy barrier of [Dy(acac)$_3$(H$_2$O)$_2$] is 64.3 K. Dynamic study clearly shows the thermal magnetic relaxation and QTM process below 8 K. The quantum tunneling is suppressed by dilution or application of a magnetic field. Meanwhile, the thermally activated relaxation happens in the broader temperature range, and the hysteresis loop becomes more apparent. Later, a large number of analogs SMMs with different diketonates were reported[47-49]. Upon ligand substitution, Tang's team notices a significant improvement in the anisotropy barriers, which can approach 187 K. Remarkably, the combination of large anisotropic Dy^{III} ions and the careful selection of an auxiliary ligand, provides a promising new method for the production of record anisotropy barriers[50-52].

In 2019, Tong's group reported a Dy(III) SIM, [Dy(bbpen)(tpo)$_2$][BPh$_4$] (bbpen = N,N'-bis(2-hydroxybenzyl)-N,N'-bis(2-picolyl)ethylene-diamine, tpo = triphenylphosphine oxide), with an energy barrier of 944 K under zero dc field and an open hysteresis loop up to 6 K (Figure 1.8). This is the highest energy barrier for a square antiprism (D_{4d}) and phosphine oxide-based Dy-SIM that has been reported[53]. The mixed ligands

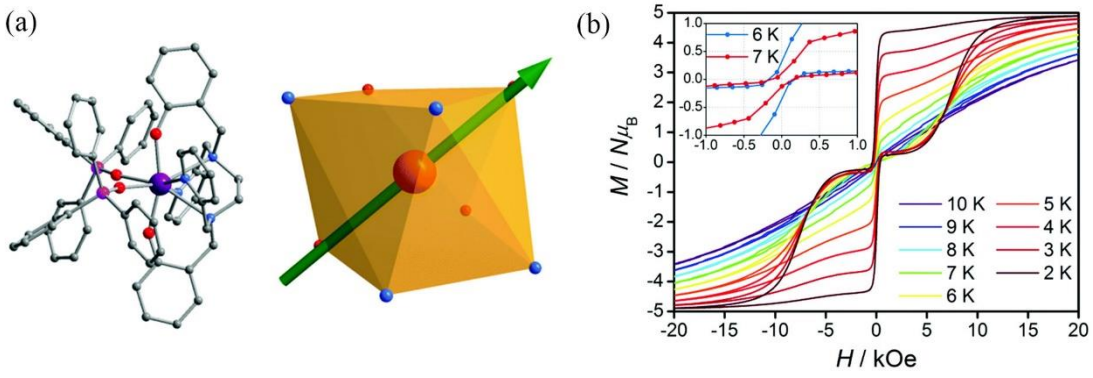

Figure 1.8 Crystal structure (a) and Variable-field magnetization data (b) of [Dy(bbpen)(tpo)$_2$][BPh$_4$]. Copyright © 2019, Royal Chemical Society.

approach involving bbpen^{2-} and tpo modify not only controls the shape of the Dy-SIM but also the energy barrier. The substantially shorter Dy-O_{bbpen} lengths, which provide a very uniaxial magnetic anisotropy, are primarily responsible for the high energy barrier.

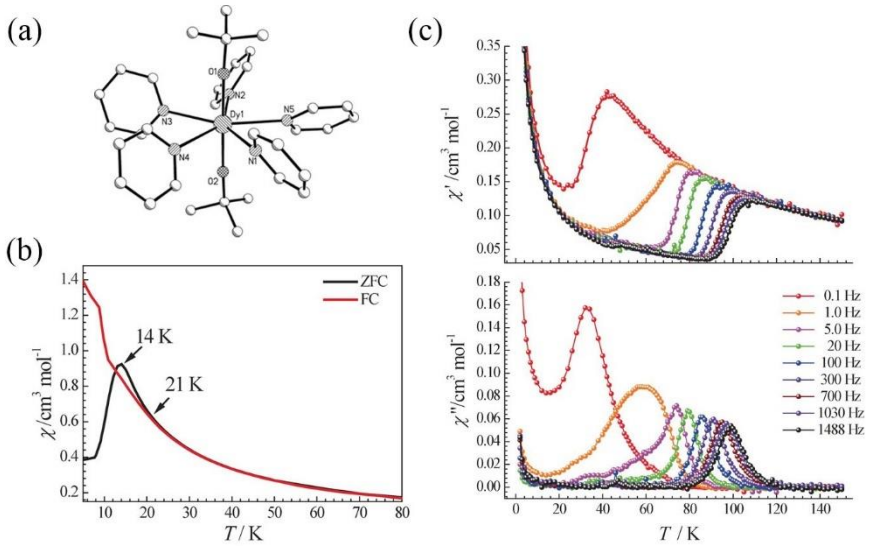

Figure 1.9 (a) Structure of the $[Dy(O^tBu)_2(py)_5]^+$ (b) Variable-temperature magnetic susceptibility of $[Dy(OtBu)_2(py)_5][BPh_4]$, under field-cooled (FC) and zero-field-cooled (ZFC) conditions with a field of 2000 Oe (c) Variable-temperature in-phase (top) and out-of-phase (bottom) magnetic susceptibility of $[Dy(OtBu)_2(py)_5][BPh_4]$ under zero dc field. Copyright © 2016 Wiley‐VCH Verlag GmbH & Co. KGaA, Weinheim.

In addition, all transverse crystal field parameters can be suppressed in SIMs with D_{5h} symmetry, which represents a new development in blocking temperature and the effective energy barrier[54-57]. Zheng Yanzhen's group reported a Dy SIM $[Dy(OtBu)_2(py)_5][BPh_4]$ (Fig 1.9)[58]. The Dy^{III} site is coordinated with two O-donors which are occupying the axial sites of a pentagonal bipyramidal coordination geometry and five N-donors from equatorial pyridine. The Dy···O bond lengths are between 2.110(2) and 2.114(2) Å while the Dy···N bonds fall in the range of 2.534(3) – 2.580(3) Å. The anionic donors will dominate the electronic structure because they are much closer to the Dy^{III} ion than the neutral ligands. The bond angles are close to those expected for a pentagonal bipyramid: O-Dy-O = 178.91(9)°, O-Dy-N angles are in the range 87.41(9) to 92.52(9)°, and the N-Dy-N angles are between 70.33(9) to 74.41(9)°. These bond length and bond angle data indicate that this molecule has a near-perfect D_{5h} configuration, which greatly enhances the axial magnetic anisotropy of the complex.

The measurement shows the largest effective energy barrier U_{eff} =1815(1) K. The blocking temperature, T_B, is 14 K. Alternating current susceptibility studies show peaks in χ'' above 100 K, as shown in Figure 1.9c.

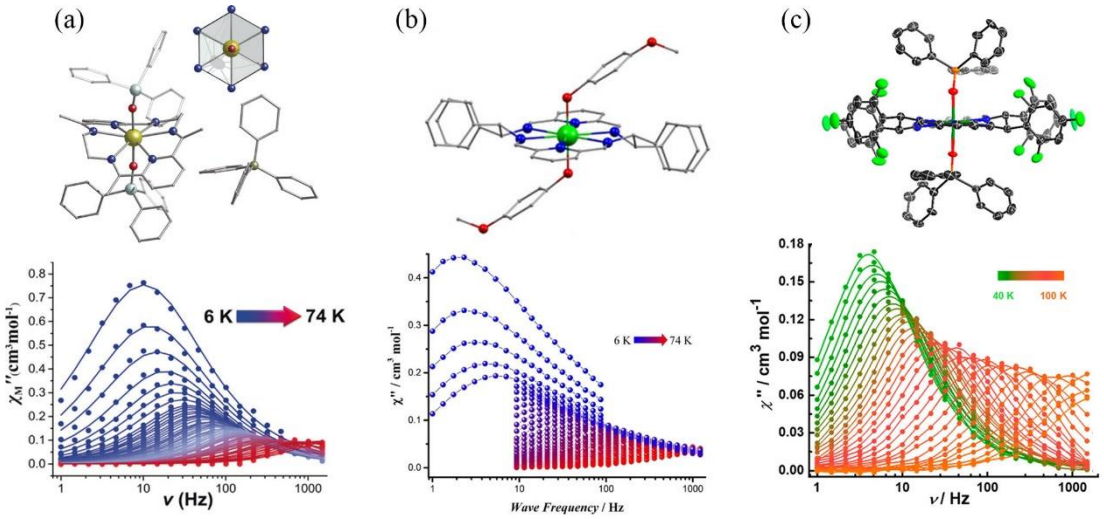

Figure 1.10 Structures (top) and $\chi''(\upsilon)$ plots (bottom) of complexes: (a) $[Dy(L^{N6})(Ph_3SiO)_2](BPh_4)$. © 2019 Wiley-VCH Verlag GmbH & Co. KGaA, Weinheim. (b) $[Dy^{III}(L^{E})(4\text{-MeO-PhO})_2](BPh_4)\cdot 3THF$. © 2019 Wiley-VCH Verlag GmbH & Co. KGaA, Weinheim. (c) $[Dy(L^{N6})(Ph_3SiO)_2](BPh_4)$. Copyright © 2021, American Chemical Society.

High energy barriers are also present in Ln SIMs with D_{6h} coordination arrangements as shown recently[59-62]. In 2019, Mark Murrie's research group reported a set of hexagonal bipyramidal SMMs $[Dy(L^{N6})(Ph_3SiO)_2](BPh_4)$ and $[Dy(L^{N6})(2,4\text{-di-}^{t}Bu\text{-PhO})_2](BPh_4)$ (Ph_3SiO^- = anion of triphenysilanol, 2,4-di-^{t}Bu-PhO$^-$ = anion of 2,4-di-tertbutylphenol and L^{N6} = N6-hexagonal plane accomplished by the neutral Schiff base ligand formed from 2,6-diacetylpyridine and ethylenediamine). The complexes are produced by coupling the weak equatorial field of the ligand L^{N6} with the strong uniaxial ligand fields produced by the Ph_3SiO^- or 2,4-di-^{t}Bu-PhO$^-$ ligands[61]. As shown in Figure 1.10a, structural analysis shows that the six Dy-N bond lengths at the equator are between 2.6057 – 2.635 Å, and the equatorial N-Dy-N angle is between 79.71 – 97.85°. The two Dy-O bond lengths in the axial position are 2.1425 Å and 2.1514 Å, respectively, and the axial O-Dy-O angle is 176.13°. AC magnetic measurements show that the complex $[Dy(L^{N6})(Ph_3SiO)_2](BPh_4)$ shows the $\chi''(\upsilon)$ peaks in the temperature range of 6-74 K. The U_{eff} reaches 1124 K, far exceeding the values reported for similar complexes[63-65]. However, the T_B of this complex is only 5 K. In the same year, Zheng Yanzhen's research group realized the regulation of the effective energy barrier of this

series of complexes by changing the axial ligand, from 1100 K to 1338 K (Fig 1.10b)[60]. In 2021, Tang Jinkui's research group formed a chiral macrocyclic ligand and introduced F substituents in the equatorial ligands (Fig 1.10c), reducing the electron donating ability of the ligands. The strategy resulted in the observation of U_{eff} = 1833 K, and T_B = 20 K[62]; the values are higher than the ones obtained for the unsubstituted ones. Overall, the authors showed a new way for the construction of chiral high-performance SMMs.

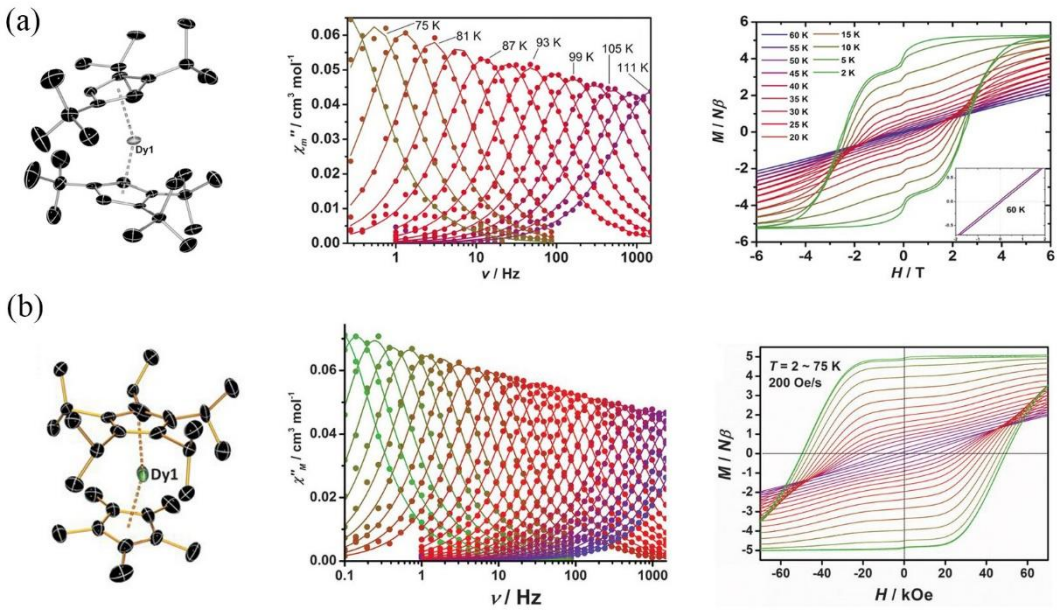

Figure 1.11 Structures, $\chi''(\upsilon)$ and hysteresis loops of complexes: (a) $[Dy(Cp^{ttt})_2][B(C_6F_5)_4]$, (b) $[(\eta^5\text{- Cp*})Dy(n^2\text{- Cp}^{iPr5})][B(C_6F_5)_4]$. Copyright © 2017 Wiley-VCH Verlag GmbH & Co. KGaA, Weinheim.

Although high symmetry can provide a strong axial crystal field, recent studies have shown that strict space group symmetry is not a necessary condition to obtain a high axial crystal field[66-68]. A case of Dy cyclopentadiene metallocene $[Dy(Cp^{ttt})_2][B(C_6F_5)_4]$ (Cp^{ttt} = 1,2,4-tri(tert-butyl)cyclopentadienide)) was reported almost simultaneously by the research groups of David P. Mills and Richard A. Layfield in 2017[66,67]. As shown in Figure 1.11, the researchers used the silane reagent $[H(SiEt_3)_2][B(CF_5)_4]$ to remove the chloride ions coordinated at the equatorial position in the precursor $[Dy(Cp^{ttt})_2(Cl)]$, reducing the equatorial ligand field. It is worth noting that the compound does not show high symmetry. The distances from Dy^{3+} to the two cyclopentadiene ligand centers are 2.318 Å and 2.314 Å, respectively. The angle formed between two cyclopentadiene ligand centers and Dy^{3+} is 152.56°, but the U_{eff} of the complex reaches 1760 K, and T_B reaches 60 K. The author proves through theoretical calculations that the reason for the

lack of quantum tunneling processes under zero field is that the unique coordination geometry of two η^5-Cp^{ttt} ligands produces confined metal-ligand vibration modes that lead to unique spin-phonon coupling. In 2018, Richard A. Layfield's group modified two cyclopentadiene ligands, using a large sterically hindered pentaisopropyl cyclopentadiene ligand and a small sterically hindered pentamethyl cyclopentadiene ligand, another example of Dy metallocene $[(\eta^5\text{- Cp*})Dy(n^2\text{- } Cp^{iPr5})][B(C_6F_5)_4]$ was synthesised[68]. Compared with the complex $[Dy(Cp^{ttt})_2][B(C_6F_5)_4]$, the angle between the two cyclopentadiene/cyclopentadienyl ligand centers and Dy^{3+} increases to 162.51°, The distance between Dy^{3+} to the two cyclopenta ligand centers is also reduced to 2.296 Å and 2.284 Å, which provides a stronger axial ligand field. Magnetic tests show that the U_{eff} of the complex reaches 1541 cm^{-1} (2217 K), and T_B reaches 80 K; for the first time T_B above liquid nitrogen temperature was achieved. The interesting results discussed above stimulated extensive research interest in Dy cyclopentadiene metallocene-based SMMs[69-71].

1.3.2 Dinuclear Ln-SMMs

Although mononuclear lanthanide complexes have demonstrated potential in achieving high energy barriers for magnetization reversal, their ability is limited to the Single-Ion Magnet behavior intrinsic to a single metal center and a limited number of unpaired electrons. To increase the effective anisotropic barrier, researchers have been seeking systems with higher nuclearity to enhance the molecule's spin ground state. Dinuclear complexes are essential compounds in investigating and comprehending magnetism due to their straightforward structural motif and advantages over SIMs. One key advantage is that the SMM behavior of dinuclear complexes can be effectively adjusted by magnetic interactions, such as dipolar interactions and exchange coupling. Moreover, recent investigations have demonstrated that QTM can be efficiently suppressed at low temperatures by intramolecular magnetic interactions[72,73].

The radical bridging ligands possessing diffuse spin orbitals that can permeate the core electron density of lanthanide ions, where the 4f spin orbitals are deeply embedded, is a viable approach to attain strong coupling. Long's group reported an N_2^{3-} radical-bridged dinuclear Dy^{III} SMM, $\{[(Me_3Si)_2N]_2(THF)Dy\}_2(\mu\text{-}\eta^2\text{:}\eta^2\text{-}N^2)$[74]. As shown in Figure 1.12, the magnetic studies give an energy barrier of U_{eff} = 178 K, blocking temperature T_B = 8.3 K. Applying a sweep rate of 0.08 T s^{-1}, the hysteresis loop remains

virtually unchanged from 2 to 6 K, with a coercive field of 1.5 T. In the same year, a second N_2^{3-} radical-bridged Tb complex, $\{[(Me_3Si)_2N]_2(THF)Tb\}_2(\mu\text{-}\eta^2\text{:}\eta^2\text{-}N^2)$ was reported by the same group[75]. It exhibits magnetic hysteresis at 14 K and a 100 s blocking temperature of 13.9 K. In 2017, based on $\{[(Me_3Si)_2N]_2(THF)Dy\}_2(\mu\text{-}\eta^2\text{:}\eta^2\text{-}N^2)$, with replacement of $[(Me_3Si)_2N]^-$ with $[Cp^{Me4H}]^{1-}$, they synthsised a new N_2^{3-} radical-bridged Tb dinuclear, $[K(crypt\text{-}222)(THF)][(Cp^{Me4H}{}_2Tb(THF))_2(\mu{-}N_2)]$ (crypt-222 = 2.2.2-cryptand, THF = tetrahydrofuran, Cp^{Me4H} = tetramethylcyclopentadienyl)[76]. Reducing the coordination number of the metal centers appears to increase axial magnetic anisotropy giving rise to a larger magnetic relaxation barrier of 397 K and 100-s magnetic blocking temperatures of up to 20 K. This means that there is a clear path toward better single-molecule magnets of this type: replacing N_2^{3-} with a radical bridge that offers stronger exchange coupling can be expected to increase the U_{eff} significantly. Further adjustment of the ligand field resulting from the capping ligands can enhance axiality, preventing the observed blocking temperature from being reduced by through-barrier relaxation processes and potentially yielding even higher coercive fields.

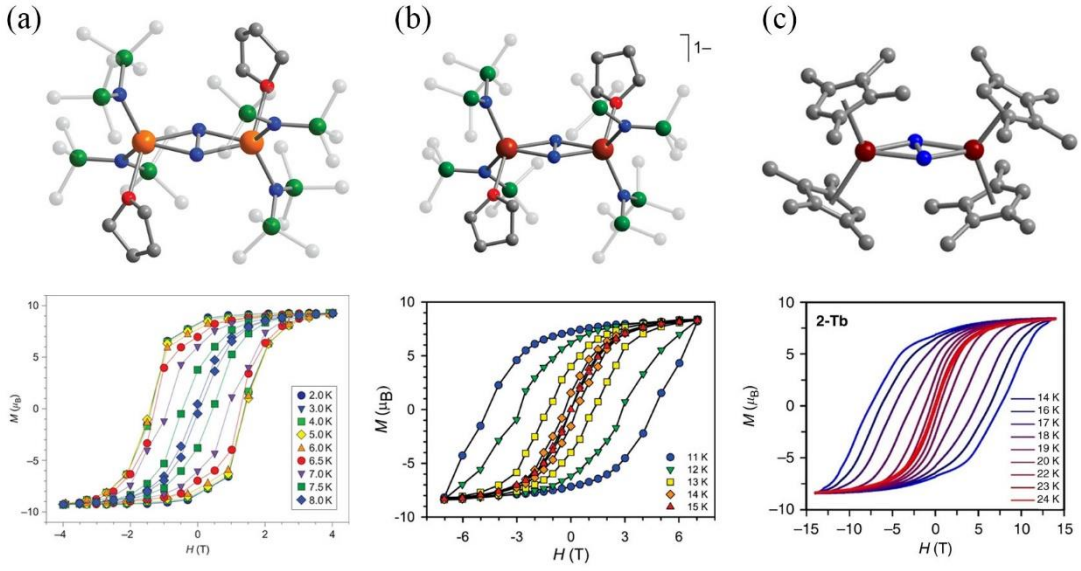

Figure 1.12 The structure (top) and hysteresis loop (bottom) of (a) $\{[(Me_3Si)_2N]_2(THF)Dy\}_2(\mu\text{-}\eta^2\text{:}\eta^2\text{-}N^2)$ Copyright © 2011, Nature Publishing Group. (b) $\{[(Me_3Si)_2N]_2(THF)Tb\}_2(\mu\text{-}\eta^2\text{:}\eta^2\text{-}N^2)$ Copyright © 2011, American Chemical Society. (c) $[K(crypt\text{-}222)(THF)][(Cp^{Me4H}{}_2Tb(THF))_2(\mu{-}N_2)]$.

In 2011, an asymmetric ferromagnetically coupled dinuclear Dy^{III} SMM, $[Dy_2ovph_2Cl_2(MeOH)_3]_3{\cdot}MeCN$ (H_2ovph = pyridine-2-carboxylic acid [(2-hydroxy-3-

methoxyphenyl)methylene] hydrazide) was reported by Tang et. al[73]. As shown in Figure 1.13, the metal centers in the dinuclear core are bridged by the alkoxido groups of two antiparallel ligands. The eight coordinate Dy1 center displays a geometry resembling that of a hula hoop, while the Dy2 center with seven coordinates has an almost perfect coordination environment in the shape of a pentagonal bipyramid. From the magnetic studies, two relaxation times are observed because of the obstruction of magnetization at high temperatures caused by individual ion anisotropy. The Dy_2 dimer reaches the exchange-blocking regime at a low enough temperature and displays a slow relaxation (τ_{QTM} = 35 s). For information storage applications, achieving such extended relaxation durations is essential[77].

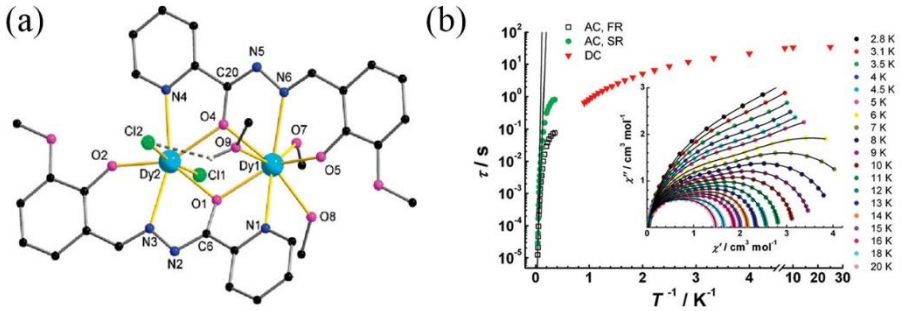

Figure 1.13 (a) Asymmetric dinuclear unit of $[Dy_2ovph_2Cl_2(MeOH)_3]_3 \cdot MeCN$. (b) Arrhenius plot constructed using ac χ'' and dc decay data, Inset: Cole–Cole plots for $[Dy_2ovph_2Cl_2(MeOH)_3]_3 \cdot MeCN$. Copyright © 2011, American Chemical Society.

In 2013, based on the previously reported $\{Dy_2\}$ SMM $[Dy_2(valdien)_2(NO_3)_2]$, Murugesu's group successfully prepared five new complexes: $[Dy_2(valdien)_2(L)_2] \cdot solvent$, L = CH_3COO^- (**2**), $ClCH_2COO^-$ (**3**), Cl_2CHCOO^- (**4**), $CH_3COCHCOCH_3^-$ (**5**), $CF_3COCHCOCF_3^-$ (**6**), solvent = 0.5 MeOH (**4**), $2CH_2Cl_2$ (**5**)[78]. The six complexes possess centrosymmetry and have a common dinuclear core structure, comprising of two Dy(III) metal ions, two dianionic tetradentate valdien ligands, and two bidentate terminal ligands (Fig 1. 14). The energy barriers U_{eff} = 34 (**2**), 50 (**3**), 60 (**4**), 16 (**5**), and 110 K (**6**). This can be attributed to the difference in the average charge distribution of the coordinated oxygen atoms in the terminal ligands. The more electron deficient the monoanionic bidenetate terminal ligand, the higher the energy barrier of the $\{Dy_2\}$. Compared with traditional and challenging methods, replacing H's with electron-withdrawing atoms on terminal ligands can be a relatively simple strategy to obtain high barrier SMMs.

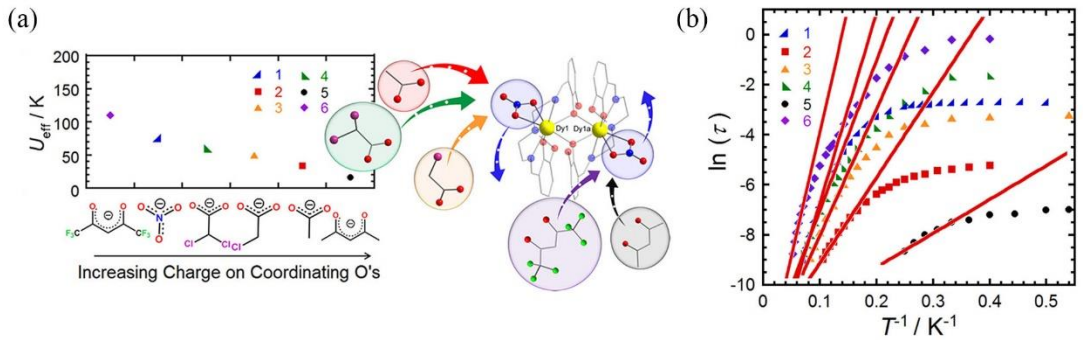

Figure 1.15 (a) Plot of U_{eff} vs increasing charge on coordinating O's of the terminal ligands for **1**–**6**. (b) Arrhenius plot showing the relaxation time of the magnetization for **1**–**6** under zero applied dc field. Copyright © 2013, American Chemical Society.

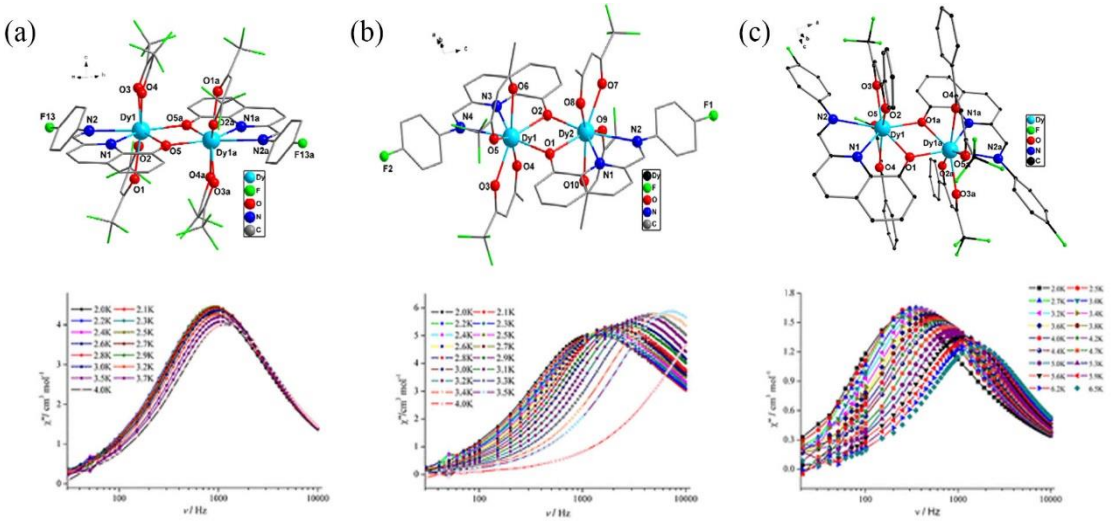

Figure 1.14 Molecular structure (top) and frequency dependence of out-of-phase (χ'') ac susceptibility (bottom) of **1** (a), **2** (b) and **3** (c) under zero dc field. Copyright © 2013, American Chemical Society.

In 2015, Cui's research group synthesized three new rare earth complexes based on 8-hydroxyquinoline derivatives as the main ligand and different β-diketones as auxiliary ligands: $[Dy_2(hfac)_4(L)_2]$ (**1**), $[Dy_2(tfac)_4(L)_2]$ (**2**) and $[Dy_2(bfac)_4(L)_2 \cdot C_7H_{16}]$ (**3**) (L = 2-[[(4-fluorophenyl)imino]methyl]-8-hydroxyquinoline, hfac = hexafluoroacetylacetonate, tfac = trifluoroacetylacetonate, bfac = benzoyltri-fluoroacetone)[79]. The molecular structures are shown in Figure 1.15, all of them are phenoxy bridged dinuclear complexes, in which each Dy^{III} ion is octacoordinated and has a deformed triangular dodecahedral coordination geometry. The AC magnetic measurements show that all three are consistent with the typical characteristics of single-molecule magnets, and the effective energy barriers obtained by fitting are

6.77 K (**1**), 19.83 K (**2**) and 25.65 K (**3**), respectively. The difference in the U_{eff} values observed for the complexes are attributed to different β-diketone ligands. The different ligand structures cause slight differences in the ligand field symmetry around the Dy^{III} centers, thereby different U_{eff} values are obtained. This fact indicates that β-diketone ligands can play an important role in the regulation of the magnetodynamic properties of rare earth complexes.

1.3.3 Trinuclear Ln-SMMs

Trinuclear complexes with a triangular arrangement of spins are of great interest in molecular magnetism because their geometry is prototypical to realize toroidal magnetism[80-83] and spin frustration[84-88]. Trinuclear complexes can also function as SMMs[89-92]. While triangular SMMs with three lanthanide centers have been investigated, further investigations are necessary to gain more knowledge on how molecular structure and intra molecular Ln^{III} interactions affect SMM properties.

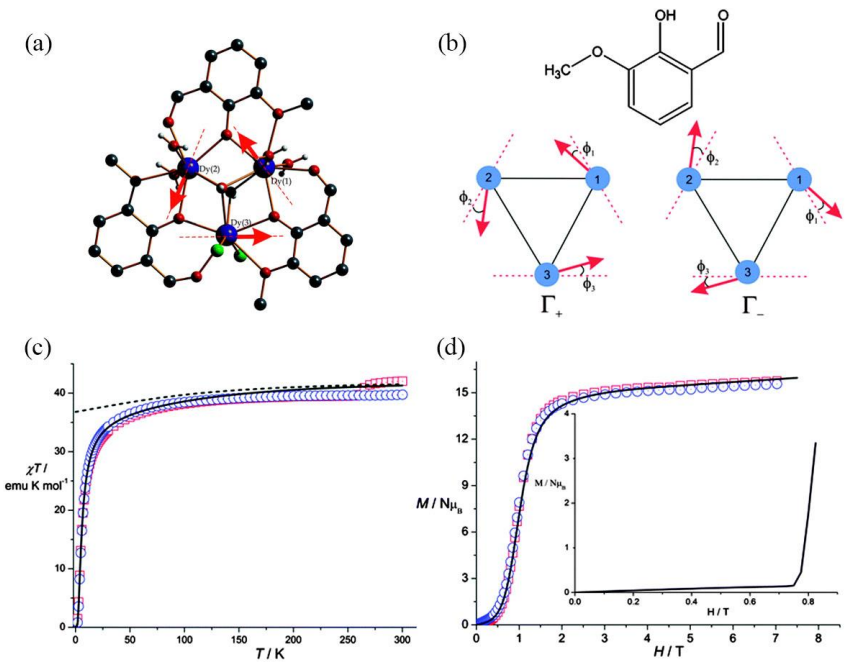

Figure 1.16 (a) Molecular structure of the Dy_3 complex with main anisotropy axes (dashed lines) and local magnetizations (arrows) in the ground state. (b) The two components of the ground Kramer's doublet. (c and d) The static magnetic properties and their *ab initio* simulations (lines). Copyright © 2006, Royal Chemical Society.

The first Dy_3 triangular SMM $[Dy_3(\mu_3\text{-}OH)_2L_3Cl_2(H_2O)_4][Dy_3(\mu_3\text{-}OH)_2L_3Cl(H_2O)_5]Cl_5\cdot 19H_2O$ (HL = *o*-vanillin) was reported by Powell and co-workers in 2006[82]. Static and dynamic magnetic measurements, as well as ab initio methodology[80], were used in the magnetic investigations, which revealed that the anisotropy axes of the ground Kramers doublet at the three dysprosium sites practically lie in the Dy_3 plane and form an almost perfect equilateral triangle (toroidal moment), as shown in Fig 1.16b. Similar to single-molecule magnets (SMMs), the Dy_3 clusters could be referred to as single-molecule toroics (SMTs)[93]. The identification of a toroidal moment in the Dy_3 triangle resulted in further investigations of the topic[93-96].

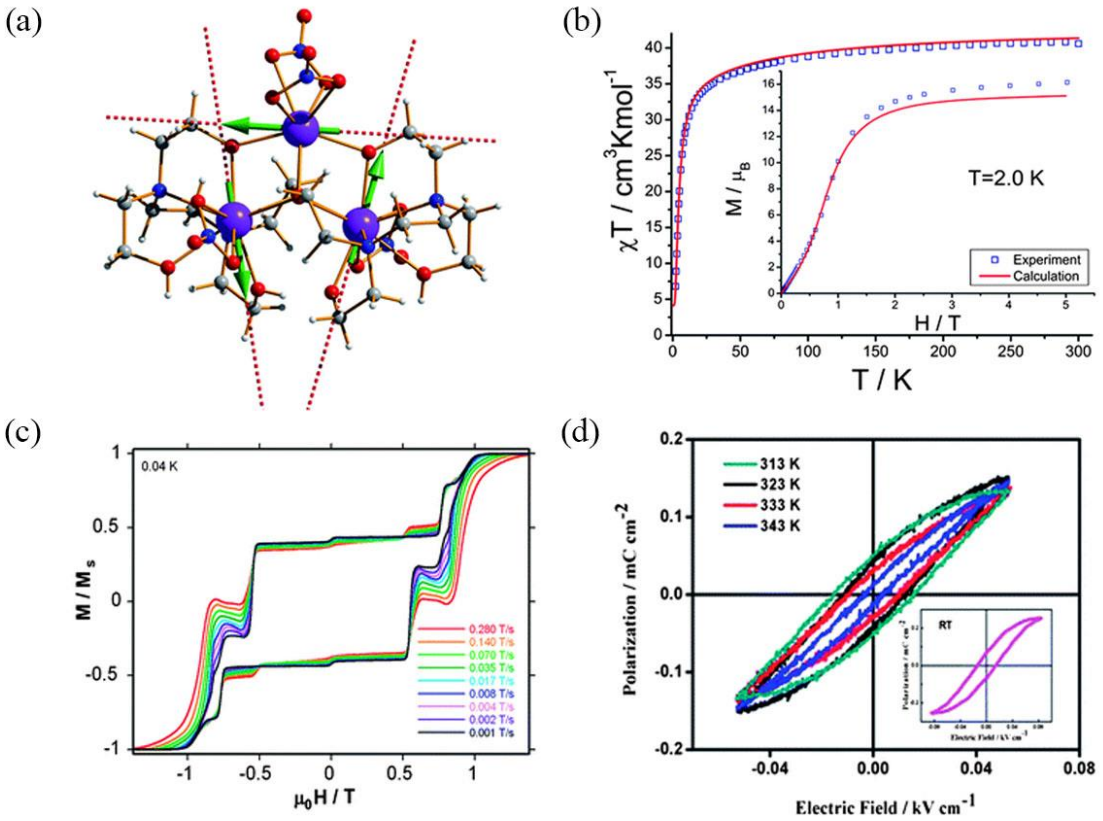

Figure 1.17 (a) The structure with main anisotropy axes (dashed lines) and local magnetizations (arrows) in the ground state; (b) the static magnetic properties; (c) (d) hysteresis loops at different field sweep rates for $[Dy_3(HL)(H_2L)(NO_3)_4]$; (d) dielectric hysteresis loops. Copyright © 2012, Royal Chemical Society.

In 2012, a novel triangular Dy_3 compound, $[Dy_3(HL)(H_2L)(NO_3)_4]$ (H_4L = *N*,*N*,*N*′,*N*′-tetrakis(2-hydroxyethyl)-ethylene-diamine), has been reported by Shi and co-workers (Fig. 1.17)[83]. According to structural studies, only two pairs of Dy ions are connected by a μ_2-O atom, and three Dy ions are doubly capped by two μ_3-O atoms from the ligands, resulting in a pseudo-isosceles triangle with the Dy···Dy distances of 3.488(1)

Å, 3.509(1) Å, and 3.898(1) Å. While Dy1 and Dy3 are in deformed capped square antiprismatic coordination spheres, Dy2 is in a distorted square antiprism coordination geometry. The complex displays both SMM behavior with characteristic hysteresis loops (Figure 1.17c), as well as a paraelectric to ferroelectric phase transition with dielectric anomalies at 470 K (Figure 1.17d).

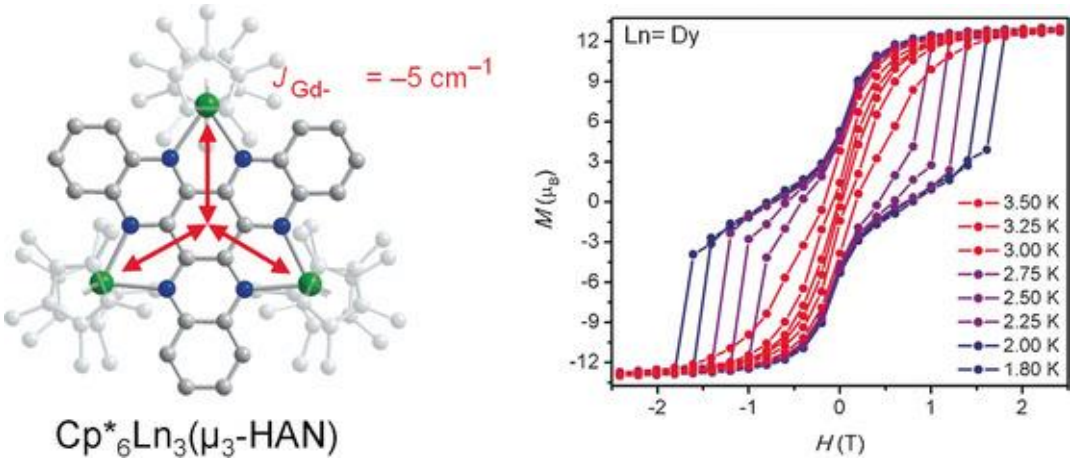

Figure 1.18 Crystal structure (left) and magnetic hysteresis measurements (right) from 1.8 to 3.5 K at a sweep rate of 4 mT s^{-1} of the triangular complex Cp*$_6$Dy$_3$(μ$_3$-HAN). Copyright © 2017 Wiley-VCH Verlag GmbH & Co. KGaA, Weinheim.

In 2017, three triangular, organic radical-bridged complexes Cp*$_6$Ln$_3$(μ$_3$-HAN) (Cp* = pentamethylcyclopentadienyl; Ln = Gd, Tb, Dy; HAN = hexaazatrinaphthylene) were synthesised through the reaction of Cp*$_2$Ln(BPh$_4$) with HAN ligand by Long group[97] (Fig 1.18). Magnetic susceptibility studies of these three complexes show that all three Ln^{III} centers are effectively magnetically coupled through the HAN$^{3-\bullet}$ radical ligand. AC susceptibility and DC magnetic relaxation measurements of Dy^{III} complex reveal slow relaxation of the magnetization, with an effective thermal relaxation barrier of U_{eff} = 51 cm^{-1}, T_B = 3 K. Magnetic hysteresis measurements displayed open hysteresis loops, including a remnant magnetization, until temperatures up to 3.5 K. The use of a radical bridging ligand in Dy^{III} complex results in a strong magnetic exchange coupling, which enhances magnetic hysteresis and leads to longer magnetic relaxation times compared to similar trinuclear lanthanide compounds[98-100].

1.4 Molecular spin qubits and qu*d*its for quantum algorithms

1.4.1 Quantum bit (Qubit)

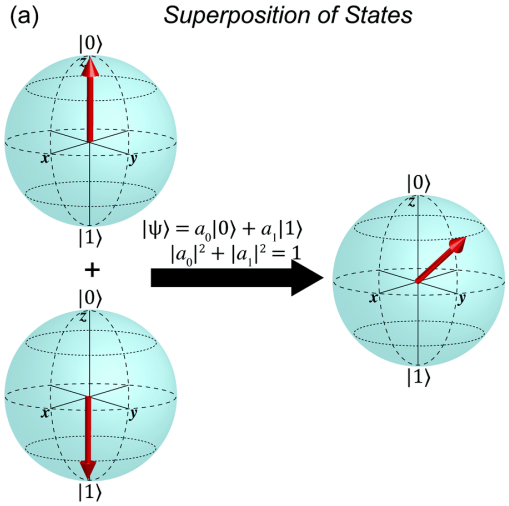

Figure 1.19 The quantum version of the bit, a qubit. Copyright © 2017, Royal Chemical Society.

The quantum bit, also known as a qubit, is the fundamental building block of a quantum computer and can carry out the same processes in either of two clearly defined states, namely |1> or |0>. On the Bloch sphere, these states are typically depicted as an arrow pointing to the north pole for the |0> state or the south pole for the |1> state (Fig. 1.19). As a result of the quantum nature of the qubit, it is possible to generate a superposition of the |1> and |0> states with $|\psi> = a_0|0> + a_1|1>$, which can point in any direction on the sphere, where the squares of a_0 and a_1 are the amplitude of the probability following $|a_0|^2 + |a_1|^2 = 1$ (Fig. 1.19). These new states lack classical equivalents and involve non-orthogonal arrangements, yielding 2^N states, where N is the number of qubits. This attribute grants quantum computing the potential ability to undertake extremely complex and intricate tasks. Moreover, an expansion of the qubit concept to include more than two levels within a given system leads to the development of qu*d*its, where the *d* denotes the multilevel nature[101,102]. In addition, qu*d*its provide d^N orthogonal states, allowing for parallelization within a single unit and lower error rates compared to qubits.

1.4.2 Nuclear spin molecular qubits

After the discovery of magnetic memory at the single-ion level[41,103], various potential uses have been envisioned for single-molecule magnets based on lanthanides (Ln-

SMMs), including data storage[104] and spintronic devices[105]. One of the most ambitious potential applications involves integrating Ln-SMMs into quantum information schemes to act as quantum bits (qubits)[14,106-108]. Despite appearing to be a long-term objective, Ln-SMMs have already demonstrated several of the necessary DiVincenzo characteristics[109,110] to function as nuclear spin qubits[111,112].

The family of terbium bis(phthalocyaninato) complexes ([$TbPc_2$]) serves as the best illustration of the diversity of quantum effects found in Ln-SMMs and their potential applications in quantum technologies[105,107,108]. In the [$TbPc_2$], the spin-orbit coupling of the Tb^{III} ion and the ligand field (LF) brought on by the phthalocyaninato moieties combine to produce strong magnetic anisotropy. The SMM property isolates the ground electronic state from excited states, the ground state, $|J = 6, J_z = \pm 6\rangle$, has been found to be separated from the first excited state, $|J = 6, J_z = \pm 5\rangle$, by about 600 K, with only the ground doublet being populated at low temperatures (10 K) and low fields (<10 T)[42] (Fig 1.20b). Multiple QTM events have been observed by μ-SQUID measurement (Fig 1.20c), which are induced by the transverse ligand field (LF) terms. The hyperfine

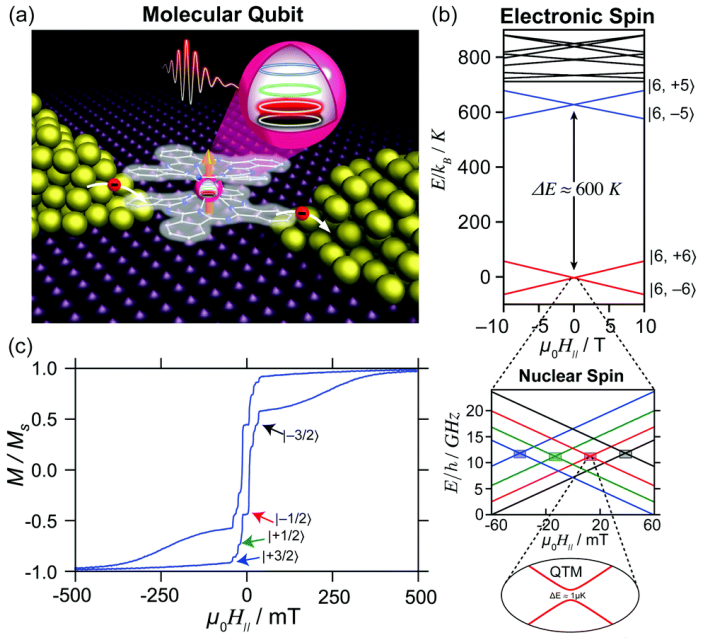

Figure 1.20 (a) Schematic representation of [$TbPc_2$] deposited between two gold leads, while current flows through the molecule. (b) Energy level diagram resulting from strong spin orbit coupling of Tb^{3+} and the ligand field exerted by the Pc groups. Zoomed regions shows the effect of strong hyperfine interaction which splits the $J_z = \pm 6$ state into four levels associated to $m_J = \pm 1/2$ and $\pm 3/2$ and avoided level crossing due to mixing of states. (c) Hysteresis loop showing quantum tunnelling events associated to the nuclear spins. Copyright © 2017, Royal Chemical Society.

interaction splits each electronic ground state doublet into four nuclear-spin–dependent levels (zoomed regions in Fig 1.20b). The initialization, manipulation, and read-out of the nuclear spin states made [$TbPc_2$] integration in hybrid devices possible (Fig 1.20a), making it a viable multilevel nuclear spin qubit[105], or qu*d*it (d = 4) for d-dimensional systems[101].

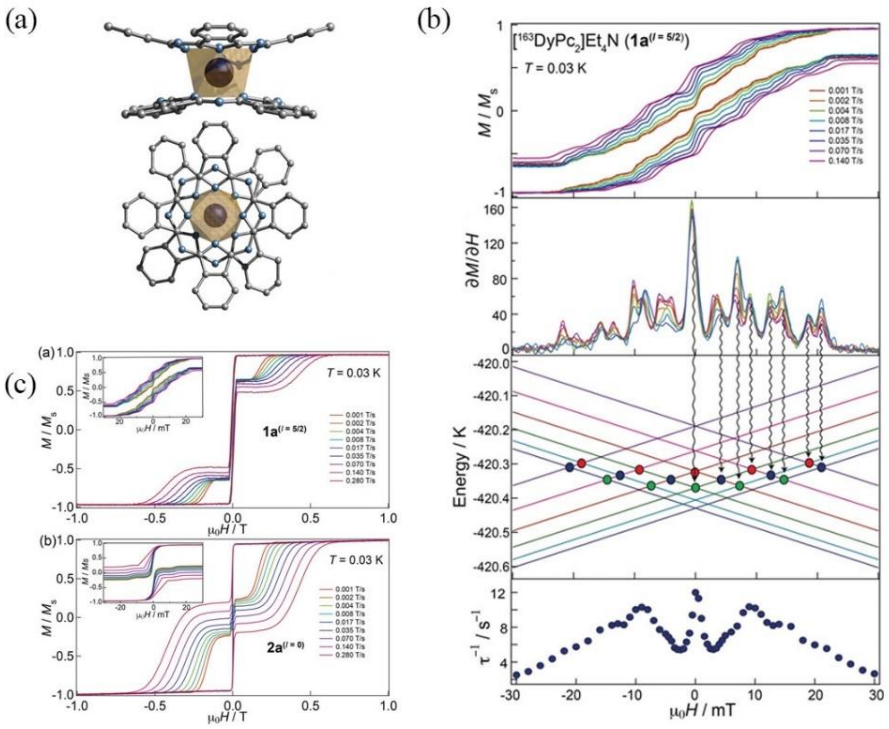

Figure 1.21 (a) Side (top) and top (bottom) view of the crystal structures of $Et_4N[^{163/164}DyPc_2]$ (b) Hystereses loops at T=0.03 K and simulated Zeeman diagram with the field parallel to the easy axes for $Et_4N[^{163}DyPc_2]$ (c) μ-SQUID measurements at T = 0.03 K for $Et_4N[^{163/164}DyPc_2]$. © 2017 Wiley-VCH Verlag GmbH & Co. KGaA, Weinheim.

In order to successfully initialize, manipulate, and read-out the nuclear states in the Tb-SMM and enable them to function as qubits, the high magnetic anisotropy is a prerequisite. Tb-based SMMs appear to be viable candidates as nuclear spin qubits in this regard. However, strong Tb-based SMMs are scarcely obtained because of the non-Kramers nature of the Tb^{III} ion[43,113-126]. Consequently, the Dy^{III}-based SMMs are predominantly studied due to the Kramers characteristic of Dy^{III} frequently producing a well-isolated ground doublet state[44,127-153]. Moreover, the natural composition of Dy^{III} possesses two different nuclear spin states, I = 0 and 5/2, allowing one to clearly elucidate nuclear spin-based effects. In this context, our group synthesized two isomeric dysprosium complexes, $Et_4N[^{163}DyPc_2]$ with I = 5/2 and $Et_4N[^{164}DyPc_2]$ with I = 0 (Pc

= phthalocyaninato), in 2017[154] (Fig 1.21a). Although both isotopologues are SMMs, there are significant differences in both relaxation times and magnetic hystereses. From the μ-SQUID studies, quantum tunneling of the magnetization (QTM) at the energy level crossings is discovered for both systems (Fig 1.21c). Due to the lack of nuclear spin, the hysteresis loops of ^{164}Dy are slightly wider than ^{163}Dy. This demonstrates that QTM can still be produced by dipolar interactions or hyperfine interactions with nearby atoms[155-157]. For quantum information processing (QIP) schemes, $Et_4N[^{163}DyPc_2]$ could be used as a multilevel nuclear spin qubit, specifically as a qu*d*it (d = 6). Such demonstrations illustrate the capable role of coordination chemistry in producing molecular QIP architectures following isotopological coordination chemistry. The results demonstrate that the lanthanide nuclear spin must be taken into account when developing the design guidelines for molecular qubits and SMMs.

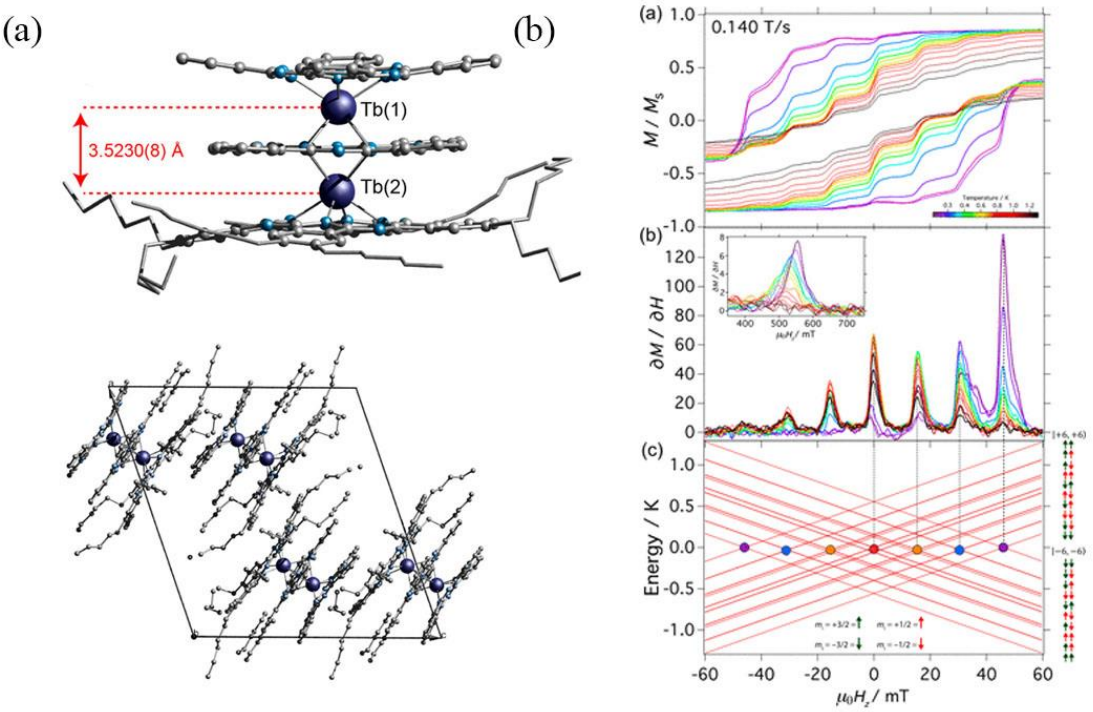

Figure 1.22 (a) Side view of the crystal structure of $[Tb_2Pc^{Hx8}Pc_2]$ (b) Zoom of the hysteresis loops (top), first field derivative for a field sweep from −60 to +60 mT of the data (middle) and simulated Zeeman diagram with the field parallel to the easy axes (bottom). Copyright © 2018, American Chemical Society.

In the pursuit of molecular systems with a greater number of available nuclear spin states, our group, in 2018, synthesized a dimeric Tb_2-SMM: $[Tb_2Pc^{Hx8}Pc_2]$ (Pc = phthalocyaninato and ^{Hx8}Pc = 2,3,9,10,16,17,23,24-octahexylphthalocyaninato)[158], to

increase the multiplicity of nuclear spin states available for manipulation. The intramolecular Tb···Tb distance observed in the crystal structure is 3.5230(8) Å (Fig. 1.22a). Between the two Tb^{III} ions, ferromagnetic interactions and QTM of the electronic spins with spin ground state $|J_z = \pm 6\rangle$ were observed (Fig 1.22b). The presence of strong hyperfine coupling with the nuclear spins of Tb^{III} results in several spin-reversal pathways, giving rise to seven distinct tunneling steps driven by strong hyperfine effects in the hysteresis loops. Our findings demonstrate the potential for reading out the Tb^{III} nuclear spin states through cooperative tunneling of the electronic spins, making the dimeric Tb_2-SMM an outstanding choice for the nuclear spin qu*d*it with $d = 16$ ($d = (2I+1)^n$, where n = 2 and $I = 3/2$).

1.5 Research Objectives

The field of molecular–magnetism has seen a significant breakthrough with the discovery of single molecule magnets (SMMs), where molecular-structure-dependent anisotropy causes slow relaxation and quantum tunneling of magnetization[17,159]. Research covering SMMs offers up a pathway for realizing molecular-level high-density data storage media and nanoscale electronic devices and sensors[147,160,161]. Additionally, SMMs offer exceptional opportunities to observe quantum effects (such as quantum phase interference and QTM), as they exhibit both classical and quantum mechanical behavior[9,162-164]. The Dy^{III} ions are highly preferred to obtain good quality SMMs as it can offer stronger magnetic anisotropy, despite having weak exchange coupling [165,166]. In particular, the Dy^{III} ion has an odd number of electrons (n = 9), thereby the ground state is the Kramers doublet[167], which is essential for the existence of typical SMM properties. Moreover, Dy^{III} ions have been extensively researched for the synthesis of Qu*d*its with huge Hilbert space: seven Dy^{III} isotopes with two distinct nuclear spin states, $I = 0$ for ^{160,162,164}Dy(III) and $I = 5/2$ for ^{161,163}Dy. Furthermore, the nuclear states in a dimeric complex can couple by the electronic spin interaction (dipolar or exchange), resulting in an exponential increase in the number of available states in the Qu*d*it.

Extensive research has been conducted to explore the correlations between coordination geometry, steric effect, electronic effect, and magnetic properties. This research has yielded valuable insights for the development and construction of advanced and technologically relevant Ln(III)-based SMMs[166-169]. It has been found that even a slight

modification in the ligand fields can effectively fine-tune the magnetic properties[170-173]. New examples examining the structural and magnetic properties of Dy(III)-based SMMs would be highly desirable in order to further deepen our knowledge of the origin of magnetic relaxation, which was accomplished by fine-tuning the coordination environment around the metal centers in the Dy-SMMs.

As classic integrated ligands have a single coordination mode, *β*-diketone ligands easily bond with rare earth Dy(III) ions and form stable complexes. At the same time, these complexes have simple geometric configurations that help explore their structure-magnetic function relationship. In Chapter 2 of this thesis, the *β*-diketone ligands are used as the primary ligand, and auxiliary ligands with various structures are introduced to adjust the metal ion's coordination environment and geometric symmetry in the target complex, thereby regulating the dynamical magnetic behavior of the complexes. In Chapters 3 and 4, a select set of highly π conjugated bridging ligands with multi-coordination sites as the main ligand scaffold has been used in combination with different *β*-diketone auxiliary ligands to design and synthesize complexes with various structures. In the resultant complexes, the Dy(III) ions are placed in different ligand field environments, thereby the SMM characteristics of the complexes are regulated.

Overall, several sets of mono, di, and trinuclear molecular complexes have been prepared and their SMM characteristics have been evaluated. Furthermore, attempts to engineer the Hilbert space of qu*d*its candidates were made by introducing ^{163}Dy (I = 5/2) and ^{164}Dy (I = 0) in select dinuclear systems to get isotopologue dysprosium dimers. μ-SQUID measurements have been used to study the magnetic interactions between the two spin carriers. The same measurements have been employed to elucidate how the presence or absence of nuclear spins affects the SMM properties of the complexes.

Chapter 2: Single-molecule magnet characteristics of mononuclear Dy(III) complexes

Mononuclear Dy^{III}-based single-molecular magnets (Dy-SMMs) are a fascinating and promising class of materials that have garnered significant attention in recent years. They exhibit unique magnetic properties, such as slow magnetic relaxation and large magnetic anisotropy[174-177]. These properties make mononuclear Dy-SMMs ideal for various applications in the fields of magnetic data storage, spintronics, and quantum computing. Therefore, single-ion anisotropy, which is sensitive to the strength and symmetry of the local crystal field, is probably the most important factor for Dy-SMMs[40] and magnetic exchange is a secondary consideration that moderates the magnetic relaxation of the single ions. How to increase single-ion anisotropy and promote magnetic coupling remains an exciting challenge in Dy^{III} systems. Hence, designing novel structures to expand the existing database is essential for advancing our understanding of the relationship between structure and properties in Dy-SMMs.

However, the magneto-dynamic behavior of single-nuclear rare earth Dy-SMMs is very sensitive to the structure, and small changes will lead to changes in its magnetic anisotropy, such as the gain and loss of non-coordinating lattice solvents, and the coordination of hydrogen atoms on water molecules.

In this chapter, six mononuclear Dy^{III}-complexes will be discussed in detail with regards to their structural features. All mononuclear complexes are composed of different β-diketonate and other ligands — 2,2':5',2"-Terpyridine (2,5-tpy) or tri-phenylphosphine oxide ($POPh_3$). The dysprosium metal center in each complex is either seven or eight coordinates in nature. All the complexes have shown SMM characteristics and the magnetization relaxation is induced by a combination of Orbach and Raman processes. In the following sections, synthesis, and characterization, single-crystal X-ray structures, and magnetic properties of the complexes are discussed.

2.1 Preparation of organic ligands

2.1.1 Synthesis of ligand 2,2′:5′,2′′-Terpyridine (2, 5-tpy)

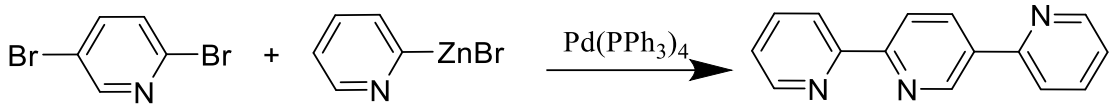

Scheme 2.1 Synthesis of 2,5-tpy.

Ligand 2, 2′: 5′, 2′′- Terpyridine was prepared according to the reported literature[178]. In a dried two neck round bottom flask 0.299 g (0.258 mmol) of $Pd(PPh_3)_4$ and 2 g (8.44 mmol) of 2,5-dibromobipyridine were added under a nitrogen atmosphere. During the addition of 38.7 ml (16.8 mmol) of 2-pyridylzinc bromide to the reaction mixture, the temperature was kept at 0 °C. The reaction mixture was then stirred overnight at room temperature under a nitrogen atmosphere. A white precipitate formed. The reaction mixture was poured into a saturated aqueous solution of EDTA/Na_2CO_3 until the precipitate dissolves and yellow flakes come. The aqueous solution was then extracted with dichloromethane, washed with brine, and dried over $MgSO_4$. The dichloromethane was evaporated at room temperature and the crude product was purified by SiO_2 column using hexane/ethyl acetate (9:1) as an eluent.

Yield: 1.09g, 4.88 mmol, 55%

^{1}H NMR (500 MHz, $CDCl_3$, δ/ppm): 7.30-7.38 (m, 1H), 7.82-7.85 (m, 2H), 7.86-7.89 (m, 1H), 8.49-8.51 (m, 2H), 8.54 (dd, 1H), 8.74 (ddd, 1H), 8.77 (dt, 1H), 9.30 (dd, 1H)

^{13}C NMR (126 MHz, $CDCl_3$, δ/ppm): 156.26, 155.81, 154.71, 150.14, 149.27, 147.69. 136.79, 136.96, 135.23, 134.69, 123.88, 122.87, 121.36, 120.99, 120.46.

2.2 Syntheses of precursors

The precursors $[Ln(tmhd)_3(H_2O)_2]$ (Ln = Dy, ^{163}Dy, ^{164}Dy; tmhd = 2,2,6,6-tetramethyl-3,5-heptanedione), $[Dy(BTFA)_3(H_2O)_2]$ (BTFA = 4,4,4-trifluoro-1-phenyl-1,3-butanedione), $[Dy(NTFA)_3(H_2O)_2]$ (NTFA = 4,4,4-Trifluoro-1-(2-naphthyl)-1,3-butanedione), and $[Dy(hfac)_3(H_2O)_2]$ (hfac = hexafluoroacetylacetonate) were prepared according to the reported literature procedures[179,180].

2.2.1 General procedure for the synthesis of precursors

10 mL of methanol solution of the appropriate β-diketone (4.0 mmol) and KO^{t}Bu (446.4 mg, 4.0 mmol) were stirred for 30 min. To this solution was added a solution of $LnCl_3 \cdot 6H_2O$ (500 mg, 1.326 mmol) in a mixture of 5 ml methanol and 5 ml H_2O. A precipitate formed immediately and the mixture was stirred for 24 h at room temperature. The slurry was filtered, the precipitate was washed with water, and dried under vacuum overnight to obtain the corresponding Dy-β-diketone complexes of the general formula: $[Dy(L)_3(H_2O)_2]$; L = tmhd, BTFA, NTFA, or hfac.

Yield for $[Dy(tmhd)_3(H_2O)_2]$: 50.5% based on Dy.
Elemental Analysis: Calculated for $C_{33}H_{61}DyO_8$ (750.5 g/mol): C, 52.76; H, 8.13. Found: C, 53.43; H, 7.87.
IR (ATR, cm^{-1}): 2955, 1571, 1505, 1383, 1352, 1238, 1133, 873, 758.

Yield for $[Dy(BTFA)_3(H_2O)_2]$: 852.0 mg (75.9%), based on Dy.
Elemental Analysis: Calculated: $C_{30}H_{22}DyF_9O_8$ (846.98 g/mol): C, 42.50; H, 2.60. Found: C, 41.82; H, 2.45.
IR (ATR, cm^{-1}): 3660, 3400, 1579, 1505, 1279, 1122, 940, 771, 680.

Yield for $[Dy(NTFA)_3(H_2O)_2]$: 1.00 g (71.02%), based on Dy.
Elemental Analysis: Calculated: for $C_{42}H_{28}DyF_9O_8$ (1062.82 g/mol): C, 47.47; H, 2.64. Found: C, 46.53; H, 2.78.
IR (ATR, cm^{-1}): 3479, 3049, 1604, 1291, 1135, 954, 784, 666, 653.

Yield for $[Dy(hfac)_3(H_2O)_2]$: 815.4 mg (74.5%), based on Dy.
Elemental Analysis: Calculated: $C_{15}H_7DyF_{18}O_8$ (822.68 g/mol): C, 21.88; H, 0.85. Found: C, 20.38; H, 0.79.
IR (ATR, cm^{-1}): 3672, 3150, 2917, 1643, 1500, 1135, 810, 654, 576.

2.3 Synthesis of mononuclear complexes

2.3.1 Synthesis of $[Dy(tmhd)_3(POPh_3)]$ (2-1) and $[Dy(tmhd)_3(2,5\text{-tpy})]$ (2-2)

A mixture of $[Dy(tmhd)_3(H_2O)_2]$ (50 mg, 0.067 mmol) precursor and $POPh_3$ (18.63 mg,

0.067 mmol) or 2,5-tpy (15.5 mg, 0.067 mmol) were stirred in EtOH (5 ml) for 24 h. The colourless solution was filtered and the filtrate left undisturbed. After a few days, colourless block crystals suitable for X-ray structure determination were collected and air dried.

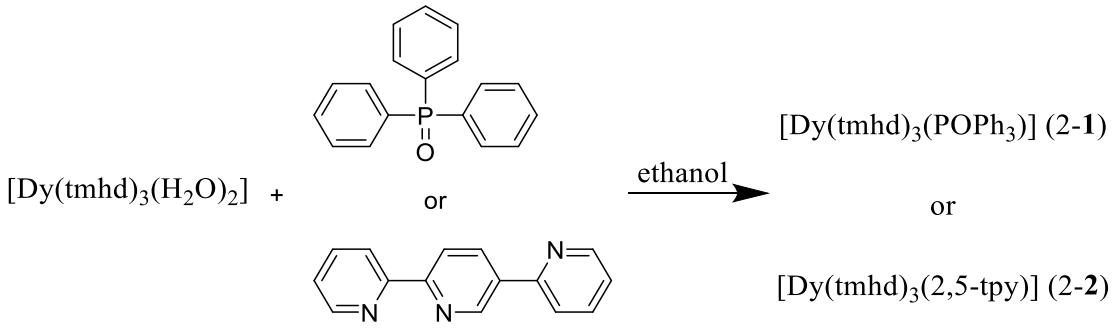

Scheme 2.2 Synthesis of complexes 2-**1** and 2-**2**.

Yield: 29.2 mg (44.04%) for $[Dy(tmhd)_3(POPh_3)]$ (2-**1**)

Elemental Analysis: Calculated: $C_{51}H_{72}DyO_7P$ (990.56 g/mol): C, 61.78; H, 7.27. Found: C, 62.98; H, 6.93.

IR (ATR, cm^{-1}): 2948, 2857, 1563, 1406, 1184, 1119, 883, 727, 709, 530, 465.

Yield: 34 mg (55.25%) for $[Dy(tmhd)_3(2,5\text{-tpy})]$ (2-**2**)

Elemental Analysis: Calculated: $C_{48}H_{68}DyN_3O_6$ (945.55 g/mol): C, 60.92; H, 7.19. Found: C, 61.53; H, 8.02.

IR (ATR, cm^{-1}): 2962, 1563, 1432, 1236, 1131, 1027, 871, 766, 596, 480.

2.3.2 Synthesis of $[Dy(BTFA)_3(2,5\text{-tpy})]$ (2-3)

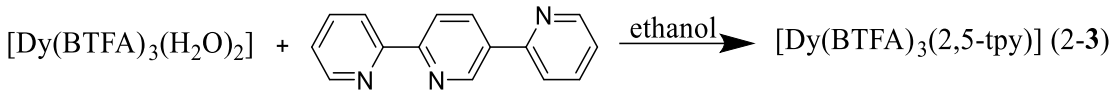

Scheme 2.3 Synthesis of complexes 2-**3**.

A mixture of $[Dy(BTFA)_3(H_2O)_2]$ (50 mg, 0.059 mmol) precursor and 2,5-tpy (13.75 mg, 0.059 mmol) was stirred in EtOH (5 ml) for 24 h. The colourless solution was filtered and left undisturbed. After a few days, block crystals suitable for X-ray analysis were collected and air dried.

Yield: 41.1 mg (66.90 %).

Elemental Analysis: Calculated: $C_{45}H_{29}DyF_9N_3O_6$ (1041.21 g/mol): C, 51.86; H, 2.78. Found: C, 53.09; H, 2.14.

IR (ATR, cm^{-1}): 3053, 3150, 1615, 1472, 1288, 1131, 949, 766, 714, 635, 582.

2.3.3 Synthesis of [Dy(NTFA)$_3$(2,5-tpy)] (2-4) and [Dy(NTFA)$_3$(2,5-tpy)·C_2H_5OH] (2-5)

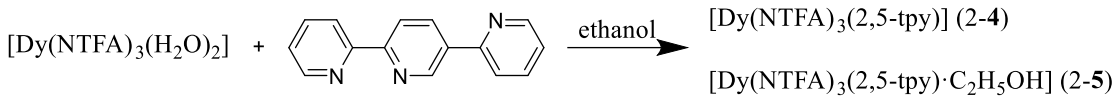

Scheme 2.4 Synthesis of complexes 2-**4** and 2-**5**.

A mixture of [Dy(NTFA)$_3$(H_2O)$_2$] (50 mg, 0.047 mmol) precursor and 2,5-tpy (10.95 mg, 0.047 mmol) was stirred in EtOH (5 ml) for 24 h. The solution was then left and undisturbed. After a few days, plate colourless [Dy(NTFA)$_3$(2,5-tpy)] (2-**4**) and block colourless [Dy(NTFA)$_3$(2,5-tpy)·C_2H_5OH] (2-**5**) crystals were formed.

Yield: 27.1 mg (48.40 %) and 30.3 mg (52.10 %) for complexes 2-**4** and 2-**5**, respectively.

Elemental Analysis: Calculated: $C_{57}H_{35}DyF_9N_3O_6$ (1191.38 g/mol): C, 57.41; H, 2.94. Found: C, 58.95; H, 2.87 for 2-**4**.

Elemental Analysis: Calculated: $C_{59}H_{41}DyF_9N_3O_7$ (1237.45 g/mol): C, 57.21; H, 3.31. Found: C, 57.64; H, 2.69 for 2-**5**.

IR (ATR, cm^{-1}) for complex 2-**4**: 3065, 1602, 1511, 1432, 1288, 1119, 949, 778, 687, 582, 465.

IR (ATR, cm^{-1}) for complex 2-**5**: 3065, 1615, 1523, 1458, 1288, 1119, 962, 778, 687, 582, 478.

2.3.4 Synthesis of [Dy(hfac)$_3$(2,5-tpy)(H_2O) (2,5-tpy)] (2-6)

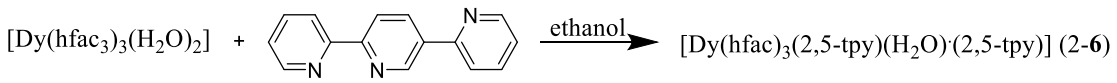

Scheme 2.5 Synthesis of complexes 2-**6**.

A mixture of [Dy(hfac)$_3$(H_2O)$_2$] (50 mg, 0.061 mmol) precursor and 2,5-tpy (14.21 mg, 0.061 mmol) was stirred in EtOH (5ml) for 24 h. The colourless solution was filtered and left undisturbed. After a few days, block crystals suitable for X-ray analysis were collected and air dried. Yield: 59.3 mg (69.79%)

Elemental Analysis: Calculated: $C_{45}H_{27}DyF_{18}N_6O_7$ (1268.23 g/mol): C, 42.58; H, 2.13. Found: C, 43.94; H, 3.35.

IR (ATR, cm^{-1}): 3144, 1732, 1641, 1458, 1261, 1145, 792, 714, 661, 596, 530.

2.4 Structures of mononuclear complexes

2.4.1 Structure of [Dy(tmhd)$_3$(POPh$_3$)] (2-1)

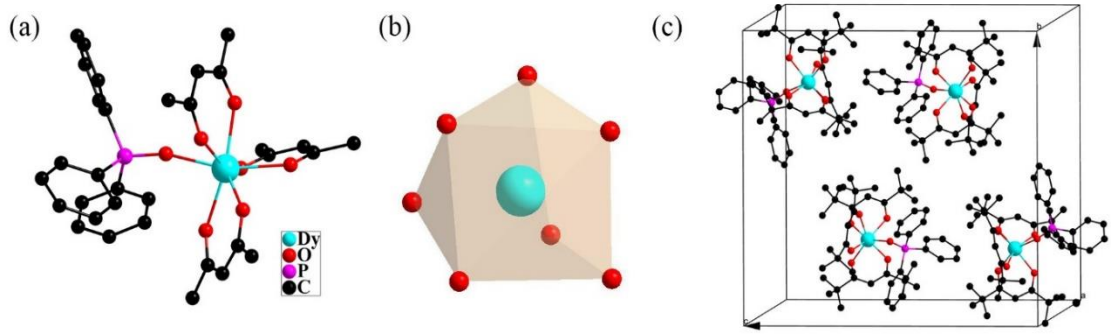

Figure 2.1 (a) Crystal structure of [(Dy(tmhd)$_3$POPh$_3$]. (b) Polyhedral representation of the Dy(III). (c) Unit cell of [(Dy(tmhd)$_3$POPh$_3$].

Complex [Dy(tmhd)$_3$(POPh$_3$)] crystallized in the monoclinic $P2_1/c$ space group (Table 2.1). The all-oxygen coordination environment around Dy ion is constituted by three bidentate tmhd ligands, and one monodendate POPh$_3$ ligand (Fig.1a, b). The Dy···O distances range between 2.2799 (13) Å-2.3106 (14) Å. A standard symmetry analysis using continuous SHAPE program was employed to define the coordination geometry of Dy(III). The lowest values suggest that the coordination geometry of the Dy(III) ion is a capped octahedron with C_{3v} symmetry for complex 2-**1** (Fig 2.1). The two closest Dy(III) ions are separated by an intermolecular distance of 10.95 Å.

2.4.2 Structure of [Dy(tmhd)$_3$(2,5-tpy)] (2-2)

[Dy(tmhd)$_3$(2,5-tpy)] crystallizes in the monoclinic $P2_1/n$ space group (Table 2.1), with a molecule as the asymmetric unit (Fig 2.2). The Dy(III) ion possesses a N_2O_6 coordination geometry formed by six oxygen atoms from the tmhd and two nitrogen atoms of the 2,5-tpy ligand (Fig 2.2b). The Dy···O distances range between 2.2836 (12) Å to 2.3355(12) Å, whilst the Dy···N distances are longer, with values ranging from 2.5495(14) Å to 2.6224(14) Å. The coordination geometry around the dysprosium ions can be best described as a square antiprism (D_{4d}) with a continuous shape measure (CShM) of 0.756 (Table 2.2). The closest intermolecular distance between two Dy(III) is 8.66 Å.

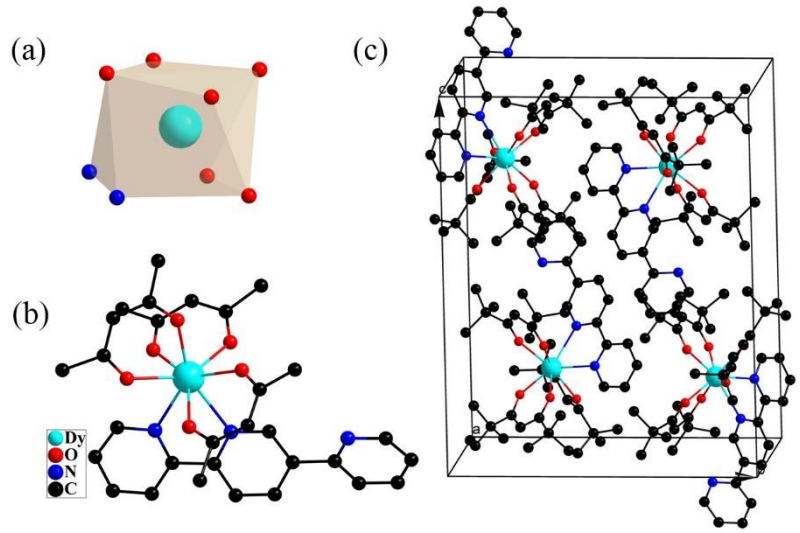

Figure 2.2. (a) Polyhedral representation of the Dy(III) in [Dy(tmhd)$_3$(2,5-tpy)]. (b) Crystal structure of [Dy(tmhd)$_3$(2,5-tpy)] and (c) Unit cell of [Dy(tmhd)$_3$(2,5-tpy)].

2.4.3 Structure of [Dy(BTFA)$_3$(2,5-tpy)] (2-3)

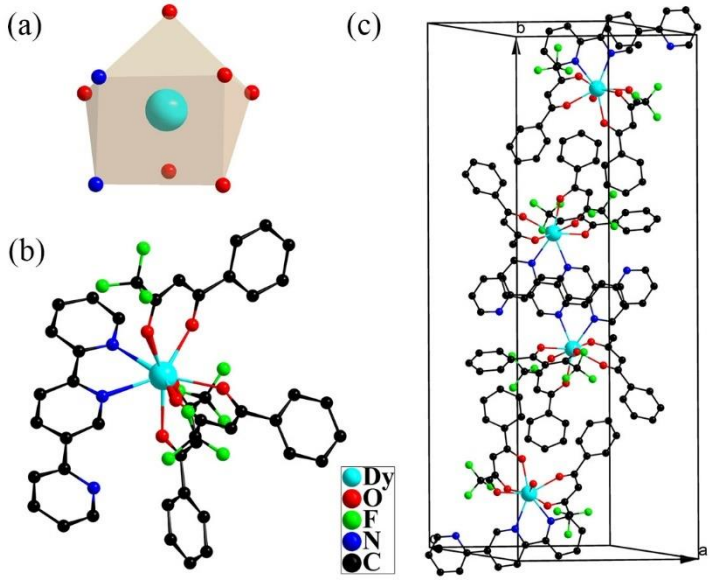

Figure 2.3 (a) Polyhedral representation of the Dy(III) in [Dy(BTFA)$_3$(2,5-tpy)]. (b) Crystal structure of [Dy(BTFA)$_3$(2,5-tpy)] and (c) Unit cell of [Dy(BTFA)$_3$(2,5-tpy)].

Single crystal X-ray diffraction analysis revealed that complex 2-**3** crystallizes in the monoclinic $P2_1/c$ space group with Z = 4 (Table 2.1). The molecular structure is composed of one 2,5-tpy ligand, one Dy (III) ion, and three $[BTFA]^-$ ligands (Fig 2.3b). The dysprosium center resides in the N_2O_6 coordination environment by virtue of three bidentate $[BTFA]^-$ ligands and two nitrogen donors of the 2,5-tpy ligand. The Dy···O distances and Dy···N distances lie in the range of 2.323(2)-2.342(2) Å, 2.525(3)-

2.538(3) Å respectively. The geometric parameters for the dysprosium center were analyzed using the SHAPE software, which revealed that the N_2O_6 coordination environment around Dy (III) can be described as a square antiprism (D_{4d}, CShM value = 0.441) as depicted in Fig 2.3a. The closest intermolecular distance between two Dy(III) is 8.26 Å.

2.4.4 Structure of [Dy(NTFA)$_3$(2,5-tpy)] (2-4)

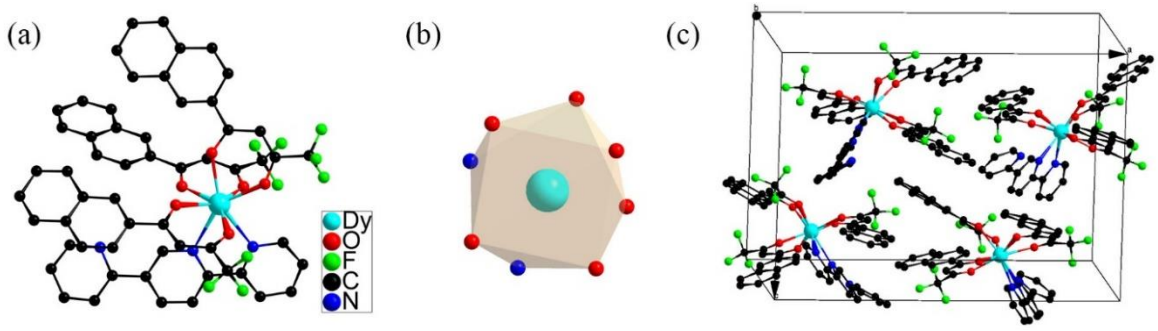

Figure 2.4 (a) Crystal structure of [Dy(NTFA)$_3$(2,5-tpy)]. (b) Polyhedral representation of the Dy(III). (c) Unit cell of [Dy(NTFA)$_3$(2,5-tpy)].

Single crystal X-ray diffraction analysis revealed that complex 2-**4** crystallizes in the orthorhombic P_{ca21} space group with Z = 4 (Table 2.1). The asymmetric unit contains one Dy(III) ion, three $NTFA^-$ and one 2,5-tpy ligand. As shown in Figure 2.4a, the Dy(III) ion is coordinated by two N from 2,5-tpy ligand and six O from three $NTFA^-$. Therefore, the Dy(III) ion is located in the N_2O_6 environment. The Dy···O distances lie in the range of 2.288(6)- 2.367(6) Å. The Dy···N bond lengths in the range of 2.548(7)-2.551(7) Å are slightly longer than those of Dy···O bonds. The metric parameters for the dysprosium centre were analyzed using the SHAPE software, which revealed that the N_2O_6 coordination environment around Dy(III) can be described as a square antiprism (Fig 2.4b and Table 2.2). The CShM values for Dy with respect to D_{4d} symmetry is 1.024. The shortest intermolecular Dy···Dy distance is 8.88 Å.

2.4.5 Structure of [Dy(NTFA)$_3$(2,5-tpy)·C_2H_5OH] (2-5)

Complex 2-**5** was obtained in the same reaction as complex 2-**4**, with a different structure. Single crystal X-ray diffraction analysis revealed that complex 2-**5** crystallizes in the triclinic *P*-1 space group with Z = 2 (Table 2.1). The asymmetric unit

of complex 2-**5** contains one Dy(III) ion, three Naph-CF_3^- and one 2,5-tpy ligand and one ethanol as crystallizing solvent (Fig 2.5a). As in 2-**4**, the dysprosium center reside in a N_2O_6 environment by virtue of three bidentate $[NTFA_3]^-$ ligands and two nitrogen donors of the 2,5-tpy ligand (Fig 2.5a). The Dy···O distances and Dy···N distances lie in the range of 2.293(3)-2.363(3) Å and 2.532(3)-2.540(3) Å, respectively. A distorted spherical capped square antiprism geometry (Fig 2.5b) around Dy(III) was inferred from the SHAPE analysis (Table 2.2). The shortest intermolecular Dy···Dy distance is 11.95 Å.

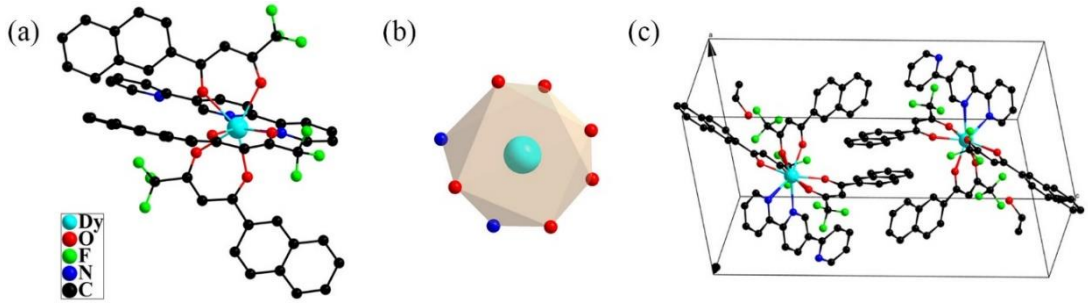

Figure 2.5 (a) Crystal structure of $[Dy(NTFA)_3(2,5\text{-tpy})\cdot C_2H_5OH]$. (b) Polyhedral representation of the Dy(III). (c) Unit cell of $[Dy(NTFA)_3(2,5\text{-tpy})\cdot C_2H_5OH]$.

2.4.6 Structure of $[Dy(hfac)_3(2,5\text{-tpy})(H_2O)\cdot(2,5\text{-tpy})]$ (2-6)

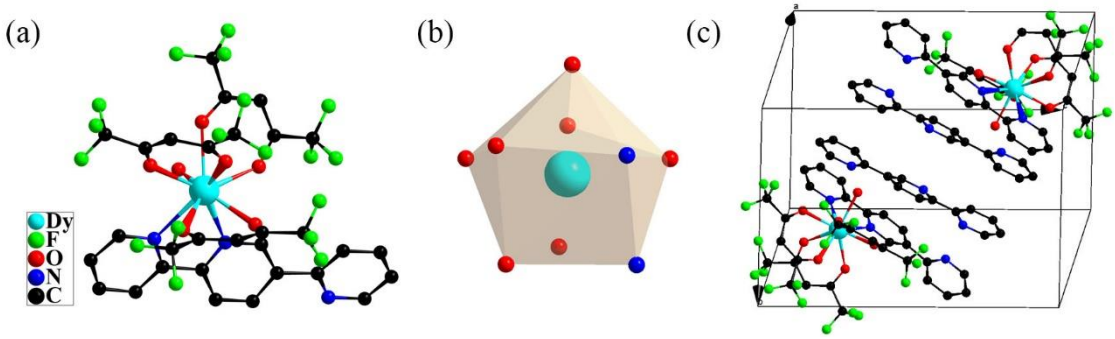

Figure 2.6 (a) Crystal structure of $[Dy(hfac)_3(2,5\text{-tpy})(H_2O)\cdot(2,5\text{-tpy})]$. (b) Polyhedral representation of the Dy(III). (c) Unit cell of $[Dy(hfac)_3(2,5\text{-tpy})(H_2O)\cdot(2,5\text{-tpy})]$.

Compound 2-**6** (Fig 2.6) crystallizes in the triclinic *P*-1 space group (Table 2.1). The asymmetric unit contains one Dy(III) ion, three $hfac^-$ ligands , one 2,5-tpy ligand, one aqua ligand and one co-crystallizing 2,5-tpy ligand. The dysprosium center resides in an N_2O_7 environment by virtue of three bidentate $[hfac]^-$ ligands, one O from water and two nitrogen donors of the 2,5-tpy ligand (Fig. 6a). The Dy···O and Dy···N distances lie in the ranges of 2.3509(18)–2.4577(19) Å, and 2.581(2)–2.611(3) Å, respectively.

The resulting coordination geometry around Dy(III) is best described as a spherical capped square antiprism with CShM values of 0.503. The closest intermolecular distance between two Dy(III) is 11.45 Å.

Table 2.1 Crystallographic information for Complexes 2-**1** – 2-**6**.

No.	**2-1**	**2-2**	**2-3**	**2-4**	**2-5**	**2-6**
Foluma	$C_{51}H_{72}$ DyPO_7	$C_{48}H_{68}$ DyN_3O_6	$C_{45}H_{29}$ Dy$F_9N_3O_6$	$C_{57}H_{35}$ Dy$F_9N_3O_6$	$C_{59}H_{41}$ Dy$F_9N_3O_7$	$C_{45}H_{27}$ Dy$F_{18}N_3O_7$
Fw	990.55	945.55	1041.21	1191.38	1237.45	1268.23
T(K)	150	150	180	180	180	150
crystal system	monoclinic	monoclinic	monoclinic	orthorhombic	triclinic	triclinic
space group	$P2_1/c$	$P2_1/n$	$P2_1/c$	$Pca2_1$	P-1	P-1
a, *Å*	11.2677(10)	13.6283(4)	12.0393(3)	22.395(2)	10.738(4)	11.3364(3)
b, *Å*	21.5675(3)	16.6895(6)	34.9433(6)	13.496(2)	12.5328(6)	12.7463(3)
c, *Å*	21.8812(3)	21.2697(6)	11.2694(3)	16.1511(2)	22.4263(10)	16.8858(4)
α, *deg*	90	90	90	90	95.148(4)	85.234(2)
β, *deg*	104.608(10)	96.364(2)	117.222(3)	90	101.901(4)	71.865(2)
γ, *deg*	90	90	90	90	115.294(4)	87.857(2)
V (Å^3)	5145.59(11)	4808.0(3)	4215.9(2)	4884.56(10)	2515.6(2)	2310.56(10)
Z	4	4	4	4	2	2
$\rho_{Calcd.}$ (mg·m^{-3})	1.279	1.306	1.64	1.621	1.571	1.823
μ (mm^{-1})	8.046	8.397	1.865	1.622	1.518	9.26
R_{int}	0.0218	0.0249	0.0640	0.0757	0.0482	0.0143
Flack factor	N/A	N/A	N/A	0.044(15)	N/A	N/A
GOF on F^2	1.034	1.046	1.039	1.124	1.022	1.032
R_1, wR_2 ($I > 2\sigma(I)$)[a]	R_1 = 0.0252, wR_2 = 0.0665	R_1 = 0.0231, wR_2 = 0.0597	R_1 = 0.0344, wR_2 = 0.0711	R_1 = 0.0455, wR_2 = 0.1004	R_1 = 0.0458, wR_2 = 0.1033	R_1 = 0.0305, wR_2 = 0.0835
R_1, wR_2(all data)	R_1 = 0.0278, wR_2 = 0.0682	R_1 = 0.0263, wR_2 = 0.0609	R_1 = 0.0464, wR_2 = 0.0778	R_1 = 0.0548, wR_2 = 0.1296	R_1 = 0.0589, wR_2 = 0.1096	R_1 = 0.0310, wR_2 = 0.0840

[a] $R_1 = ||F_o| - |F_c||/\mathring{a}|F_o|$, $wR_2 = \{w[(F_o)^2 - (F_c)^2]^2/w[(F_o)^2]^2\}^{1/2}$

Table 2.2 The CShM values calculated using SHAPE 2.1 for complexes 2-**1** – 2-**5**.

	2-**1**		2- **2**	2-**3**	2-**4**	2-**5**
HP-7	35.863	**OP-8**	30.371	30.264	30.824	30.056
HPY-7	19.596	**HPY-8**	21.708	22.145	22.966	22.729
PBPY-7	7.264	**HBPY-8**	15.922	16.844	14.415	15.273
COC-7	**0.248**	**CU-8**	9.145	10.000	8.055	8.096
CTPR-7	1.707	**SAPR-8**	**0.756**	**0.441**	**1.024**	**0.778**
JPBPY-7	10.815	**TDD-8**	2.354	2.407	1.342	1.601
JETPY-7	19.332	**JGBF-8**	15.209	16.933	14.636	16.300
		JETBPY-8	27.181	27.966	27.753	27.678
		JBTPR-8	2.857	3.045	2.476	2.927
		BTPR-8	2.154	2.375	1.932	2.396
		JSD-8	5.099	5.314	4.364	4.703
		TT-8	9.863	10.790	8.756	8.805
		ETBPY-8	23.876	23.979	22.633	23.343

HP-7 = (*D*7h) Heptagon, HPY-7 = (C_{6v}) Hexagonal pyramid , PBPY-7 = (D_{5h}) Pentagonal bipyramid, COC-7 = (C_{3v}) Capped octahedron, CTPR-7 = (C_{2v}) Capped trigonal prism, JPBPY-7 = (D_{5h}) Johnso pentagonal bipyramid J13, JETPY-7 = (C_{3v}) Johnson elongated triangular pyramid J7, OP-8 = (D_{8h}) Octagon, HPY-8 = (C_{7v}) Heptagonal pyramid, HBPY-8 = (D_{6h}) Hexagonal bipyramid, CU-8 = (O_h) Cube, SAPR-8 = (D_{4d}) Square antiprism, TDD-8 = (D_{2d}) Triangular dodecahedron, JGBF-8 = (D_{2d}) Johnson gyrobifastigium J26, JETBPY-8 = (D_{3h}) Johnson elongated triangular bipyramid J14, JBTPR-8 = (C_{2v}) Biaugmented trigonal prism J50, BTPR-8 = (C_{2v}) Biaugmented trigonal prism, JSD-8 = (D_{2d}) Snub diphenoid J84, TT-8 = (T_d) Triakis tetrahedron, ETBPY-8 = (D_{3h}) Elongated trigonal bipyramid

Table 2. 3 The CShM values calculated using SHAPE 2.1 for complexes 2-**6**.

	2-**6**
Enneagon (D_{9h})	36.777
Octagonal pyramid (C_{8v})	22.013
Heptagonal bipyramid (D_{7h})	18.915
Johnson triangular cupola J3 (C_{3v})	15.452
Capped cube J8 (C_{4v})	8.876
Spherical-relaxed capped cube (C_{4v})	8.031
Capped square antiprism J10 (C_{4v})	1.196
Spherical capped square antiprism (C_{4v})	**0.503**
Tricapped trigonal prism J51 (D_{3h})	2.420
Spherical tricapped trigonal prism (D_{3h})	1.027
Tridiminished icosahedron J63 (C_{3v})	12.391
Hula-hoop (C_{2v})	12.339
Muffin (C_s)	1.158

2.5 SMM characteristics of the Dy-complexes 2-1 – 2-6

2.5.1 SMM characteristic of [Dy(tmhd)$_3$(POPh$_3$)] (2-1)

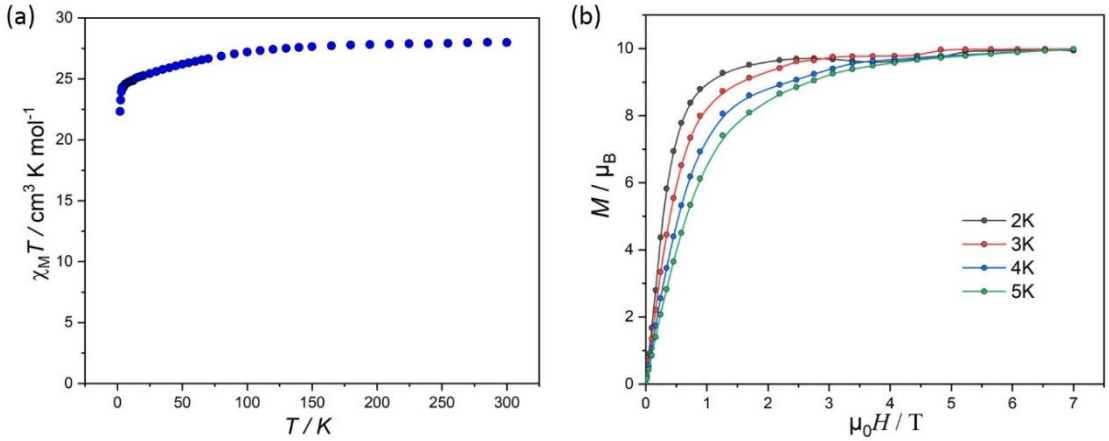

Figure 2.7 The $\chi_M T$ vs. T plots for complex [Dy(tmhd)$_3$(POPh$_3$)] (2-**1**) (a). Plots of M vs. H at different temperatures (b).

The static magnetic (DC) properties of complex 2-**1** was probed employing polycrystalline samples in the temperature range of 2–300 K and under an applied field of 1000 Oe. The $\chi_M T(T)$ plots are shown in Figure 2.7a, the room temperature $\chi_M T$ values of complex 2-**1** is 14.02 cm^3 K mol^{-1}, which is comparable with the expected value of 14.17 cm^3 K mol^{-1} for a free Dy^{III} with J = 15/2 and g_J = 4/3. Upon cooling, the $\chi_M T$ value gradually decreased down to a value of 11.2 cm^3 K mol^{-1} at 2 K, which might occur due to the thermal depopulation of the Stark sub-levels of Dy^{III} ion[47,181-183]. The magnetizations of complex 2-**1** measured against applied magnetic fields at 2, 3, 4 and 5 K reveal a rapid increase at low magnetic fields (Fig 2.7b). At high magnetic fields, magnetization increases gradually and finally reaches ca. 4.45 μ_B at 7 T (Fig 2.7b), which almost meets the saturation value of 5 μ_B for an Ising-like Dy(III)[184].
Alternating current (ac) susceptibility measurements for complex 2-**1** under a zero-dc field show that the out-of-phase susceptibility (χ'') diverges at various frequencies, but without reaching any maxima, possibly due to a much faster relaxation such as the quantum tunneling of magnetization (QTM) and Raman process. The QTM process could be suppressed when a dc field is applied[185]. A field-dependent study reveals an optimal field of 1200 Oe, where the relaxation characteristic of 2-**1** is slower (Fig 2.8).

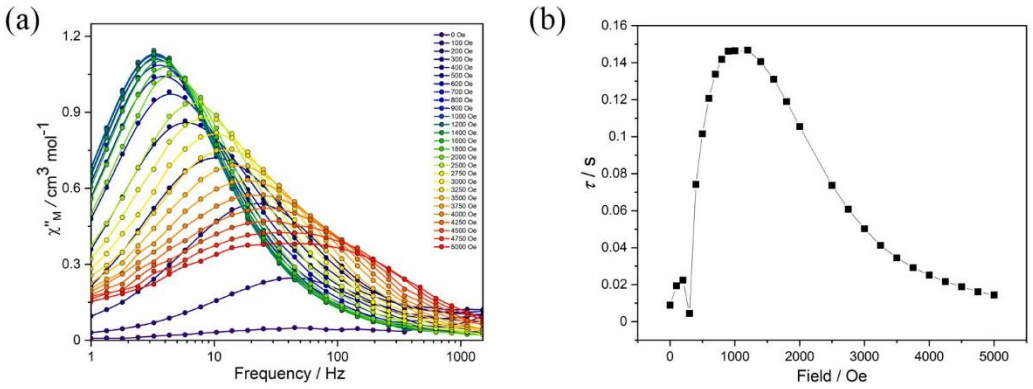

Figure 2.9 Study of χ_M"(v) at fields between 0 and 5 kOe conducted on 2-**1** to determine the field at which relaxation is slowest, i.e., the optimal field; (b) $\tau(H)$ plot for the data obtained in panel (a). The slowest relaxation is found to occur at 1200 Oe. The data was collected employing an oscillating field of 3.5 Oe.

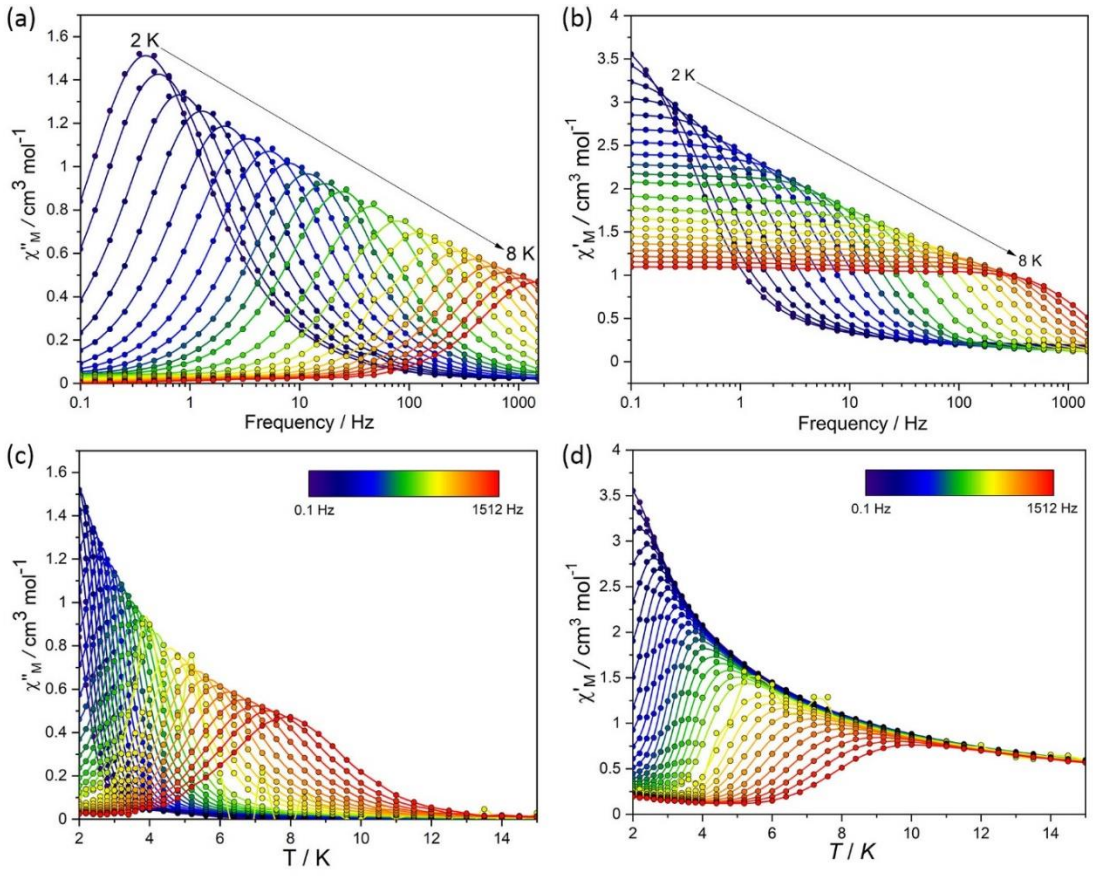

Figure 2.8 Experimental frequency dependent magnetic susceptibility data at 1200 Oe applied DC (H_{dc}) field and varied temperatures (χ_M"(v)) for 2-**1** (a) and (b). Panel (c) and (d) show the tempreture dependence of the out-of-phase ac magnetic susceptibility data under a 1200 Oe dc field for 2-**1**, respectively.

Thus, ac susceptibility measurements were performed at an applied dc field of 1200 Oe. The in phase (χ_M') and out of phase (χ_M'') ac susceptibility components show typical SMM behaviour (Fig 2.9). The out of phase component exhibits a clear frequency-dependent maximum below 8 K for 2-**1** until the highest frequency measureable (1512 Hz) by the magnetometer. The ac data of 2-**1** was well fitted employing the generalized Debye model. The Cole-Cole plots are close to semicircles (Fig 2.10a), in agreement with generalized Debye model. The various temperature relaxation times for complex 2-**1** are depicted in Figure 2.10b. The ln(τ) versus 1/T plots deviate from a straight line in the low temperature region and bend, which means that Raman process exists.

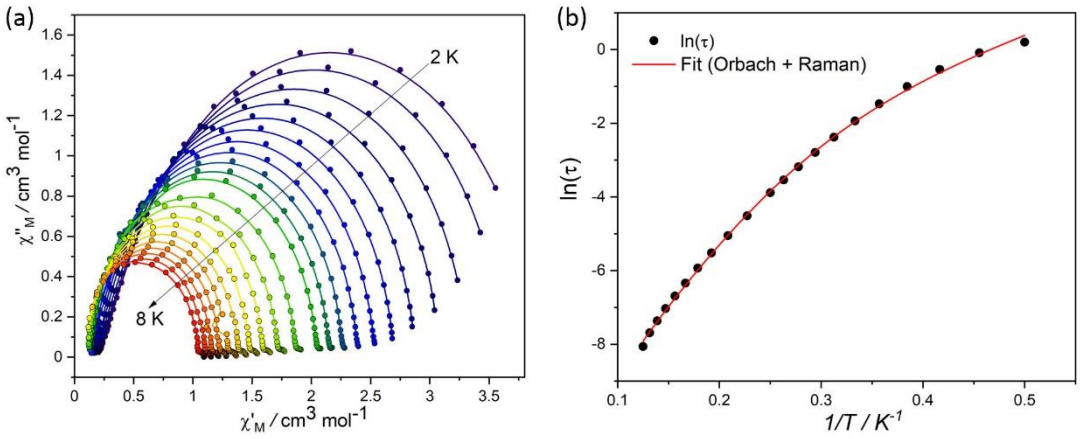

Figure 2.10 Cole–Cole plots under a 1200 Oe dc field for (a) 2-**1**. The solid lines represent the best fits. (b) Temperature dependence of the magnetic relaxation time τ under 1200 Oe is shown as ln(τ) versus T^{-1} for 2-**1**. The solid red lines are the best fit to the multiple relaxation equation.

To investigate mechanisms inducing magnetization relaxation, the measured relaxation time was fitted with the equation [Eq. (1)]:

$$\tau^{-1} = \tau_0^{-1} \exp(-U_{eff}/k_B T) + CT^n \qquad (1)$$

where the Orbach [$\tau_0^{-1} \exp(-U_{eff}/k_B T)$] and Raman ($CT^n$) relaxation processes were taken into account. As shown in Figure 2.10b, the fitting curves are basically consistent with the data of τ vs T^{-1}. The best fitting affords an U_{eff} of 35.5(1) K, $\tau_0 = 8.3 \times 10^{-6}$ s, C = 0.015(3) s^{-1} K^{-n}, n = 5.4(2). The values of τ_0 agree with the expected characteristic relaxation time 10^{-6}-10^{-11} s for SMMs.

2.5.2 SMM characteristic of [Dy(tmhd)$_3$(2,5-tpy)] (2-2)

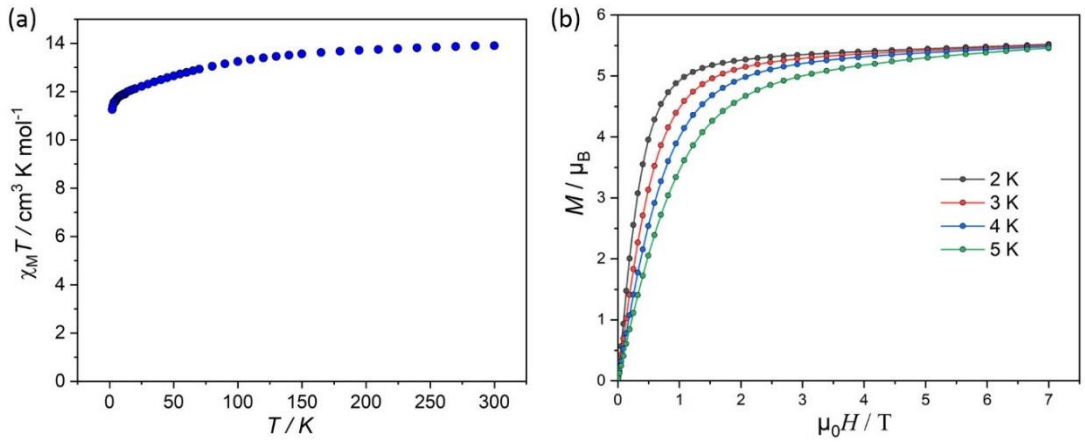

Figure 2.11 The $\chi_M T$ vs. T plots for complex 2-**2** (a). Plots of M vs. H at different temperatures (b).

Direct current (DC) magnetic susceptibility data were collected for crushed crystals of 2-**2** from 2 to 300 K under an applied magnetic field of 1000 Oe. At room temperature, the $\chi_M T$ product is 13.90 cm^3 K mol^{-1} (Fig 2.11a). This value agrees with the expected 14.17 cm^3 K mol^{-1} for free Dy^{3+} (J = 15/2, g = 4/3) ions. Upon cooling, the $\chi_M T$ product remains nearly constant until ca. 150 K then a gradual decrease of the value is observed. $\chi_M T$ product of about 11.2 cm^3 K mol^{-1} is obtained at 2 K. This might be due to the thermal depopulation of the Stark sublevels of Dy^{III} ion[47,181-183].

Besides temperature-dependent studies, we performed measurements of the molar magnetization versus the applied magnetic field. It shows common behaviour, of a rapid increase in magnetization, which strongly flattens upon reaching higher fields. With values around 5.5 μ_B at 7 T, the value is in good agreement with expected values for one Dy ion, i.e., ~5 μ_B.

We studied the dynamic behaviour of the sample through AC susceptibility measurements. Complex 2-**2** shows a single maximum in the frequency-dependent out-of-phase component of the magnetic susceptibility $\chi''(\nu)$, in 800 Oe applied DC field, which starts shifting to higher frequencies upon increasing the temperature (Fig 2.12). At the lowest temperature of 2 K, the maximum lies below the minimum working frequency (0.1 Hz) of the magnetometer, while for temperatures between 3 K and 12 K the relaxation shows a strong temperature dependence. The temperature-dependent shifting of the signal is typically ascribed to the Orbach relaxation of SMMs. By fitting

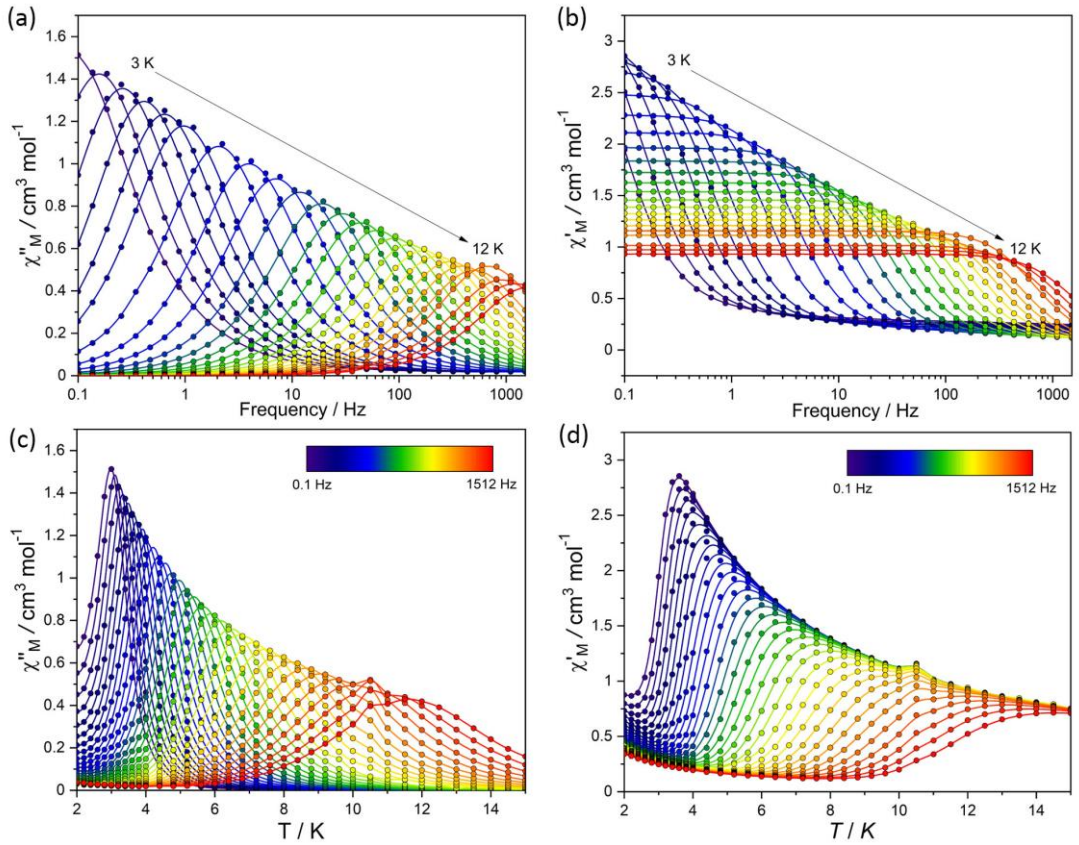

Figure 2.13 Experimental frequency dependent magnetic susceptibility data at 800 Oe applied DC (H_{dc}) field and varied temperatures (χ_M"(ν)) for 2-**2** (a) and (b). Panel (c) and (d) show the tempreture dependence of the out-of-phase ac magnetic susceptibility data under an 800 Oe dc field for 2-**2**, respectively.

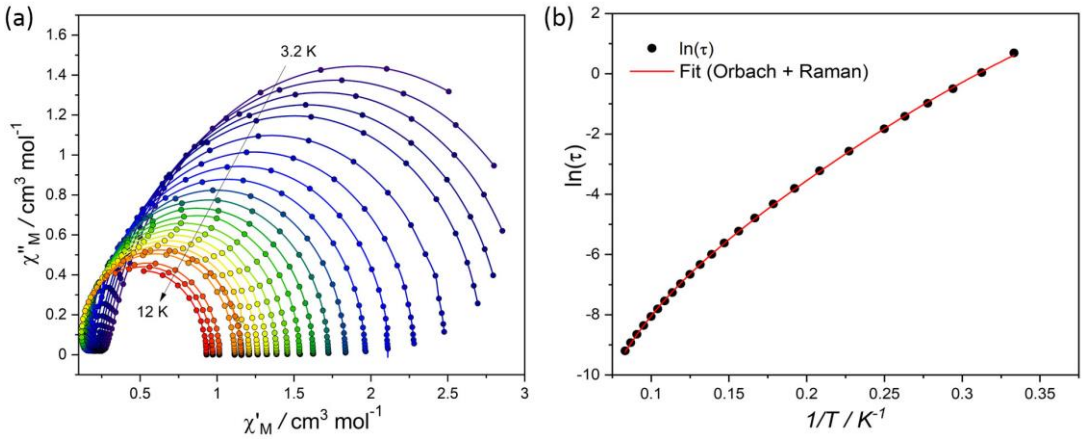

Figure 2.12 Cole–Cole plots under a 800 Oe dc field for (a) 2-**2**. The solid lines represent the best fits. (b) Temperature dependence of the magnetic relaxation time τ under 800 Oe is shown as ln(τ) versus T^{-1} for 2-**2**. The solid red lines are the best fit to the multiple relaxation equation.

the in-phase and out-of-phase signals using a generalized Debeye model (Fig 2.13a), we obtained an α parameter between 0.01-0.13. The distribution of the relaxation parameter (α) indicates a narrow distribution of relaxation times.

Examination of the temperature dependence of the relaxation times shows a strongly-temperature-dependent regime at high temperatures, and a power-law temperature dependence at lower temperatures, suggesting exponential (Orbach-like) and Raman relaxation mechanisms, respectively (Fig 2.13b). The ln(τ) versus 1/T data can be modelled with the [Eq. (1)], with best-fit parameters U_{eff} of 36.7(1) K, $\tau_0 = 3.4 \times 10^{-5}$ s, $C = 1.4 \times 10^{-4}(1)$ s^{-1} K^{-n}, n = 7.2(1).

2.6.3 SMM characteristic of [Dy(BTFA)$_3$(2,5-tpy)] (2-3)

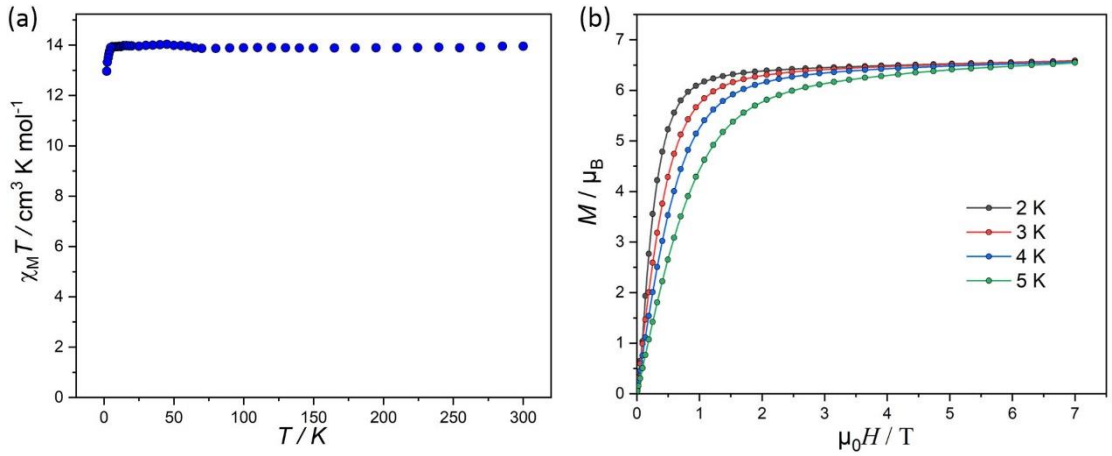

Figure 2.14 The $\chi_M T$ vs. T plots for complex 2-**3** (a). Plots of M vs. H at different temperatures (b).

The variable temperature magnetic susceptibility of a polycrystalline sample of 2-**3** was measured under a 1000 Oe direct current (dc) field over the temperature range of 2–300 K (Fig. 13a). The $\chi_M T$ value at room temperature is 13.95 cm^3 K mol^{-1}, which is close to the spin-only value of 14.12 cm^3 K mol^{-1} expected for one Dy^{III} ions ($^6H_{15/2}$, S = 5/2, L = 5, J = 15/2, g = 4/3). As the temperature is lowered, the $\chi_M T$ product remains nearly constant until 6 K. Then the $\chi_M T$ value dropped sharply to 12.9 cm^3 K mol^{-1} at 2 K. The drop is attributed to the thermal depopulation of Dy^{III} Stark sublevels upon cooling[47,181-183]. The field dependence of the magnetization of 2-**3** was measured at 2–5 K (Fig 2.14b). The magnetization increases very fast at low fields, indicating the very well separated excited Kramers doublets, and it reaches the "saturation" of 4.9 μ_B.

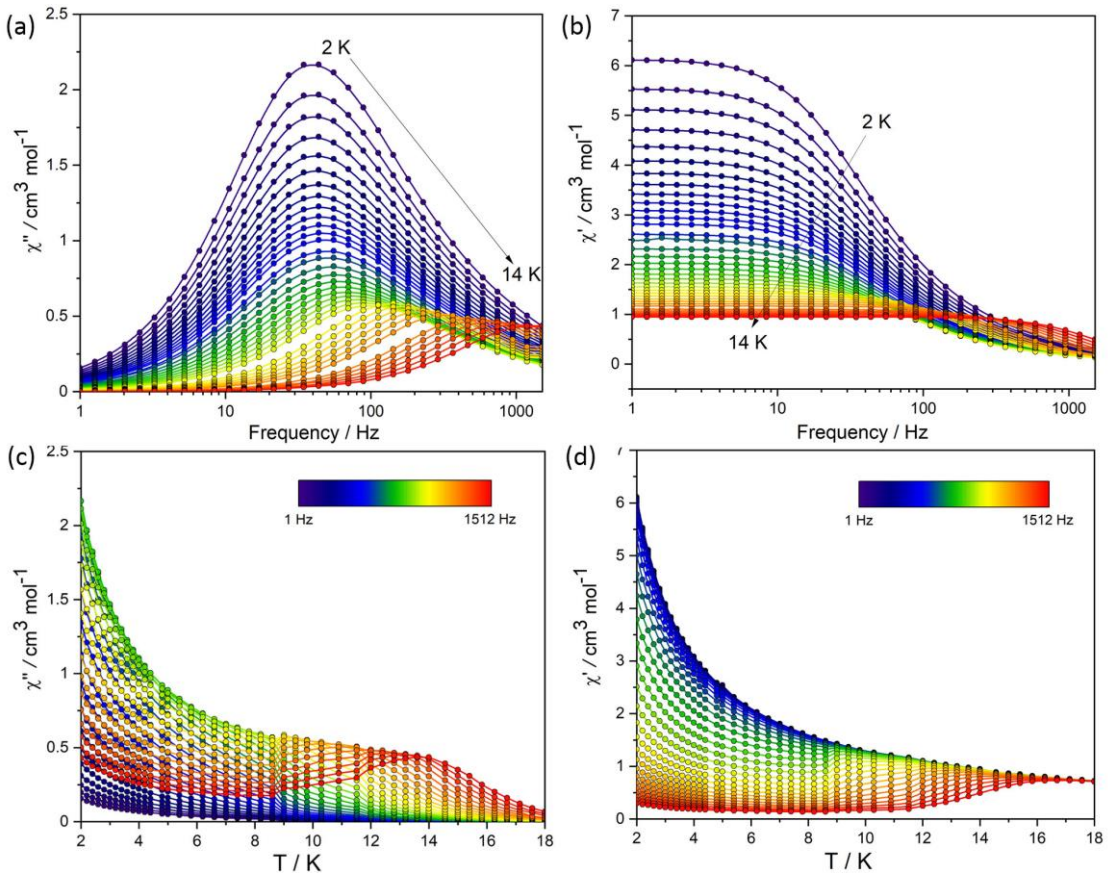

Figure 2.15 Experimental frequency-dependent magnetic susceptibility data at zero applied DC (H_{dc}) field and varied temperatures (χ_M'' (v)) for 2-**3** (a) and (b). Panel (c) and (d) show the tempreture dependence of the out-of-phase ac magnetic susceptibility data under a zero dc field for 2-**3**, respectively.

Alternating-current (AC) susceptibility measurements were performed to study the SMM characteristic of the complex (Fig 2.15). In zero DC field, both in-phase (χ') and out-of-phase (χ'') susceptibilities show significant frequency dependence peaks at a temperature range 2–14 K, which clearly indicates that the slow relaxation of magnetization arises from SMM properties. At the lowest temperature of 2 K, the maximum is centerd around 40 Hz, and stays practically constant until reaching 5 K. Above 5 K, the maximum in $\chi(v; T)$ is clearly temperature dependent, shifting swiftly up to 14 K. The in-phase (χ') and out-of-phase (χ'') components show one relaxation process for 2-**3**, and thus we fit the Cole−Cole plots with a generalized Debye function. we obtained an α-parameter between 0.03-0.19, indicating a narrow distribution of relaxation times. α becomes larger at lower temperatures due to the onset of a different relaxation mechanism (Fig 2.16a).

The temperature dependence of magnetization dynamics can be fitted with the equation [Eq. (2)] considering multiple relaxation mechanisms.

$$\tau^{-1} = \tau_0^{-1} \exp(-U_{eff}/k_B T) + CT^n + \tau_{QTM}^{-1} \qquad \text{[Eq. (2)]}$$

The fit shown in Fig. 15b afforded U_{eff}/k_B = 16.6(2) K, τ_0 = 5.0(1) × 10^{-4} s, C = 4.1 (1) × 10^{-5} s^{-1} K^{-n}, n = 6.9(5), τ_{QTM} = 0.00325(6) s under zero dc field.

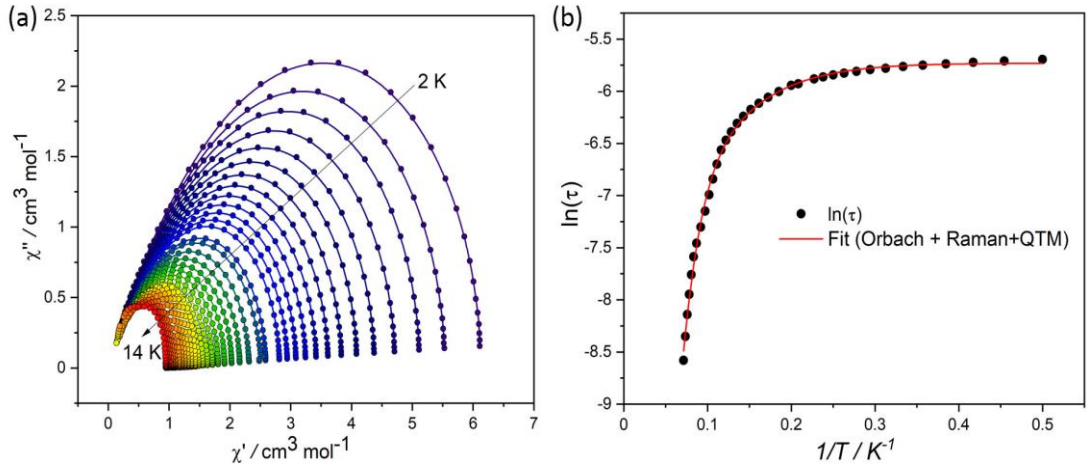

Figure 2.16 (a) Cole–Cole plots under a zero dc field for 2-**3**. The solid lines represent the best fits. (b) Temperature dependence of the magnetic relaxation time τ under zero applied field (H_{dc}) is shown as ln(τ) versus T^{-1} plot. The solid red line is the best fit of the experimental data obtained employing equation 2.

2.6.4 SMM characteristic of [Dy(NTFA)$_3$(2,5-tpy)] (2-4)

Direct current (dc) magnetic susceptibility of the polycrystalline sample of 2-**4** was measured in the temperature range of 2–300 K under an external field of 1000 Oe. At room temperature, the $\chi_M T$ = 13.70 cm^3 K mol^{-1} (Fig 2.17) is obtained for the complex, which is slightly lower than the expected value for a free Dy^{III} ion (14.17 cm^3 K mol^{-1}). The smaller $\chi_M T$ value observed for the complex than the expected one is attributed to the splitting of the $^6H_{15/2}$ ground state. Upon cooling, $\chi_M T$ first decreases slowly due to the thermal depopulation of the Stark sublevels of Dy^{III} ion. And then it dramatically drops at low temperature and reaches the value of 10.3 cm^3 K mol^{-1} at 2 K, implying the possible presence of magnetic blocking.

The magnetization of complex 2-**4** measured against applied magnetic fields at 2, 3, 4 and 5 K reveal a rapid increase at low magnetic fields (Fig 2.17b). At high magnetic

fields, magnetization increases gradually and finally reaches ca. 5.1 μ_B at 7 T (Fig 2.17b), which is close to the saturation value of 5 μ_B for an Ising-like Dy(III)[184].

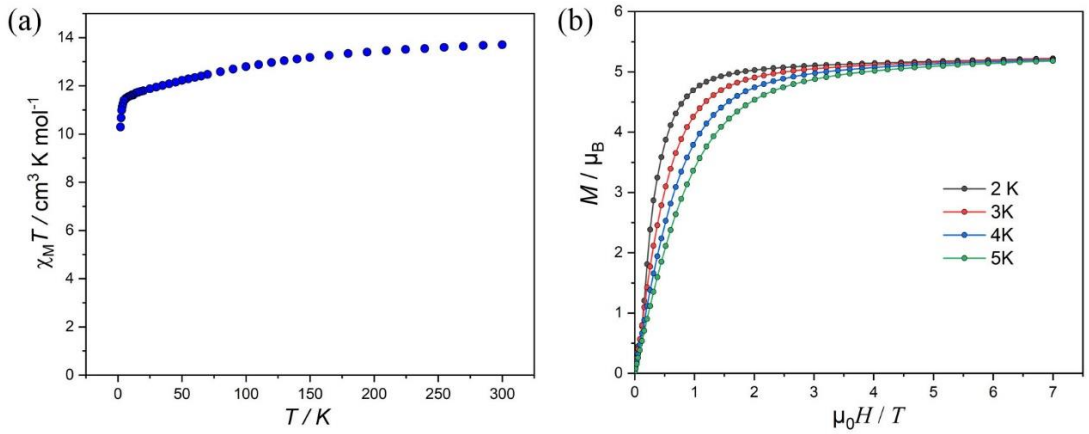

Figure 2.17 The $\chi_M T$ vs. T plots for complex 2-**4** (a). Plots of M vs. H at different temperatures (b).

To get insight of dynamic magnetic behaviour—that is, SMM characteristic—of the complex, temperature-dependent alternating current (ac) susceptibility measurements were carried out at varying frequencies under H_{dc} = 0 Oe. The in-phase (χ') and out-of phase (χ'') ac susceptibility components show typical SMM behaviour (Fig 2.18). At the lowest temperature of 2 K, the maximum is centred around 120 Hz, and stays practically constant until reaching 9 K. Above 9 K the maximum in $\chi(v; T)$ is clearly temperature-dependent, shifting swiftly up to 20 K. A Cole–Cole plot — χ'' versus χ' plot— for 2-**4** shows semicircular shapes in the temperature range 2 - 20 K (Fig 2.19a). The fitting via the generalized Debye model yields α values in the range 0.02 – 0.19, which, as expected, suggest a narrow distribution of relaxation times.

In order to explore the mechanisms inducing the magnetization relaxation process of the complex, the temperature-dependence of relaxation times was thermally induced using the equation 1. The fitting results suggest that the magnetic relaxation is mediated through a combination of Raman and thermally assisted Orbach mechanisms (Fig 2.19b). The anisotropic energy barrier is U_{eff}/k_B = 75.5(1) K with the pre-exponential factor $\tau_0 = 6.9(1) \times 10^{-6}$ s, C = 791(4) s^{-1} K^{-n}, n = 0.13. Note that the Raman n parameter is lower than the expected for a purely Kramers ion, implying that acoustic and optic phonons are active[186,187].

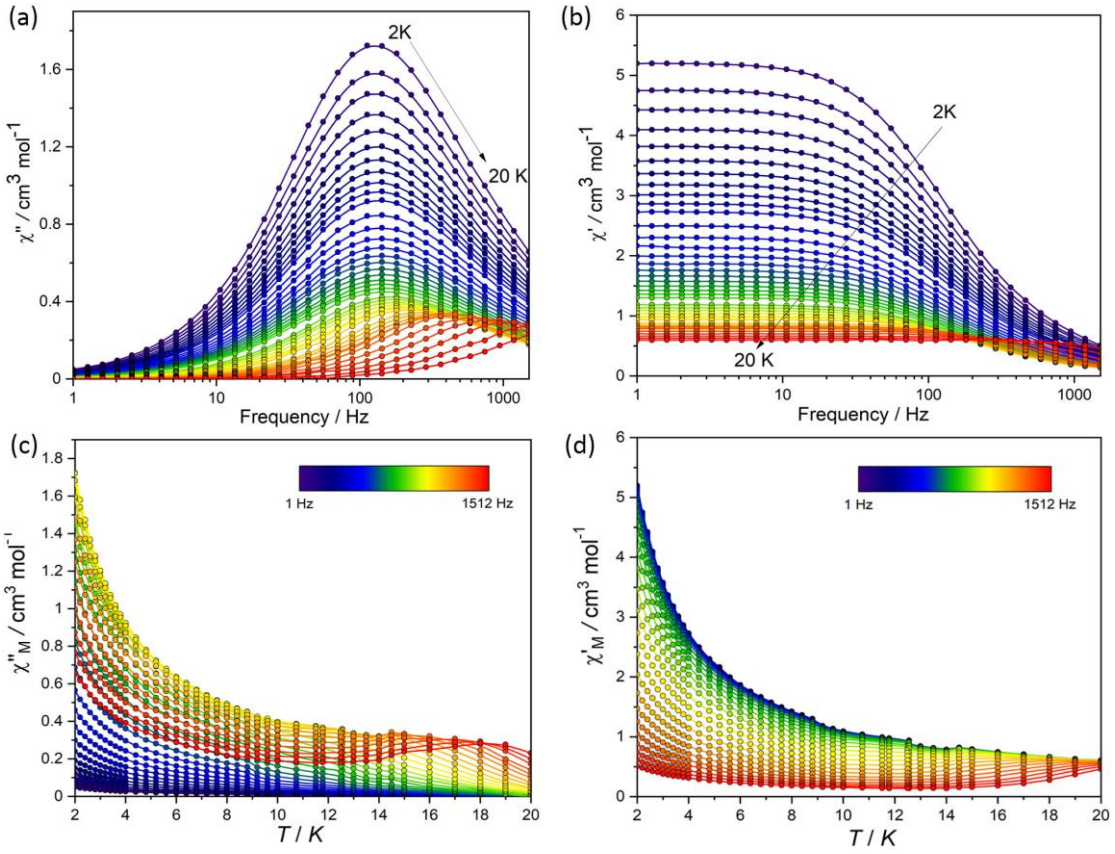

Figure 2.19 Experimental frequency-dependent magnetic susceptibility data at zero applied DC (H_{dc}) field and varied temperatures (χ_M" (v)) for 2-**4** (a) and (b). Panel (c) and (d) show the tempreture dependence of the in-phase and out-of-phase ac magnetic susceptibility data, respectively, of 2-**4** under a zero-dc field.

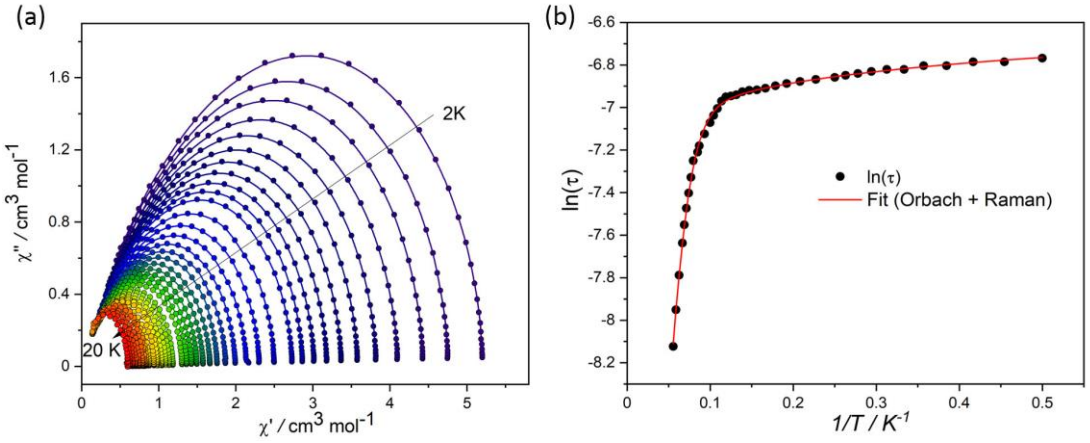

Figure 2.18 (a) Cole–Cole plots under a zero dc field for 2-**4**. The solid lines represent the best fits. (b) Temperature dependence of the magnetic relaxation time τ under H_{DC} = 0 is shown as ln(τ) versus T^{-1} for 2-**4**. The solid red lines are the best fit to the multiple relaxation equation composed of Orbach and Raman relaxation mechanisms.

2.6.5 SMM characteristic of [Dy(NTFA)$_3$(2,5-tpy)·C_2H_5OH] (2-5)

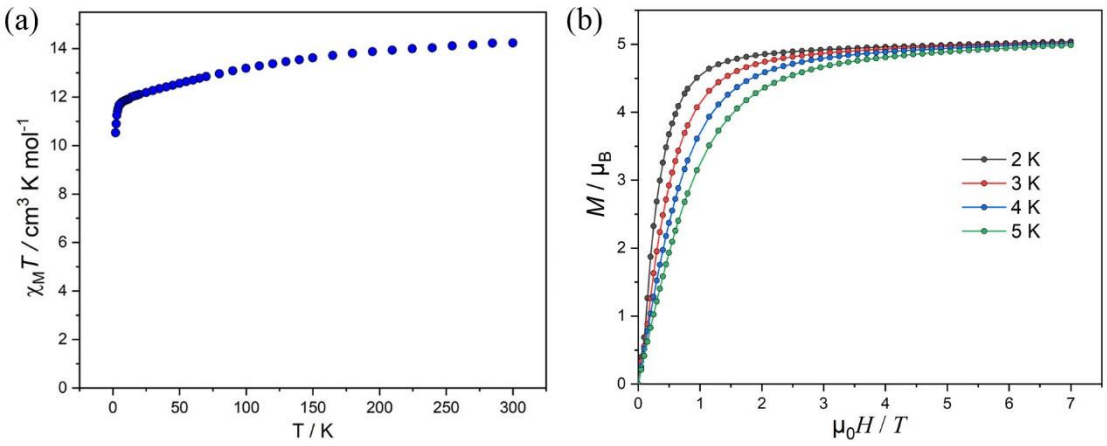

Figure 2.20 The $\chi_M T$ vs. T plots for complex 2-**5** (a). Plots of M vs. H at different temperatures (b).

The temperature dependence (2–300 K) of direct current (dc) magnetic susceptibility data of polycrystalline sample of 2-**5** was measured under an applied magnetic field of 1.0 kOe (Fig 2.20). As can be seen from the figure, the $\chi_M T$ value at room temperature is 14.2 cm^3 K mol^{-1} for the complex, which is in agreement with the expected values of a free Dy^{III} ions (14.17 cm^3 K mol^{-1}, J = 15/2, g = 4/3). As the temperature is lowered, the $\chi_M T$ product of complex 2-**5** gradually decrease to attain a value of 11.7 cm^3 K mol^{-1}, at around 6 K and thereafter decreases rapidly until 2 K is reached, indicating magnetic blocking below this temperature.

The *M vs. H* data collected at temperatures of 2, 3, 4 and 5 K showed a rapid increase at low magnetic fields (Fig 2.20b). The saturation of magnetization was observed at high magnetic fields with values of 4.98 μ_B for 2-**5** at 7 T. The $M(H)$ values are reasonably consistent with those predicted for one Dy(III) ions with well-defined J = 15/2 ground doublet, i.e., ~5 μ_B.

The ac magnetic characteristics gathered with an oscillating ac field of 3.5 Oe indicate the presence of slow magnetic relaxation in complex 2-**5** at zero-dc field (Fig 2.21). In the frequency range of 1–1512 Hz, the non-negligible ac signal was found from 2 K to 18 K, which shows typical SMM behaviour. At the lowest temperature of 2 K, the maximum is centered around 142 Hz, and stays practically constant until reaching 8 K. Above 8 K the maximum in $\chi(v; T)$ is clearly temperature dependent, shifting swiftly up to 18 K. A Cole–Cole plot for 2-**5** shows semicircular shapes in the temperature

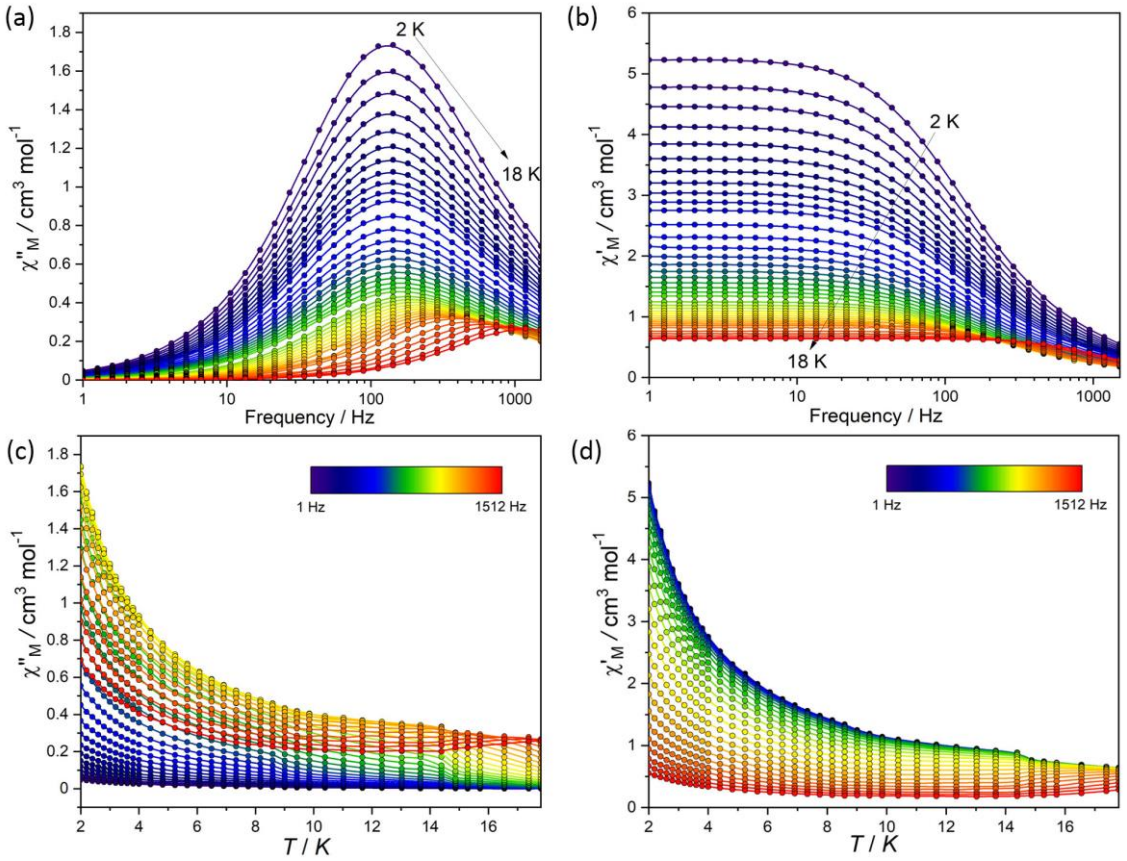

Figure 2.22 Experimental frequency dependent magnetic susceptibility data at zero applied DC (H_{dc}) field and varied temperatures (χ_M"(ν)) for 2-**5** (a) and (b). Panel (c) and (d) show the tempreture dependence of the out-of-phase ac magnetic susceptibility data under a zero-dc field for 2-**5**, respectively.

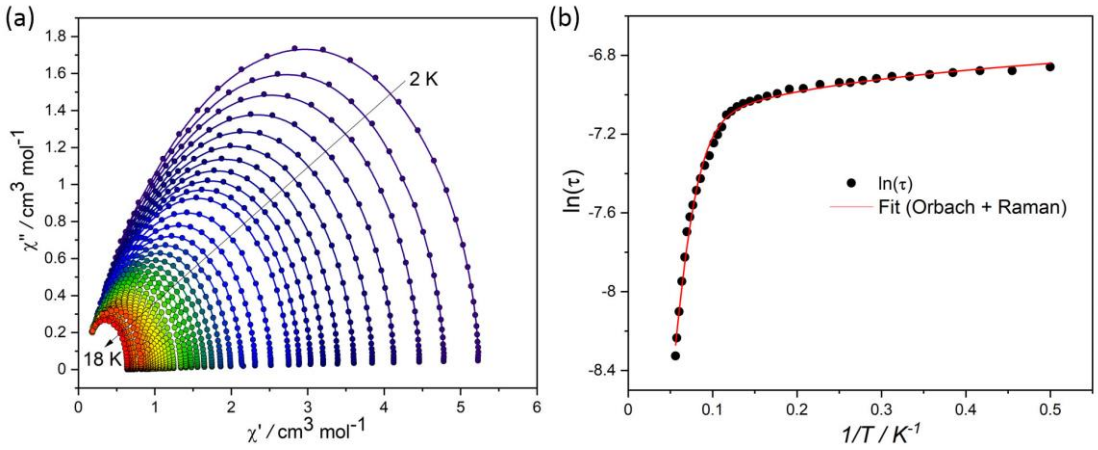

Figure 2.21 Cole–Cole plots under a zero-dc field for (a) **2-5**. The solid lines represent the best fits. (b) Temperature dependence of the magnetic relaxation time τ under zero is shown as ln(τ) versus T^{-1} for **2-5**. The solid red lines are the best fit to the multiple relaxation equation.

range of 2–18 K (Fig 2.22a). The fitting via the generalized Debye model yields α

values in the range of 0.02 – 0.20, which, as expected, suggest a narrow distribution of relaxation times associated with the complex.

To investigate mechanisms inducing magnetization relaxation, the measured temperature-dependent relaxation time data was fitted with the equation [Eq. (1)], where the Orbach [τ_0^{-1} exp ($-U_{eff}/k_BT$)] and Raman (CT^n) relaxation processes were taken into account. As shown in Fig 2.22b, the fitting curve is basically consistent with the data of τ vs T^{-1}. The best fitting affords an U_{eff} of 63.9(2) K, $\tau_0 = 1.1 \times 10^{-5}$ s, C = 838.3(18) s^{-1} K^{-n}, n = 0.15(1).

2.6.6 SMM characteristic of [Dy(hfac)$_3$(2,5-tpy)(H$_2$O)·(2,5-tpy)] (2-6)

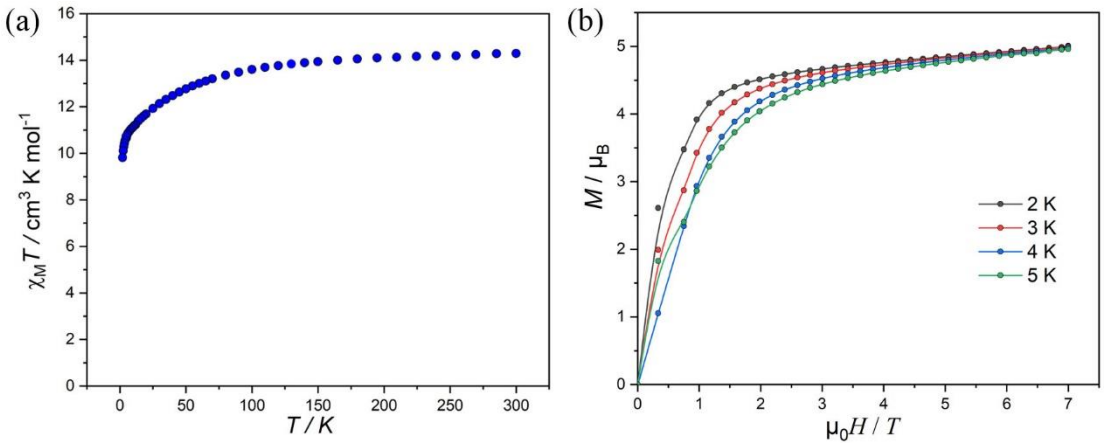

Figure 2.23 The $\chi_M T$ vs. T plots for complex 2-**6** (a). Plots of M vs. H at different temperatures (b).

Temperature-dependence of the direct current magnetic susceptibility data for complex 2-**6** (polycrystalline) was evaluated in the temperature range of 2–300 K under a 1000 Oe external magnetic field. The experimental $\chi_M T$ value of complex 2-**6** is 14.28 cm^3 K mol^{-1} at 300 K, in accordance with the theoretical value for an isolated Dy^{III} ion (14.17 cm^3 K mol^{-1}, J = 15/2, g = 4/3). The $\chi_M T$ value of complex 2-**6** decreases gradually in the temperature range of 300–25 K and then declines sharply and reached minimum values of 9.8 cm^3 K mol^{-1}at 2 K (Fig 2.23).

The field dependence of magnetization of complex 2-**6** was evaluated at different temperatures 2, 3, 4, and 5 K in the magnetic field range of 0–7 T (Fig 2.23b). The sharp increase of magnetization at low field at low temperatures reveals a significant energy difference between the ground and excited states. Additionally, as the external field is increased, the magnetization value increases and reaches saturation at 4.96 μ_B

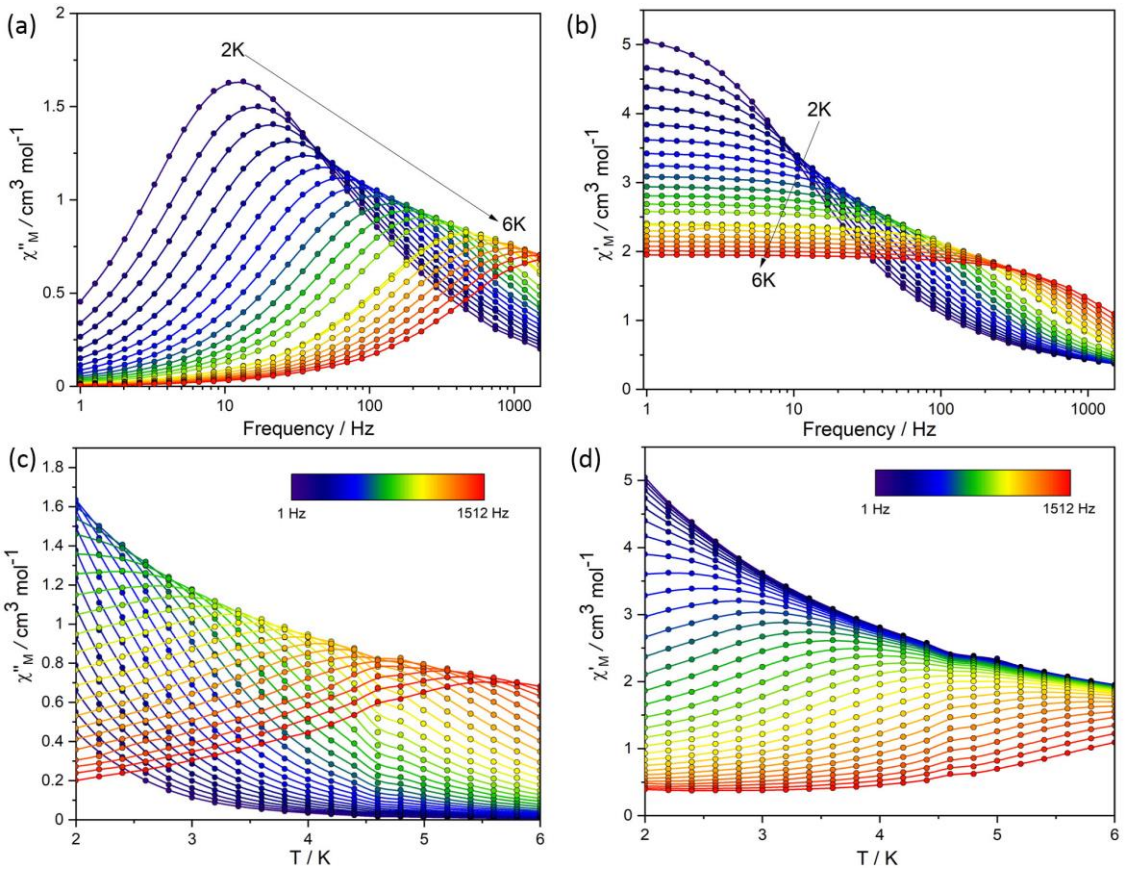

Figure 2.24 Experimental frequency dependent magnetic susceptibility data at 800 Oe applied DC (H_{dc}) field and varied temperatures ($\chi_M''(\nu)$) for 2-**6** (a) and (b). Panel (c) and (d) show the tempreture dependence of the out-of-phase and in-phase, respectively, ac magnetic susceptibility data under a zero dc field for **2-6**.

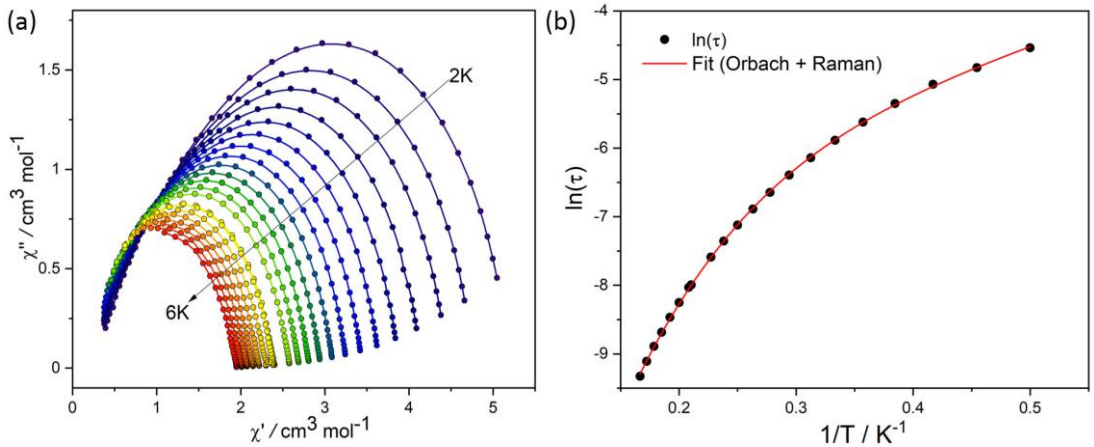

Figure 2.25 Cole–Cole plots under a zero-dc field for 2-**6**(a). The solid lines represent the best fits. (b) Temperature dependence of the magnetic relaxation time τ under H_{dc} = 800 Oe is shown as ln(τ) versus T^{-1} for 2-**6**. The solid red lines are the best fit to the multiple relaxation equation.

at 7 T. The $M(H)$ value is consistent with the expected one (5 μ_B) for one Dy(III) ions with a well-defined J = 15/2 ground doublet.

To probe the possible slow magnetization relaxation, ac magnetic measurements were carried out for 2-**6**. The out-of-phase signal (χ") was observed after a 800 Oe static dc field (Fig 2.24) was applied, indicating the presence of field-induced SMM behaviour. The out-of-phase χ" ac susceptibility data exhibit strong frequency dependent peaks with well-defined maxima at temperatures up to 6 K. The relaxation times, τ, were extracted by fitting the Cole-Cole plots of χ" vs. χ' using the generalized Debye model (Fig 2.25). The α parameters found are in the range of 0.18–0.27 (2–6 K) for complex 2-**6**. Fitting the full temperature range data to the equation $\tau^{-1} = \tau_0^{-1} \exp(-U_{eff}/k_BT) + CT^n$, gives energy barriers of U_{eff} = 5.3(1) K, $\tau_0 = 9.4 \times 10^{-4}$ s, C = 0.27(3) s^{-1} K^{-n}, n = 5.9(1).

2.7 Conclusion

In this chapter, six mononuclear Dy^{III} complexes were characterized, both structurally and magnetically. The mononuclear complexes were successfully synthesized with two different ligands by tailoring the terminal ligands. The Dy(III) ion in complex 2-**1** is placed in a N_2O_6 coordination environment. The overall geometry is best described as a Capped octahedron with C_{3v} ligand field symmetry around the Dy(III). In complexes 2-**2**, 2-**3**, 2-**4**, and 2-**5**, the Dy(III) ions are placed in a N_2O_6 coordination environment. The geometry of the complexes is best described as square antiprism with D_{4d} symmetry. The geometry of complex 2-**6** is the spherical capped square antiprism with C_{4v} symmetry; the Dy(III) ion is placed in the N_2O_7 coordination environment. The dc and ac magnetic properties of all complexes were measured. Magnetic investigations evidenced that all the complexes are SMMs with the energy barriers (U_{eff}) of 35.5 K (2-**1**, H_{dc} = 1200 Oe), 36.7 K (2-**2**, H_{dc} = 800 Oe), 16.6 K (2-**3**, H_{dc} = 0 Oe), 75.5 K (2-**4**, H_{dc} = 0 Oe), 63.9 K (2-**5**, H_{dc} = 0 Oe), 5.3 K (2-**6**, H_{dc} = 800 Oe). The unique relaxation properties exhibited by the complexes are a result of the varying coordination environment surrounding the Dy(III) ions. This work demonstrates that the SMM property can be modulated by subtle changes in the coordination environment resulting from changes in the substituents of β-diketonate ligands. These complexes will be a good reference for SMM properties of dysprosium analogues.

Chapter 3. Single-molecule magnet characteristics of dinuclear Dy(III) complexes

Introducing intramolecular magnetic coupling, which could significantly impact the molecular magnetic anisotropy, is one of the strategies adopted to achieve high spin-reversal barriers in single-molecule magnets (SMMs)[74,188,189]. Therefore, dinuclear complexes featuring significant intramolecular coupling are promising candidates for studying the relation between the single-ion anisotropy and exchange interactions governing the relaxation mechanism. The choice of the Dy^{III} ion is obvious because it has significant magnetic anisotropy, large spin ground state (m_J = 15/2), and as a Kramers ion reduces the possibility of QTM hence improving the SMM behavior. In this regard, the construction of dinuclear Dy^{III} complexes with slight differences in their coordination environments might be a promising approach to obtain insights into magnetic interactions between the Dy centers as well as the way uniaxial anisotropies affect the dynamic magnetic behaviors[190-192]. On the other hand, the natural composition of Dy^{III} comprises seven isotopes, possessing two different nuclear spin states, I = 0 and 5/2. In the nuclear spin scheme, the strong anisotropic character of the single-molecule magnet (SMM) isolates the ground doublet state, which is then coupled to the nuclear spins present within the lanthanide through a strong hyperfine interaction. As a result, the ground doublet state splits into ($2I$ + 1) states, where I is the nuclear spin of the lanthanide. The multilevel nature of the nuclear states within the lanthanides allows for the operation of multiple states within a single unit. As an extension of two-level quantum bits (qubits), multilevel systems, so-called qu*d*its, where *d* represents the Hilbert space dimension, have been predicted to reduce the number of iterations in quantum - computation algorithms[15,193].

In this chapter, seven dinuclear Dy complexes are successfully synthesized using three distinct set of ligands to modulate the magnetization relaxation dynamics. The set is composed of different β-diketonate co-ligands, bisbpy and TAPE. A series of isotopically enriched (I = 0 and 5/2) complexes have also been prepared to study the effect of nuclear spin on the magnetization relaxation dynamics.

Structures of the ligands used to prepare the complexes are discussed in this chapter. All the complexes show SMMs properties, as inferred from the alternative current (AC) susceptibility studies. μ-SQUID measurements and calculation for complexes 3-**2**$^{(I = 5/2)}$, 3-**3**$^{(I = 0)}$, 3-**6**$^{(I = 5/2)}$, and 3-**7**$^{(I = 0)}$ are used to investigate the impact of the nuclear spin. In the following sections, structural and single-molecule magnetic characteristics of the complexes will be discussed.

3.1 Syntheses and characterization

3.1.1 Synthesis of ligand 2, 2': 5', 5": 2", 2"'-Quaterpyridine (bisbpy)

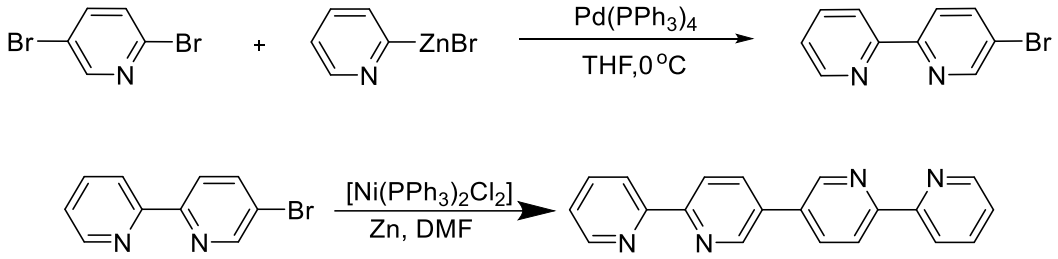

Scheme 3.1 Synthesis of ligand bisbpy.

Ligand bisbpy was prepared according to the procedure reported in the literature[194]. [$Pd(PPh_3)_4$] (0.3 g, 0.26 mmol) and 2,5-dibromobipyridine (2.0 g, 8.44 mmol) were added to a dry two-neck round-bottom flask and cooled to 0 °C under an argon atmosphere. The reaction mixture turned brown upon the addition of 2-pyridylzinc bromide (8.44 mmol) in THF (19.4 mL). A white precipitate was formed while stirring the mixture overnight at RT under argon atmosphere. The reaction mixture was then poured into a saturated 200 mL aqueous solution of 1:1 ethylenediaminetetraacetic acid (EDTA) and Na_2CO_3 and stirred until the white solid turned entirely yellow. The aqueous suspension was extracted with dichloromethane (3×50 mL), the combined organic layers were dried over anhydrous sodium sulphate, and the solvent was evaporated under reduced pressure. The crude product was purified by flash column chromatography, using hexane and ethyl acetate (9.5:0.5) as an eluent, to obtain 5-bromo-2,2'-bipyridine as pale-yellow powder (63.2 %).

^{1}H NMR (500 MHz, $CDCl_3$, δ/ppm): 8.75 (sd, 2H), 8.69 (d, 2H), 8.40 (d, 2H), 8.34 (d, 2H), 7.97 (dd, 2H), 7.84 (td, 2H), 7.35 (ddd, 2H).

^{13}C NMR (126 MHz, $CDCl_3$) δ/ppm): 155.19, 154.66, 150.22, 149.28, 139.53, 137.05, 124.03, 122.36, 121.16, 120.99.

To an anhydrous DMF (10 mL) solution was added [$Ni(PPh_3)_2Cl_2$] (0.557 g, 0.85 mmol). The mixture was stirred for a few minutes at RT under an argon atmosphere until it turned blue. After adding 0.056 g (0.85 mmol) of zinc powder, the liquid was stirred at room temperature for 45 minutes in an argon environment while the color changed from blue to green to deep brown. To the reaction mixture 5-bromo-2,2'-bipyridine (0.200 g, 0.85 mmol) was added, and the mixture was stirred at room temperature overnight. After that, the mixture was poured into an aqueous solution of NH_4OH (2M, 150 mL), leading to the formation of a greyish product. After extracting the precipitate with ethyl acetate (3×50 mL) and drying the mixed organic phases over anhydrous $MgSO_4$, the volatile solvents were evaporated under reduced pressure. The crude product was purified by column using hexane and ethyl acetate solvent mixture (9:1) as an eluent to obtain bisbpy in 75.6 % yield.

^{1}H NMR (500 MHz, $CDCl_3$, δ/ppm): 9.01 (s, 2H), 8.74 (d, 2H), 8.57 (d, 2H), 8.49 (d, 2H), 8.12 (dd, 2H), 7.88 (td, 2H), 7.37 (td, 2H).

^{13}C NMR (126 MHz, $CDCl_3$) δ/ppm): 155.81, 155.59, 149.33, 147.45, 137.03, 135.18, 133.13, 123.97, 121.21.

3.1.2 Syntheses of precursors

3.1.2.1 Synthesis of [Ln(tmhd)$_3$(H$_2$O)$_2$] (Ln = ^{163}Dy, ^{164}Dy)

$^{163}DyCl_3·6H_2O$ and $^{164}DyCl_3·6H_2O$ were prepared by mixing $^{163/164}Dy_2O_3$ with hydrochloric acid. [$^{163/164}$Dy(tmhd)$_3$(H$_2$O)$_2$] was synthesized following the same method used for [Dy(tmhd)$_3$(H$_2$O)$_2$], $^{163}DyCl_3·6H_2O$ or $^{164}DyCl_3·6H_2O$ was used instead of $DyCl_3·6H_2O$. 10 mL of methanol solution of tmhd (203.4 mg, 1.11 mmol) and KO^tBu (126.8 mg, 1.11 mmol) were allowed to stir for 30 min. To this solution was added another solution of $^{163}DyCl_3·6H_2O$ or $^{164}DyCl_3·6H_2O$ (100 mg, 0.37 mmol) in a mixture of 5 ml methanol and 5 ml H_2O). A precipitate formed immediately, and the mixture was stirred for 24 h at room temperature. The precipitate was filtered, washed with water, and dried under vacuum overnight to obtain the respective isotopically enriched [$^{163/164}$Dy(tmhd)$_3$(H$_2$O)$_2$].

Yield (based on Dy): 83.7% for [^{163}Dy(tmhd)$_3$(H$_2$O)$_2$] and 90.1% for [^{164}Dy(tmhd)$_3$(H$_2$O)$_2$].

Elemental Analysis: Calculated for $C_{33}H_{61}{}^{163}DyO_8$ (751.0 g/mol): C, 52.73; H, 8.12. Found: C, 53.43; H, 7.87.

IR (ATR, cm^{-1}): 2955, 1571, 1504, 1384, 1351, 1238, 1133, 873, 758.

Elemental Analysis: Calculated for $C_{33}H_{61}{}^{164}DyO_8$ (752.0 g/mol): C, 52.76; H, 8.13. Found: C, 53.43; H, 7.87.

IR (ATR, cm^{-1}): 2956, 1571, 1504, 1383, 1352, 1238, 1134, 873, 758.

3.1.2.2 Synthesis of [$^{163,\ 164}$Dy(BTFA)$_3$(H$_2$O)$_2$]

[$^{163/164}$Dy(BTFA)$_3$(H$_2$O)$_2$] was synthesized following the same method for [Dy(tmhd)$_3$(H$_2$O)$_2$], phen-CF_3 was used instead of tmhd.

Yield (based on Dy): 92.3% for [^{163}Dy(BTFA)$_3$(H$_2$O)$_2$], 85.3% for [^{164}Dy(BTFA)$_3$(H$_2$O)$_2$].

Elemental Analysis: Calculated for. $C_{30}H_{22}{}^{163}DyF_9O_8$ (847.98 g/mol): C, 42.45; H, 2.59. Found: C, 42.95; H, 2.03.

IR (ATR, cm^{-1}): 3660, 3400, 1578, 1505, 1280, 1121, 940, 771, 679.

Elemental Analysis: Calculated for $C_{30}H_{22}{}^{164}DyF_9O_8$ (849.98 g/mol): C, 42.35; H, 2.59. Found: C, 42.63; H, 2.48.

IR (ATR, cm^{-1}): 3660, 3400, 1579, 1505, 1279, 1122, 940, 771, 680.

3.1.3 Synthesis of dinuclear complexes

3.1.3.1 Synthesis of [(Dy(tmhd)$_3$)$_2$(bisbpy)·CH$_2$Cl$_2$] (3-1)

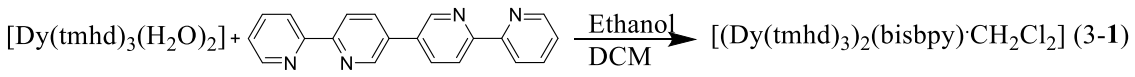

Scheme 3.2 Synthetic route of complex 3-**1**.

[Dy(tmhd)$_3$(H$_2$O)$_2$] (50 mg, 0.067 mmol) and 2, 2':5', 3'':6'', 2'''-quaterpyridine ligand (bisbpy) (10.33 mg, 0.034 mmol) were added to a mixture of 5 mL of ethanol and 2 mL DCM (dichloromethane), and the mixture was stirred overnight at room temperature. The mixture was filtered, and slow evaporation of the filtrate over a few days resulted in the formation of colourless plate-like crystals.

Yield: 31.0 mg (51.62 %)

Elemental Analysis: Calculated for $C_{87}H_{130}N_4Dy_2O_{12}$ (1819.86 g/mol) (3-**1**): C, 57.37; H, 7.14. Found: C, 57.47; H, 7.01.

3.1.3.2 Syntheses of [(^{163}Dy(tmhd)$_3$)$_2$(TAPE)] (3-2(I = 5/2)), [(^{164}Dy(tmhd)$_3$)$_2$(TAPE)] (3-3(I = 0)), [(Dy(BTFA)$_3$)$_2$(TAPE)] (3-4) and [(Dy(NTFA)$_3$)$_2$(TAPE)·CH$_2$Cl$_2$] (3-5)

This work on the TAPE-ligand was carried out in collaboration with Prof. H.-J. Holdt, Univeristy of Potsdam, Germany.

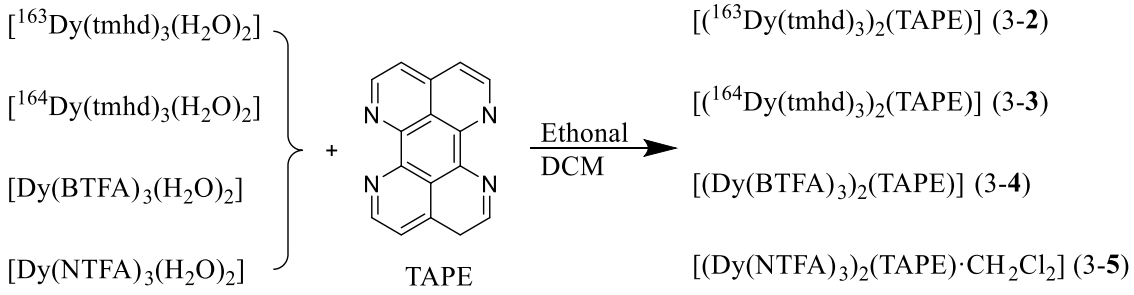

Scheme 3.3 Synthetic route of complex 3-**2**-3-**5.**

Complexes 3-**2**-3-**5** were synthesized by treating one equivalent of TAPE ligand with two equivalents of [Ln(tmhd)$_3$(H$_2$O)$_2$], [Dy(BTFA)$_3$(H$_2$O)$_2$] or [Dy(NTFA)(H$_2$O)$_2$] precursor (where Ln=^{163}Dy (I=5/2), ^{164}Dy (I=0)). A representative procedure for [$^{163/164}$Dy$_2$(tmhd)$_6$(TAPE)] is presented below.

A mixture of the respective [^{163}Dy(tmhd)$_3$(H$_2$O)$_2$] and [^{163}Dy(tmhd)$_3$(H$_2$O)$_2$] precursor (50.0 mg, 0.06 mmol) and TAPE (8.6 mg, 0.03 mmol) was stirred in a mixture of EtOH (5 mL) and DCM (2 mL) for 24 hours. After a few days, block crystals suitable for X-ray analysis were collected and air dried.

Yield: 21.6 mg (38.38 %) for 3-**2**, 22.9 mg (40.64 %) for 3-**3.**

Elemental Analysis: Calculated for C$_{82}$H$_{122}$N$_4$^{163}Dy$_2$O$_{12}$ (1681.84 g/mol) (3-**2**): C, 58.54; H, 7.26; N, 3.33. Found: C, 57.64; H, 6.93; N, 3.49.

Elemental Analysis: Calculated for C$_{82}$H$_{122}$N$_4$^{164}Dy$_2$O$_{12}$ (1683.84 g/mol) (3-**3**): C, 58.44; H, 7.24; N, 3.32. Found: C, 57.46; H, 6.87; N, 3.25.

[Dy$_2$(BTFA)$_6$(TAPE)] (3-**4**): Yield: 22.0 mg (39.83 %) of yellow block crystals

Elemental Analysis: Calculated for C$_{76}$H$_{44}$F$_{18}$N$_4$Dy$_2$O$_{12}$ (1872.15 g/mol) (3-**4**): C, 48.71; H, 2.35; N, 2.99. Found: C, 48.38; H, 2.52; N, 2.99.

[Dy$_2$(NTFA)$_6$(TAPE)] (3-**5**): Yield: 17.7 mg (32.67 %) red block crystals

Elemental Analysis: Calculated for C$_{101}$H$_{58}$F$_{18}$N$_4$Cl$_2$Dy$_2$O$_{12}$ (2257.42 g/mol) (3-**5**): C, 53.69; H, 2.57; N, 2.48. Found: C, 55.06; H, 2.46; N, 2.66.

3.1.3.3 Synthesis of $[(^{163}Dy(BTFA)_2)_2(PHZP)_2]$ (3-6) and $[(^{164}Dy(BTFA)_2)_2(PHZP)_2]$ (3-7)

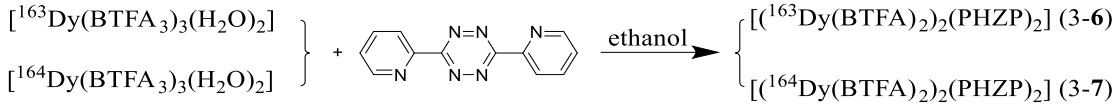

Scheme 3.4 Synthetic route of complexes 3-**6** and 3-**7**.

$[^{163}Dy(BTFA)_3(H_2O)_2]$ (50 mg, 0.059 mmol) or $[^{164}Dy(BTFA)_3(H_2O)_2]$ (50 mg, 0.059 mmol) were added to a mixture of 5 ml ethanol and 1 mL dichloromethane, then 3,6-bis(2-pyridyl)-1,2,4,5-tetrazine (bptz) (6.97 mg, 0.03 mmol) ligand was added, the mixture was stirred overnight at room temperature. After the evaporation at room temperature in few days, orange block crystals were obtained.

Yield: 22.0 mg (46.02 %) for 3-**6**, 27.3 mg (56.56 %) for 3-**7**.

Elemental Analysis: Calculated for $C_{64}H_{42}F_{12}N_4{}^{163}Dy_2O_{10}$ (1637.06 g/mol) (3-**6**): C, 46.97; H, 2.57. Found: C, 46.57; H, 2.41.

Elemental Analysis: Calculated for $C_{64}H_{42}F_{12}N_4{}^{164}Dy_2O_{10}$ (1639.06 g/mol) (3-**7**): C, 46.91; H, 2.56. Found: C, 46.32; H, 2.63.

3.2 Structures of complexes 3-1 – 3-7

3.2.1 Structure of $[(Dy(tmhd)_3)_2(bisbpy)\cdot CH_2Cl_2]$ (3-1)

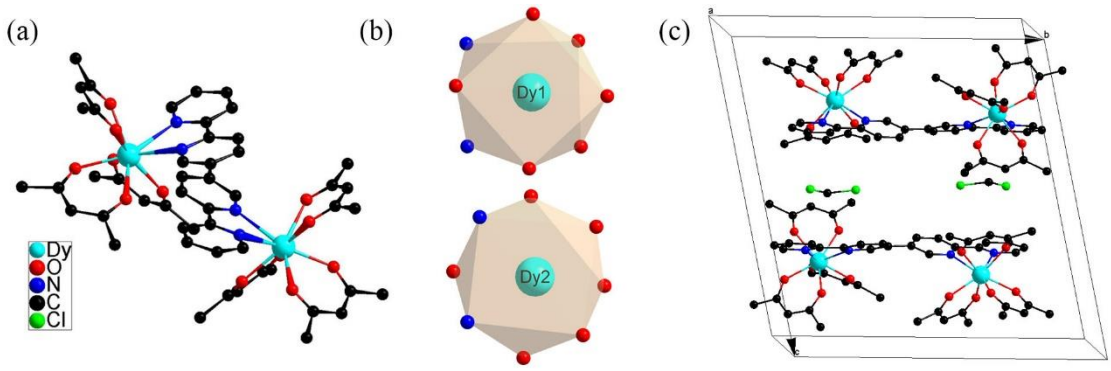

Figure 3.1 (a) Crystal structure of $[(Dy(tmhd)_3)_2(bisbpy)\cdot CH_2Cl_2]$. (b) Polyhedral representation of the Dy(III). (c) Unit cell of $[(Dy(tmhd)_3)_2(bisbpy)\cdot CH_2Cl_2]$.

$[(Dy(tmhd)_3)_2(bisbpy)\cdot CH_2Cl_2]$ (3-**1**) crystallizes in the *P*-1 space group (Fig 3.1). The asymmetric unit contains two Dy^{3+} ions, six tmhd ligands, one bispy ligand, and one CH_2Cl_2. Dy(III) is eight-coordinated by six oxygen atoms from three tmhd ligands and

two nitrogen atoms from bisbpy ligand. The Dy···O distances range between 2.284(2) Å to 2.362(2) Å, whilst the Dy···N distances are longer, with values ranging from 2.596(3) Å to 2.615(3) Å. The intramolecular Dy···Dy distance is 10.3131(2) Å. The coordination geometry around Dy1 and Dy2 can be best described as a square antiprism (D_{4d}) with a continuous shape measure (CShM) of 0.612 and 0.546, respectively (Table 3.1).

3.2.2 Structures of [(^{163}Dy(tmhd)$_3$)$_2$(TAPE)] (3-2), [(^{164}Dy(tmhd)$_3$)$_2$(TAPE)] (3-3), [(Dy(BTFA)$_3$)$_2$(TAPE)] (3-4) and [(Dy(NTFA)$_3$)$_2$(TAPE)·CH$_2$Cl$_2$] (3-5)

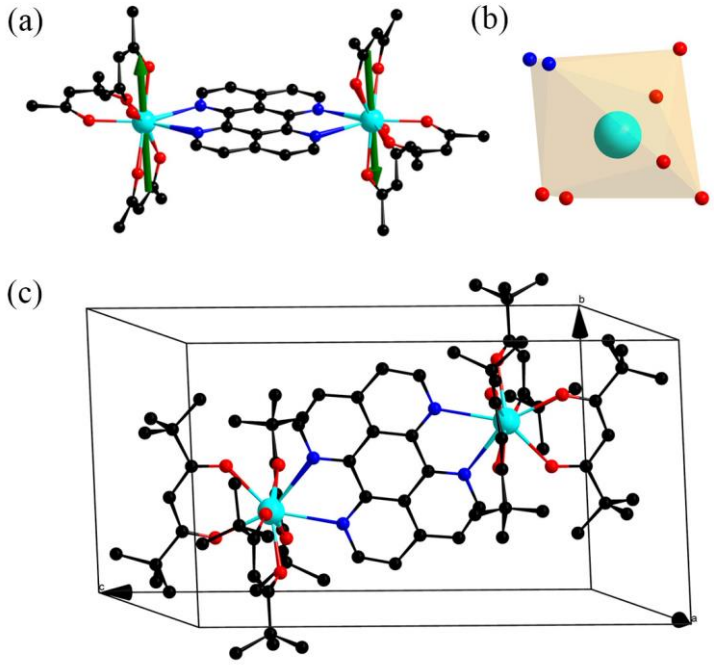

Figure 3.2 (a) Crystal structures of [(Dy(tmhd)$_3$)$_2$(TAPE)]. The green arrows represent the anisotropy axis for each Dy(III) obtained from ab-initio CASSCF calculations. (b) Polyhedral representations of the Dy(III) sites on a N_2O_6 geometry in 3-**2**. (c) unit cell of complex 3-**2**. Hydrogen and methyl groups are omitted for clarity. Color code: C, black; N, blue; O, red; Dy, bright blue.

X-ray structural data suggest that complexes 3-**2** – 3-**5** are dinuclear dysprosium motifs. In each complex, one TAPE ligand is coordinated to two Dy(III) and the dysprosium ions are related by an inversion symmetry. All complexes crystallize in the triclinic $P\bar{1}$ space group. Among these crystals [(^{163}Dy(tmhd)$_3$)$_2$(TAPE)] (3-**2**$^{(I = 5/2)}$) and [(^{164}Dy(tmhd)$_3$)$_2$(TAPE)] (3-**3**$^{(I = 0)}$) are isostructural. In all the

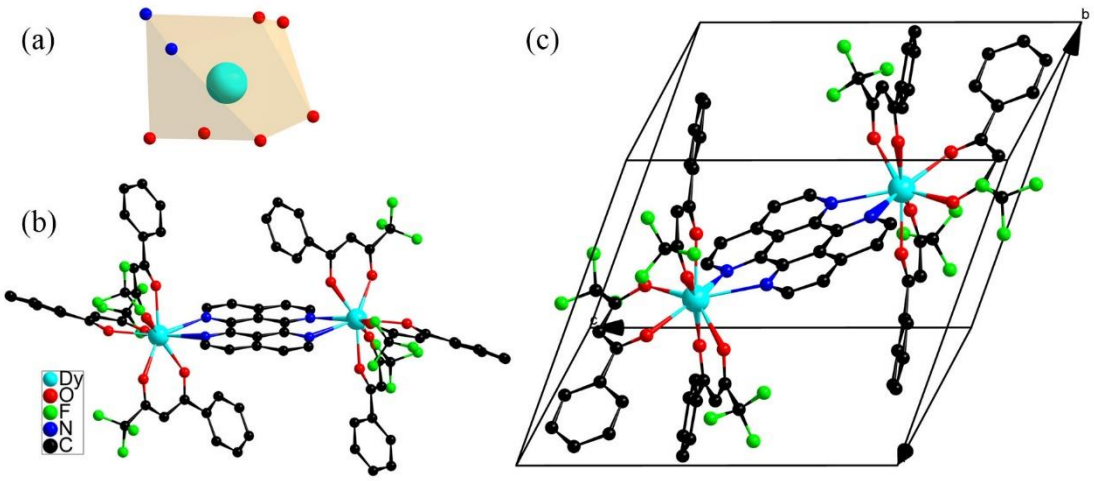

Figure 3.4 (a) Polyhedral representations of the Dy(III) sites on a N_2O_6 geometry in $[(Dy(BTFA)_3)_2(TAPE)]$ (3-**4**). (b) Crystal structures of complex 3-**4**. (c) Unit cell of complex 3-**4**.

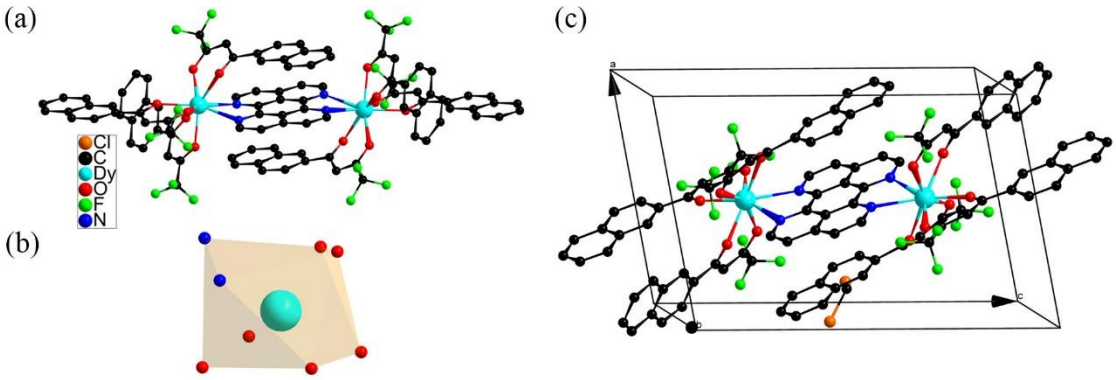

Figure 3.3 (a) Crystal structures of $[(Dy(NTFA)_3)_2(TAPE)]\cdot CH_2Cl_2$. (b) Polyhedral representations of the Dy(III) sites on a N_2O_6 geometry. (c)Unit cell of complexe 3-**5**.

structures, the asymmetric units are composed of half of the molecule. The molecular structures of complexes 3-**2** – 3-**5** are depicted in Fig 3.2–3.4. For crystals 3-**2** and 3-**3**, Dy is surrounded by three tmhd and two nitrogens from the TAPE ligand, forming a N_2O_6 coordination environment (Fig 3.2). The Dy-O distances are in the range of 2.251(1)-2.350(8) Å for 3-$\mathbf{2}^{(I = 5/2)}$ and 2.262(7)-2.356(8) Å for 3-$\mathbf{3}^{(I = 0)}$, Dy-N distances range between 2.617(7)-2.662(8) Å for 3-**2** and 2.618(7)-2.657(8) Å for 3-**3**. The same N_2O_6 coordination environment, formed by two nitrogen atoms of the TAPE and six oxygen atoms from the BTFA, was observed for complexes 3-**4** (Fig 3.3) and 3-**5** (Fig 3.4). The Dy···O and Dy···N bond lengths are in the range of 2.301(2)-2.343(2) Å and 2.586(3)-

2.615(3) Å, respectively, for 3-**4**. In the case of 3-**5**, Dy···O and Dy···N bond lengths in the range of 2.300(2)-2.3651(19) Å and 2.561(2)-2.600(2) Å, respectively, were observed. The intramolecular Dy···Dy distances are 9.3326(5) Å, 9.3276(5) Å, 9.1966(6) Å, 9.0968(6) Å for 3-**2**$^{(I = 5/2)}$, 3-**3**$^{(I = 0)}$, 3-**4**, and 3-**5**, respectively.

The local coordination symmetries of the Dy(III) ions were analyzed using the SHAPE 2.1 software[195] and are best described as having triangular dodecahedron geometry with deviation values of 0.615, 0.603, and 1.057 for 3-**2**$^{(I = 5/2)}$, 3-**3**$^{(I = 0)}$, and 3-**5**, respectively. While the coordination geometry around the dysprosium ion can be best described as a square antiprism with deviation values of 1.300 for 3-**4** (Table 3.1).

Table 3.1 The CShM values calculated using SHAPE 2.1 for complex 3-**1** – 3-**5**.

	3-1(Dy1)	**3-2**(Dy2)	**3-2**	**3-3**	**3-4**	**3-5**
Octagon (D_{8h})	30.797	30.004	32.727	32.948	30.998	28.912
Heptagonal pyramid (C_{7v})	21.965	22.682	22.888	22.886	22.807	23.701
Hexagonal bipyramid (D_{6h})	15.683	16.575	12.889	12.950	15.016	15.754
Cube (Oh)	9.013	9.696	7.572	7.586	10.178	9.804
Square antiprism (D_{4d})	**0.612**	**0.546**	2.869	2.869	**1.297**	1.344
Triangular dodecahedron (D_{2d})	2.502	2.097	**0.615**	**0.603**	1.726	**1.053**
Johnson - Gyrobifastigium J26 (D_{2d})	16.087	16.595	14.913	15.014	14.183	14.612
Johnson - Elongated triangular bipyramid J14 (D_{3h})	28.148	27.559	28.497	28.484	26.692	28.331
Johnson - Biaugmented trigonal prism J50 (C_{2v})	3.224	2.935	3.083	3.078	2.137	1.838
Biaugmented trigonal prism (C_{2v})	2.604	2.397	2.509	2.530	1.703	1.225
Snub disphenoid J84 (D_{2d})	5.589	4.880	3.685	3.642	3.783	3.3400
Triakis tetrahedron (T_d)	9.784	10.349	8.352	8.348	10.820	10.418
Elongated trigonal bipyramid (D_{3h})	24.259	23.550	24.463	24.634	23.511	23.494

3.2.3 Structures of [(^{163}Dy(BTFA)$_2$)$_2$(PHZP)$_2$] (3-6$^{(I = 5/2)}$) and [(^{164}Dy(BTFA)$_2$)$_2$(PHZP)$_2$] (3-7$^{(I = 0)}$)

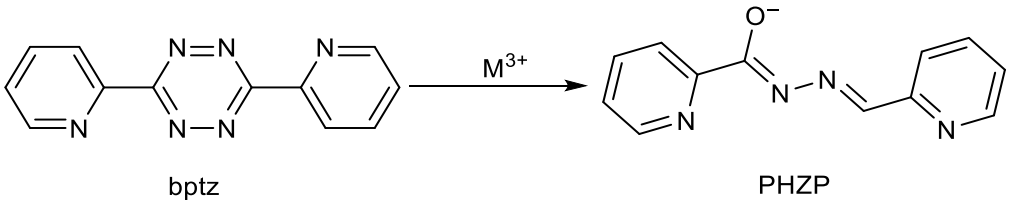

Scheme 3.5 Schematic representation of the process that emphasizes the metal-assisted hydrolysis that changed the ligand from 3,6-dipyrazin-2-yl-1,2,4,5-tetrazine (bptz, left) to N'-[(E)-pyrazin-2-yl)methylidene]pyrazine-2-carbohydrazonate (PHZP, right).

The isostructural complexes 3-**6**$^{(I = 5/2)}$ and 3-**7**$^{(I = 0)}$ crystallize in the triclinic space group $P\bar{1}$. The molecular structures are depicted in Fig 3.5. According to the structural information, when the heterocyclic bptz was reacting with the lanthanide salts in

methanol, the tetrazine ring was opened, producing the asymmetrical N'-[(E)-pyrazin-2-yl)methylidene]pyrazine-2-carbohydrazonate (PHZP) ligand (Scheme 3.5)[196,197].

As shown in Figure 3.5, two PHZP ligands coordinate to two Dy (III) cores in a μ_2:η^1:η^1:η^2:η^1 mode, resulting in a head-to-tail pattern with the tridentate group (N1, N2, and O1) and the bidentate picolinoyl component (O1 and N3). The Dy···O and Dy···N bond lengths are in the range of 2.325(3)–2.46(3) Å and 2.497(3)–2.721(3) Å for 3-**6**$^{(I\ =\ 5/2)}$ and 2.325(2)–2.460(2) Å and 2.485(3)–2.712(3) Å for **3-7**$^{(I\ =\ 0)}$, respectively. The ligands' carbonyl O atoms (O1 and O2) form a bond in the deprotonated enol mode (O^-), linking the two Dy (III) ions together and resulting in the formation of a Dy_2O_2 quadrilateral with four members. The Dy1–O–Dy2 angles are 115.66° for 3-**6**$^{(I\ =\ 5/2)}$ and 115.68° for 3-**7**$^{(I\ =\ 0)}$. The intramolecular Dy···Dy distance for 3-**6**$^{(I\ =\ 5/2)}$ and 3-**7**$^{(I\ =\ 0)}$ is 4.065(5) Å and 4.064(3) Å, respectively. Each Dy (III) center is surrounded by a uniform N_3O_6 nine-coordinate environment, wherein the remaining four coordination sites of each Dy (III) center are filled by four O atoms originating from two BTFA units. By employing the SHAPE program, the assessment of the distorted extent of the DyN_3O_6 polyhedra in complexes 3-**6**$^{(I\ =\ 5/2)}$ and 3-**7**$^{(I\ =\ 0)}$ relative to the ideal nine-vertex sphere demonstrates that the DyN_3O_6 combinations in both complexes exhibit an intermediate between various coordination geometries (Table 3.2). The geometry around the nine-coordinated Dy1 ions in both 3-**6**$^{(I\ =\ 5/2)}$ and 3-**7**$^{(I\ =\ 0)}$ is spherical tricapped trigonal prism D_{3h} symmetry. For Dy2 in 3-**6**$^{(I\ =\ 5/2)}$ and 3-**7**$^{(I\ =\ 0)}$, the geometry is better described as Muffin architecture with *C*s symmetry.

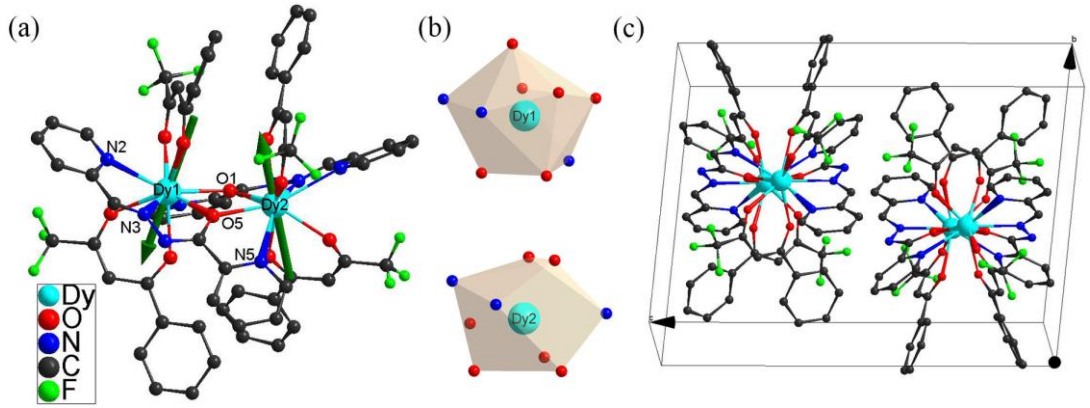

Figure 3.5 (a) Crystal structure of $[(Dy(BTFA)_2)_2(PHZP)_2]$. The green arrows represent the anisotropy axis for each Dy(III) obtained from ab-initio CASSCF calculations. (b) Polyhedral representation of of the Dy (III). (c) Unit cell of $[(Dy(BTFA)_2)_2(PHZP)_2]$.

Table 3.2 The CShM values calculated using the programme SHAPE 2.1 for complexes 3-**6**$^{(I = 5/2)}$ and 3-**7**$^{(I = 0)}$.

Configuration	Complex 3-**6**$^{(I = 5/2)}$		Complex 3-**7**$^{(I = 0)}$	
	Dy1	**Dy2**	**Dy1**	**Dy2**
Enneagon (D_{9h})	33.930	32.429	33.894	32.449
Octagonal pyramid (C_{8v})	22.997	23.174	23.008	23.262
Heptagonal bipyramid (D_{7h})	17.426	17.452	17.524	17.442
Johnson triangular cupola J3	15.245	15.132	15.211	15.109
Capped cube J8 (C_{4v})	8.679	8.564	8.696	8.543
Spherical-relaxed capped cube	7.795	7.718	7.794	7.716
Capped square antiprism J10	2.678	3.088	2.661	3.082
Spherical capped square	2.112	2.435	2.064	2.424
Tricapped trigonal prism J51	2.041	2.340	2.020	2.340
Spherical tricapped trigonal prism	**1.885**	2.648	**1.858**	2.641
Tridiminished icosahedron J63	11.277	10.500	11.268	10.575
Hula-hoop (C_{2v})	8.269	7.461	8.290	7.448
Muffin (C_s)	1.990	**2.253**	1.987	**2.250**

Table 3.3 Crystallographic parameters of complexes 3-**1** – 3-**7**$^{(I = 0)}$.

No.	**3-1**	**3-2**$^{(I = 5/2)}$	**3-3**$^{(I = 0)}$	**3-4**	**3-5**	**3-6**$^{(I = 5/2)}$	**3-7**$^{(I = 0)}$
Formula	$Dy_2N_4O_{12}C_{86}H_{128}{\cdot}CH_2Cl_2$	$C_{82}H_{122}Dy_2N_4O_{12}$	$C_{82}H_{122}Dy_2N_4O_{12}$	$C_{76}H_{44}Dy_2F_{18}N_4O_{12}$	$C_{101}H_{58}Cl_2Dy_2F_{18}N_4$	$C_{64}H_{42}Dy_2F_{12}N_8O_{10}$	$C_{64}H_{42}Dy_2F_{12}N_8O_{10}$
Fw	1819.84	1679.83	1680.84	1872.15	2257.41	1635.05	1637.05
T(K)	180.15	293	180	180	180	160	180
crystal system	triclinic	triclinic	triclinic	triclinic	triclinic	triclinic	triclinic
space group	*P*-1	*P*-1	*P*-1	*P*-1	*P*-1	*P*-1	*P*-1
a, *Å*	12.7841(3)	9.9047(3)	9.9022(3)	11.1750(5)	11.1583(4)	13.5218(5)	13.5306(5)
b, *Å*	18.7611(4)	11.1967(4)	11.1999(4)	12.2044(6)	11.5481(4)	13.9480(7)	13.9571(6)
c, *Å*	20.0253(4)	19.5255(5)	19.5392(5)	14.4783(7)	17.9821(6)	18.7575(7)	18.7997(6)
α, *deg*	76.904(2)	79.377(3)	79.353(2)	114.003(4)	98.538(3)	92.973(3)	92.968(3)
β, *deg*	82.020(2)	88.081(2)	88.065(2)	93.530(4)	101.116(3)	100.359(3)	100.310(3)
γ, *deg*	89.160(2)	77.349(3)	77.288(3)	101.928(4)	93.498(3)	116.822(4)	116.870(4)
V (Å^3)	4632.03(18)	2076.54(12)	2077.41(11)	1741.32(16)	2238.84(14)	3069.89(3)	3080.0(2)
Z	2	1	1	1	1	2	2
$\rho_{Calcd.}$ (mg·m^{-3})	1.305	1.247	1.344	1.785	1.679	1.77	1.764
μ (mm^{-1})	1.714	1.840	1.843	2.245	1.82	2.519	2.511
R_{int}	0.051	0.057	0.061	0.055	0.050	0.072	0.050
GOF on F^2	1.123	1.188	1.047	1.026	1.056	0.978	1.031
R_1, wR_2 (I > 2σ(I))[a]	R_1 = 0.0378, wR_2 = 0.0928	R_1 = 0.0384, wR_2 = 0.1014	R_1 = 0.0348, wR_2 = 0.752	R_1 = 0.0330, wR_2 = 0.0727	R_1 = 0.0357, wR_2 = 0.0907	R_1 = 0.0434, wR_2 = 0.0917	R_1 = 0.0323, wR_2 = 0.752
R_1, wR_2(all data)	R_1 = 0.0509, wR_2 = 0.1177	R_1 = 0.0435, wR_2 = 0.1223	R_1 = 0.427, wR_2 = 0.0847	R_1 = 0.0383, wR_2 = 0.0755	R_1 = 0.0405, wR_2 = 0.0944	R_1 = 0.0680, wR_2 = 0.1022	R_1 = 0.427, wR_2 = 0.0796

[a] $R_1 = ||F_o| - |F_c||/\mathring{a}|F_o|$, $wR_2 = \{w[(F_o)^2 - (F_c)^2]^2/w[(F_o)^2]^2\}^{1/2}$

3.3 SMM characteristics of the dinuclear Dy-complexes 3-1 – 3-7$^{(I = 0)}$

3.3.1 SMM characteristic of [(Dy(tmhd)$_3$)$_2$(bisbpy)·CH$_2$Cl$_2$] (3-1)

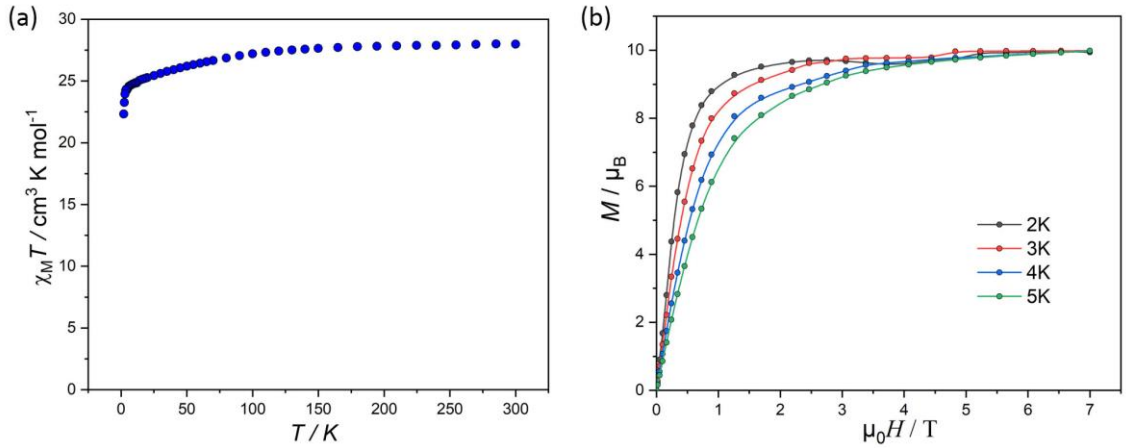

Figure 3.6 (a) The $\chi_M T$ vs. T plot for complex 3-**1**. (b) Plots of M vs. H at different temperatures.

Direct current (dc) susceptibility measurements of 3-**1** were performed under a 1000 Oe dc field in the range of 2−300 K. As shown in Figure 3.6a, the $\chi_M T$ value at room temperature is 27.98 cm^3 K mol^{-1}, which is close to the expected value of 28.34 cm^3 K mol^{-1} for two uncoupled Dy(III) ions ($^6H_{15/2}$, g = 4/3). The $\chi_M T$ value decreases gradually in the temperature range of 300−6 K and then drops sharply and reached a minimum value of 22.33 cm^3 K mol^{-1} at 2 K. The trend of the $\chi_M T$ value at low temperatures can be attributed to either the thermal depopulation of low-lying excited states or the presence of weak antiferromagnetic interactions between the Dy^{3+} ions within the complex.

The field dependence of magnetization of complex 3-**1** was evaluated at different temperatures 2, 3, 4, and 5 K in the magnetic field range of 0−7 T (Fig 3.6b). The sharp increase of magnetization at low field at low temperatures reveals a significant energy difference between the ground and excited states. Additionally, as the external field is increased, the magnetization value increases and reaches saturation at 9.98 μ_B for complex 3-**1** at 7 T. The M (H) value is consistent with the expected one (10 μ_B) for two Dy(III) ions with a well-defined J = 15/2 ground doublet.

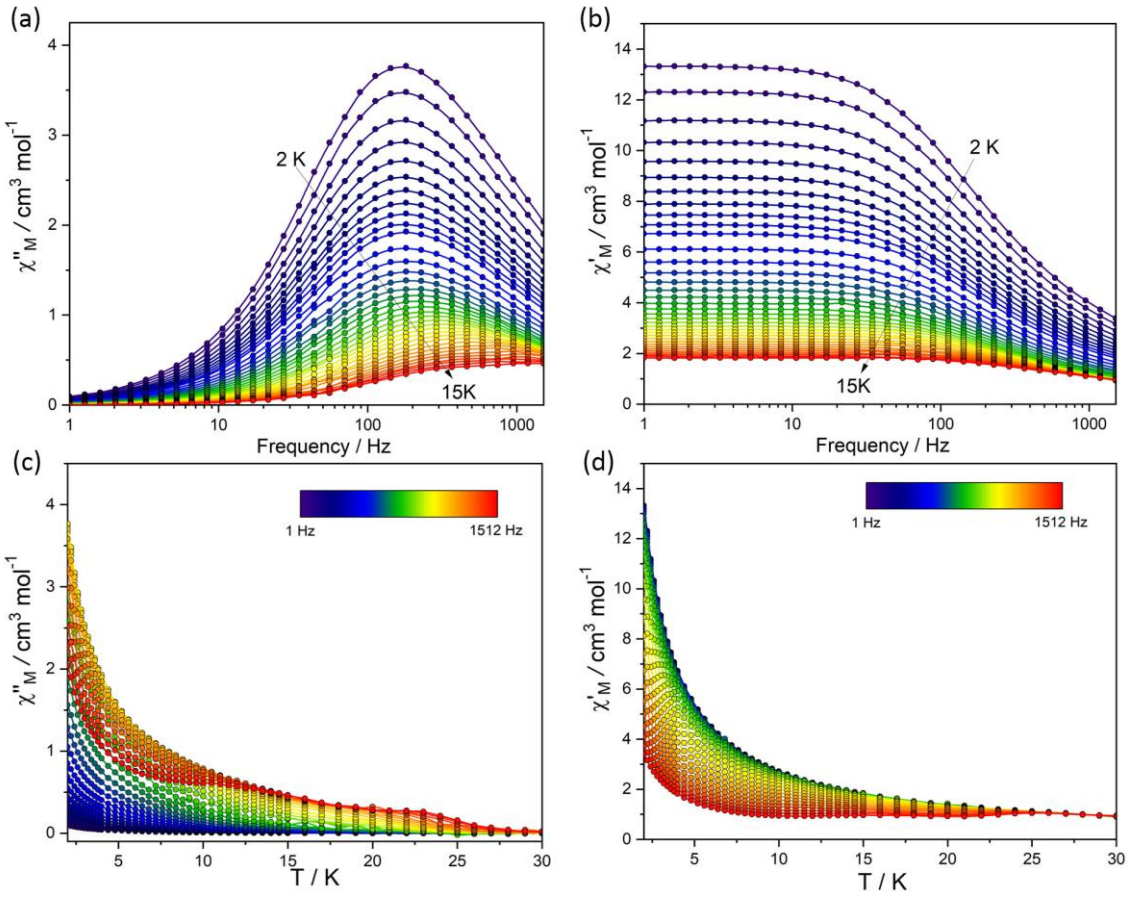

Figure 3.7 (a-b) Experimental frequency-dependent (($\chi_M''(v)$) and $\chi_M''(v)$) magnetic susceptibility data at zero applied DC (H_{dc}) field at varied temperatures for 3-**1**. Panels (c) and (d) show the tempreture dependence of the out-of-phase and in phase ac magnetic susceptibility data under a zero-dc field for 3-**1**.

The AC susceptibility was determined for the complex 3-**1** under a zero-dc field in the frequency range of 1 to 1512 Hz. The frequency dependence of the AC susceptibility signal reveals the SMM character of Complex 3-**1** (Fig 3.7). The out-of-phase (χ'') susceptibility component displays a peak centered around 180 Hz at 2 K, which remains almost unchanged up to 6 K. Above 6 K, the peak moves to higher frequencies as the temperature increases until 15 K. The Cole-Cole plots show nearly symmetrical semi-circular curves which were fitted from frequency-dependent AC data collected at different temperatures by a generalized Debye model (Fig 3.8a). This indicates that a single relaxation process occurs[198,199]. The value of α for 3-**1** is 0.18 − 0.23, indicating a wide distribution of relaxation times.

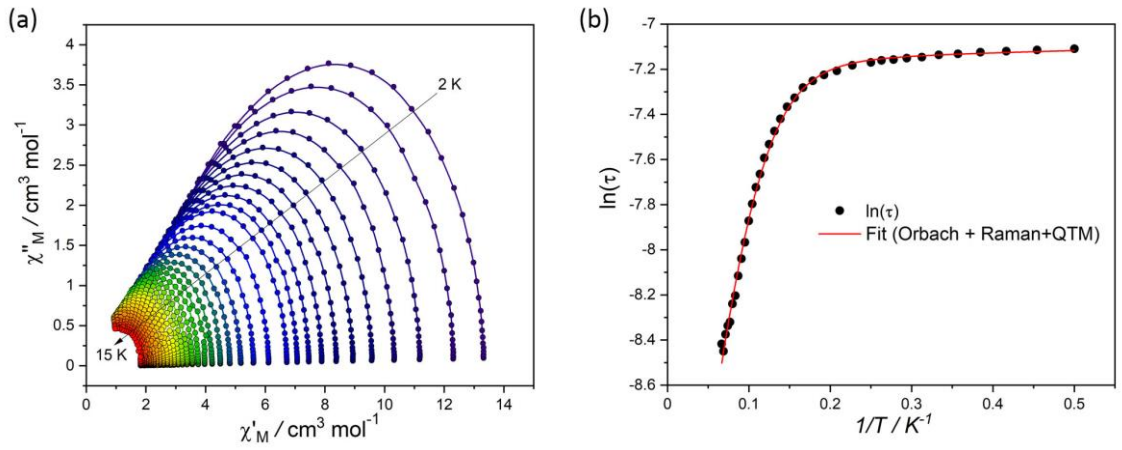

Figure 3.8 (a) Cole–Cole plots under a zero dc field for 3-**1**. The solid lines represent the best fits. (b) Temperature dependence of the magnetic relaxation time τ under zero field is shown as ln(τ) versus T^{-1} for 3-**1**. The solid red line is the best fit to the multiple relaxation equation.

In the high-temperature region, the plots of ln τ vs T^{-1} are approximately linear, but deviation from linearity is observed in the ln τ vs T^{-1} plots in the low-temperature region (Fig 3.8b), suggesting the presence of other magnetic relaxation processes. Because the ac susceptibility data were gathered in a zero-dc field, it is noteworthy that QTM was taken into account. Therefore, the data in the whole temperature range were fitted by using the equation 2:

$$\tau^{-1} = \tau_0^{-1} \exp(-U_{eff}/k_B T) + CT^n + \tau_{QTM}^{-1}$$

The fit gives U_{eff} = 30.8 (1) K, C = 1031.6(4) K^{-n} s^{-1}, n = 0.05(1), $\tau_0 = 3.58 \times 10^{-5}$ s, τ_{QTM} = 0.006(1) s. It should be noted that the Raman n parameter is lower than what is expected for a purely Kramers ion, indicating the presence of active optical and acoustic phonons[186,187,200].

3.3.2 SMM characteristic of [(^{163}Dy(tmhd)$_3$)$_2$(TAPE)] (3-**2**$^{(I = 5/2)}$) and [(^{164}Dy(tmhd)$_3$)$_2$(TAPE)] (3-**3**$^{(I = 0)}$)

The static magnetic properties of 3-**2**$^{(I = 5/2)}$ and 3-**3**$^{(I = 0)}$ were investigated within a temperature range of 2−300 K and under an applied dc field of 1 kOe. The $\chi_M T(T)$ values for 3-**2**$^{(I = 5/2)}$ and 3-**3**$^{(I = 0)}$ are very similar, the $\chi_M T(T)$ values are 28.14 (3-**2**) and

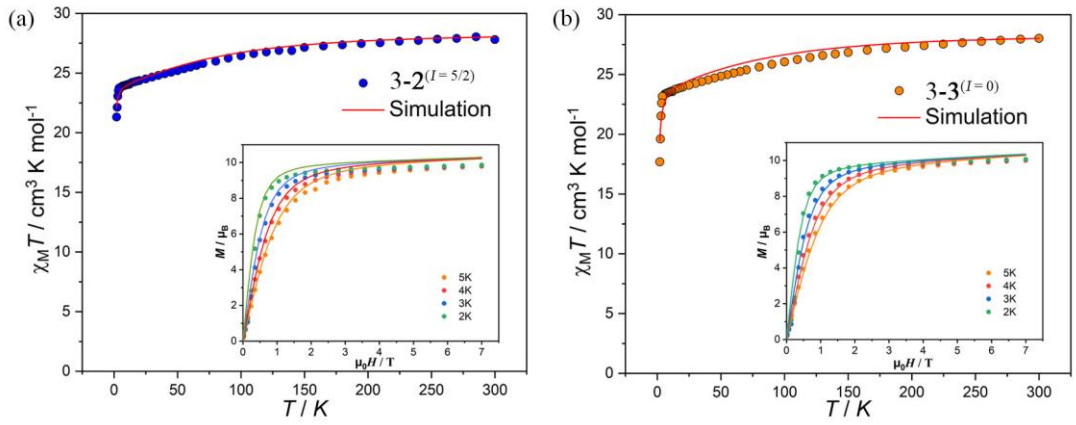

Figure 3.9 The $\chi_M T$ vs. T for complex 3-**2**$^{(I = 5/2)}$ (a) and complex 3-**3**$^{(I = 0)}$ (b), respectively. Inset: Plots of M vs. H at different temperatures. Solid lines represent the fitting from ab initio calculation.

28.00 (3-**3**) cm^3 K mol^{-1} at room temperature (Fig 3.9a and b). The values agree with the expected value of 28.34 cm^3 K mol^{-1} for two isolated Dy(III) with J = 15/2 and g_J = 4/3. As the temperature decreases, the $\chi_M T$ (T) values initially decrease gradually until reaching 150 K. There is a rapid decrease below 5 K, resulting in a minimum value of 21.5 cm^3 K mol^{-1}, and 18.4 cm^3 K mol^{-1} (at 2 K) for 3-**2**$^{(I = 5/2)}$ and 3-**3**$^{(I = 0)}$, respectively. The sudden decrease in $\chi_M T$ as the temperature is reduced can be attributed to either the reduction in the population of crystal field levels or antiferromagnetic interactions.

The *M vs. H* data collected at temperatures of 2, 3, 4 and 5 K showed a rapid increase at low magnetic fields (Fig 3.9 inset). The saturation of magnetization was observed at high magnetic fields with values of 9.86 μ_B for 3-**2**$^{(I = 5/2)}$ and 9.26 μ_B for 3-**3**$^{(I = 0)}$, both at 7 T. The M (H) values are reasonably consistent with those predicted for two Dy(III) ions with well-defined J = 15/2 ground doublet, i.e., ~10 μ_B, typical of anisotropic Dy(III) SMMs.

To explore the dynamics of magnetization reversal, temperature - and frequency-dependent in-phase (χ') and out-of-phase (χ'') ac measurements were performed (Fig 3.10, 11). The ac measurements under zero applied dc field exhibited a maximum in the out of phase $\chi''(T;\nu)$ and a clear frequency-dependent signal below 20 K for 3-**2**$^{(I = 5/2)}$ and 3-**3**$^{(I = 0)}$, indicating SMM behavior. The susceptibility's frequency dependence

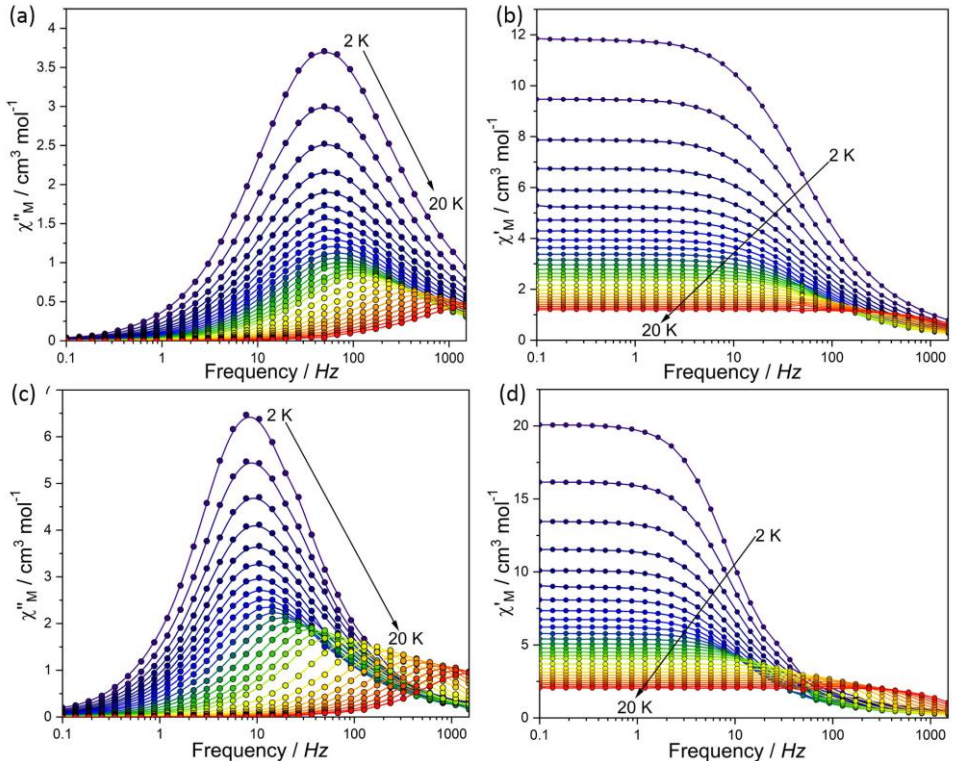

Figure 3.10 Frequency dependence of χ" and χ' susceptibilities for complexes 3-**2**$^{(I = 5/2)}$ (a, b) and 3-**3**$^{(I = 0)}$ (c, d) without the static field.

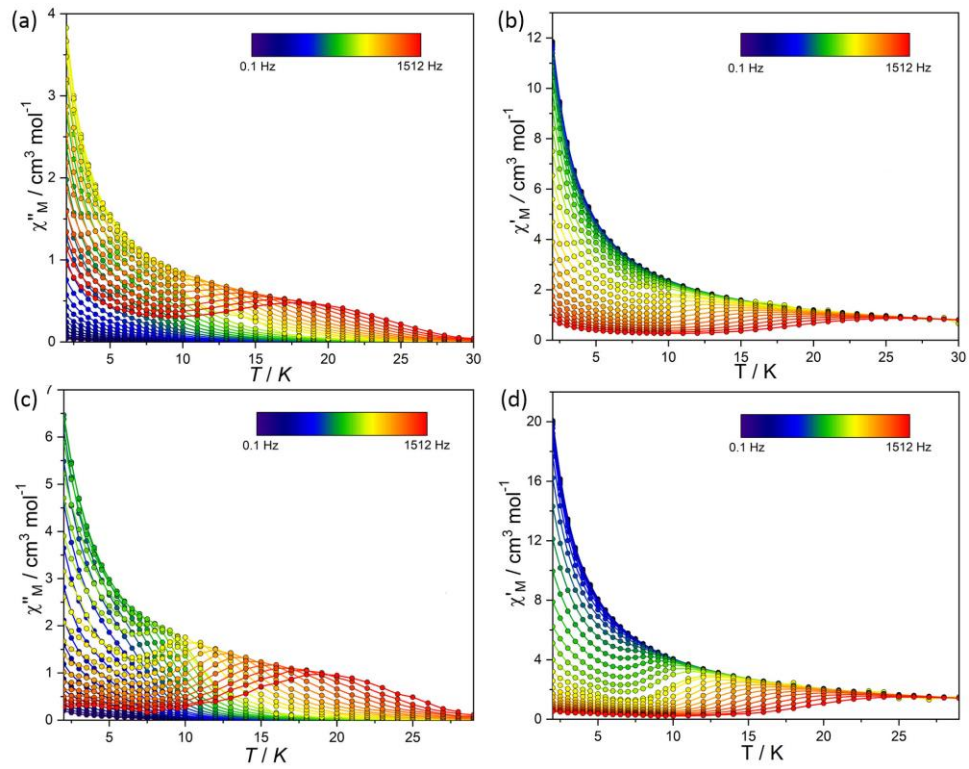

Figure 3.11 Temperature dependence of χ" and χ' susceptibilities for complexes 3-**2**$^{(I = 5/2)}$ (a, b) and 3-**3**$^{(I = 0)}$ (c, d) without the static field.

displays a distinct difference between the two isotopologues (see Fig 3.10). Complex 3-**2**$^{(I = 5/2)}$ shows a maximum near 50 Hz at 2 K and remains relatively close to this peak until reaching 6 K. The maximum of 3-**3**$^{(I = 0)}$ displays a maximum centered around 10 Hz and maintains this position until 6 K. Beyond 6 K, the maximum for 3-**2**$^{(I = 5/2)}$ and 3-**3**$^{(I = 0)}$ shifts upward as temperature rises until 20 K. Complex 3-**3**$^{(I = 0)}$ shows a stronger temperature dependence of magnetization relaxation dynamics above 6 K than 3-**2**$^{(I = 5/2)}$.

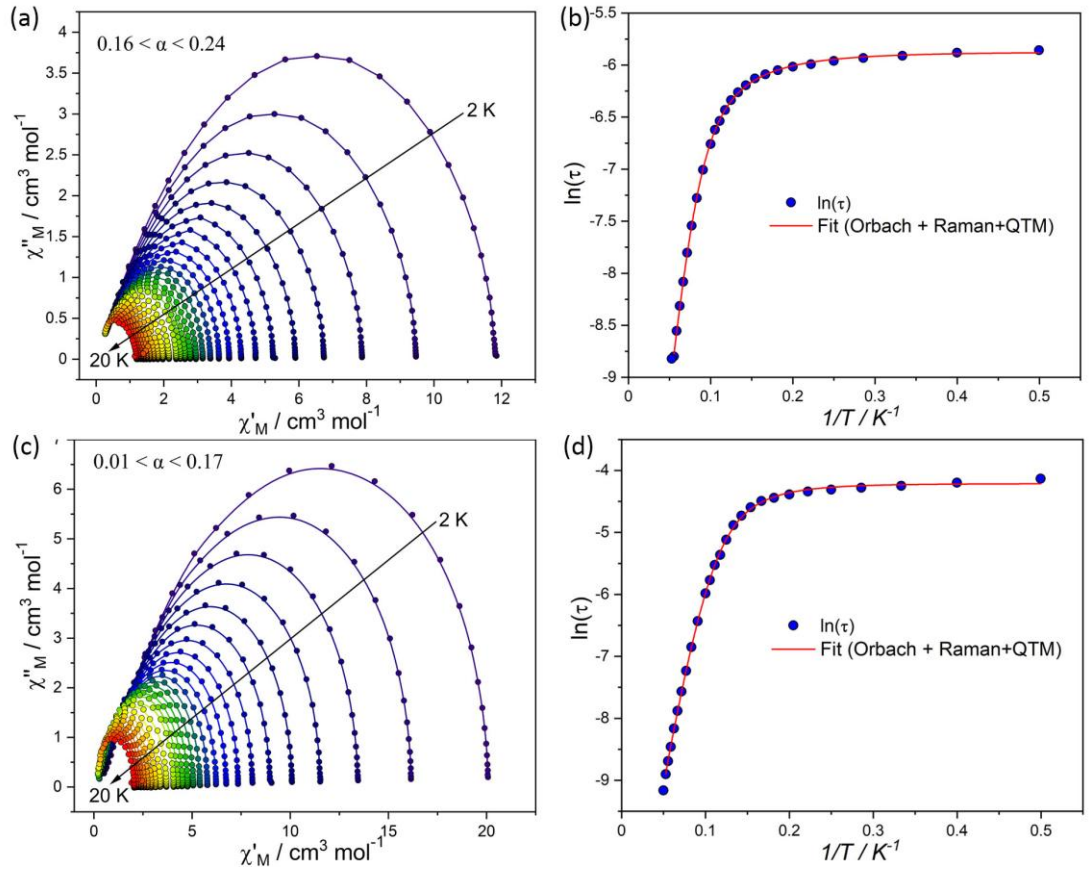

Figure 3.12 Cole–Cole plots under a zero dc field for 3-**2**$^{(I = 5/2)}$ (a) and 3-**3**$^{(I = 0)}$ (c). The solid lines represent the best fits. Temperature dependence of the magnetic relaxation time τ under zero field is shown as ln(τ) versus T^{-1} for 3-**2**$^{(I = 5/2)}$ (b) and 3-**3**$^{(I = 0)}$ (d). The solid red lines are the best fit to the multiple relaxation equation.

The ac data of 3-**2**$^{(I = 5/2)}$ and 3-**3**$^{(I = 0)}$ can be fitted to a generalized Debye model. As expected, the Cole–Cole plots are close to semicircles (Fig 3.12). The relaxation time parameter α is in the ranges between 0.16(8)-0.24(5) for 3-**2**$^{(I = 5/2)}$ and 0.01(2)-0.17(1)

for 3-**3**$^{(I\ =\ 0)}$. It has been observed that at lower temperatures, the distribution of relaxations for 3-**3**$^{(I\ =\ 0)}$ is narrower compared to that for 3-**2**$^{(I\ =\ 5/2)}$, however, at higher temperatures the distribution for both becomes quite similar.

Figure 3.12b and d show the ln(τ) *vs.* 1/*T* data for complexes 3-**2**$^{(I\ =\ 5/2)}$ and 3-**3**$^{(I\ =\ 0)}$. The data was fitted to Eq.2 to investigate the mechanisms of magnetization relaxation. The best fitting affords an U_{eff} of 80.6(2) K, $\tau_0 = 2.8 \times 10^{-6}$ s, $C = 0.49(1)$ s^{-1} K^{-n}, n = 2.9(2), $\tau_{QTM} = 0.0028$ s for 3-**2**$^{(I\ =\ 5/2)}$, and U_{eff} of 73.3(2) K, $\tau_0 = 4.8 \times 10^{-6}$ s, $C = 0.012(8)$ s^{-1} K^{-n}, n = 4.18(3), τ_{QTM} = 0.015 s for 3-**3**$^{(I\ =\ 0)}$. As anticipated, both barriers exhibit similarities, however, the value of C exhibits a significant difference in the Raman process, implying that the Raman relaxation process is significantly improved by the presence of the nuclear spin in the 3-**2**$^{(I\ =\ 5/2)}$ compound[201].

To examine the characteristics of the isotopologues complexes as molecule-based qu*d*its, we focus on sub-kelvin temperature μ-SQUID studies. These studies enable us to analyze the impact of nuclear spin on the variations in relaxation dynamics. Additionally, the μ-SQUID approach allows us to examine hyperfine-driven quantum tunneling magnetic states (*hf*-QTM)[186,202] and exchange-bias QTM[203,204,205,206], which are crucial for utilizing SMMs in quantum computing applications. The investigations were performed on single crystals of 3-**2**$^{(I\ =\ 5/2)}$ and 3-**3**$^{(I\ =\ 0)}$ with the field directed along the easy axis of the crystal[207,208]. Hysteresis loop measurements were conducted at various sweeping speeds, ranging from 0.5 to 128 mT/s, and at temperatures from 5 K down to 30 mK (Fig 3.13).

Both complexes exhibit a prominent step at zero field in the sweeping rate and temperature dependence of the loops. This is a typical observation for single ion magnets (SIMs), where fast relaxation, typically via quantum tunneling of magnetic states (QTM), leads to a lack of S-shape hysteresis loops around zero field, which are a hallmark of dimeric SMMs. This absence of S-shape hysteresis loops suggests a negligible dipolar/exchange interaction between the Dy(III) centers. As shown in Figure 3.13, with increasing temperatures and decreasing sweep rates, the hysteresis

loops become narrow, confirming the SMM behavior of 3-**2**$^{(I = 5/2)}$ and 3-**3**$^{(I = 0)}$. The loops feature a broad step above $\mu_0 H_Z = \pm 0.25$ T, which is a result of the direct relaxation process and is highly dependent on field sweep rate. Due to the lack of nuclear spins, bigger loops are seen for 3-**3**$^{(I = 0)}$ than 3-**2**$^{(I = 5/2)}$.

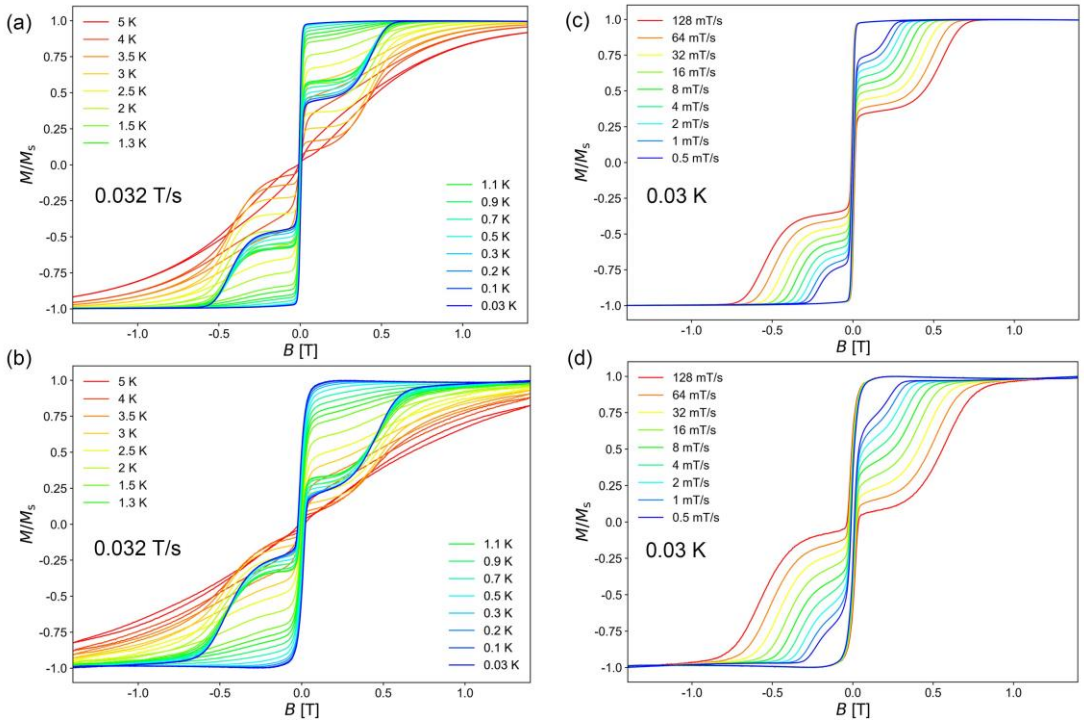

Figure 3.13 Temperature-dependent μ-SQUID studies for (a) 3-**2**$^{(I = 5/2)}$ and (c) 3-**3**$^{(I = 0)}$ at a field sweep rate of 32 mT/s and sweep-rate dependence of the μ-SQUID data for (b) 3-**2**$^{(I = 5/2)}$ and (d) 3-**3**$^{(I = 0)}$ collected at 30 mK.

3.3.3 SMM characteristic of [(Dy(BTFA)$_3$)$_2$(TAPE)] (3-4)

The static magnetic properties of polycrystalline complex 3-**4** was investigated in the temperature range of 2−300 K. The $\chi_M T(T)$ plot of 3-**4** is shown in Fig 3.14a. The room temperature $\chi_M T$ value obtained for the complex is 28.08 cm^3 K mol^{-1}. The value is comparable with the expected value of 28.34 cm^3 K mol^{-1} for two isolated Dy^{III} with J = 15/2 and g_J = 4/3. Upon cooling, the $\chi_M T$ value gradually decreased until 150 K. Below 5 K, a rapid drop in $\chi_M T$ was observed and $\chi_M T$ = 20.1 cm^3 K mol^{-1} was observed

at 2 K. The decrease of $\chi_M T$ upon cooling could be due to depopulation of crystal field levels and/or antiferromagnetic interactions.

The magnetization vs. field data of complexes measured against applied magnetic fields at 2, 3, 4 and 5 K reveal a rapid increase at low magnetic fields (Fig 3.14b). At high magnetic fields, saturation of magnetization was observed; a value 10.54 μ_B was observed for 3-**4** at 7 T. The magnetisation values are in good agreement with the expected values for two Dy(III) ions—10 μ_B.

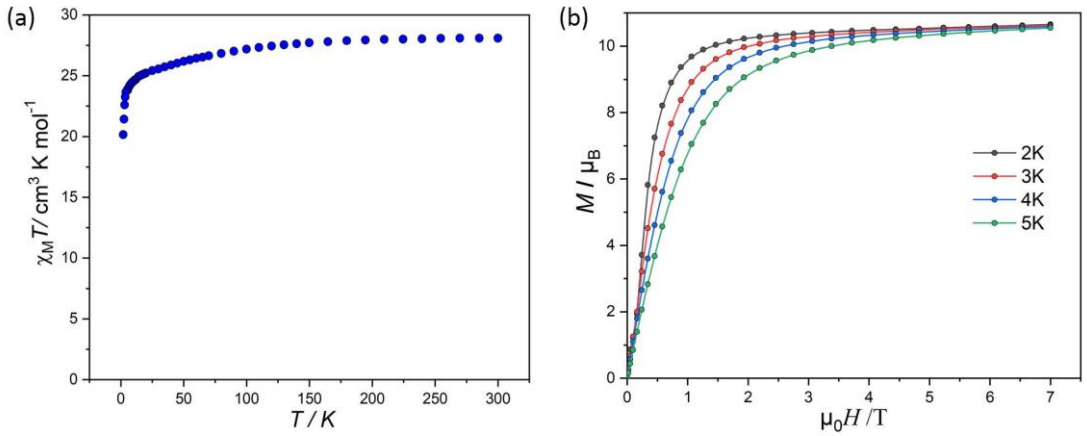

Figure 3.14 The $\chi_M T$ vs. T plot for complex 3-**4** (a). Plots of M vs. H at different temperatures (b).

To explore the dynamics of magnetization reversal, temperature-and frequency-dependent in-phase (χ') and out-of-phase (χ'') ac measurements were performed (Fig 3.15). The ac measurements under zero applied dc field exhibited a clear frequency-dependent signal below 20 K for **4**, indicating that the complex is a zero-field SMM. The out-of-phase $\chi''(\nu)$ reveals a temperature-dependent maxima at temperatures between 6–20 K, whilst below 6 K the maximum in χ_M'' (ν) remains practically constant around 6 Hz (Fig 3.15a).

The ac data of 3-**4** were well fitted employing the generalized Debye model. The Cole–Cole plots are close to semicircles (Fig 3.16a), in agreement with the generalized Debye model. The relaxation time distribution parameter α varies in the range of 0.02 − 0.26. The wide distribution of α and its decrease with temperature indicate the presence of multiple relaxation channels that affect the relaxation time. The various temperature

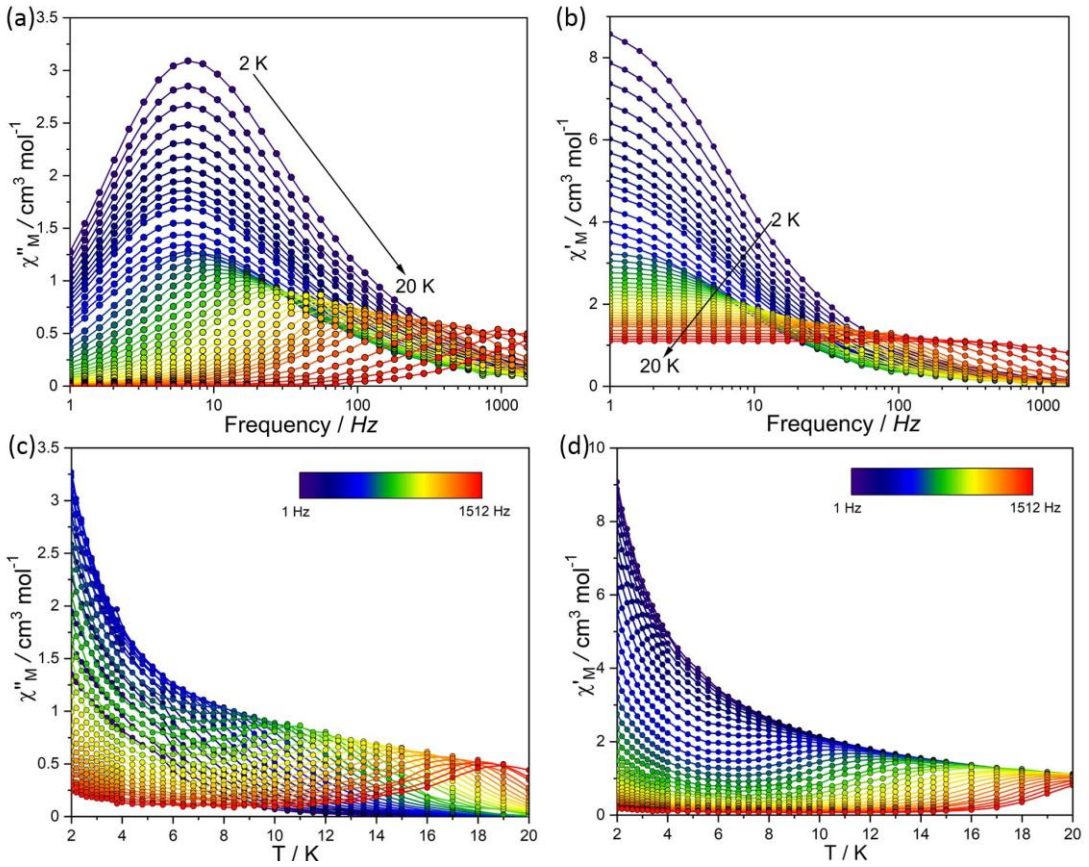

Figure 3.15 Experimental frequency-dependent ($\chi_M''(\nu)$) and ($\chi_M'(\nu)$) magnetic susceptibility data at zero applied DC (H_{dc}) field and varied temperatures for 3-**4** (a) and (b). Panels (c) and (d) show the temperature dependence of the out-of-phase and in-phase ac magnetic susceptibility data under a zero-dc field for 3-**4**.

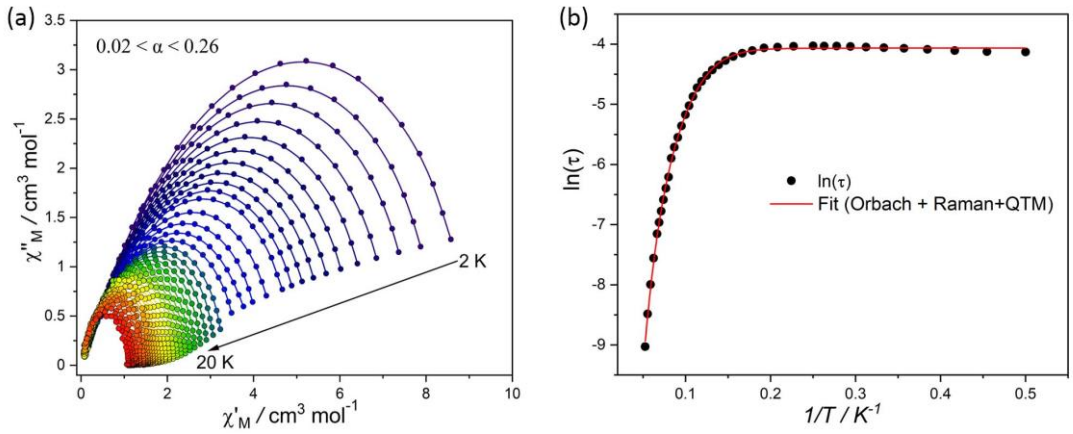

Figure 3.16 (a) Cole – Cole plots under a zero dc field for 3-**4**. The solid lines represent the best fits. (b) Temperature dependence of the magnetic relaxation time τ under zero field is shown as ln(τ) versus T^{-1} for 3-**4**. The solid red lines are the best fit to the multiple relaxation equation.

relaxation times for complex 3-**4** under zero-field are depicted in Fig 3.16b. To investigate mechanisms inducing magnetization relaxation at lower temperatures, the measured relaxation time was fitted with Eq. 2. The best fits gave U_{eff} = 47.0(2) K, τ_0 = 9.3 × 10^{-5} s, C = 2.0 × 10^{-8}(3) s^{-1} K^{-n}, n = 9.0(5), τ_{QTM} = 0.017 s.

3.3.4 SMM characteristic of [(Dy(NTFA)$_3$)$_2$(TAPE)] (3-5)

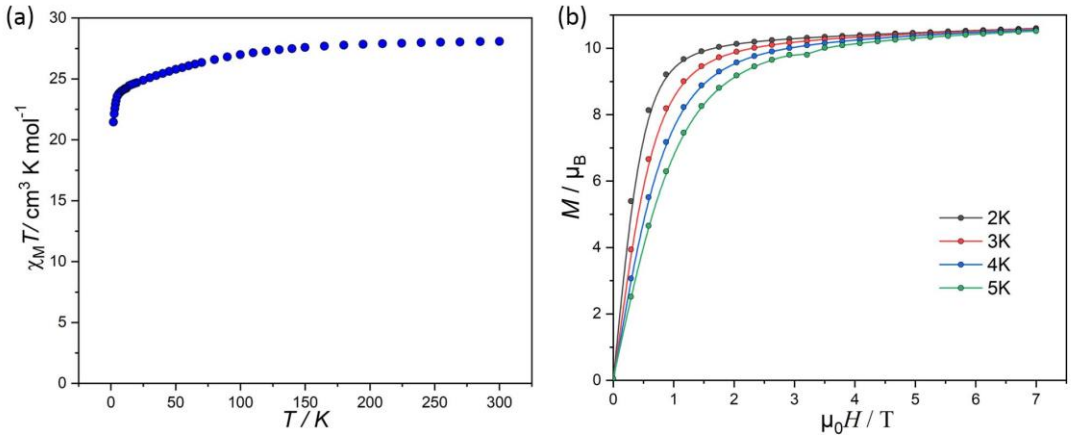

Figure 3.17 The $\chi_M T$ vs. T plot for complex 3-**5** (a). Plots of M vs. H at different temperatures (b).

The direct current (dc) magnetic susceptibility data of the polycrystalline samples of 3-**5** was measured over a temperature range of 2−300 K under an applied magnetic field of 1.0 kOe (as shown in Fig 3.17a). The results indicate that the susceptibility value ($\chi_M T$) at room temperature is 28.07 cm^3 K mol^{-1}, matching the expected values for two uncoupled Dy(III) ions with J = 15/2 and g_J = 4/3. As the temperature is lowered, the $\chi_M T$ products gradually decreased until around 150 K and thereafter decreased rapidly; at 2 K $\chi_M T$ = 21.4 cm^3 K mol^{-1} is reached. The decrease in $\chi_M T$ on cooling can be assigned to the depopulation of excited m_J sublevels and the weak antiferromagnetic coupling between the two Dy(III) ions in 3-**5**[209-211].

Data on magnetization (M (H)) for complex 3-**5** were gathered between 0−7 T in the 2−5 K temperature range. Figure 3.17b demonstrates how the magnetization values increase quickly at low field, then gradually increase until they reach their maximum

values of 10.51 μ_B for 3-**5**. The value agrees well with the expected value of 10.46 μ_B for two Dy(III) ions.

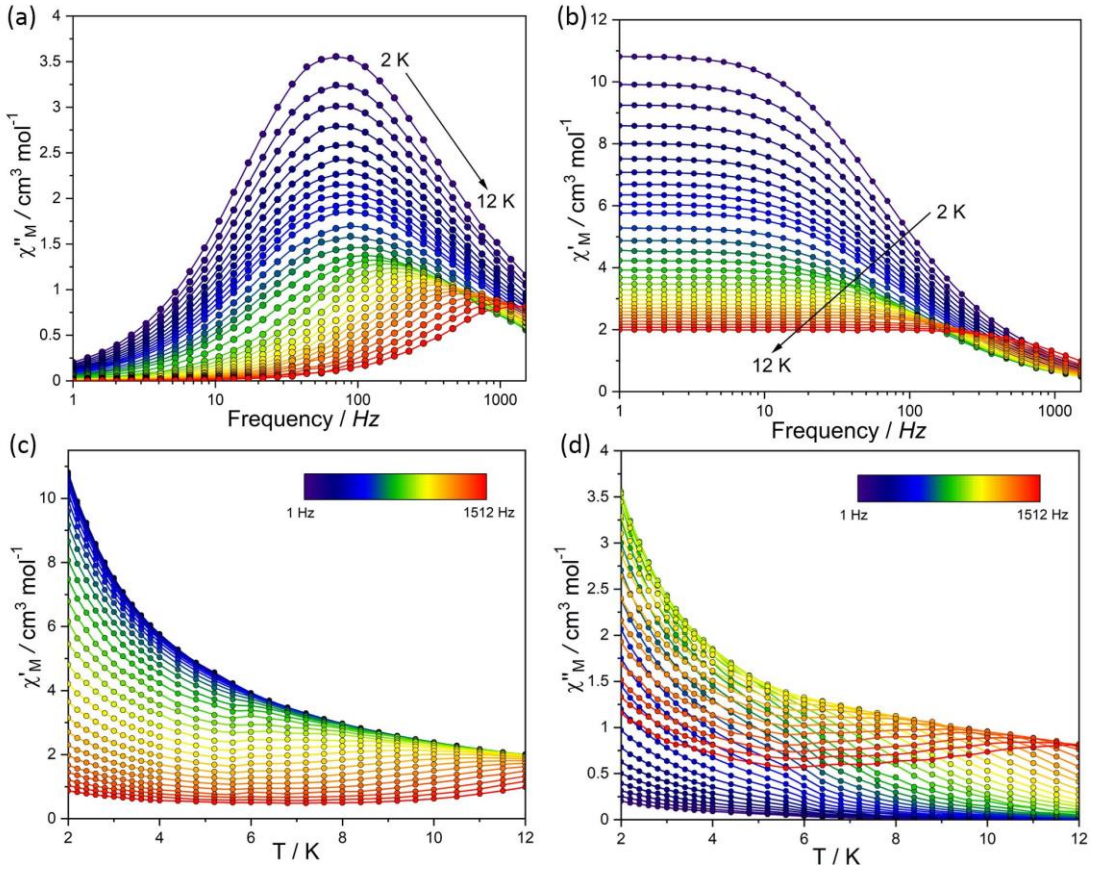

Figure 3.18 Experimental frequency-dependent magnetic susceptibility data at zero applied DC (H_{dc}) field and varied temperatures (χ_M" (v)) for 3-**5** (a) and (b). Panel (c) and (d) show the tempreture dependence of the out-of-phase and in-phase ac magnetic susceptibility data under a zero-dc field for 3-**5**, respectively.

Alternating current (ac) magnetic susceptibility measurements were carried out in the temperature range of 2.0−12.0 K without an added dc field at frequencies between 1 and 1512 Hz to investigate the slow magnetic relaxation behavior of complex 3-**5**. As shown in Fig 3.18, frequency dependence in the out-of-phase (χ") signal is clearly visible, which implies the SMM behaviour. The symmetric semicircle Cole – Cole data is fitted by using a generalized Debye model. The relaxation time distribution parameter α varies in the ranges of 0.02-0.22. The wide distribution of α and its decrease with temperature show the presence of multiple relaxation process (Fig. 17a). The ln(τ)

versus T^{-1} plot was fitted with Eq. 2 to give values of U_{eff} = 24.5(2) K, $\tau_0 = 2.12 \times 10^{-4}$ s, C = 0.09(7) s^{-1} K^{-n}, n = 4.2(2), τ_{QTM} = 0.0017 s.

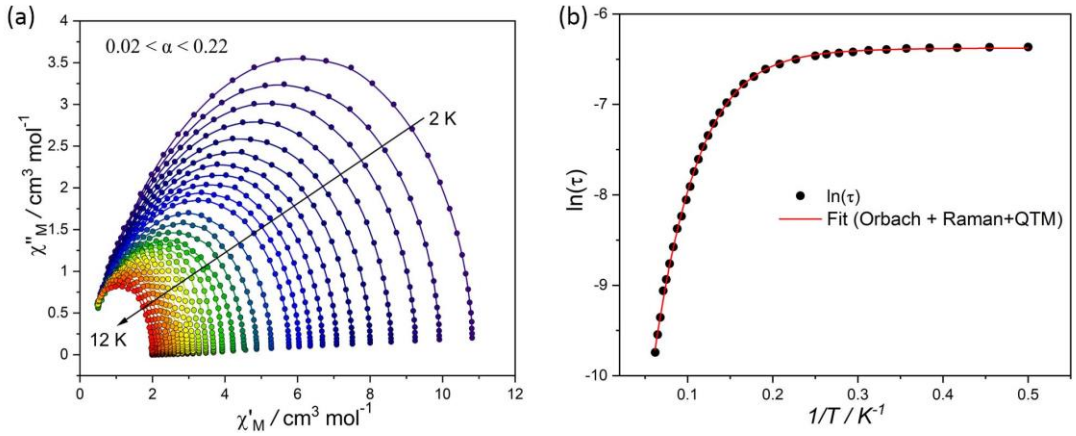

Figure 3.19 (a) Cole–Cole plots under a zero dc field for 3-**5**. The solid lines represent the best fits. (b) Temperature dependence of the magnetic relaxation time τ under zero field is shown as ln(τ) versus T^{-1} for 3-**5**. The solid red line is the best fit to the multiple relaxation equation.

3.3.5 SMM characteristic of [(^{163}Dy(BTFA))$_2$(PHZP)$_2$] (3-**6**$^{(I = 5/2)}$) and [(^{164}Dy(BTFA))$_2$(PHZP)$_2$] (3-**7**$^{(I = 0)}$)

The static and dynamic magnetic properties were measured through magnetometry to investigate the SMM behavior of the complexes 3-**6**$^{(I = 5/2)}$ and 3-**7**$^{(I = 0)}$ (Fig 3.20-3.23). Both complexes' static magnetic susceptibility investigations were carried out using polycrystalline samples in a dc field of 1 kOe between 2 K and 300 K (Fig 3.20a and c). At room temperature, the experimental $\chi_M T$ values are 28.45 and 28.09 cm^3 K mol^{-1} for 3-**6**$^{(I = 5/2)}$ and 3-**7**$^{(I = 0)}$, respectively. The results are consistent with the expected value of two uncoupled Dy^{3+} ions in the ground state J= 15/2 and g_J= 4/3. The $\chi_M T$ products progressively droped until the temperature drops to about 20 K, following which they drop quickly until 15.2 cm^3 K mol^{-1} for 3-**6**$^{(I = 5/2)}$ and 16.3 cm^3 K mol^{-1} for 3-**7**$^{(I = 0)}$ are attained at the lowest temperature 2 K. The explanations for theis observation are the depopulation of the excited Stark sublevels and the antiferromagnetic exchange coupling between the two Dy^{3+} ions in the complexes.

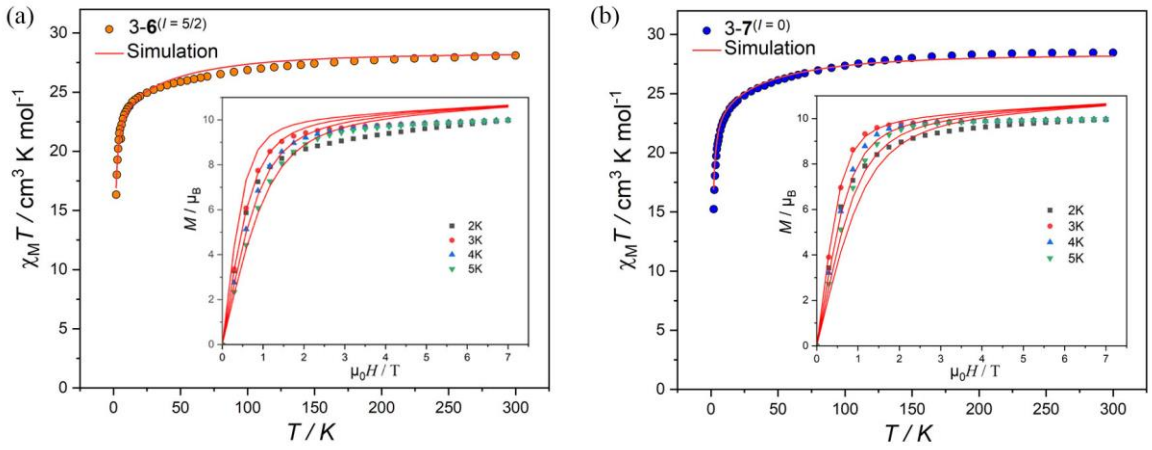

Figure 3.21 The $\chi_M T$ vs. T for complex 3-**6**$^{(I = 5/2)}$ (a) and complex 3-**7**$^{(I = 0)}$ (b), respectively. Inset: Plots of M vs. H at different temperatures. Solid lines represent the fitting from ab initio calculation.

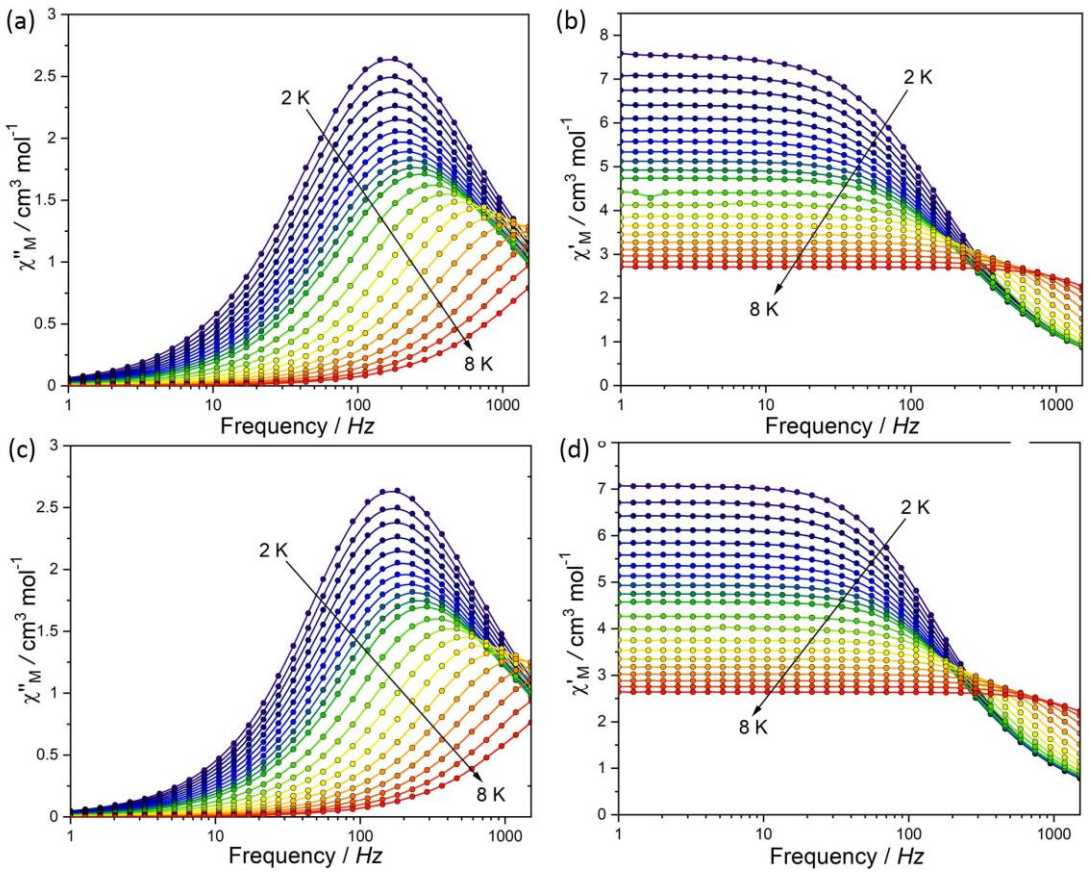

Figure 3.20 Frequency dependence of χ'' and χ' susceptibilities for complexes 3-**6**$^{(I = 5/2)}$ (a, b) and 3-**7**$^{(I = 0)}$ (c, d) without the static field, respectively.

The magnetization versus field *M* (*H*) for both complexes were also investigated in the field range of 0−7 T and 2−5 K temperature range (Figure 3.20b and d). At the lowest temperature and highest field, the magnetization reaches a value of 9.98 μ_B for 3-**6**$^{(I = 5/2)}$ and 9.97 μ_B for 3-**7**$^{(I = 0)}$, characteristic of two $m_J = \pm 15/2$ ground doublets.

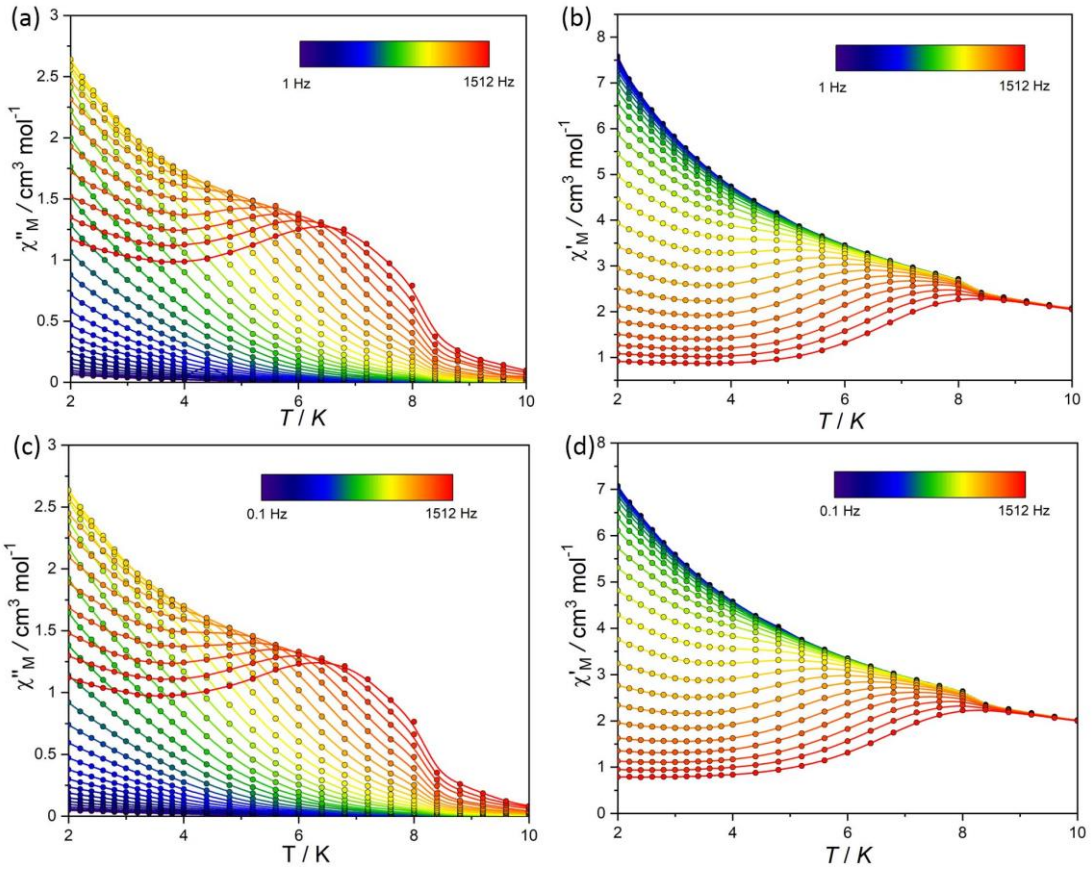

Figure 3.22 Temperature dependence of χ'' and χ' susceptibilities for complexes 3-**6**$^{(I = 5/2)}$ (a, b) and 3-**7**$^{(I = 0)}$ (c, d) without the static field, respectively.

Using alternating current (AC) magnetic susceptibility measurements, dynamic magnetic investigations were conducted to examine whether 3-**6**$^{(I = 5/2)}$ and 3-**7**$^{(I = 0)}$ are SMMs (Fig 3.21). Both complexes show SMM signature at zero applied field. The ac susceptibilities for 3-**6**$^{(I = 5/2)}$ and 3-**7**$^{(I = 0)}$ are quite comparable to each other as shown in figure 3.21-23. A maximum is shown at 180 Hz in the frequency-dependent behavior (χ'), which remains the constant until 3 K then changes toward higher frequencies as temperature rises. The symmetric semicircle Cole–Cole data are fitted by using a generalized Debye model between 2 and 8 K, allowed the extraction of the relaxation

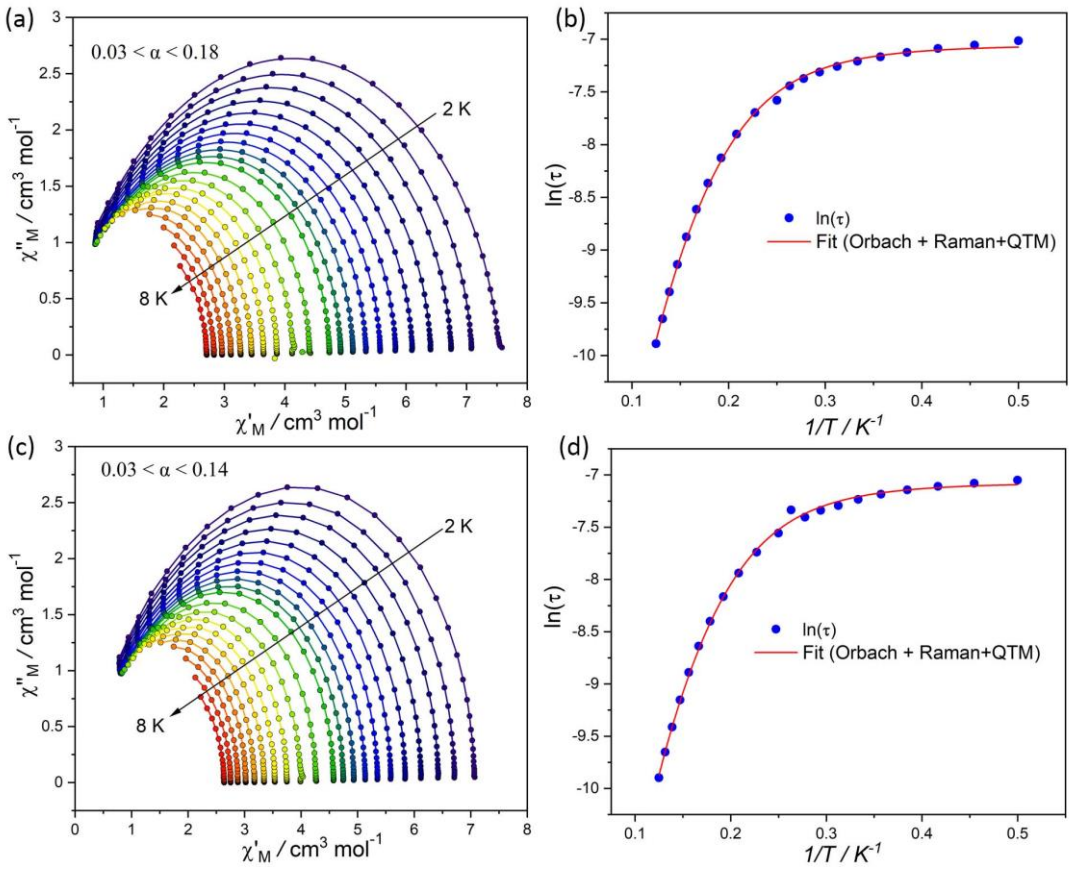

Figure 3.23 Cole–Cole plots under a zero dc field for 3-**6**$^{(I = 5/2)}$ (a) and 3-**7**$^{(I = 0)}$ (c). The solid lines represent the best fits. Temperature dependence of the magnetic relaxation time τ under zero field is shown as ln(τ) versus T^{-1} for 3-**6**$^{(I = 5/2)}$ (b) and 3-**7**$^{(I = 0)}$ (d). The solid red lines are the best fit to the multiple relaxation equation.

times (τ) and α values; 0.03 < α < 0.18 for 3-**6**$^{(I = 5/2)}$, 0.03 < α < 0.14 for 3-**7**$^{(I = 0)}$, with α being larger at lower temperatures (Figure 3.21a, c). Multiple relaxation channels that influence the relaxation time are present, as seen by the wide distribution of α and its reduction with temperature (more so for 3-**6**$^{(I = 5/2)}$ than for 3-**7**$^{(I = 0)}$). The temperature dependence of the relaxation times τ for both complexes can be fitted with Eq.2, indicating the Orbach, Raman, and QTM processes contributing to the magnetization relaxation. The best fit yields values of U_{eff} = 50.7(3) K, $\tau_0 = 1.8 \times 10^{-7}$ s, C = 6.4(2) s^{-1} K^{-n}, n = 3.5(2), $\tau_{QTM} = 9.4 \times 10^{-4}$ s for 3-**6**$^{(I = 5/2)}$, and U_{eff} = 57.1(2) K, $\tau_0 = 1.5 \times 10^{-7}$ s, C = 2.2(1) s^{-1} K^{-n}, n = 4.2(5), $\tau_{QTM} = 8.8 \times 10^{-4}$ s for 3-**7**$^{(I = 0)}$. As expected, both complexes exhibit similarities.

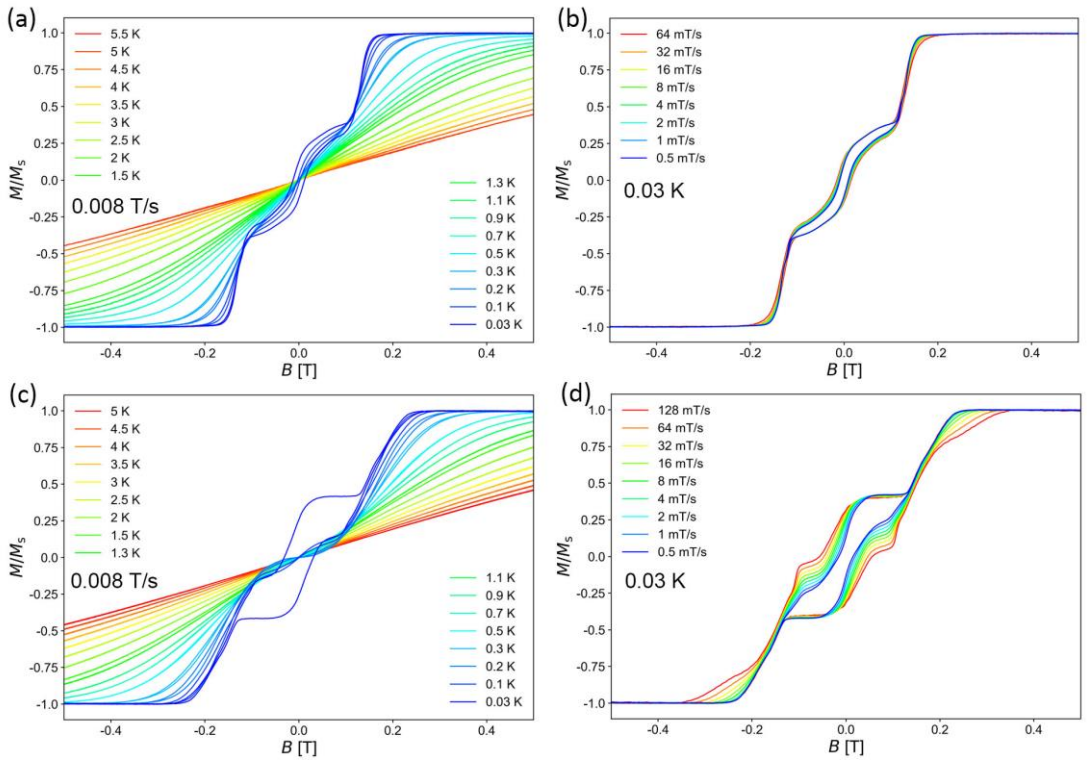

Figure 3.24 Temperature-dependent μ-SQUID studies of (a) 3-**6**$^{(I = 5/2)}$ and (c) 3-**7**$^{(I = 0)}$ at a field sweep rate of 8 mT/s and sweep-rate dependence of the μ-SQUID data for (b) 3-**6**$^{(I = 5/2)}$ and (d) 3-**7**$^{(I = 0)}$ collected at 30 mK.

Although dynamic magnetic studies showed the expected SMM signatures under zero DC field, we are not be able to see a clear difference between the two isotopologues. In order to investigate the variations in relaxation dynamics and nuclear spin effects, magnetic hysteresis curves were measured at sub-Kelvin temperatures on a single crystal employing μ-SQUID. Single crystals of 3-**6**$^{(I = 5/2)}$ and 3-**7**$^{(I = 0)}$ were subjected to μ-SQUID experiments with the field applied along the principal anisotropic axis[207]. Hysteresis loops studies were performed at different sweep rates and temperatures (Fig 3.24). The SMM behavior of the complexes was confirmed by the well-resolved two-step hysteresis loops found for 3-**6**$^{(I = 5/2)}$ and 3-**7**$^{(I = 0)}$ with the breadth of the loops increasing with falling temperatures and rising sweep speeds.

The loops display a classical Ising-like spin antiferromagnetically linked profile[201,206,212]. The S-shaped loops and two tunnel steps at ±0.2 T indicate that there are two antiferromagnetically coupled Dy^{3+} ions in the system. The transition from the

parallel (ferromagnetic) to the antiparallel (antiferromagnetic) alignment of the Dy^{3+} anisotropic moments result in these steps. Because some of the molecules do not tunnel to the antiferromagnetic ground state but instead stay stuck to the ferromagnetic state, the loops also show a minor amount of hysteresis around zero field[158,201,213]. A comparison of the hysteresis curves for 3-**6**$^{(I = 5/2)}$ and 3-**7**$^{(I = 0)}$ reveals that the nuclear spin carrying system produces narrower loops, indicating the relaxation process is more effective in this system.

3.4 Theoretical calculations

3.4.1 Calculation of complexes 3-2$^{(I = 5/2)}$ and 3-3$^{(I= 0)}$

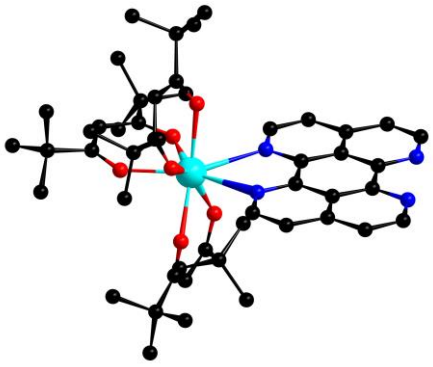

Figure 3.25 Molecular fragment employed for the CASSCF-SO calculations 3-**2**$^{(I = 5/2)}$ and (c) 3-**3**$^{(I = 0)}$.

To understand the mechanisms that govern the magnetic relaxation of 3-**2**$^{(I = 5/2)}$ and 3-**3**$^{(I= 0)}$, CASSCF calculations on the individual Dy^{III} fragments (Fig 3.25) of 3-**2**$^{(I = 5/2)}$ and 3-**3**$^{(I= 0)}$ were performed with MOLCAS 8.2 and SINGLE_ANISO programs. In Tables 3.4, the lowest Kramer's doublets (KDs) and the g factors of 3-**2**$^{(I = 5/2)}$ and 3-**3**$^{(I= 0)}$ were listed. The effective g_z tensors for 3-**2**$^{(I = 5/2)}$ and 3-**3**$^{(I= 0)}$ are 19.4268 and 19.4918, respectively, which are close to the Ising-limit value of 20, illuminating that each Dy^{III} fragment presents significant uniaxial anisotropy. The m_J components for the lowest two KDs of each Dy^{III} ion for complexes 3-**2**$^{(I = 5/2)}$ and 3-**3**$^{(I= 0)}$ are shown in Tables 3.5 respectively, where the ground KDs for Dy^{III} fragments are all predominantly composed of $m_J = \pm 15/2$, and their first excited states are mostly composed of a mixture of several

m_J states. As proposed, the energy barrier of the thermally excited Orbach process relates to the energy gap between the ground state and first excited state. Thus, the CASSCF/RASSI program was used to calculate the energy spectrum of 3-**2**$^{(I = 5/2)}$ and 3-**3**$^{(I= 0)}$ (Tables 3.4). The obtained energy gaps for the Dy fragments of 3-**2**$^{(I = 5/2)}$ and 3-**3**$^{(I= 0)}$ between the ground and the first excited KD are 236.9 K (164.7 cm^{-1}) and 251.2 K (174.6 cm^{-1}) respectively, which are much bigger than U_{eff} = 80.6 (2) K (3-**2**$^{(I = 5/2)}$) and 73.3 (2) K (3-**3**$^{(I = 0)}$) obtained from the dynamic susceptibility measurements. The observed discrepancies are likely attributed to the simultaneous presence of multiple relaxation processes. The corresponding magnetization blocking barriers of each Dy^{III} ion is shown in Figure 3.26, where the transversal magnetic moments in the ground states of individual Dy^{III} fragments is about 10^{-4} μ_B, and thus the quantum tunnelling of magnetization (QTM) in their ground KDs could be blocked at low temperature. The transversal magnetic moments in their first excited states of individual Dy^{III} fragments for 3-**2**$^{(I = 5/2)}$ and 3-**3**$^{(I= 0)}$ are large (about 10 μ_B) and therefore allow a fast QTM in their first excited states.

Table 3.4 Electronic structure of [Dy(tmhd)$_3$TAPE)] calculated with CASSCF-SO using solid state geometry from 3-**2**$^{(I = 5/2)}$ and 3-**3**$^{(I = 0)}$.

	Energy (cm^{-1})	Energy(K)	g_x	g_y	g_z	Angle (º)
3-**2**$^{(I = 5/2)}$	0.0	0.0	0.0130	0.0231	19.4268	
	164.7	236.9	0.3083	0.5674	15.3841	5.8
	249.0	358.3	1.6367	1.8689	12.2266	25.1
	317.9	457.4	2.1923	4.5353	8.6085	36.9
	362.9	522.1	2.4667	4.7135	14.1325	87.3
	446.8	642.9	0.0615	0.7291	17.3190	61.0
	490.3	705.4	0.3289	1.1064	16.4009	84.6
	565.9	814.2	0.0757	0.1987	18.9314	58.1
3-**3**$^{(I= 0)}$	0.0	0.0	0.0084	0.0142	19.4918	
	174.6	251.2	0.2239	0.3946	15.5951	4.9
	264.6	380.7	1.3779	1.5499	12.3882	23.0
	331.4	476.8	3.1592	5.0286	8.5064	40.5
	374.6	538.9	2.0332	4.4878	14.2277	84.4
	457.8	658.7	0.1199	1.0003	16.7811	61.5
	496.8	714.8	0.3582	1.4812	15.6522	84.9
	559.1	804.4	0.1092	0.3239	18.5476	58.9

Table 3.5 Wave functions with definite projection of the total moment $|m_J>$ for the lowest two KDs of individual Dy(III) fragments for for 3-**2**$^{(I = 5/2)}$ and 3-**3**$^{(I = 0)}$.

	Energy (cm^{-1})	Wave functions
3-**2**$^{(I = 5/2)}$	0.0	92% |±15/2>
	164.7	68.7% |±13/2> +27.1% |±9/2>
3-**3**$^{(I = 0)}$	0.0	93% |±15/2>
	174.6	72.2% |±13/2> +24.5% |±9/2>

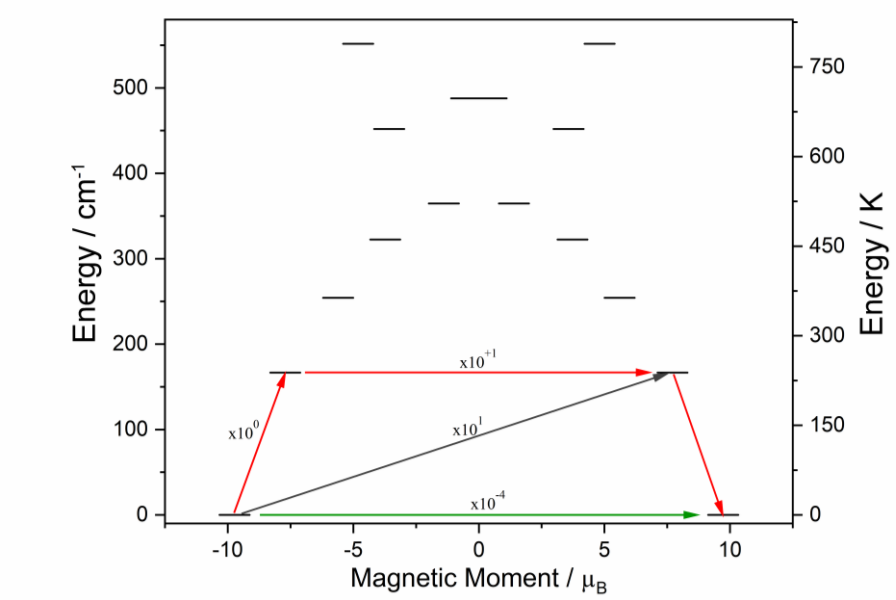

Figure 3. 26 Ab initio doublet states and proposed relaxation pathway for complexe 3-**2**$^{(I = 5/2)}$ and 3-**3**$^{(I = 0)}$.

While the magnetic anisotropies in binuclear complexes often originate from single Dy^{III} ions, the interactions between Dy atoms also play a significant role in the slow relaxation of magnetization. Therefore, the program POLY_ANISO employing the Lines model was used to fit the magnetic susceptibilities of complexes 3-**2**$^{(I = 5/2)}$ and 3-**3**$^{(I = 0)}$[214], which employs an isotropic exchange between the spin component of the angular momenta (S = 5/2 for Dy^{III}) and has been used previously to model interactions between lanthanides[212,215]. Employing this model with PHI[216] we find J_{Lines}=-0.006 (3) cm^{-1} for 3-**2**$^{(I = 5/2)}$ and -0.022 (1) cm^{-1} for and 3-**3**$^{(I = 0)}$, which gives excellent fits to both $\chi_M T(T)$ and $M(H)$ (Fig. 2). The dipolar interaction can be determined employing the parameters determined from ab-initio calculations and equation (3):

$$J_{1,2}^{dip} = \frac{\mu_B^2}{r^3} - [g_1 g_2 \quad - 3(\frac{(Rg_1)(Rg_2)}{|R|^2})] \qquad (3)$$

The J^{dip} values is calculated to be 1.36 mK.

By examining the derivative of the temperature-dependent hysteresis loops as shown in Figure 3.27, it is evident that a tunneling event occurs at ±12 mT in 3-**3**$^{(I = 0)}$, while in 3- **2**$^{(I = 5/2)}$ the tunneling is spread out over a ±50 mT range. The tunneling event at ±12 mT in 3-**3**$^{(I = 0)}$ enables a direct estimation of the exchange coupling J_{ex} between the two Dy(III) ions using the equation $H_{ex} = J_{ex} m_J / g_J \mu_\beta$, where $m_J = 15/2$, $g_J = 4/3$, and μ_β is the Bohr magneton. J_{ex} is determined to be 1.43 mK (9.91×10^{-4} cm^{-1}) for 3-**3**$^{(I = 0)}$. The calculated J_{ex} is in good agreement with the one estimated from a purely point dipolar approximation: $J_{1,2}^{dip}$ = 1.36 mK (9.45×10^{-4} cm^{-1}) for a ^{164}Dy···^{164}Dy distance of 9.3326(5) Å, indicating that the interaction between the Dy(III) pairs is entirely of dipolar origin.

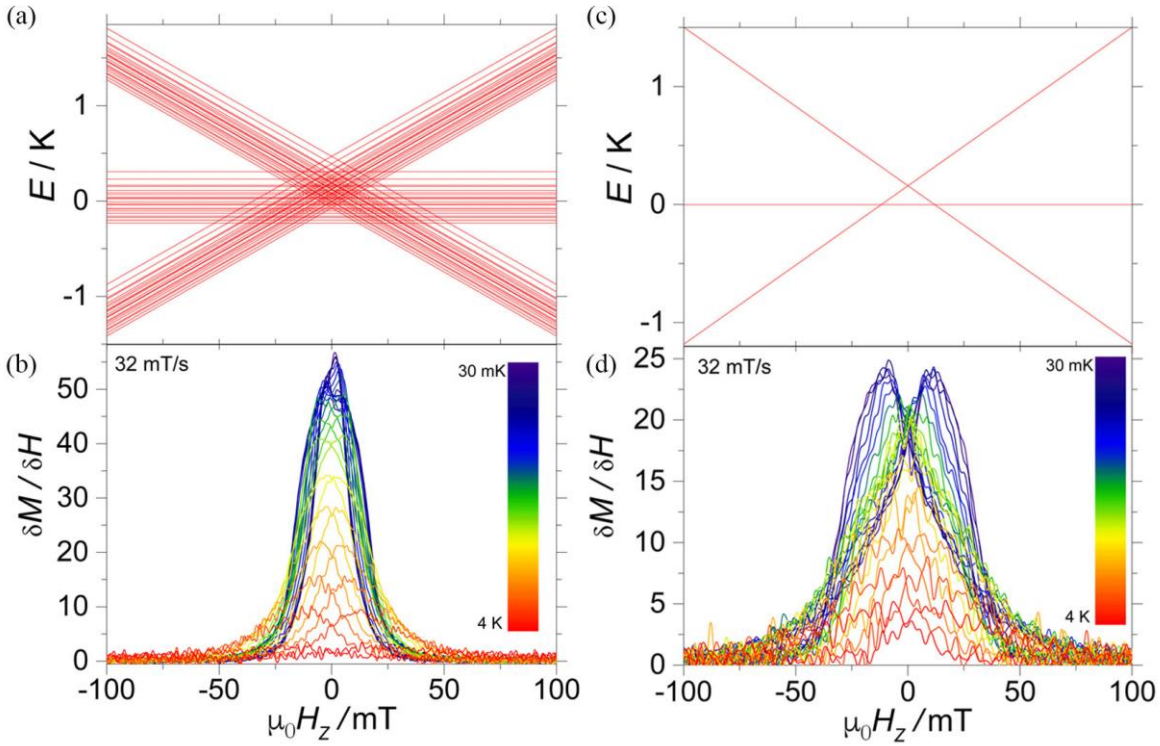

Figure 3.27 Zeeman diagram obtained employing eq. (4) and eq. (5) for (a) 3-**2**$^{(I = 5/2)}$ and c) 3-**3**$^{(I = 0)}$, respectively. Derivative of the temperature dependent hysteresis loops from μ-SQUID studies for (b) 3-**2**$^{(I = 5/2)}$ and (d) 3-**3**$^{(I = 0)}$.

In order to better understand the results obtained from the μ-SQUID, we created a

model to examine the low-temperature magnetic properties of 3-**2**$^{(I = 5/2)}$ and 3-**3**$^{(I = 0)}$. Initially, we focused solely on 3-**3**$^{(I = 0)}$ for the sake of simplicity. The magnetic properties of the single ion in the SMM are primarily influenced by spin-orbit coupling and its interaction with surrounding ligands. As a result, there is a significant gap between the ground $m_J = \pm 15/2$ and the first excited $m_J = \pm 13/2$ multiplets. This allowed us to treat the complex as two independent Ising spins (s = 1/2) that are coupled through an effective interaction $J_{ex}\sigma_{1z}\sigma_{2z}$, where J_{ex} is the effective coupling and $\sigma_{1z}\sigma_{2z}$ are the z-Pauli matrices. Thus, the Hamiltonian for 3-**3**$^{(I = 0)}$ can be expressed as follows when subjected to an external magnetic field along the easy axis:

$$^{164}\mathcal{H} = g_{\text{eff}}\mu_B\mu_0 H_z(\sigma_{1z} + \sigma_{2z}) + J_{\text{ex}}\sigma_{1z}\sigma_{2z} \qquad (4)$$

where $g_{\text{eff}} = 20$ and J_{ex} represents the interaction between the ions which is projected onto a s = 1/2 basis. In the case of 3-**2**$^{(I = 5/2)}$, complex bearing a nuclear spin, which is a complex containing a nuclear spin, the Hamiltonian includes both the hyperfine (A_{hyp}) and quadrupolar (P_{quad}) interactions:

$$^{163}\mathcal{H} = {}^{164}\mathcal{H} + \sum_{i=1}^{2} A_{hyp}\, \boldsymbol{I}^i \cdot \boldsymbol{\sigma}_i + P_{quad} I_z^i I_z^i \qquad (5)$$

Figure 3.27a depicts the Zeeman diagram for 3-**3**$^{(I = 0)}$. In the case of 3-**2**$^{(I = 5/2)}$, the Zeeman diagram was obtained by maintaining J_{ex} at the same value obtained for 3-**3**$^{(I = 0)}$, while the hyperfine and quadrupolar interactions were set to A_{hyp} = 107.1 mK (0.074 cm^{-1}) and P_{quad} = 19.6 mK (0.014 cm^{-1})[201] (Fig 3.27c). As can be seen, QTM is possible for 3-**3**$^{(I = 0)}$ at the intersections between the ground singlet and the excited doublet (±12 mT) due to the absence of nuclear spin states. In contrast, 3-**2**$^{(I = 5/2)}$ contains a nuclear spin, which can induce *hf*-QTM, causing the QTM event to shift from zero to certain field values. However, the interaction between the Dy(III) centers can result in the indirect coupling of nuclear states, thereby creating a $(2I+1)^n$ states, with multiple intersections where *hf*-QTM is active and the system can relax.

3.4.2 Calculation of complexes 3-6$^{(I = 5/2)}$ and 3-7$^{(I = 0)}$

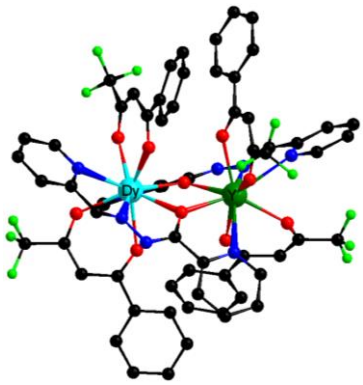

Figure 3.28 Molecular fragment employed for the CASSCF-SO calculations 3-**6**$^{(I = 5/2)}$ and (c) 3-**7**$^{(I = 0)}$.

This passage discusses the results of calculations performed on binuclear Dy(III) models for complexes 3-**6**$^{(I = 5/2)}$ and 3-**7**$^{(I = 0)}$ (Fig 3.28). The calculations were done using Complete-active-space self-consistent field (CASSCF) and Single_Aniso programs with geometries determined by X-ray experiments. The Table 3.6 and 3.7 show the lowest Kramer's doublets (KDs) and the g factors for 3-**6**$^{(I = 5/2)}$ and 3-**7**$^{(I = 0)}$, as well as the effective g_z tensors for each Dy(III) fragment. The effective g_z tensors indicate that each fragment has significant uniaxial anisotropy, approaching the Ising-limit value of 20. Additionally, the passage mentions that wave functions with definite projection of the total moment $|m_J>$ for the lowest two KDs of individual Dy(III) fragments have been summarized in Table 3.7. The energy gaps between the ground and the first excited Kramer's doublet for each Dy(III) fragment are obtained as 91.7 K (64.2 cm^{-1}, Dy1) and 111.3 K (77.9 cm^{-1}, Dy2) in 3-**6**$^{(I = 5/2)}$, 91.2 K (63.8 cm^{-1}, Dy1) and 121.7 K (85.2 cm^{-1}, Dy2) in 3-**7**$^{(I = 0)}$. These gaps are larger than the fitting barriers of 50.7 K for 3-**6**$^{(I = 5/2)}$ and 57.1 K for 3-**7**$^{(I = 0)}$, indicating the presence of multiple relaxation processes. As mentioned previously, the ln τ vs. T^{-1} plots were fitted through a sum of three relaxation mechanisms for both complexes. The magnetization blocking barriers are also shown in Figure 3.29. The matrix element of the transition magnetic moment of the ground state indicating that the approximate QTM may be observed in both complexes (Fig 3.29, green line).

Table 3.6 Calculated energy levels, g (g_x, g_y, g_z) tensors and m_J values of the lowest eight Kramers doublets (KDs) of individual Dy(III) fragments of complex 3-**6**$^{(I = 5/2)}$ using CASSCF/RASSI with MOLCAS 8.2.

	Energy (cm^{-1})	Energy(K)	g_x	g_y	g_z	Angle (°)
3-**6**$^{(I = 5/2)}$ (Dy1)	0.0	0.0	0.1270	0.2123	19.5920	
	64.2	91.7	2.1567	3.3455	14.1170	82.8
	87.9	125.6	9.7702	6.0402	1.2417	88.7
	112.7	161.0	9.3013	6.0992	2.3640	44.6
	165.8	236.9	0.9060	2.0077	13.8335	71.1
	212.7	303.9	3.5360	4.8972	10.1428	57.9
	245.8	351.2	3.2330	5.5899	11.7978	87.6
	309.3	441.9	0.2439	0.4109	18.2398	89.9
3-**6**$^{(I = 5/2)}$ (Dy2)	0.0	0.0	0.1374	0.2240	19.5186	
	77.9	111.3	1.9399	3.3141	14.6945	78.9
	97.4	139.2	9.9252	6.8578	0.0420	70.9
	134.2	191.7	2.2179	4.6029	10.0722	72.9
	182.8	261.2	0.9230	3.4866	12.4208	86.0
	220.7	315.3	0.4333	3.4735	12.2524	67.8
	269.1	384.5	0.8007	3.5949	14.2039	74.7
	300.4	429.2	0.5619	2.3228	16.6253	87.7

Table 3.7 Calculated energy levels, g (g_x, g_y, g_z) tensors and mJ values of the lowest eight Kramers doublets (KDs) of individual Dy(III) fragments of complex 3-**7**$^{(I = 0)}$ using CASSCF/RASSI with MOLCAS 8.2.

	Energy (cm^{-1})	Energy(K)	g_x	g_y	g_z	Angle (°)
3-**7**$^{(I = 0)}$ (Dy1)	0.0	0.0	0.1059	0.1740	19.5772	
	63.8	91.2	2.3158	4.0831	13.9450	79.2
	90.2	128.9	0.7642	4.6922	9.1240	7.9
	113.8	162.6	9.6585	6.9934	2.7444	37.1
	165.3	236.2	0.8918	1.7038	14.0929	74.8
	213.7	305.3	3.5333	5.5426	9.6008	60.6
	245.9	351.3	3.1457	6.2442	11.2294	86.6
	311.9	445.6	0.2284	0.3691	18.3112	89.1
3-**7**$^{(I = 0)}$ (Dy2)	0.0	0.0	0.1335	0.2358	19.5362	
	85.2	121.7	2.0092	5.3978	12.3817	66.6
	99.6	142.3	9.1636	5.7883	2.3075	53.7
	137.8	196.9	2.2964	4.7120	9.8173	76.6
	188.6	269.5	0.9496	3.0787	12.8107	82.1
	227.8	325.5	0.1500	3.6551	12.3256	66.6
	273.6	390.9	1.1684	3.6231	14.2851	76.8
	307.0	438.6	0.5037	1.8134	16.8961	88.9

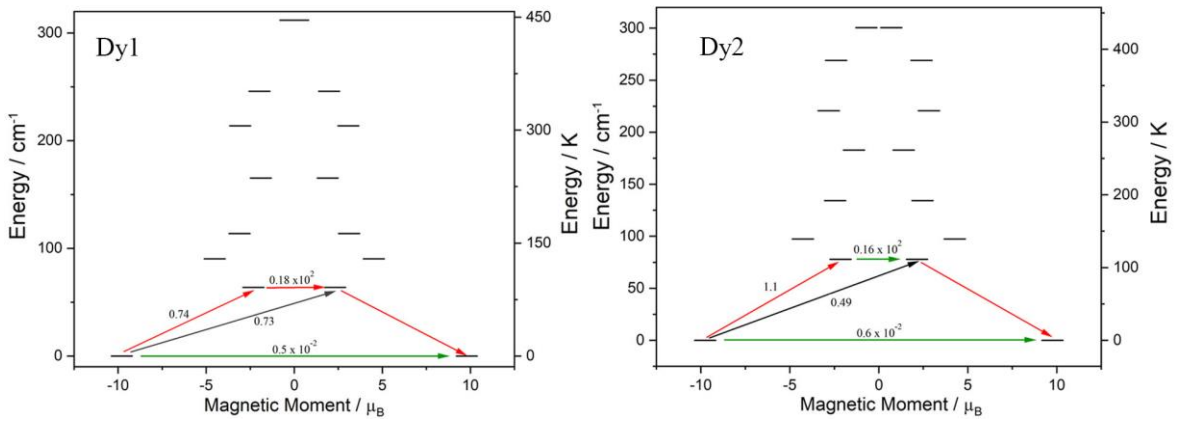

Figure 3.29 Relaxation of the magnetisation for individual Dy1 (left) and Dy2 (right) in 3-**6**$^{(I = 5/2)}$ and 3-7$^{(I = 0)}$. Red arrows show the most probable relaxation route and light green and blue arrows indicate less significant but non-negligible matrix elements between states.

Table 3.8 Wave functions with definite projection of the total moment $|m_J>$ for the lowest two KDs of individual Dy(III) fragments for for 3-**2**$^{(I = 5/2)}$ and 3-**3**$^{(I = 0)}$.

	Energy (cm^{-1})	Wave functions
3-**6**$^{(I = 5/2)}$ (Dy1)	0.0	97.1% |±15/2>
	64.2	17.4% |±13/2> +13.9% |±5/2>+17.3%|±3/2>+29.8%|±1/2>
3-**6**$^{(I = 5/2)}$ (Dy2)	0.0	95.6% |±15/2>
	77.9	19.7% |±13/2> +10.1% |±11/2>+11.9%|±5/2>+16%|±3/2>29.4%|±1/2>
3-**7**$^{(I = 0)}$ (Dy1)	0.0	96.8% |±15/2>
	63.8	19.6% |±13/2>+12.4% |±5/2>+14.8%|±3/2>+27.8%|±1/2>
3-**7**$^{(I = 0)}$ (Dy2)	0.0	95.8% |±15/2>
	85.2	30.6% |±13/2>+11.5% |±11/2>+11.8%|±3/2>+23.9%|±1/2>

While magnetic anisotropies in binuclear complexes commanlly originate from single Dy(III) ions, the slow relaxation of magnetization is also significantly influenced by Dy-Dy interactions. The Lines model was used to fit the magnetic susceptibilities of complexes 3-**6**$^{(I = 5/2)}$ and 3-**7**$^{(I = 0)}$[214]. The fitting gives J_{Lines}=-0.036 (5) cm^{-1} for 3-**6**$^{(I = 5/2)}$ and -0.045 (2) cm^{-1} for and 3-**7**$^{(I = 0)}$. The derivative of the temperature-dependent hysteresis loops as shown in Figure 3.30, a tunneling event occurs at ±130 mT in 3-**7**$^{(I = 0)}$, while in 3-**6**$^{(I = 5/2)}$ the tunneling is spread out over a ±200 mT range. A direct estimation of the exchange coupling is made possible by the tunneling event occurring at ±130 mT in 3-**7**$^{(I=0)}$ gives J_{ex} = 208.6 mK (0.145 cm^{-1}), much larger than the one

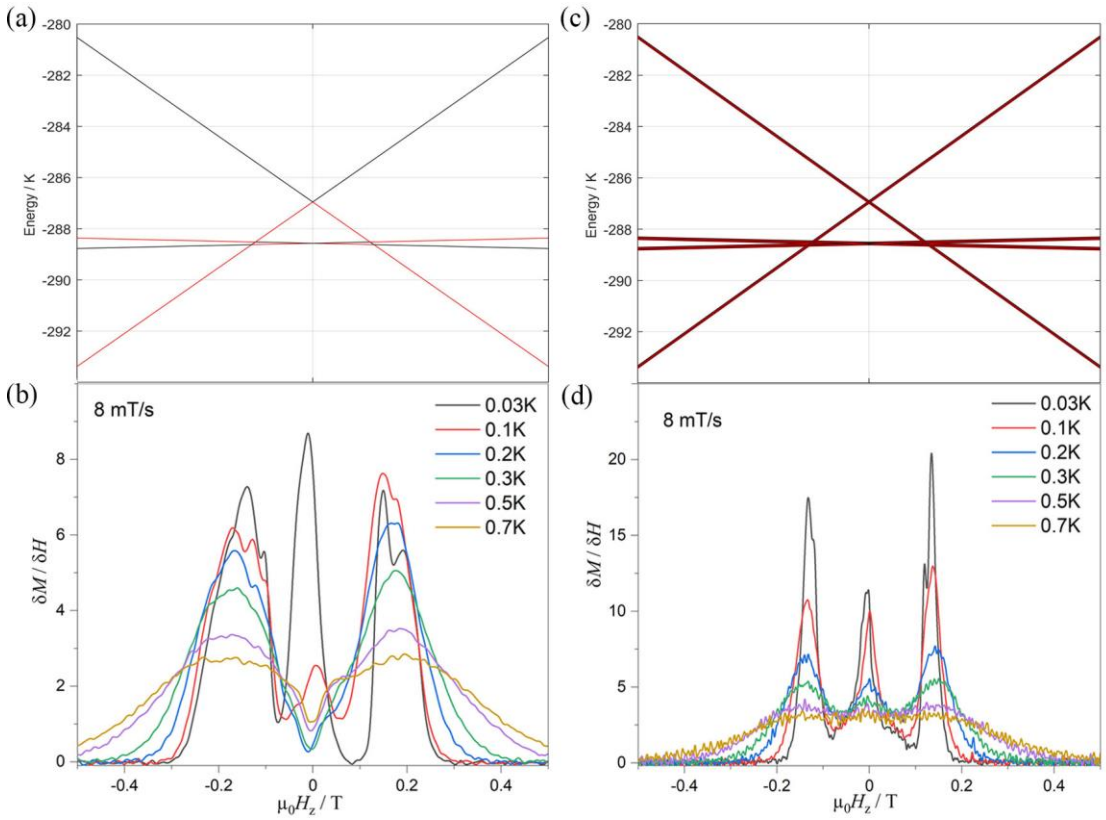

Figure 3.30 Zeeman diagram obtained employing eq. (4) and eq. (5) for (a) 3-**7**$^{(I = 0)}$ and c) 3-**6**$^{(I = 5/2)}$, respectively. Derivative of the temperature dependent hysteresis loops from μ-SQUID studies for (b) 3-**7**$^{(I = 0)}$ and (d) 3-**6**$^{(I = 5/2)}$.

obtained from a purely point dipolar approximation: $J_{1,2}^{dip}$ = 32.6 mK (0.023 cm^{-1}) for a ^{164}Dy···^{164}Dy distance of 4.064(3) Å, indicating that the interaction between the Dy(III) pairs is mainly of exchange contribution.

In order to enhance the understanding of the μ-SQUID results, in the first step, we utilize the spin effective formalism with a value of S_{eff} equal to 1/2[217], and we use pure axial *g*-tensors, specifically $g_{xx} = g_{yy} = 0$ and $g_{zz} = 20$. We obtain the projection angles of the $m_J = \pm 15/2$ state for each Dy(III) ion from the electrostatic analysis. However, we find that $S_{eff} = 1/2$ can be quickly mixed by transverse fields, resulting in a large tunnelling splitting that is not reflective of the system. In order to overcome this problem, we resort to using a theoretical spin value of S = 3/2 with a large, arbitrary value for the LFS (D) set at −100 cm^{-1}. This is because we have found that this spin value is less susceptible to mixing by transverse fields. We maintain isotropic *g*-values

($g_{xx} = g_{yy} = g_{zz} = 20/3$) and adjust the LFS by rotating it using the Euler angles obtained from the electrostatic analysis[218]. The Zeeman diagram was acquired by fixing J_{ex} to the one obtained for 3-**7**$^{(I=0)}$, as shown in Figurre 3.30. This has enabled us to initiate comprehension of the hysteresis loops of the 3-**7**$^{(I=0)}$ complex (Fig 3.30a). At H_z = -1 T (with O_z chosen along the easy axis of the Dy(III) ions) the sample is polarised and all the spins are in the ground state |+15/2,+15/2>. As the magnetic field is swept, the molecules remain in the ground state until the external field compensates the bias field, $\mu_0 H_r$ ~ 0.14 T, and the SMM makes a transition from the ferromagnetic to the antiferromagnetic order by quantum tunnelling. The next transition happens at $\mu_0 H_r$ ~ 0.14 T where the molecules relax non adiabatically from the state |+15/2, –15/2> to |–15/2, –15/2>.

3.5 Conclusions

In chapter 3, seven dinuclear Dy(III) complexes were thoroughly analyzed, encompassing both their structure and magnetic properties. The dinuclear complexes were successfully synthesized with three types of ligands. Complexes 3-**2**$^{(I = 5/2)}$ – 3-**5** were synthesized by tuning the terminal ligands or the Dy(III) isotopes with the same ligand TAPE. The different terminal β-diketonate coligands in 3-**2**$^{(I = 5/2)}$ – 3-**5** obviously cause a structural difference that influences the dynamic magnetic behaviors. The complexes 3-**2**, 3-**3**, 3-**4**, and 3-**5** exhibit anisotropic barriers with U_{eff} values of 80.6, 73.3, 47.0 and 24.5 K, respectively. As inferred from the ac studies of complexes 3-**2**$^{(I = 5/2)}$ and 3-**3**$^{(I = 0)}$, the presence of the nuclear spin makes the Raman relaxation process become more important, while the high temperature data is insensitive to the nuclear spins. A large step at zero field μ-SQUID loops was observed for both complexes due to the faster relaxation around zero field, which are the typical loops commonly observed in single-ion lanthanide-based SMMs, indicates there are no interactions between the two Dy^{III} ions, which could be due to the large intramolecular Dy-Dy distance (9.3326(5) Å, 9.3276(5) Å in 3-**2**$^{(I = 5/2)}$ and 3-**3**$^{(I = 0)}$). Complexes 3-**6**$^{(I = 5/2)}$ and 3-**7**$^{(I = 0)}$ were synthesized starting from ligand BPTZ. The final composition of

complexes 3-**6**$^{(I = 5/2)}$ and 3-**7**$^{(I = 0)}$ are composed of the ligand PHZP, which formed due to the insitu hydrolysis of BPTZ. µ-SQUID loops reveal an interaction between the two Dy(III) ions; the S-shaped hysteresis loops are characteristic of antiferromagnetically coupled Ising spins. The relaxation in 3-**7**$^{(I = 0)}$ is slower than in 3-**6**$^{(I = 5/2)}$, this can be attributed to the absence of nuclear spins in 3-**7**$^{(I = 0)}$. The studies between 3-**2**$^{(I = 5/2)}$, 3-**3**$^{(I = 0)}$ and 3-**6**$^{(I = 5/2)}$, 3-**7**$^{(I = 0)}$ indicated that the strength of the intramolecular exchange coupling is sensitive to the Dy···Dy distances (4.065(5) Å, 4.064(3) Å in 3-**6**$^{(I = 5/2)}$ and 3-**7**$^{(I = 0)}$). Therefore, closer spacing between Dy(III) atoms is preferred.

Chapter 4. Single-molecule magnet characteristics of trinuclear Dy(III) complexes

In recent times, there has been a growing interest in trinuclear metal clusters having a triangular core. The clusters display antiferromagnetic interactions between metal centers due to spin frustration effects [82,97,219,220]. To explore any possible correlations between this triangular geometry and magnetic properties, design and synthesis of novel trinuclear lanthanide complexes and magnetic property studies of the complexes are warranted.

With this in mind, we have prepared two trinuclear complexes (4-**1** and 4-**2**) composed of bipyridine-based scaffolds and studied their magnetic properties. In the trinuclear complexes, three Dy(III) metal centers are arranged in a triangular fashion. Each Dy(III) ion in the complexes is placed in an N_2O_6 eight coordinate environment. Complexes 4-**1** and 4-**2** are zero-field SMMs, as inferred from the AC studies. Synthesis of the ligands and complexes as well as the structural and magnetic properties of the complexes are discussed in the following sections of this chapter.

4.1 Preparation of organic ligands

4.1.1 Synthesis of 1,3,5-tri(2,2′-bipyridin-5-yl)benzene (TBB)

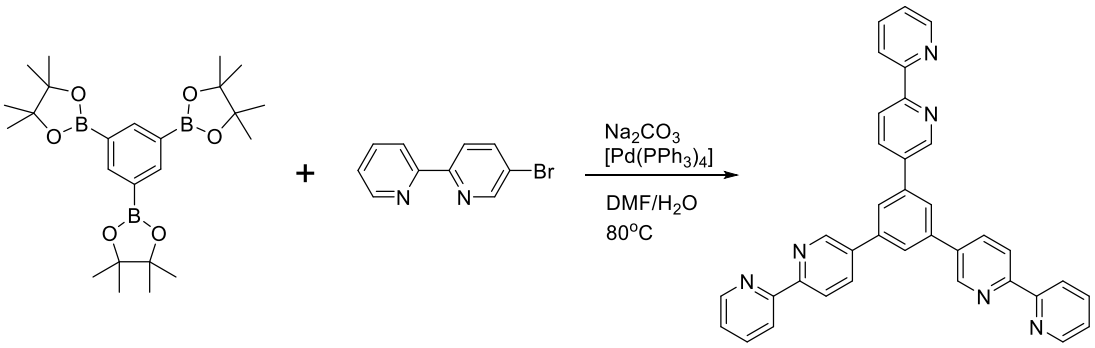

Scheme 4.1 Synthesis of 1,3,5-tri(2,2′-bipyridin-5-yl)benzene (TBB).

The ligand TBB was prepared following the reported procedure[221]. To a solvent mixture of DMF (30 mL) and water (10 mL), 1,3,5-tris(4,4,5,5-tetramethyl-1,3,2-dioxaborolan-2-yl)benzene (400 mg, 0.876 mmol), 5-bromo-2,2´-bipyridine (824 mg, 3.49 mmol) and Na_2CO_3 (5.96 g, 56.2 mmol) were added. The solution was degassed by freeze-pump-thaw. After that $[Pd(PPh_3)_4]$ (200 mg, 0.132 mmol) was added and the mixture was stirred at 80 °C for overnight. The reaction was stopped by the addition of water (100 mL) and extracted with CH_2Cl_2 (3×50mL). The organic layers were combined, washed with saturated EDTA solution (50mL), dried over $MgSO_4$, and evaporated under reduced pressure. The crude product was recrystallized from acetonitrile to give TBB (183 mg, 46.7%) as an analytically pure white powder.

^{1}H NMR (500 MHz, $CDCl_3$, δ/ppm): 9.00 (d, 3H), 8.69 (d, 3H), 8.54 (d, 3H), 8.48 (d, 3H), 8.15 (dd, 3H), 7.97 (s, 3H), 7.84 (td, 3H), 7.33 (m, 3H).
^{13}C NMR (126 MHz, $CDCl_3$) δ/ppm): 155.72, 155.68, 149.31, 147.73, 139.81, 137.01, 135.92, 135.64, 125.72, 123.97, 121.31, 121.20.

4.1.2 Synthesis of 1, 3, 5-tris{[2,2'-bipyridin-5-ylethynyl]phenyl}benzene (TBPB)

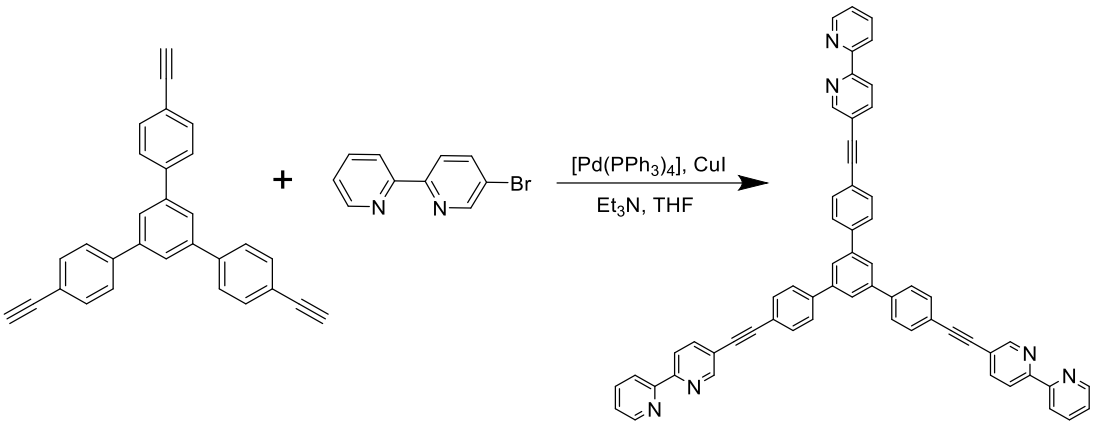

Scheme 4.2 Synthesis of 1, 3, 5-tris{[2,2'-bipyridin-5-ylethynyl]phenyl}benzene (TBPB).

The ligand TBPB was synthesized according to the literature[222,223]. A mixture of 1,3,5-Tris(4-ethynylphenyl)benzene (200 mg, 0.528 mmol), 5-bromo-2, 2'-bipyridine (559

mg, 2.38 mmol), [$Pd(PPh_3)_4$] (18 mg, 9.0 μmol) and CuI (3 mg, 15.8 μmol) in dried and degassed THF (5 mL) and triethylamine (0.5 mL) mixture was heated at 70 °C for 72 h under an argon atmosphere. The mixture was cooled to room temperature and extracted with dichloromethane (3×50 mL). The combined organic layers were dried over anhydrous sodium sulphate, and the solvent was evaporated under reduced pressure. The crude product was purified by flash column chromatography using hexane-ethyl acetate (3:2) mixture as an eluent to yield TBPB (36.9%).

^{1}H NMR (500 MHz, $CDCl_3$, δ/ppm): 8.85 (s, 3H), 8.69 (d, 3H), 8.44 (d, 6H), 7.97 (dd, 3H), 7.84 (dt, 6H), 7.72 (td, 12H), 7.33 (dd, 3H).

^{13}C NMR (126 MHz, $CDCl_3$) δ/ppm): 155.48, 154.91, 151.68, 149.31, 141.73, 141.06, 139.01, 137.01, 132.32, 127.37, 125.32, 123.97, 122.08, 121.41, 120.40, 120.28, 93.33, 84.45.

4.2 Synthesis of trinuclear complexes

4.2.1 Synthesis of $[Dy_3(tmhd)_9(TBB)]$ (4-1)

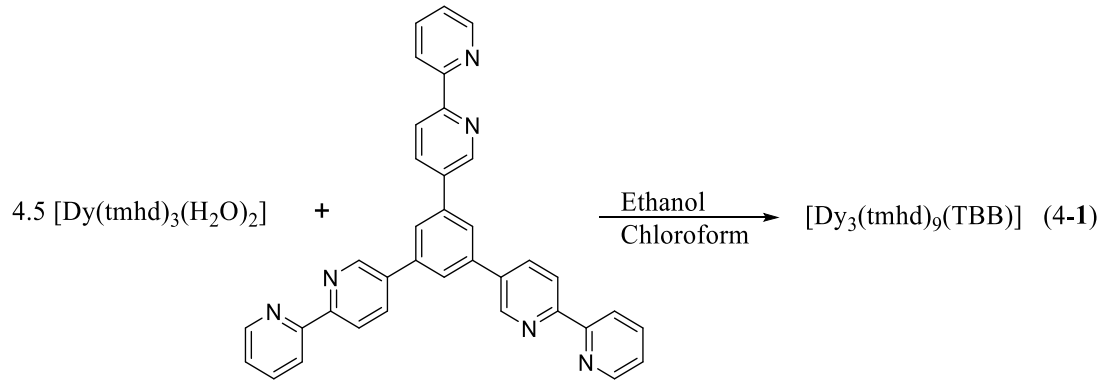

Scheme 4.3 Synthetic route of complex 4-**1.**

[$Dy(tmhd)_3(H_2O)_2$] (73.9 mg, 0.067 mmol) and TBB ligand (12.0 mg, 0.022 mmol) were added to a mixture of 8 mL ethanol and 3 mL chloroform, and the mixture was stirred overnight and filtered. The colourless filtrate was left undisturbed in an open vial. Colourless block crystals were obtained after a few days.

Yield: 31.0 mg (51.62%)

Elemental Analysis: Calculated.: $C_{135}H_{195}Dy_3N_6O_{18}$ (2677.46 g/mol): C, 60.50; H, 7.28; N, 3.81.

Found: C, 60.71; H, 7.34; N, 3.69.

4.2.2 Synthesis of $[Dy_3(tmhd)_9(TBPB)\bullet CH_2Cl_2]$ (4-2)

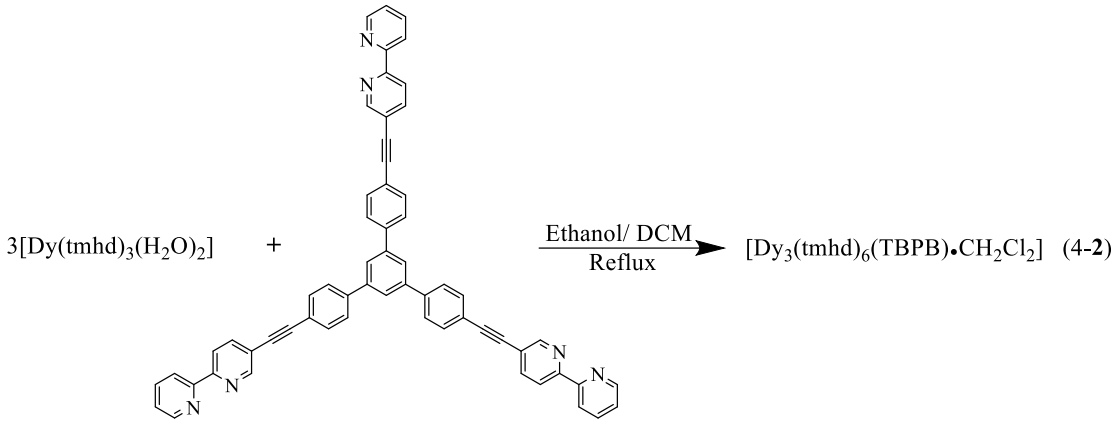

Scheme 4.4 Synthetic route of complex 4-**2**.

$[Dy(tmhd)_3(H_2O)_2]$ (50 mg, 0.067 mmol) and TBPB ligand (18.76 mg, 0.022 mmol) were added to a mixture of 5 mL ethanol and 2 mL dichloromethane (DCM), and the mixture was refluxed for 3 h and filtered. The yellowish filtrate was cooled to room temperature and left undisturbed in an open vial. Yellowish plate-like crystals were obtained after a few days.

Yield: 31.0 mg (51.62%)

Elemental Analysis: Calculated: $C_{160}H_{209}Cl_2Dy_3N_6O_{18}$ (3062.78 g/mol): C, 62.69; H, 6.82; N, 2.74. Found: C, 62.59; H, 6.65; N, 2.58.

4.3 Structures of trinuclear complexes

4.3.1 Structure of $[Dy_3(tmhd)_9(TBB)]$ (4-1).

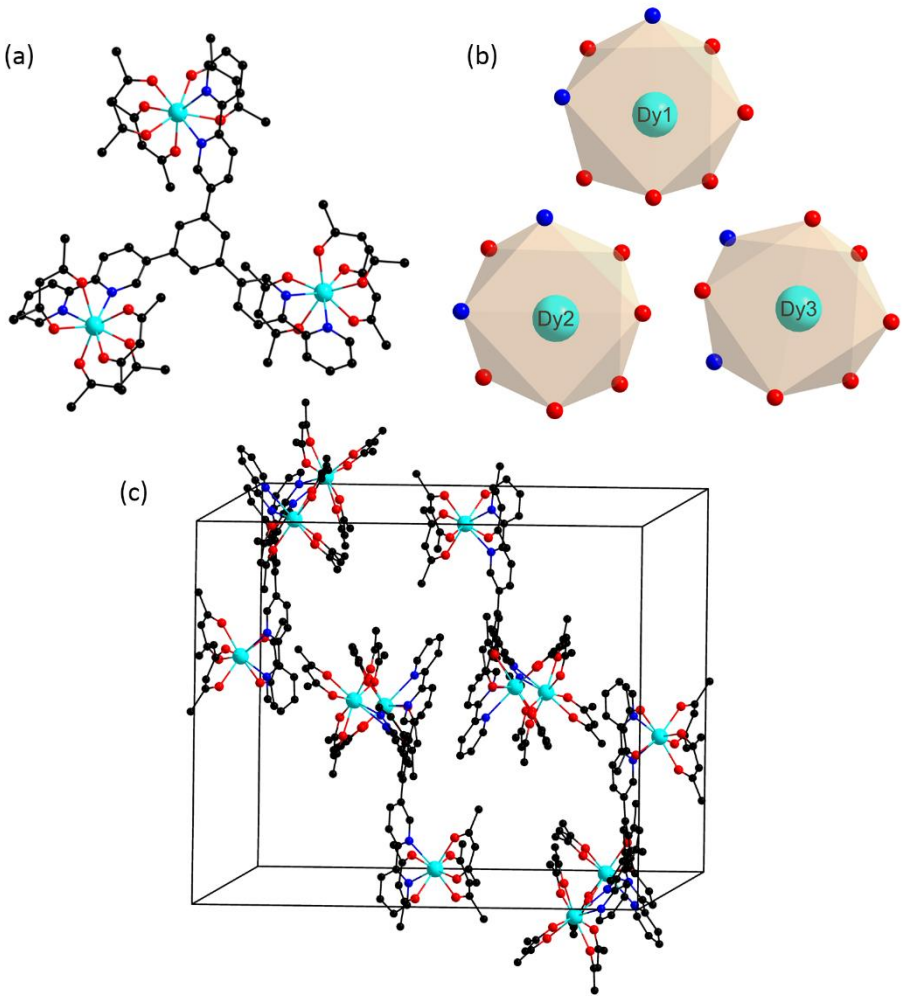

Figure 4.1 (a) Crystal structure of $[Dy_3(tmhd)_9(TBB)]$ (4-**1**), (b) Polyhedral representation of the Dy(III) sites in an N_2O_6 coordination environment, and (c) unit cell of $[Dy_3(tmhd)_9(TBB)]$. Colour code: Dy, bright blue; O, red; N, blue; C, black.

Complex 4-**1** crystallized in the $P2_1/c$ space group. In complex 4-**1**, there are three dysprosium centers. Each Dy(III) center is placed in an N_2O_6 coordination environment originate from three bidentate $[tmhd]^-$ ligands and two nitrogen donors from the TBB ligand (Figure 4.1). The Dy···O distances for Dy(1) are in the range 2.289(5)-2.342(5), whereas the corresponding distances for Dy(2) and Dy(3) are 2.295(7)-2.321(8) and 2.278(6)-2.356(8), respectively. The Dy···N distances in 4-**1** are 2.554(6)-2.607(7) Å.

The Dy(1)···Dy(2), Dy(1)···Dy(3) and Dy(2)···Dy(3) separations are 11.723(7) Å, 12.311(7) Å and 12.209(7) Å, respectively. The N_2O_6 coordination environment around each Dy(III) can be defined as square antiprism (D_{4d}) after the metric parameters for the dysprosium centers were examined using the SHAPE software. The CShM values for Dy(1), Dy(2), and Dy(3) are 0.464, 0.639, and 0.649, respectively (Table 4.2).

4.3.2 Structure of $[Dy_3(tmhd)_9(TBPB)\cdot CH_2Cl_2]$ (4-2).

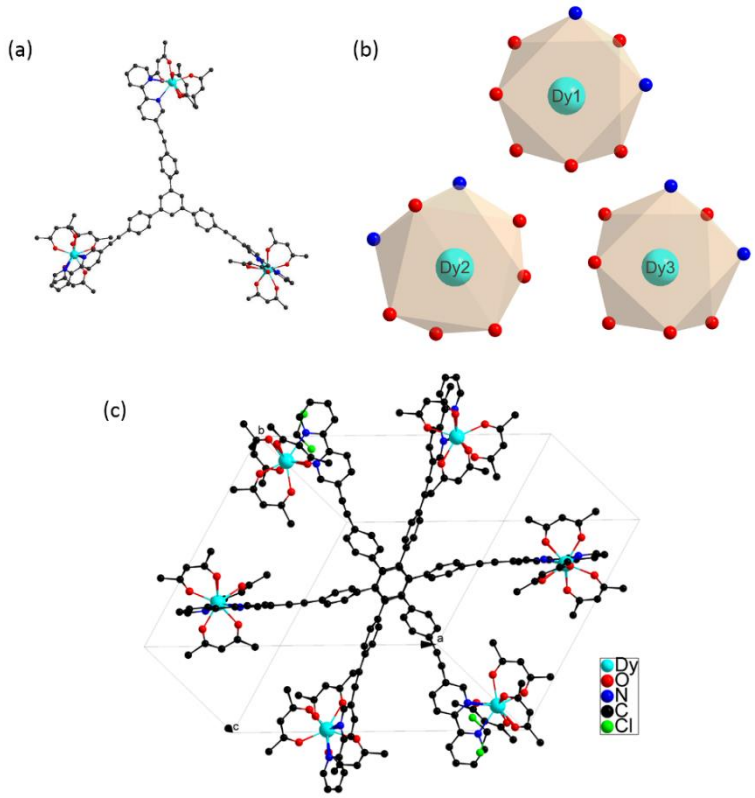

Figure 4.2 (a) Crystal structure of $[Dy_3(tmhd)_9(TBPB)\cdot CH_2Cl_2]$ (4-**2**). (b) Polyhedral representation of the Dy(III) site in an N_2O_6 coordination environment. (c) unit cell of $[Dy_3(tmhd)_9(TBPB)\cdot CH_2Cl_2$ (4-**2**).

$[Dy_3(tmhd)_9(TBPB)\cdot CH_2Cl_2]$ (4-**2**) crystallized in the $P\bar{1}$ space group (Fig 4.2). Its asymmetric unit contains three Dy^{3+} ions, nine tmhd ligands, one TBPB ligand and CH_2Cl_2 lattice solvent. Dy(III) is eight-coordinated by six oxygen atoms from three tmhd ligands and two nitrogen atoms from TBPB ligand. The Dy···O distances range between 2.264(3) Å to 2.346(3) Å, whilst the Dy···N distances are longer, with values ranging from 2.556(3) Å to 2.605(4) Å. The intramolecular distance between

Dy1···Dy2, Dy1···Dy3, and Dy2···Dy3 are 23.451(2) Å, 22.412 Å, and 23.885 Å, respectively. The coordination geometry around Dy1, Dy2, and Dy3 can be best described as a square antiprism (D_{4d}) with continuous shape measures (CShM) of 0.533, 0,570, and 0.575, respectively, implying that the three metal centers occupy very similar geometries (Table 4.2).

Table 4.1 Crystallographic parameters of complexes 4-**1** and 4-**2**.

No.	4-**1**	4-**2**
Formula	$C_{135}H_{195}Dy_3N_6O_{18}$	$C_{160}H_{209}Cl_2Dy_3N_6O_{18}$
Fw	2677.48	3062.78
T(K)	180	180
crystal system	monoclinic	triclinic
space group	$P2_1/c$	P-1
a, *Å*	23.5013(5)	22.1149(6)
b, *Å*	23.1814(5)	22.1421(6)
c, *Å*	26.8234(7)	22.8040(7)
α, *deg*	90	63.349(3)
β, *deg*	99.205(2)	66.327(3)
γ, *deg*	90	62.448(3)
V (Å^3)	14425.0(6)	8578.9(5)
Z	4	2
$\rho_{Calcd.}$ (mg·m^{-3})	1.233	1.186
μ (mm^{-1})	1.597	1.381
R_{int}	0.170	0.040
GOF on F^2	1.020	1.027
R_1, wR_2 ($I > 2\sigma(I)$)[a]	R_1 = 0.0765, wR_2 = 0.1784	R_1 = 0.0489, wR_2 = 0.1184
R_1, wR_2(all data)	R_1 = 0.1674, wR_2 = 0.227	R_1 = 0.0660, wR_2 = 0.1267

[a] $R_1 = ||F_o| - |F_c||/å|F_o|$, $wR_2 = \{w[(F_o)^2 - (F_c)^2]^2/w[(F_o)^2]^2\}^{1/2}$

Table 4.2 The CShM values calculated using SHAPE 2.1 programme for complexes 4-**1** and 4-**2.**

	Complex 4-**1**			Complex 4-**2**		
	Dy1	**Dy2**	**Dy3**	**Dy1**	**Dy2**	**Dy3**
Octagon (D_{8h})	29.863	30.772	30.458	30.656	30.123	30.848
Heptagonal pyramid (C_{7v})	22.691	22.797	22.648	21.474	22.281	22.015
Hexagonal bipyramid (D_{6h})	16.751	15.301	14.763	16.676	16.818	16.776
Cube (Oh)	9.906	9.160	8.723	10.256	10.331	10.335
Square antiprism (D_{4d})	**0.464**	**0.639**	**0.649**	**0.533**	**0.570**	**0.575**
Triangular dodecahedron (D_{2d})	2.268	2.290	2.578	2.819	2.025	2.340
Johnson - Gyrobifastigium J26 (D_{2d})	16.732	15.547	15.383	16.808	15.693	16.147
Johnson - Elongated triangular bipyramid J14 (D_{3h})	27.660	28.097	27.312	27.851	28.260	28.312
Johnson - Biaugmented trigonal prism J50 (C_{2v})	2.917	2.576	2.838	3.031	2.720	2.948
Biaugmented trigonal prism (C_{2v})	2.319	2.075	2.204	2.554	2.216	2.311
Snub disphenoid J84 (D_{2d})	5.241	5.148	5.112	5.557	4.674	5.142
Triakis tetrahedron (T_d)	10.668	9.861	9.495	10.996	10.993	11.036
Elongated trigonal bipyramid (D_{3h})	23.770	23.921	23.372	24.216	24.127	24.554

4.4 SMM characteristics of the trinuclear complexes 4-1 and 4-2

4.4.1 SMM characteristic of [Dy_3(tmhd)$_9$(TBB)] (4-1)

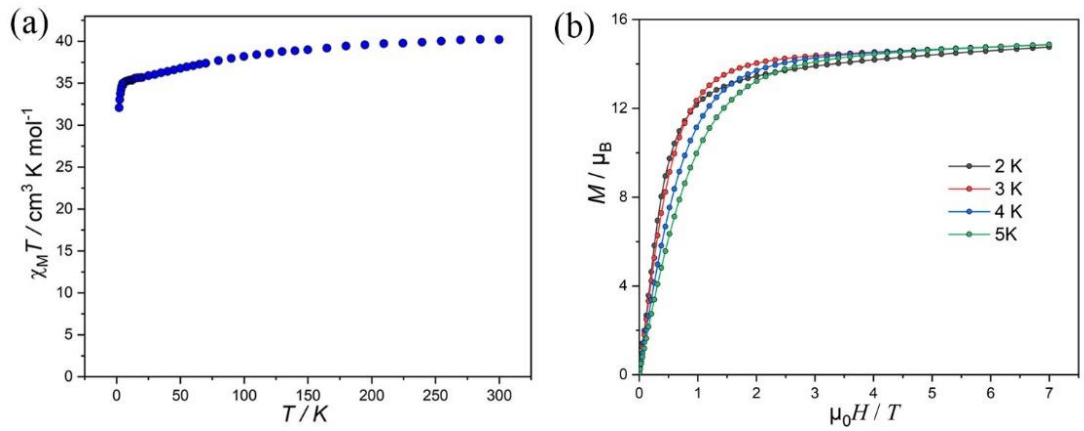

Figure 4.3 (a) The $\chi_M T$ vs. T plot for complex 4-**1**. (b) Plots of M vs. H at different temperatures.

The magnetic susceptibility (χ_M) of 4-**1** was measured in a static field (H_{dc}) of 1 kOe in the temperature range 2–300 K (Fig 4.3). At 300 K, $\chi_M T$ is 40.20 cm^3 K mol^{-1}, which is slightly lower than the value of 42.51 cm^3 K mol^{-1} predicted for three non-interacting

Dy^{3+} ions with $^6H_{15/2}$ ground terms and g = 4/3. This is due to the crystal-filed effect and substantial uniaxial magnetic anisotropy. The $\chi_M T$ gradually drops when the temperature is lowered to 7 K, after that $\chi_M T$ decreases sharply and reaches 32.06 cm^3 K mol^{-1} at 2 K. In principle, the temperature-dependent behavior of $\chi_M T$ can be attributed to the thermal depopulation of the excited m_J sublevels of Dy(III) ions.

The field dependence of magnetization of complex 4-**1** was evaluated at different temperatures 2, 3, 4, and 5 K in the magnetic field range of 0–7 T (Fig 4.3b). The sharp increase of magnetization at low field at low temperatures reveals a significant energy difference between the ground and excited states. Additionally, as the external field is increased, the magnetization value increases and reaches saturation at 14.98 μ_B for complex 4-**1** at 7 T. The M (H) value is consistent with the expected one (15 μ_B) for three Dy(III) ions with a well-defined m_J = 15/2 ground doublet.

We examined the AC (3.5 Oe) magnetic properties of complex 4-**1** with zero applied dc field with a frequency range of 1 to 1512 Hz (Fig 4.4). The AC susceptibility signal's shape and frequency dependence demonstrate the zero-field SMM characteristic of the complex 4-**1**. The out-of-phase χ_M'' peak is centered around 100 Hz at 2 K and remains at the frequency up to 5 K. Beyond 5 K, a shift to higher frequencies is observed until 18 K. A generalized Debye model was used to fit nearly symmetrical semi-circular curves observed in Cole-Cole plots derived from frequency-dependent AC data gathered at various temperatures (Fig 4.5a). The relaxation time parameter α is in the range of 0.19 - 0.26, implying a wide distribution of relaxation times.

Further insight into the ac susceptibility of 4-**1** was obtained from the relationship between the τ and temperature. The plot of ln τ versus T^{-1} for the zero-field data is shown in Figure 4.5b. Using Eq. 2, the entire temperature range data was fitted. The following parameters were obtained U_{eff} = 75.6 (2) K, C = 15.3 (1) K^{-n} s^{-1}, n = 1.80 (1), $\tau_0 = 7.56 \times 10^{-6}$ s, τ_{QTM} = 0.00147 (5) s.

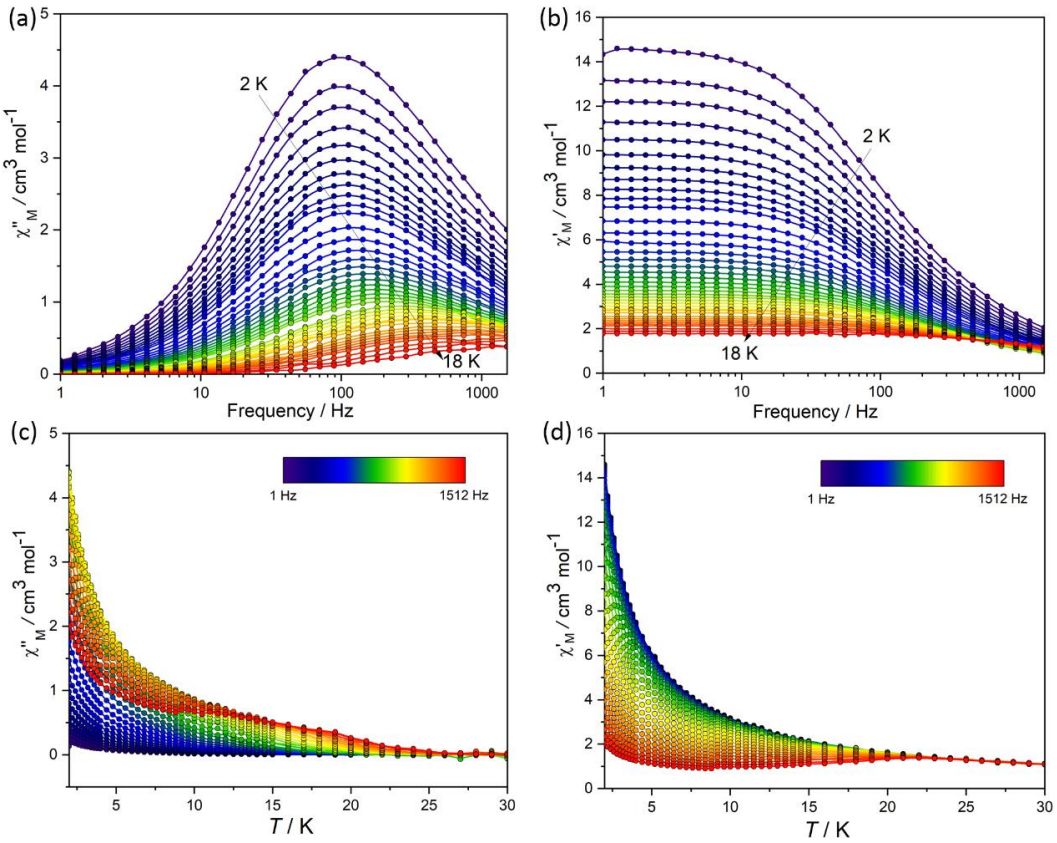

Figure 4.5 Experimental frequency dependent magnetic susceptibility data at zero applied DC (H_{dc}) field and varied temperatures (χ_M'' (ν)) for 4-**1** (a) and (b). Panel (c) and (d) show the temperature dependence of the out-of-phase and in-phase ac magnetic susceptibility data under a zero-dc field for 4-**1**, respectively.

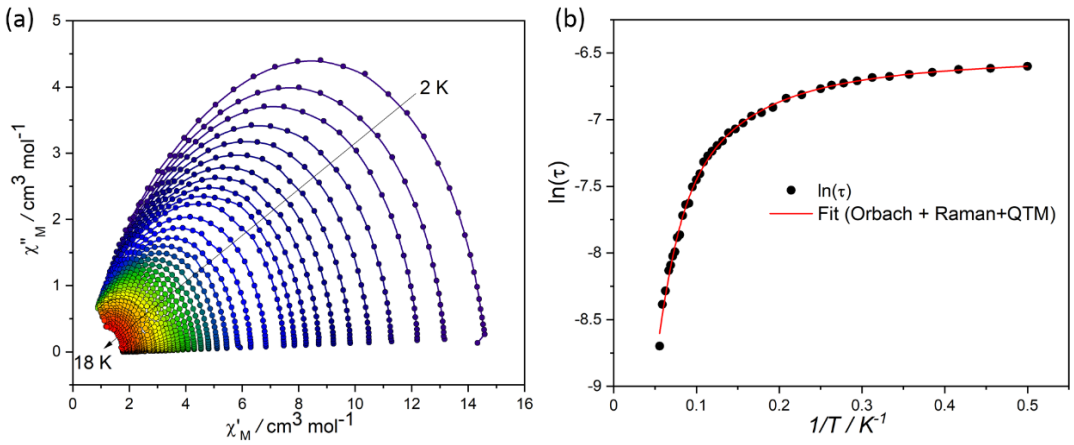

Figure 4.4 Cole – Cole plots under a zero-dc field for 4-**1**. The solid lines represent the best fits. (b) Temperature dependence of the magnetic relaxation time τ under zero field is shown as ln(τ) versus T^{-1} for 4-**1**. The solid red lines are the best fit to the multiple relaxation equation.

4.4.1 SMM characteristic of $[Dy_3(tmhd)_9(TBPB)\cdot CH_2Cl_2]$ (4-2)

The direct-current (dc) magnetic susceptibility measurements of 4-**2** were carried out on polycrystalline samples under a 1 kOe applied dc field from 2 to 300 K (Fig 4.6). The $\chi_M T$ value reached 42.13 cm^3 K mol^{-1} at room temperature, in good agreement with three non-interacting Dy(III) ions ($^6H_{15/2}$, g = 4/3, 42.51 cm^3 K mol^{-1}). The $\chi_M T$ value continuously fell as the temperature was lowered, reaching 35.06 cm^3 K mol^{-1} at 7 K. Further cooling resulted in a rapid drop in the $\chi_M T$ value, which fell to 32.46 cm^3 K mol^{-1}. The thermal depopulation of the excited m_J sublevels of Dy(III) ions is mostly responsible for the drop in the $\chi_M T$ value in 4-**2**.

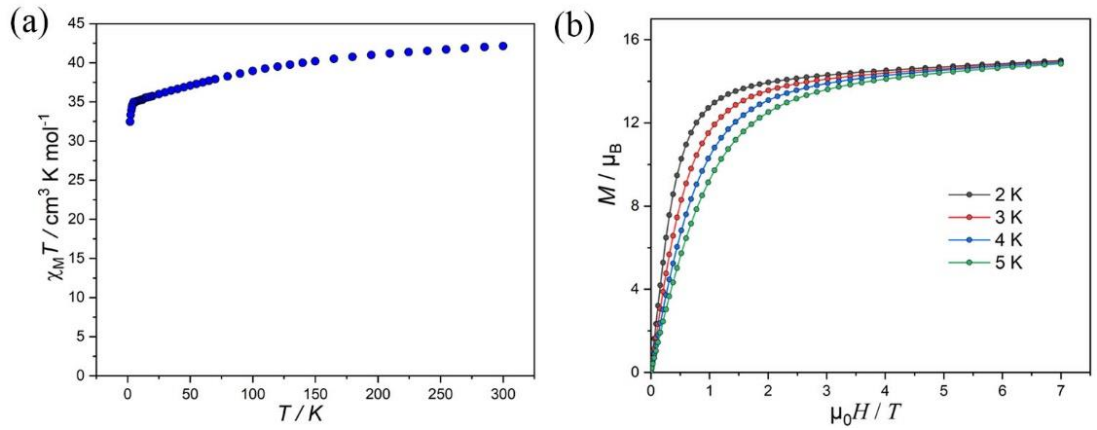

Figure 4.6 (a) The $\chi_M T$ vs. T plot for complex 4-**2**. (b) Plots of M vs. H at different temperatures.

The field dependence of magnetization of complex 4-**2** was evaluated at different temperatures 2, 3, 4, and 5 K in the magnetic field range of 0–7 T (Fig 4.6b). The sharp increase of magnetization at low field at low temperatures reveals a significant energy difference between the ground and excited states. Additionally, as the external field is increased, the magnetization value increases and reaches saturation at 14.84 μ_B for complex 4-**2** at 7 T. The M (H) value is consistent with the expected one (15 μ_B) for three Dy(III) ions with a well-defined J = 15/2 ground doublet.

By investigating the temperature and frequency-dependent alternating current (ac) magnetic susceptibility of 4-**2**, the typical characteristics of SMM behavior can be observed in its magnetic dynamics. As shown in Figure 4.7, it is obvious that, under a

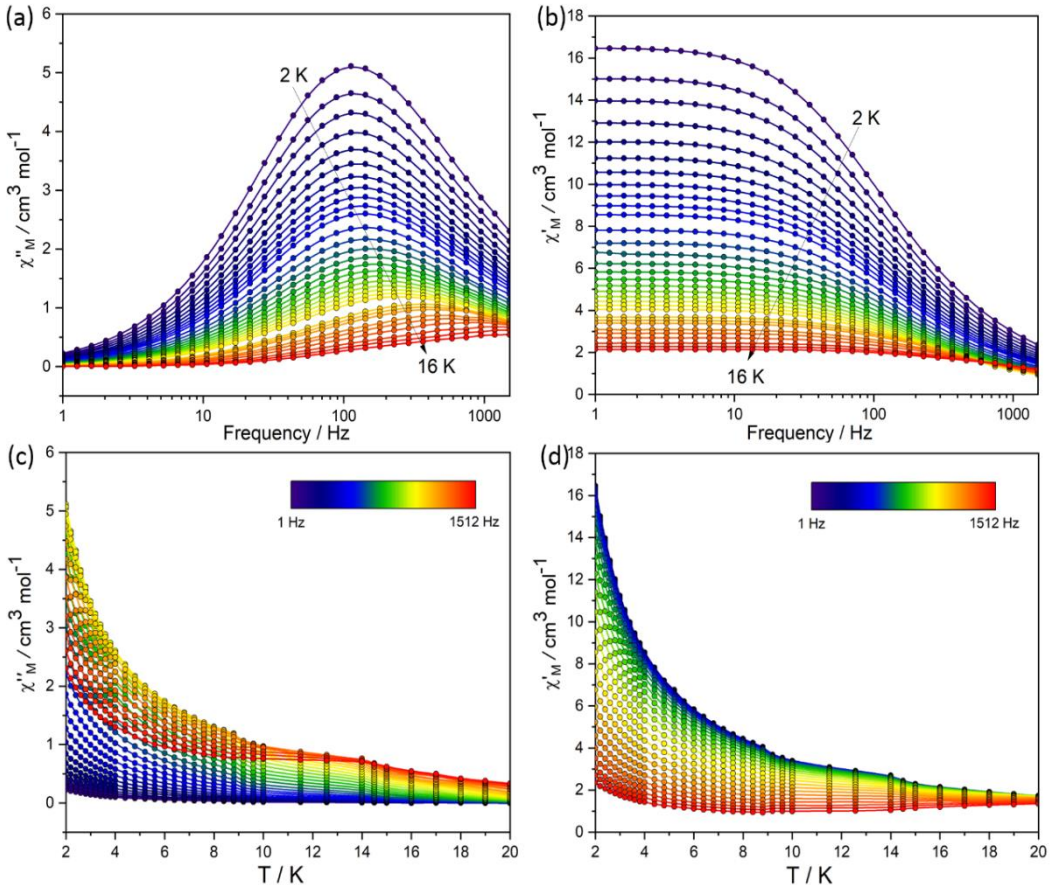

Figure 4.8 Experimental frequency dependent magnetic susceptibility data at zero applied DC (H_{dc}) field and varied temperatures ($\chi_M''(\nu)$) for 4-**2** (a) and (b). Panel (c) and (d) show the tempreture dependence of the out-of-phase and in-phase ac magnetic susceptibility data under a zero-dc field for 4-**2**, respectively.

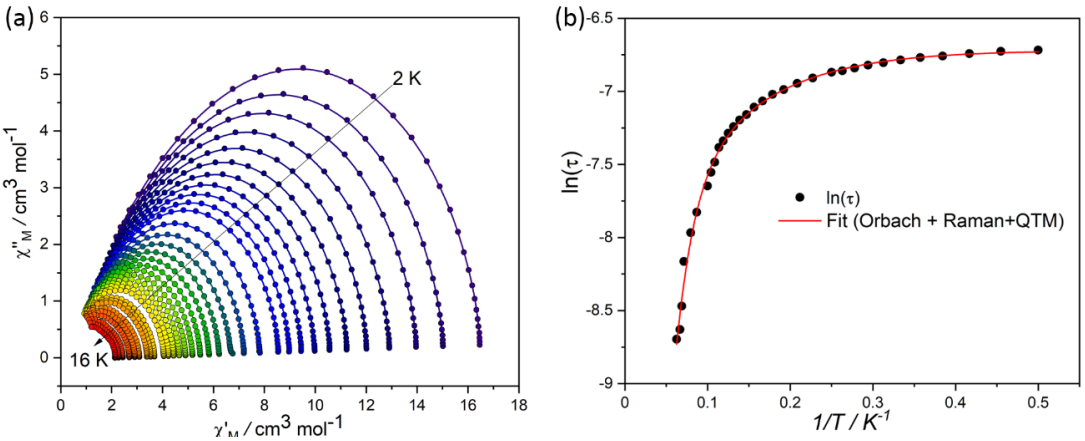

Figure 4.7 Cole–Cole plots under a zero dc field for 4-**2**. The solid lines represent the best fits. (b) Temperature dependence of the magnetic relaxation time τ under zero field is shown as ln(τ) versus T^{-1} for 4-**2**. The solid red lines are the best fit to the multiple relaxation equation.

zero field, the in-phase(χ') and out-of-phase (χ'') ac susceptibility signals of 4-**2** exhibit temperature and frequency dependence, and χ'' peaks can be observed in the range of 2−16 K. Moreover, the Cole−Cole plots exhibit nearly semicircular shapes, which can be fitted by considering a single relaxation process and employing the generalized Debye model (Fig 4.8a). The value of α is 0.25-0.32, indicating a wide distribution of relaxation times. The plot of ln (τ) vs T^{-1} is shown in Fig. 8b. Fitting of the data with Eq.2 gave the following parameters: U_{eff} = 92.5 (5) K, C = 10.8(1) K^{-n} s^{-1}, n = 2.0(1), $\tau_0 = 1.17 \times 10^{-6}$ s, τ_{QTM} = 0.00127(6) s.

4.5 Conclusion

This chapter presents the synthesis and characterization of two trinuclear Dy(III) complexes. In both complexes, the Dy(III) ions are in a square-antiprismatic N_2O_6 coordination environment with D_{4d} axial symmetry. The dc magnetic susceptibilities for both complexes were measured and the room temperature values are in good agreement with the expected values for three Dy(III) metal ions. Dynamic magnetic susceptibility measurements in zero applied field reveal SMM behaviour of the complexes. Modest anisotropy barriers of 75.6 K and 92.5 K were determined for complexes 4-**1** and 4-**2**, respectively. The different natures of the N-donor ligands induce changes in the coordination microenvironment, giving rise to distinct dynamic magnetic behaviors. To establish a relationship between the molecular structure and SMM behavior, it will be imperative to conduct ab-initio calculations in the future.

5. Conclusion and outlook

This thesis explores the synthesis and magnetic properties of single-molecule magnets (SMMs) based on Dy(III) ions. Dy(III) ions are known for their strong spin-orbital coupling effect and high magnetic anisotropy, making them excellent candidates for making SMMs. The chapters follow a sequence of increasing nuclearity, starting from mononuclear to trinuclear Dy(III) complexes. A total of fifteen Dy(III) complexes, partially isotopologues were synthesized and their molecular structures were determined using single crystal X-ray crystallography. Slow relaxation of magnetizations in the complexes were probed by performing SQUID and μ-SQUID measurements.

Chapter 2 details the preparation and structural characterization of six mononuclear Dy(III) complexes—$Dy(thmd)_3(POPh_3)$ (2-**1**), $Dy(thmd)_3$(2,5-tpy) (2-**2**), $Dy(BTFA)_3$(2,5-tpy) (2-**3**), $Dy(NTFA)_3$(2,5-tpy) (2-**4**), $Dy(NTFA)_3$(2,5-tpy)·C_2H_5OH (2-**5**) and $Dy(hfac)_3$(2,5-tpy)(H_2O)·(2,5-tpy) (2-**6**). Two different neutral capping auxiliary ligands and four different *β*-diketonate ligands were used to prepare the complexes. The structures of the complexes exhibit various coordination numbers. The magnetic investigations showed that all six complexes exhibit SMM behavior with varying energy barriers, depending on the coordination environment surrounding the Dy(III) ions. The results demonstrate that subtle changes in the coordination environment resulting from changes in the substituents of *β*-diketonate ligands can modulate the magnetic properties.

In chapter 3, seven dinuclear Dy(III) complexes were characterized structurally and magnetically. They were synthesized using different bridging ligands and *β*-diketonate co-ligands. In complexes 3-**2** to 3-**5**, the various terminal *β*-diketonate coligands and the resultant changes in the coordination environment around Dy(III) centers result in varying dynamic magnetic behaviors. The ac studies of the isotopologue complexes 3-$\mathbf{2}^{(I = 5/2)}$, -$\mathbf{3}^{(I = 0)}$ and 3-$\mathbf{6}^{(I = 5/2)}$, 3-$\mathbf{7}^{(I = 0)}$ show that only the low temperature data are insensitive to the presence or absence of nuclear spins. This has become visible in the

μ-SQUID experiments of 3-**2**$^{(I = 5/2)}$, 3-**3**$^{(I = 0)}$ and 3-**6**$^{(I = 5/2)}$, 3-**7**$^{(I = 0)}$. μ-SQUID loops of 3-**2**$^{(I = 5/2)}$ and 3-**3**$^{(I = 0)}$ including the TAPE-bridging ligand exhibited a distinct step at zero field, which is a common feature observed in single-ion lanthanide-based SMMs due to faster relaxation around zero field, suggesting the absence of interactions between the two Dy(III) ions. This may be attributed to the relatively large distance between the Dy ions within the molecule. On the other hand, the μ-SQUID loops for 3-**6**$^{(I = 5/2)}$ and 3-**7**$^{(I = 0)}$ featuring a deprotonated enol mode O–bridge displayed S-shaped hysteresis loops, indicating an interaction between the two Dy(III) ions that leads to antiferromagnetically coupled Ising spins. The results showed that the nuclear spin and Dy···Dy distances (9.3326(5) Å, 9.3276(5) Å in 3-**2**$^{(I = 5/2)}$, 3-**3**$^{(I = 0)}$ *vs.* 4.065(5) Å, 4.064(3) Å in 3-**6**$^{(I = 5/2)}$, 3-**7**$^{(I = 0)}$) play a crucial part in the relaxation process, and a closer spacing between Dy(III) ions is preferred. These results must be considered for Ln-SMMs suggested for very low-temperature applications, like qubits and in particular qu*d*its, where the nuclear states embedded in lanthanide ions can be used as quantum registers. Electronic states mediating the coupling between nuclear states could potentially expand the number of nuclear states that can be utilized for implementing intricate quantum algorithms.

In Chapter 4, two trinuclear Dy(III) complexes were synthesized using two different bridging ligands. The magnetic properties of these complexes were investigated, and it was found that the complexes exhibited SMM behavior with energy barriers of U_{eff} = 75.6 K and 92.5 K. The results indicate that the choice of bridging ligand plays an important role in determining the magnetic properties of trinuclear Dy(III) complexes. Overall, this thesis emphasizes the significance of the coordination environment in defining the magnetic characteristics of Dy(III) SMMs and offers insights into how minute adjustments to the ligands can modulate the magnetic characteristics of SMMs. On the other hand, the nuclear states of a dimeric (or multimeric) complex can pair through interaction (dipolar or exchange) between the electronic spins, increasing the number of states that are possible in the molecular qu*d*it exponentially. Hence, to investigate how hyperfine interaction affects the operation of single-molecule magnets, it is necessary to introduce dysprosium isotopes instead of naturally occurring ones, as

well as carefully choose bridging ligands to create new binuclear or multinuclear complexes[224].

6. Materials and Equipment

Commercially available chemicals were used as received without further purification. Thin-layer chromatography (TLC) was performed on aluminum plates precoated with Merck 5735 silica gel 60 F254. Column chromatography was performed with Merck silica gel 60 (230-400 mesh). ^{1}H-NMR and ^{13}C-NMR spectra were recorded on a Bruker Ultrashield plus 500 spectrometer employing deuterated solvents. IR spectra were collected using a Nicolet Is50 FTIR (Fourier-transform infrared) spectrometer with ATR (attenuated total reflection) technology in the region of 4000-400 cm^{-1}.

Magnetic susceptibility measurements were performed using Quantum Design MPMS-XL SQUID magnetometers on polycrystalline material in the temperature range of 2-300 K under an applied DC magnetic field (H_{DC}) of 1 kOe. AC data were collected using an oscillating magnetic field of 3.5 Oe and frequencies between 1 and 1512 kHz. Magnetisation data was collected with a Quantum Design MPMS3 SQUID magnetometer equipped with a 7 T magnet. The samples were embedded in solid eicosane to prevent the torque. DC data were corrected for diamagnetic contributions from the eicosane and core diamagnetism employing Pascal's constants. Low temperature (0.03–5 K) magnetisation measurements were performed on single crystals using a μ-SQUID apparatus at different sweep rates between 0.128 and 0.005 T s^{-1}. The time resolution is approximately 1 ms. The magnetic field can be applied in any direction of the micro-SQUID plane with precision much better than 0.1° by separately driving three orthogonal coils. In order to ensure good thermalisation, each sample was fixed with apiezon grease.

The single-crystal X-ray diffraction data of the complexes were collected using STOE StadiVari 25 diffractometer with a Pilatus300K detector using GeniX 3D HF micro focus with MoKα radiation (λ= 0.71073 Å). The structures were solved using direct methods and were refined by full-matrix least square methods and using SHELX-2014[225] inbuilt in Olex2[226]. All non-hydrogen atoms were refined anisotropically,

whereas the hydrogen atoms were calculated geometrically, riding on their parent atoms. Continuous SHAPE analysis was used to determine the most probable coordination geometry around Ln(III) centers discussed in this thesis. The lowest possible values suggest the most probable coordination geometry.

Theoretical calculations For the Complete-active-space self-consistent field (CASSCF) calculations of compounds 3-**2**$^{(I = 5/2)}$, 3-**3**$^{(I = 0)}$, 3-**5**$^{(I = 5/2)}$ and 3-**7**$^{(I = 0)}$, we employed MOLCAS 8.2 program[227-229]. CASSCF-SO calculation was performed only on a single Dy^{III} fragment, the molecules are centrosymmetric, using the crystallographic coordinates obtained from the SCXRD structures with no further optimisations. Basis sets from ANO-RCC library[230-232] were employed with VTZP quality for Dy, VDZP quality for the coordinated N and O atoms, and VDZ quality for all distant atoms, using the second-order DKH transformation[233]. The molecular orbitals (MOs) were optimized in state-averaged CASSCF calculations. For this, the active space was defined by the nine 4f electrons in the seven 4f orbitals of Dy^{III}. Three calculations were performed independently for each possible spin state, where 21 roots were included for S = 5/2, 224 roots for S = 3/2, and 490 roots for S = 1/2 (RASSCF routine). The wavefunctions obtained from these CASSCF calculations were posteriorly mixed by spin orbit coupling, where all 21 of the S = 5/2 states, 128 of the S = 3/2 states, and 130 of the S = 1/2 states were included (RASSI routine[234]). The resulting spin orbit wavefunctions were decomposed into their CF wavefunctions in the $^{6}H_{15/2}$ basis, employing the SINGLE_ANISO[214,235] routine, and the magnetic susceptibility was calculated.

7. Abbreviations

General

AC	Alternating Current
CASSCF	Complete-active-space self-consistent field
DC	Direct Current
hf	hyperfine
IR	Infra-Red
KDs	Kramer's doublets
LF	Ligand field
NMR	Nuclear Magnetic Resonance
QIP	quantum information processing
QTM	Quantum Tunneling of Magnetization
Qubit	Quantum bit
RT	Room Temperature
SMMs	Single-Molecule Magnets
SIM	Single-Ion Magnet
SQUID	Super Conducting Quantum Interference Device
T_B	Blocking Temperature
TLC	Thin-layer chromatography
μ-SQUID	Mirco- Super Conducting Quantum Interference Device

Chemicals

2,5-tpy	2, 2′: 5′, 2″- Terpyridine
Bisbpy	2,2':5',5'':2'',2'''-Quaterpyridine
Bptz	3,6-bis(2-pyridyl)-1,2,4,5-tetrazine
BTFA	4,4,4-trifluoro-1-phenyl-1,3-butanedione
DCM	Dichloromethane
DMF	Dichloromethane

EDTA	ethylenediaminetetraacetic acid
Hfac	hexafluoroacetylacetonate
NTFA	4,4,4-Trifluoro-1-(2-naphthyl)-1,3-butanedione
PHZP	N'-[(E)-pyrazin-2-yl)methylidene]pyrazine-2-carbohydrazonate
$POPh_3$	triphenylphosphine oxide
TBB	1,3,5-tri(2,2′-bipyridin-5-yl)benzene
TBPB	1,3,5-tris{[2,2'-bipyridin-5-ylethynyl]phenyl}benzene
TAPE	1,6,7,12-Tetraazaperylene
Tmhd	2,2,6,6-tetramethyl-3,5-heptanedione
THF	Tetrahydrofuran

8. Bibliography

1. S. Singamaneni, V. N. Bliznyuk, C. Binek and E. Y. Tsymbal, *J. Mater. Chem.*, 2011, **21**.
2. N. Jones, *Nature.*, 2011, **472**, 22-24.
3. O. Gutfleisch, M. A. Willard, E. Bruck, C. H. Chen, S. G. Sankar and J. P. Liu, *Adv. Mater.*, 2011, **23**, 821-842.
4. P. W. Shor, *SIAM rev.*, 1999, **41**, 303-332.
5. L. K. Grover, *Phys. Rev. Lett.*, 1997, **79**, 4709.
6. J. S. Miller and D. Gatteschi, *Chem. Soc. Rev.*, 2011, **40**, 3065-3066.
7. K. S. Murray, *Aust. J. Chem.*, 2009, **62**, 1081-1101.
8. R. Sessoli, H. L. Tsai, A. R. Schake, S. Wang, J. B. Vincent, K. Folting, D. Gatteschi, G. Christou and D. N. Hendrickson, *J. Am. Chem. Soc.*, 1993, **115**, 1804-1816.
9. L. Thomas, F. Lionti, R. Ballou, D. Gatteschi, R. Sessoli and B. Barbara, *Nature.*, 1996, **383**, 145-147.
10. A. Caneschi, D. Gatteschi, N. Lalioti, C. Sangregorio, R. Sessoli, G. Venturi, A. Vindigni, A. Rettori, M. G. Pini and M. A. Novak, *Angew. Chem. Int. Ed.*, 2001, **40**, 1760-1763.
11. D.-F. Weng, Z.-M. Wang and S. Gao, *Chem. Soc. Rev.*, 2011, **40**, 3157-3181.
12. D. Gatteschi, R. Sessoli and J. Villain, *Molecular Nanomagnets*, Oxford University Press, 2006.
13. S. T. Liddle and J. van Slageren, *Chem. Soc. Rev.*, 2015, **44**, 6655-6669.
14. M. N. Leuenberger and D. Loss, *Nature.*, 2001, **410**, 789-793.
15. E. Moreno-Pineda, C. Godfrin, F. Balestro, W. Wernsdorfer and M. Ruben, *Chem. Soc. Rev.*, 2018, **47**, 501-513.
16. E. Moreno-Pineda and W. Wernsdorfer, *Nat. Rev. Phys.*, 2021, **3**, 645-659.
17. R. Sessoli, D. Gatteschi, A. Caneschi and M. Novak, *Nature*, 1993, **365**, 141-143.
18. T. Lis, *Acta Crystallogr. Sect. B: Struct. Science.*, 1980, **36**, 2042-2046.
19. C. J. Milios, A. Vinslava, W. Wernsdorfer, S. Moggach, S. Parsons, S. P. Perlepes, G. Christou and E. K. Brechin, *J. Am. Chem. Soc.*, 2007, **129**, 2754-2755.
20. H. Miyasaka, R. Clerac, W. Wernsdorfer, L. Lecren, C. Bonhomme, K. Sugiura and M. Yamashita, *Angew. Chem. Int. Ed.*, 2004, **43**, 2801-2805.

21. E. K. Brechin, *Chem. Commun.*, 2005, 5141-5153.

22. C. J. Milios, R. Inglis, R. Bagai, W. Wernsdorfer, A. Collins, S. Moggach, S. Parsons, S. P. Perlepes, G. Christou and E. K. Brechin, *Chem. Commun.*, 2007, 3476-3478.

23. D. E. Freedman, W. H. Harman, T. D. Harris, G. J. Long, C. J. Chang and J. R. Long, *J. Am. Chem. Soc.*, 2010, **132**, 1224-1225.

24. W. H. Harman, T. D. Harris, D. E. Freedman, H. Fong, A. Chang, J. D. Rinehart, A. Ozarowski, M. T. Sougrati, F. Grandjean and G. J. Long, *J. Am. Chem. Soc.*, 2010, **132**, 18115-18126.

25. P. H. Lin, N. C. Smythe, S. I. Gorelsky, S. Maguire, N. J. Henson, I. Korobkov, B. L. Scott, J. C. Gordon, R. T. Baker and M. Murugesu, *J. Am. Chem. Soc.*, 2011, **133**, 15806-15809.

26. S. Mossin, B. L. Tran, D. Adhikari, M. Pink, F. W. Heinemann, J. r. Sutter, R. K. Szilagyi, K. Meyer and D. J. Mindiola, *J. Am. Chem. Soc.*, 2012, **134**, 13651-13661.

27. T. Jurca, A. Farghal, P. H. Lin, I. Korobkov, M. Murugesu and D. S. Richeson, *J. Am. Chem. Soc.*, 2011, **133**, 15814-15817.

28. Y.-Y. Zhu, C. Cui, Y.-Q. Zhang, J.-H. Jia, X. Guo, C. Gao, K. Qian, S.-D. Jiang, B.-W. Wang, Z.-M. Wang and S. Gao, *Chem. Sci.*, 2013, **4**. 1802-1806.

29. Y. Rechkemmer, F. D. Breitgoff, M. van der Meer, M. Atanasov, M. Hakl, M. Orlita, P. Neugebauer, F. Neese, B. Sarkar and J. van Slageren, *Nat. Commun.*, 2016, **7**, 10467.

30. Z.-Y. Ding, Y.-S. Meng, Y. Xiao, Y.-Q. Zhang, Y.-Y. Zhu and S. Gao, *Inorg. Chem. Front.*, 2017, **4**, 1909-1916.

31. P. C. Bunting, M. Atanasov, E. Damgaard-Moller, M. Perfetti, I. Crassee, M. Orlita, J. Overgaard, J. van Slageren, F. Neese and J. R. Long, *Science.*, 2018, **362**.

32. R. C. Poulten, M. J. Page, A. G. Algarra, J. J. Le Roy, I. Lopez, E. Carter, A. Llobet, S. A. Macgregor, M. F. Mahon, D. M. Murphy, M. Murugesu and M. K. Whittlesey, *J. Am. Chem. Soc.*, 2013, **135**, 13640-13643.

33. D. Lomjansky, J. Moncol, C. Rajnak, J. Titis and R. Boca, *Chem. Commun.*, 2017, **53**, 6930-6932.

34. K. TI, *J. chem. soc., Chem. Commun.*, 1995, 2517.

35. D. Hendrickson, C. Grant and S. Castro, *Chem. Commun.*, 1998, 721-722.

36. S. L. Castro, Z. Sun, J. C. Bollinger, D. N. Hendrickson and G. Christou, *J. Chem. Soc., Chem. Commun.*, 1995, 2517-2518.

37. A. M. Ako, I. J. Hewitt, V. Mereacre, R. Clérac, W. Wernsdorfer, C. E. Anson and A. K. Powell, *Angew. Chem. Int. Ed.*, 2006, **118**, 5048-5051.

38. A. J. Tasiopoulos, A. Vinslava, W. Wernsdorfer, K. A. Abboud and G. Christou, *Angew. Chem. Int. Ed.*, 2004, **116**, 2169-2173.

39. E. Ruiz, J. Cirera, J. Cano, S. Alvarez, C. Loose and J. Kortus, *Chem. Commun.*, 2008, 52-54.

40. D. N. Woodruff, R. E. Winpenny and R. A. Layfield, *Chem. Rev.*, 2013, **113**, 5110-5148.

41. N. Ishikawa, M. Sugita, T. Ishikawa, S.-y. Koshihara and Y. Kaizu, *J. Am. Chem. Soc.*, 2003, **125**, 8694-8695.

42. N. Ishikawa, M. Sugita, T. Okubo, N. Tanaka, T. Iino and Y. Kaizu, *Inorg. Chem.*, 2003, **42**, 2440-2446.

43. N. Ishikawa, M. Sugita, N. Tanaka, T. Ishikawa, S.-y. Koshihara and Y. Kaizu, *Inorg. Chem.*, 2004, **43**, 5498-5500.

44. N. Ishikawa, Y. Mizuno, S. Takamatsu, T. Ishikawa and S.-y. Koshihara, *Inorg. Chem.*, 2008, **47**, 10217-10219.

45. Y. Chen, F. Ma, X. Chen, B. Dong, K. Wang, S. Jiang, C. Wang, X. Chen, D. Qi, H. Sun, B. Wang, S. Gao and J. Jiang, *Inorg. Chem.*, 2017, **56**, 13889-13896.

46. S. D. Jiang, B. W. Wang, G. Su, Z. M. Wang and S. Gao, *Angew. Chem. Int. Ed.*, 2010, **49**, 7448-7451.

47. K. Qian, J. J. Baldovi, S. D. Jiang, A. Gaita-Arino, Y. Q. Zhang, J. Overgaard, B. W. Wang, E. Coronado and S. Gao, *Chem. Sci.*, 2015, **6**, 4587-4593.

48. W.-B. Sun, B. Yan, Y.-Q. Zhang, B.-W. Wang, Z.-M. Wang, J.-H. Jia and S. Gao, *Inorg. Chem. Front.*, 2014, **1**, 503-509.

49. S. S. Liu, K. Lang, Y. Q. Zhang, Q. Yang, B. W. Wang and S. Gao, *Dalton Trans.*, 2016, **45**, 8149-8153.

50. Y. Bi, Y. N. Guo, L. Zhao, Y. Guo, S. Y. Lin, S. D. Jiang, J. Tang, B. W. Wang and S. Gao, *Chemistry.*, 2011, **17**, 12476-12481.

51. G. J. Chen, C. Y. Gao, J. L. Tian, J. Tang, W. Gu, X. Liu, S. P. Yan, D. Z. Liao and P. Cheng, *Dalton Trans.*, 2011, **40**, 5579-5583.

52. G. J. Chen, Y. N. Guo, J. L. Tian, J. Tang, W. Gu, X. Liu, S. P. Yan, P. Cheng and D. Z. Liao, *Chemistry.*, 2012, **18**, 2484-2487.

53. S. Bala, G. Z. Huang, Z. Y. Ruan, S. G. Wu, Y. Liu, L. F. Wang, J. L. Liu and M. L. Tong, *Chem. Commun.*, 2019, **55**, 9939-9942.

54. Y. C. Chen, J. L. Liu, L. Ungur, J. Liu, Q. W. Li, L. F. Wang, Z. P. Ni, L. F. Chibotaru, X. M. Chen and M. L. Tong, *J. Am. Chem. Soc.*, 2016, **138**, 2829-2837.

55. J. Liu, Y. C. Chen, J. L. Liu, V. Vieru, L. Ungur, J. H. Jia, L. F. Chibotaru, Y. Lan, W. Wernsdorfer, S. Gao, X. M. Chen and M. L. Tong, *J. Am. Chem. Soc.*, 2016, **138**, 5441-5450.

56. Y. C. Chen, J. L. Liu, Y. Lan, Z. Q. Zhong, A. Mansikkamaki, L. Ungur, Q. W. Li, J. H. Jia, L. F. Chibotaru, J. B. Han, W. Wernsdorfer, X. M. Chen and M. L. Tong, *Chemistry.*, 2017, **23**, 5708-5715.

57. J.-L. Liu, Y.-C. Chen, Y.-Z. Zheng, W.-Q. Lin, L. Ungur, W. Wernsdorfer, L. F. Chibotaru and M.-L. Tong, *Chem. Sci.*, 2013, **4**.

58. Y. S. Ding, N. F. Chilton, R. E. Winpenny and Y. Z. Zheng, *Angew. Chem. Int. Ed.*, 2016, **55**, 16071-16074.

59. Z. Zhu, C. Zhao, Q. Zhou, S. Liu, X.-L. Li, A. Mansikkamäki and J. Tang, *CCS. Chem.*, 2022, **4**, 3762-3771.

60. Z. H. Li, Y. Q. Zhai, W. P. Chen, Y. S. Ding and Y. Z. Zheng, *Chemmistry.*, 2019, **25**, 16219-16224.

61. A. B. Canaj, S. Dey, E. R. Marti, C. Wilson, G. Rajaraman and M. Murrie, *Angew. Chem. Int. Ed.*, 2019, **58**, 14146-14151.

62. Z. Zhu, C. Zhao, T. Feng, X. Liu, X. Ying, X. L. Li, Y. Q. Zhang and J. Tang, *J. Am. Chem. Soc.*, 2021, **143**, 10077-10082.

63. J. Li, S. Gomez-Coca, B. S. Dolinar, L. Yang, F. Yu, M. Kong, Y. Q. Zhang, Y. Song and K. R. Dunbar, *Inorg. Chem.*, 2019, **58**, 2610-2617.

64. Q. W. Li, R. C. Wan, Y. C. Chen, J. L. Liu, L. F. Wang, J. H. Jia, N. F. Chilton and M. L. Tong, *Chem. Commun.*, 2016, **52**, 13365-13368.

65. W. Zhao, H. Cui, X. Y. Chen, G. Yi, L. Chen, A. Yuan and C. L. Luo, *Dalton Trans.*, 2019, **48**, 5621-5626.

66. F. S. Guo, B. M. Day, Y. C. Chen, M. L. Tong, A. Mansikkamaki and R. A. Layfield, *Angew. Chem. Int. Ed.*, 2017, **56**, 11445-11449.

67. C. A. P. Goodwin, F. Ortu, D. Reta, N. F. Chilton and D. P. Mills, *Nature.*, 2017, **548**, 439-442.

68. F.-S. Guo, B. M. Day, Y.-C. Chen, M.-L. Tong, A. Mansikkamäki and R. A. Layfield, *Science.*, 2018, **362**, 1400-1403.

69. P. Evans, D. Reta, G. F. Whitehead, N. F. Chilton and D. P. Mills, *J. Am. Chem. Soc.*, 2019, **141**, 19935-19940.

70. M. J. Giansiracusa, A. K. Kostopoulos, D. Collison, R. E. Winpenny and N. F. Chilton, *Chem. Commun.*, 2019, **55**, 7025-7028.

71. J. C. Vanjak, B. O. Wilkins, V. Vieru, N. S. Bhuvanesh, J. H. Reibenspies, C. D. Martin, L. F. Chibotaru and M. Nippe, *J. Am. Chem. Soc.*, 2022, **144**, 17743-17747.

72. A. Bhunia, M. T. Gamer, L. Ungur, L. F. Chibotaru, A. K. Powell, Y. Lan, P. W. Roesky, F. Menges, C. Riehn and G. Niedner-Schatteburg, *Inorg. Chem.*, 2012, **51**, 9589-9597.

73. Y. N. Guo, G. F. Xu, W. Wernsdorfer, L. Ungur, Y. Guo, J. Tang, H. J. Zhang, L.

F. Chibotaru and A. K. Powell, *J. Am. Chem. Soc.*, 2011, **133**, 11948-11951.

74. J. D. Rinehart, M. Fang, W. J. Evans and J. R. Long, *Nat. Chem.*, 2011, **3**, 538-542.

75. J. D. Rinehart, M. Fang, W. J. Evans and J. R. Long, *J. Am. Chem. Soc.*, 2011, **133**, 14236-14239.

76. S. Demir, M. I. Gonzalez, L. E. Darago, W. J. Evans and J. R. Long, *Nat. Commun.*, 2017, **8**, 2144.

77. C. Aronica, G. Pilet, G. Chastanet, W. Wernsdorfer, J. F. Jacquot and D. Luneau, *Angew. Chem. Int. Ed.*, 2006, **45**, 4659-4662.

78. F. Habib, G. Brunet, V. Vieru, I. Korobkov, L. F. Chibotaru and M. Murugesu, *J. Am. Chem. Soc.*, 2013, **135**, 13242-13245.

79. W. M. Wang, H. X. Zhang, S. Y. Wang, H. Y. Shen, H. L. Gao, J. Z. Cui and B. Zhao, *Inorg. Chem.*, 2015, **54**, 10610-10622.

80. L. F. Chibotaru, L. Ungur and A. Soncini, *Angew. Chem. Int. Ed.*, 2008, **120**, 4194-4197.

81. L. Ungur, S. Y. Lin, J. Tang and L. F. Chibotaru, *Chem. Soc. Rev.*, 2014, **43**, 6894-6905.

82. J. Tang, I. Hewitt, N. T. Madhu, G. Chastanet, W. Wernsdorfer, C. E. Anson, C. Benelli, R. Sessoli and A. K. Powell, *Angew. Chem. Int. Ed.*, 2006, **118**, 1761-1765.

83. Y.-X. Wang, W. Shi, H. Li, Y. Song, L. Fang, Y. Lan, A. K. Powell, W. Wernsdorfer, L. Ungur, L. F. Chibotaru, M. Shen and P. Cheng, *Chem. Sci.*, 2012, **3**.

84. Y.-S. Meng, Y.-S. Qiao, M.-W. Yang, J. Xiong, T. Liu, Y.-Q. Zhang, S.-D. Jiang, B.-W. Wang and S. Gao, *Inorg. Chem. Front.*, 2020, **7**, 447-454.

85. J. Schnack, *Dalton Trans.*, 2010, **39**, 4677-4686.

86. V. Vieru, L. Ungur and L. F. Chibotaru, *J. Phys. Chem. Lett.*, 2013, **4**, 3565-3569.

87. G. Lu, Y. Liu, W. Deng, G.-Z. Huang, Y.-C. Chen, J.-L. Liu, Z.-P. Ni, M. Giansiracusa, N. F. Chilton and M.-L. Tong, *Inorg, Chem. Front.*, 2020, **7**, 2941-2948.

88. R. Westerström, J. Dreiser, C. Piamonteze, M. Muntwiler, S. Weyeneth, K. Krämer, S.-X. Liu, S. Decurtins, A. Popov and S. Yang, *Phys. Rev. B.*, 2014, **89**, 060406.

89. S.-Y. Lin, Y.-N. Guo, Y. Guo, L. Zhao, P. Zhang, H. Ke and J. Tang, *Chem. Commun.*, 2012, **48**, 6924-6926.

90. S.-G. Wu, C.-Y. Zhan, G.-Z. Huang, Z.-Y. Ruan, J.-L. Liu and M.-L. Tong, *Dalton Trans.*, 2020, **49**, 4164-4171.

91. K. R. Vignesh, A. Soncini, S. K. Langley, W. Wernsdorfer, K. S. Murray and G. Rajaraman, *Nat. Commun.*, 2017, **8**, 1023.

92. M. M. Hänninen, A. J. Mota, D. Aravena, E. Ruiz, R. Sillanpää, A. Camón, M. Evangelisti and E. Colacio, *Chem.–A Eur. J.*, 2014, **20**, 8410-8420.

93. D. I. Plokhov, A. I. Popov and A. K. Zvezdin, *Phys. Rev. B.*, 2011, **84**.

94. J. Luzon, K. Bernot, I. J. Hewitt, C. E. Anson, A. K. Powell and R. Sessoli, *Phys. Rev. Lett.*, 2008, **100**.

95. Z. Salman, S. R. Giblin, Y. Lan, A. K. Powell, R. Scheuermann, R. Tingle and R. Sessoli, *Phy. Rev. B.*, 2010, **82**.

96. D. I. Plokhov, A. K. Zvezdin and A. I. Popov, *Phys. Rev. B.*, 2011, **83**.

97. C. A. Gould, L. E. Darago, M. I. Gonzalez, S. Demir and J. R. Long, *Angew. Chem. Int. Ed.*, 2017, **56**, 10103-10107.

98. T. Pugh, F. Tuna, L. Ungur, D. Collison, E. J. McInnes, L. F. Chibotaru and R. A. Layfield, *Nat. Commun.*, 2015, **6**, 7492.

99. T. Pugh, V. Vieru, L. F. Chibotaru and R. A. Layfield, *Chem. Sci.*, 2016, **7**, 2128-2137.

100. T. Pugh, N. F. Chilton and R. A. Layfield, *Chem. Sci.*, 2017, **8**, 2073-2080.

101. M. Mohammadi, A. Niknafs and M. Eshghi, *Quantum Information Processing*, 2011, **10**, 241-256.

102. M. Luo and X. Wang, *Sci. China. Phys., Mechanics & Astronomy*, 2014, **57**, 1712-1717.

103. R. Giraud, W. Wernsdorfer, A. Tkachuk, D. Mailly and B. Barbara, *Phys. Rev. Lett.*, 2001, **87**, 057203.

104. D. Gatteschi, R. Sessoli and J. Villain, *Molecular nanomagnets*, Oxford University Press on Demand, 2006.

105. S. Thiele, F. Balestro, R. Ballou, S. Klyatskaya, M. Ruben and W. Wernsdorfer, *Sci.*, 2014, **344**, 1135-1138.

106. D. P. O'Leary, G. K. Brennen and S. S. Bullock, *Phys. Rev. A.*, 2006, **74**, 032334.

107. R. Vincent, S. Klyatskaya, M. Ruben, W. Wernsdorfer and F. Balestro, *Nature.*, 2012, **488**, 357-360.

108. S. Thiele, R. Vincent, M. Holzmann, S. Klyatskaya, M. Ruben, F. Balestro and W. Wernsdorfer, *Phys. Rev. Lett.*, 2013, **111**, 037203.

109. D. Aguila, L. A. Barrios, V. Velasco, O. Roubeau, A. Repollés, P. J. Alonso, J. Sesé, S. J. Teat, F. Luis and G. Aromí, *J. Am. Chem. Soc.*, 2014, **136**, 14215-14222.

110. K. S. Pedersen, A.-M. Ariciu, S. McAdams, H. Weihe, J. Bendix, F. Tuna and S. Piligkos, *J. Am. Chem. Soc.*, 2016, **138**, 5801-5804.

111. M. Affronte, F. Troiani, A. Ghirri, A. Candini, M. Evangelisti, V. Corradini, S. Carretta, P. Santini, G. Amoretti and F. Tuna, *J. Phys. D: Appl. Phys.*, 2007, **40**, 2999.

112. G. Aromí, D. Aguilà, P. Gamez, F. Luis and O. Roubeau, *Chem. Soc. Rev*, 2012, **41**, 537-546.

113. F. Pointillart, K. Bernot, G. Poneti and R. Sessoli, *Inorg. Chem.*, 2012, **51**, 12218-12229.

114. S. Sakaue, A. Fuyuhiro, T. Fukuda and N. Ishikawa, *Chem. Commun.*, 2012, **48**, 5337-5339.

115. N. Ishikawa, S. Otsuka and Y. Kaizu, *Angew. Chem. Int. Ed.*, 2005, **117**, 741-743.

116. J. D. Rinehart, M. Fang, W. J. Evans and J. R. Long, *J. Am. Chem. Soc.*, 2011, **133**, 14236-14239.

117. S. Demir, J. M. Zadrozny, M. Nippe and J. R. Long, *J. Am. Chem. Soc.*, 2012, **134**, 18546-18549.

118. K. Katoh, Y. Horii, N. Yasuda, W. Wernsdorfer, K. Toriumi, B. K. Breedlove and M. Yamashita, *Dalton Trans.*, 2012, **41**, 13582-13600.

119. P. Hu, M. Zhu, X. Mei, H. Tian, Y. Ma, L. Li and D. Liao, *Dalton Trans.*, 2012, **41**, 14651-14656.

120. E. Coronado, C. Gimenez-Saiz, A. Recuenco, A. Tarazon, F. M. Romero, A. Camon and F. Luis, *Inorg. Chem.*, 2011, **50**, 7370-7372.

121. K. Katoh, T. Kajiwara, M. Nakano, Y. Nakazawa, W. Wernsdorfer, N. Ishikawa, B. K. Breedlove and M. Yamashita, *Chem.–A Eur. J.*, 2011, **17**, 117-122.

122. M. Gonidec, D. B. Amabilino and J. Veciana, *Dalton Trans.*, 2012, **41**, 13632-13639.

123. S. Takamatsu, T. Ishikawa, S.-y. Koshihara and N. Ishikawa, *Inorg. Chem.*, 2007, **46**, 7250-7252.

124. M. Gonidec, E. S. Davies, J. McMaster, D. B. Amabilino and J. Veciana, *J. Am. Chem. Soc.*, 2010, **132**, 1756-1757.

125. F. Branzoli, P. Carretta, M. Filibian, G. Zoppellaro, M. J. Graf, J. R. Galan-Mascaros, O. Fuhr, S. Brink and M. Ruben, *J. Am. Chem. Soc.*, 2009, **131**, 4387-4396.

126. X.-L. Wang, L.-C. Li and D.-Z. Liao, *Inorg. Chem.*, 2010, **49**, 4735-4737.

127. P.-E. Car, M. Perfetti, M. Mannini, A. Favre, A. Caneschi and R. Sessoli, *Chem. Commun.*, 2011, **47**, 3751-3753.

128. A. Bhunia, M. T. Gamer, L. Ungur, L. F. Chibotaru, A. K. Powell, Y. Lan, P. W. Roesky, F. Menges, C. Riehn and G. Niedner-Schatteburg, *Inorg. Chem.*, 2012, **51**, 9589-9597.

129. F. Habib, P.-H. Lin, J. Long, I. Korobkov, W. Wernsdorfer and M. Murugesu, *J. Am. Chem. Soc.*, 2011, **133**, 8830-8833.

130. P.-H. Lin, W.-B. Sun, M.-F. Yu, G.-M. Li, P.-F. Yan and M. Murugesu, *Chem. Commun.*, 2011, **47**, 10993-10995.

131. G. Brunet, F. Habib, I. Korobkov and M. Murugesu, *Inorg. Chem.*, 2015, **54**, 6195-6202.

132. U. J. Williams, B. D. Mahoney, P. T. DeGregorio, P. J. Carroll, E. Nakamaru-Ogiso, J. M. Kikkawa and E. J. Schelter, *Chem. Commun.*, 2012, **48**, 5593-5595.

133. F. H. Allen, *Acta Crystallogr. Sect. B: Struct. Sci.*, 2002, **58**, 380-388.

134. P.-H. Lin, I. Korobkov, T. J. Burchell and M. Murugesu, *Dalton Trans.*, 2012, **41**, 13649-13655.

135. A. Venugopal, F. Tuna, T. P. Spaniol, L. Ungur, L. F. Chibotaru, J. Okuda and R. A. Layfield, *Chem. Commun.*, 2013, **49**, 901-903.

136. Y.-N. Guo, X.-H. Chen, S. Xue and J. Tang, *Inorg. Chem.*, 2011, **50**, 9705-9713.

137. K. R. Meihaus, J. D. Rinehart and J. R. Long, *Inorg. Chem.*, 2011, **50**, 8484-8489.

138. L. Zou, L. Zhao, P. Chen, Y.-N. Guo, Y. Guo, Y.-H. Li and J. Tang, *Dalton Trans.*, 2012, **41**, 2966-2971.

139. M. Waters, F. Moro, I. Krivokapic, J. McMaster and J. van Slageren, *Dalton Trans.*, 2012, **41**, 1128-1130.

140. H. Wang, K. Wang, J. Tao and J. Jiang, *Chem. Commun.*, 2012, **48**, 2973-2975.

141. J. Long, F. Habib, P.-H. Lin, I. Korobkov, G. Enright, L. Ungur, W. Wernsdorfer, L. F. Chibotaru and M. Murugesu, *J. Am. Chem. Soc.*, 2011, **133**, 5319-5328.

142. G. Cucinotta, M. Perfetti, J. Luzon, M. Etienne, P. E. Car, A. Caneschi, G. Calvez, K. Bernot and R. Sessoli, *Angew. Chem. Int. Ed.*, 2012, **51**, 1606-1610.

143. M. E. Boulon, G. Cucinotta, J. Luzon, C. Degl'Innocenti, M. Perfetti, K. Bernot, G. Calvez, A. Caneschi and R. Sessoli, *Angew. Chem. Int. Ed.*, 2013, **52**, 350-354.

144. C. Ritchie, M. Speldrich, R. W. Gable, L. Sorace, P. Kögerler and C. Boskovic, *Inorg. Chem.*, 2011, **50**, 7004-7014.

145. G.-J. Chen, C.-Y. Gao, J.-L. Tian, J. Tang, W. Gu, X. Liu, S.-P. Yan, D.-Z. Liao and P. Cheng, *Dalton Trans.*, 2011, **40**, 5579-5583.

146. M. Menelaou, F. Ouharrou, L. Rodríguez, O. Roubeau, S. J. Teat and N. Aliaga-Alcalde, *Chem.–A Eur. J.*, 2012, **18**, 11545-11549.

147. J. D. Rinehart, M. Fang, W. J. Evans and J. R. Long, *Nat. Chem.*, 2011, **3**, 538-542.

148. A. Watanabe, A. Yamashita, M. Nakano, T. Yamamura and T. Kajiwara, *Chem.–*

A Eur. J., 2011, **17**, 7428-7432.

149. K. Katoh, K. Umetsu, K. Breedlove Brian and M. Yamashita, *Sci. China Chem.*, 2012, **55**, 918-925.

150. S. D. Jiang, B. W. Wang, G. Su, Z. M. Wang and S. Gao, *Angew. Chem. Int. Ed.*, 2010, **122**, 7610-7613.

151. Y.-N. Guo, G.-F. Xu, W. Wernsdorfer, L. Ungur, Y. Guo, J. Tang, H.-J. Zhang, L. F. Chibotaru and A. K. Powell, *J. Am. Chem. Soc.*, 2011, **133**, 11948-11951.

152. F. Pointillart, S. Klementieva, V. Kuropatov, Y. Le Gal, S. Golhen, O. Cador, V. Cherkasov and L. Ouahab, *Chem. Commun.*, 2012, **48**, 714-716.

153. F. Tuna, C. A. Smith, M. Bodensteiner, L. Ungur, L. F. Chibotaru, E. J. McInnes, R. E. Winpenny, D. Collison and R. A. Layfield, *Angew. Chem. Int. Ed.*, 2012, **124**, 7082-7086.

154. E. Moreno-Pineda, M. Damjanovic, O. Fuhr, W. Wernsdorfer and M. Ruben, *Angew. Chem. Int. Ed.*, 2017, **56**, 9915-9919.

155. Y. Kishi, F. Pointillart, B. Lefeuvre, F. Riobé, B. Le Guennic, S. Golhen, O. Cador, O. Maury, H. Fujiwara and L. Ouahab, *Chem. Commun.*, 2017, **53**, 3575-3578.

156. F. Pointillart, K. Bernot, S. Golhen, B. Le Guennic, T. Guizouarn, L. Ouahab and O. Cador, *Angew. Chem. Int. Ed.*, 2015, **127**, 1524-1527.

157. W. Wernsdorfer, T. Ohm, C. Sangregorio, R. Sessoli, D. Mailly and C. Paulsen, *Phys. Rev. Lett.*, 1999, **82**, 3903.

158. E. Moreno-Pineda, S. Klyatskaya, P. Du, M. Damjanovic, G. Taran, W. Wernsdorfer and M. Ruben, *Inorg. Chem.*, 2018, **57**, 9873-9879.

159. G. Christou, D. Gatteschi, D. N. Hendrickson and R. Sessoli, *MRS Bull.*, 2000, **25**, 66-71.

160. L. Bogani and W. Wernsdorfer, *Nat. Mater.*, 2008, **7**, 179-186.

161. M. Mannini, F. Pineider, C. Danieli, F. Totti, L. Sorace, P. Sainctavit, M.-A. Arrio, E. Otero, L. Joly and J. C. Cezar, *Nature.*, 2010, **468**, 417-421.

162. W. Wernsdorfer, N. Aliaga-Alcalde, D. N. Hendrickson and G. Christou, *Nature*, 2002, **416**, 406-409.

163. D. Gatteschi and R. Sessoli, *Angew. Chem. Int. Ed.*, 2003, **42**, 268-297.

164. W. Wernsdorfer and R. Sessoli, *science*, 1999, **284**, 133-135.

165. C. Benelli and D. Gatteschi, *Chem. Rev.*, 2002, **102**, 2369-2388.

166. J. D. Rinehart and J. R. Long, *Chem. Sci.*, 2011, **2**, 2078-2085.

167. L. Sorace, C. Benelli and D. Gatteschi, *Chem. Soc. Rev.*, 2011, **40**, 3092-3104.

168. Y. Chen, F. Ma, X. Chen, B. Dong, K. Wang, S. Jiang, C. Wang, X. Chen, D. Qi and H. Sun, *Inorg. Chem.*, 2017, **56**, 13889-13896.

169. X. Liu, X. Ma, W. Yuan, P. Cen, Y.-Q. Zhang, J. s. Ferrando-Soria, G. Xie, S. Chen and E. Pardo, *Inorg. Chem.*, 2018, **57**, 14843-14851.

170. P. Cen, X. Liu, Y.-Q. Zhang, J. Ferrando-Soria, G. Xie, S. Chen and E. Pardo, *Dalton Trans.*, 2020, **49**, 808-816.

171. W.-B. Sun, P.-F. Yan, S.-D. Jiang, B.-W. Wang, Y.-Q. Zhang, H.-F. Li, P. Chen, Z.-M. Wang and S. Gao, *Chem. Sci.*, 2016, **7**, 684-691.

172. X. Liu, F. Li, X. Ma, P. Cen, S. Luo, Q. Shi, S. Ma, Y. Wu, C. Zhang and Z. Xu, *Dalton Trans.*, 2017, **46**, 1207-1217.

173. Y. Wu, D. Tian, J. Ferrando-Soria, J. Cano, L. Yin, Z. Ouyang, Z. Wang, S. Luo, X. Liu and E. Pardo, *Inorg. Chem. Front.*, 2019, **6**, 848-856.

174. P. Zhang, L. Zhang, C. Wang, S. Xue, S. Y. Lin and J. Tang, *J. Am. Chem. Soc.*, 2014, **136**, 4484-4487.

175. P. B. Jin, Y. Q. Zhai, K. X. Yu, R. E. P. Winpenny and Y. Z. Zheng, *Angew. Chem. Int. Ed.*, 2020, **59**, 9350-9354.

176. K. L. Harriman, J. L. Brosmer, L. Ungur, P. L. Diaconescu and M. Murugesu, *J. Am. Chem. Soc.*, 2017, **139**, 1420-1423.

177. Y. C. Chen and M. L. Tong, *Chem Sci*, 2022, **13**, 8716-8726.

178. S. Soman, G. Singh Bindra, A. Paul, R. Groarke, J. C. Manton, F. M. Connaughton, M. Schulz, D. Dini, C. Long, M. T. Pryce and J. G. Vos, *Dalton Trans.*, 2012, **41**, 12678-12680.

179. X. Yao, P. Yan, G. An, C. Shi, Y. Li and G. Li, *New J. Chem.*, 2018, **42**, 8438-8444.

180. S. Katagiri, Y. Tsukahara, Y. Hasegawa and Y. Wada, *Bull. Chem. Soc. Jpn.*, 2007, **80**, 1492-1503.

181. S. Biswas, S. Das, J. Acharya, V. Kumar, J. van Leusen, P. Kogerler, J. M. Herrera, E. Colacio and V. Chandrasekhar, *Chemistry*, 2017, **23**, 5154-5170.

182. T. Pugh, N. F. Chilton and R. A. Layfield, *Chem Sci*, 2017, **8**, 2073-2080.

183. P. P. Cen, S. Zhang, X. Y. Liu, W. M. Song, Y. Q. Zhang, G. Xie and S. P. Chen, *Inorg. Chem.*, 2017, **56**, 3644-3656.

184. J. L. Liu, Y. C. Chen and M. L. Tong, *Chem. Soc. Rev.*, 2018, **47**, 2431-2453.

185. D. Gatteschi and R. Sessoli, *Angew. Chem. Int. Ed.*, 2003, **42**, 268-297.

186. N. Ishikawa, M. Sugita and W. Wernsdorfer, *Angew. Chem. Int. Ed.*, 2005, **44**, 2931-2935.

187. C. A. P. Goodwin, D. Reta, F. Ortu, N. F. Chilton and D. P. Mills, *J. Am. Chem. Soc.*, 2017, **139**, 18714-18724.

188. F. Habib and M. Murugesu, *Chem. Soc. Rev.*, 2013, **42**, 3278-3288.

189. G. F. Xu, Q. L. Wang, P. Gamez, Y. Ma, R. Clerac, J. Tang, S. P. Yan, P. Cheng

and D. Z. Liao, *Chem. Commun.*, 2010, **46**, 1506-1508.

190. D. Li, M. M. Ding, Y. Huang, D. F. Tello Yepes, H. Li, Y. Li, Y. Q. Zhang and J. Yao, *Dalton Trans.*, 2021, **50**, 217-228.

191. K. Pramanik, Y.-C. Sun, P. Brandão, N. C. Jana, X.-Y. Wang and A. Panja, *New J. Chem.*, 2022, **46**, 11722-11733.

192. P. Cen, X. Liu, Y. Q. Zhang, J. Ferrando-Soria, G. Xie, S. Chen and E. Pardo, *Dalton Trans.*, 2020, **49**, 808-816.

193. M. Luo and X. Wang, *Sci. China Phys., Mech. & Astron.*, 2014, **57**, 1712-1717.

194. N. Das, G. S. Bindra, A. Paul, J. G. Vos, M. Schulz and M. T. Pryce, *Chemistry*, 2017, **23**, 5330-5337.

195. S. Alvarez, P. Alemany, D. Casanova, J. Cirera, M. Llunell and D. Avnir, *Coord. Chem. Rev.*, 2005, **249**, 1693-1708.

196. P. Richardson, R. Marin, Y. Zhang, B. Gabidullin, J. Ovens, J. O. Moilanen and M. Murugesu, *Chemistry*, 2021, **27**, 2361-2370.

197. L. Panayiotidou, C. Drouza, N. Arabatzis, P. Lianos, E. Stathatos, Z. Viskadourakis, J. Giapintzakis and A. D. Keramidas, *Polyhedron*, 2013, **64**, 308-320.

198. Y. N. Guo, G. F. Xu, Y. Guo and J. Tang, *Dalton Trans.*, 2011, **40**, 9953-9963.

199. D. Reta and N. F. Chilton, *Phys. Chem. Chem. Phys.*, 2019, **21**, 23567-23575.

200. K. Chakarawet, P. C. Bunting and J. R. Long, *J. Am. Chem. Soc.*, 2018, **140**, 2058-2061.

201. E. Moreno-Pineda, G. Taran, W. Wernsdorfer and M. Ruben, *Chem Sci*, 2019, **10**, 5138-5145.

202. Y. C. Chen, J. L. Liu, W. Wernsdorfer, D. Liu, L. F. Chibotaru, X. M. Chen and M. L. Tong, *Angew. Chem. Int. Ed.*, 2017, **56**, 4996-5000.

203. F. Habib, P. H. Lin, J. Long, I. Korobkov, W. Wernsdorfer and M. Murugesu, *J. Am. Chem. Soc.*, 2011, **133**, 8830-8833.

204. J. Long, F. Habib, P. H. Lin, I. Korobkov, G. Enright, L. Ungur, W. Wernsdorfer, L. F. Chibotaru and M. Murugesu, *J. Am. Chem. Soc.*, 2011, **133**, 5319-5328.

205. E. M. Pineda, Y. Lan, O. Fuhr, W. Wernsdorfer and M. Ruben, *Chem Sci*, 2017, **8**, 1178-1185.

206. M. Dolai, E. Moreno-Pineda, W. Wernsdorfer, M. Ali and A. Ghosh, *J. Phys. Chem. A*, 2021, **125**, 8230-8237.

207. W. Wernsdorfer, N. E. Chakov and G. Christou, *Phys. Rev. B*, 2004, **70**.

208. W. Wernsdorfer, *Supercond. Sci. Technol.*, 2009, **22**.

209. L. M. Toma, R. Lescouezec, J. Pasan, C. Ruiz-Perez, J. Vaissermann, J. Cano, R. Carrasco, W. Wernsdorfer, F. Lloret and M. Julve, *J. Am. Chem. Soc.*, 2006,

128, 4842-4853.

210. K. Liu, H. Li, X. Zhang, W. Shi and P. Cheng, *Inorg. Chem.*, 2015, **54**, 10224-10231.

211. G. M. Risica, V. Vieru, B. O. Wilkins, T. P. Latendresse, J. H. Reibenspies, N. S. Bhuvanesh, G. P. Wylie, L. F. Chibotaru and M. Nippe, *Angew. Chem. Int. Ed.*, 2020, **59**, 13335-13340.

212. J. Long, F. Habib, P. H. Lin, I. Korobkov, G. Enright, L. Ungur, W. Wernsdorfer, L. F. Chibotaru and M. Murugesu, *J. Am. Chem. Soc.*, 2011, **133**, 5319-5328.

213. S. A. Sulway, R. A. Layfield, F. Tuna, W. Wernsdorfer and R. E. Winpenny, *Chem. Comm.*, 2012, **48**, 1508-1510.

214. L. F. Chibotaru and L. Ungur, *J. Chem. Phys.*, 2012, **137**, 064112.

215. W. W. Lukens and M. D. Walter, *Inorg. Chem.*, 2010, **49**, 4458-4465.

216. N. F. Chilton, R. P. Anderson, L. D. Turner, A. Soncini and K. S. Murray, *J. Comput. Chem.*, 2013, **34**, 1164-1175.

217. A. Abragam and B. Bleaney, *Electron paramagnetic resonance of transition ions*, Oxford University Press, 2012.

218. S. Stoll and A. Schweiger, *J. of magne resonance.*, 2006, **178**, 42-55.

219. R. Grindell, V. Vieru, T. Pugh, L. F. Chibotaru and R. A. Layfield, *Dalton Trans.*, 2016, **45**, 16556-16560.

220. M. Gysler, F. El Hallak, L. Ungur, R. Marx, M. Hakl, P. Neugebauer, Y. Rechkemmer, Y. Lan, I. Sheikin, M. Orlita, C. E. Anson, A. K. Powell, R. Sessoli, L. F. Chibotaru and J. van Slageren, *Chem Sci*, 2016, **7**, 4347-4354.

221. W. Dai, L. T. Lee, A. Schutz, B. Zelenay, Z. Zheng, A. Borgschulte, M. Dobeli, W. Abuillan, O. V. Konovalov, M. Tanaka and A. D. Schluter, *Langmuir*, 2017, **33**, 1646-1654.

222. P. Das, A. Kumar, A. Chowdhury and P. S. Mukherjee, *ACS Omega*, 2018, **3**, 13757-13771.

223. N. Kobayashi and M. Kijima, *J. Mater. Chem.*, 2008, **18**, 1037-1045.

224. W. Wernsdorfer and M. Ruben, *Adv. Mater.*, 2019, **31**, 1806687.

225. G. M. Sheldrick, *Acta Crystallogr A*, 2008, **64**, 112-122.

226. O. V. Dolomanov, L. J. Bourhis, R. J. Gildea, J. A. K. Howard and H. Puschmann, *J. Appl. Crystallogr.*, 2009, **42**, 339-341.

227. F. Aquilante, J. Autschbach, R. K. Carlson, L. F. Chibotaru, M. G. Delcey, L. De Vico, I. Fdez Galvan, N. Ferre, L. M. Frutos, L. Gagliardi, M. Garavelli, A. Giussani, C. E. Hoyer, G. Li Manni, H. Lischka, D. Ma, P. A. Malmqvist, T. Muller, A. Nenov, M. Olivucci, T. B. Pedersen, D. Peng, F. Plasser, B. Pritchard, M. Reiher, I. Rivalta, I. Schapiro, J. Segarra-Marti, M. Stenrup, D. G. Truhlar,

L. Ungur, A. Valentini, S. Vancoillie, V. Veryazov, V. P. Vysotskiy, O. Weingart, F. Zapata and R. Lindh, *J. Comput. Chem.*, 2016, **37**, 506-541.

228. D. Ma, G. Li Manni and L. Gagliardi, *J. Chem. Phys.*, 2011, **135**, 044128.

229. P. E. M. Siegbahn, J. Almlöf, A. Heiberg and B. O. Roos, *J. Chem. Phys.*, 1981, **74**, 2384-2396.

230. B. O. Roos, R. Lindh, P. A. Malmqvist, V. Veryazov and P. O. Widmark, *J. Phys. Chem. A*, 2004, **108**, 2851-2858.

231. B. O. Roos, R. Lindh, P. A. Malmqvist, V. Veryazov, P. O. Widmark and A. C. Borin, *J. Phys. Chem. A*, 2008, **112**, 11431-11435.

232. P. Widmark, *A. Acta*, 1990, **77**, 291.

233. D. Peng and K. Hirao, *J. Chem. Phys.*, 2009, **130**, 044102.

234. P. AA, *Chem. Phys. Lett*, 2002, **357**, 230.

235. L. Ungur and L. F. Chibotaru, *Chemistry*, 2017, **23**, 3708-3718.

9. Appendix

9.1 Publications

1. **Ting-Ting Ruan**, Eufemio Moreno-Pineda, Michael Schulze, Sören Schlittenhardt, Matthias Kirste, Hans-Jürgen Holdt, Senthil Kumar Kuppusamy,Wolfgang Wernsdorfer, and Mario Ruben. Hilbert Space in Isotopologues Dy(III) SMM Dimers: Dipole Interaction Limit in $[^{163/164}Dy_2(tmhd)_6(tape)]^0$ Complexes. Submitted to Inorg. Chem.

2. **Ting-Ting Ruan**, Chun-Li Hu, Jiang-He Feng, Fei-Fei Mao, and Jiang-Gao Mao. Three Cadmium Tartratoborates with Good Second Harmonic Generation (SHG) or Luminescence Performances. Inorg. Chem. 2019, 58, 594-602.

3. **Ting-Ting Ruan**, Wen-Wen Wang, Chun-Li Hu, Xiang Xu and Jiang-Gao Mao. $Pb_4(BO_3)_2(SO_4)$ and $Pb_2[(BO_2)(OH)](SO_4)$: new lead(II) borate-sulfate mixed-anion compounds with two types of 3D network structures. J. Solid State Chem. 260 (2018) 39-45.

4. Wen-Wen Wang, **Ting-Ting Ruan**, Xiang Xu, Jiang-Gao Mao. $AgCu(IO_3)_3$: Synthesis, Crystal Structure and Magnetic Property. Chines. J. Struct. Chem., 2017, 36, 1456-1464.

5. Dong Yan, Fei- Fei Mao, **Ting-Ting Ruan** and Jiang-Gao Mao, Two tartratoborates with hybrid anionic groups from unusual condensation reactions. Dalton Trans, 2017, 46, 7361-7368.

Conference Presentation:

1. **Ting-Ting Ruan**, Sagar Paul, Michael Schulze, Wolfgang Wernsdorfer and Mario Ruben Multinuclear Isotopologues: Nuclear Spin Qudit Cooperativity Induced by Electronic Spin Coupling. 3MET PhD Meeting 12.10.2022, Heidelberg, Germany.

2. **Ting-Ting Ruan** and Jiang-Gao Mao. One Tartratoborate with Hybrid Anionic Groups from Unusual Condensation Reactions. The 7th Chinese Coordination Chemistry Conference, China Chemical Society, July 2017, Da Lian, China.

9.2 Acknowledgements

First of all, I would like to express my sincere appreciation to all the people who accompanied and helped me during this long but brief period of my Ph.D. life.

My deepest gratitude goes first and foremost to Prof. Mario Ruben, my supervisor, for allowing me to work in his group, who has offered me numerous valuable comments and suggestions with incomparable patience and encouraged me profoundly throughout my studies. Completing this thesis was only possible with his patient guidance, continuous support, and encouragement.

I would also like to thank Dr. Eufemio Moreno Pineda, Dr. Asato Mizuno, and Dr. Svetlana Klyatskaya for supervising and teaching me all the instruments, experiments, and fundamental knowledge when I started working in the lab, always taking time to answer my questions and giving me much advice, helpful discussion, ideas, and guidance during the studies.

I am very grateful to Dr. Senthil Kumar Kuppusamy and Dr. Eufemio Moreno Pineda for his guidance, ongoing study advice, patience, and effective counter-reading of my Ph.D. thesis and publication drafts.

I would also like to thank all my lab mates. I thank Dr. Eufemio Moreno Pineda, Dr. Asato Mizuno, and Sören Schlittenhardt for assisting me with the X-ray measurements, calculation, and simulation when I had problems. I thank Dr. Liang Xu and Dr. Nico Balzer for sharing many experiences and suggestions on organic synthesis work with me. I thank Dr. Conchi Molina Jiron de Moreno, Dr. Nithin Suryadevara, Shirin Shakouri, Sai Prasanna Kumar, Patrick Lawes, Zhaoyang Jing, Joe Komeda, Yaorong Chen, Dr. Camila Gouveia Barbosa, Moritz Rodert, Dr. Michal Valasek, Dr. Pinar Arpacay, who have provided a stimulating and collaborative environment in which to work. Most importantly, thank you for being my friend. Their friendship, encouragement, and support have been essential to my Ph.D. experience. I feel fortunate to have had the opportunity to work with such an outstanding group of people.

I also would like to express my gratitude to Mr. Hagen Sparrenberger for his assistance and for supplying the lab supplies.

I would also like to thank our collaborators - Prof. Wolfgang Wernsdorfer group from Physikalisches Institut, especially Michael Schulze, for performing μ-SQUID experiments with our samples provided.

I would like to thank Prof. Dieter Fenske, Dr. Olaf Fuhr for measuring the crystal for single crystal XRD measurements. I also thank Nicolai Bartnick for help in the elemental analysis.

I thank my friends, Rui, Qianqian, Yimin, Zhenyu, Ningning, Tongying, Feifei, Mingli, Baolin, Jin, Jinyu, Xiaoyu, Minting, Yucheng, for their friendship, their kindness, and their support.

I would like to thank the China Scholarship Council (CSC) for funding my whole Ph. D period and offering this great opportunity to study in Germany.

Last, I would like to express my gratitude to my beloved family and boyfriend for their unwavering love, support, and encouragement throughout my Ph. D journey. My parents' tireless efforts to provide me with the best education and opportunities, their unconditional love and belief in me have given me the confidence and resilience to overcome challenges and persevere towards my goals. I must thank my brother for accompanying my parents, caring for them, and supporting me. I thank my Indian brother Sai Prasanna Kumar for caring for me, sharing happiness, and bringing many joys to my life. I would also like to thank my boyfriend for his support and tolerance during difficult times. I am forever grateful for his presence in my life and for the unwavering strength and inspiration he provided me. I could not have done this without them; their tolerance, understanding, and faith in me have been a continuous source of courage.